Version 1.1

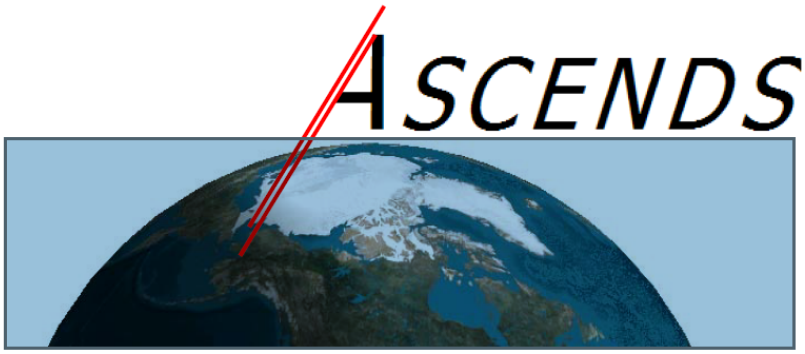

Active Sensing of CO_2 Emissions over Nights, Days, and Seasons (ASCENDS) Mission

Science Mission Definition Study

Draft

ASCENDS Ad Hoc Science Definition Team:

Kenneth W. Jucks,[1] Steven Neeck,[2] James B. Abshire,[3] David F. Baker,[4] Edward V. Browell,[5] Abhishek Chatterjee,[6] David Crisp,[7] Sean M. Crowell,[8] Scott Denning,[9] Dorit Hammerling,[10] Fenton Harrison,[11] Jason J. Hyon,[12] Stephan R. Kawa,[13] Bing Lin,[14] Byron L. Meadows,[15] Robert T. Menzies,[16] Anna Michalak,[17] Berrien Moore,[18] Keith E. Murray,[19] Lesley E. Ott,[20] Peter Rayner,[21] Otilia I. Rodriguez,[22] Andrew Schuh,[23] Yoichi Shiga,[24] Gary D. Spiers,[25] James Shih Wang,[26] and T. Scott Zaccheo.[27]

August 19, 2015

1: NASA; 2: NASA; 3: Goddard Space Flight Center (GSFC); 4: Cooperative Institute for Research in the Atmosphere (CIRA) at Colorado State University (CSU); 5: Langley Research Center (LaRC)/STARSS-II Affiliate; 6: Universities Space Research Association/Goddard Space Flight Center (USRA/GSFC); 7: Jet Propulsion Laboratory (JPL), California Institute of Technology; 8: University of Oklahoma (OU); 9: Colorado State University (CSU); 10: Institute for Mathematics Applied to Geosciences (IMAGe) at the National Center for Atmospheric Research (NCAR); 11: Langley Research Center (LaRC); 12: Jet Propulsion Laboratory (JPL), California Institute of Technology; 13: Goddard Space Flight Center (GSFC); 14: Langley Research Center (LaRC); 15: Langley Research Center (LaRC); 16: Jet Propulsion Laboratory (JPL), California Institute of Technology; 17: Department of Global Ecology at the Carnegie Institution for Science; 18: University of Oklahoma (OU); 19: Langley Research Center (LaRC); 20: Goddard Space Flight Center (GSFC); 21: University of Melbourne; 22: Goddard Space Flight Center (GSFC); 23: Colorado State University (CSU); 24: Stanford University & Department of Global Ecology at the Carnegie Institution for Science; 25: Jet Propulsion Laboratory (JPL), California Institute of Technology; 26: Universities Space Research Association/Goddard Space Flight Center (USRA/GSFC); and 27: Atmospheric and Environmental Research, Inc (AER).

Revision History:

Version	Date	Description/Comments
1.0	4/15/2015	ASCENDS NASA Science Definition Study
1.1	8/19/2015	ASCENDS NASA Science Definition Study

Edited By:

Emily A. Greene, Raytheon
Autumn M. Burdick, Raytheon
Felicia M. Vilnrotter, Raytheon

TABLE OF CONTENTS

LIST OF FIGURES

LIST OF TABLES

LIST OF BOXES

Executive Summary

Improved remote sensing observations of atmospheric CO_2 are critically needed to quantify, monitor, and understand the Earth's carbon cycle and its evolution in a changing climate. The processes governing ocean and terrestrial carbon uptake remain poorly understood, especially in dynamic regions with large carbon stocks and strong vulnerability to climate change, for example, the tropical land biosphere, the northern hemisphere high latitudes, and the Southern Ocean. Because the passive spectrometers used by GOSAT and OCO-2 require sunlit and cloud-free conditions, current observations over these regions remain infrequent and are subject to biases. These shortcomings limit our ability to understand the processes controlling the carbon cycle on regional to global scales.

In contrast, active CO_2 remote-sensing techniques allow accurate measurements to be taken day and night, over ocean and land surfaces, in the presence of thin or scattered clouds, and at all times of year. Because of these benefits, the National Research Council recommended the NASA Active Sensing of CO_2 Emissions over Nights, Days, and Seasons (ASCENDS) mission in the 2007 report Earth Science and Applications from Space: National Imperatives for the Next Decade and Beyond. The ability of ASCENDS to collect low-bias observations in these key regions is expected to address important gaps in our knowledge of the contemporary carbon cycle.

The ASCENDS ad hoc Science Definition Team (SDT), comprised of carbon cycle modeling and active remote sensing instrument teams throughout the U.S., has worked to develop the mission's requirements and advance its readiness since 2008. Numerous scientific investigations have been carried out to identify the benefit of active CO_2 remote sensing measurements for improving our understanding of CO_2 sources and sinks. This report summarizes their findings and recommendations to date, based on mission modeling studies, analysis of ancillary meteorological data products, development and demonstration of candidate technologies, and design studies of the ASCENDS mission concept.

To date, the ASCENDS modeling studies have demonstrated that:

1. ASCENDS will resolve statistically significant differences in total column CO_2 concentrations, resulting from foreseeable changes in surface flux over the entire globe. These flux changes could include identifying CO_2 emissions from permafrost thaw at high latitudes, shifting patterns in regional fossil fuel emissions, the evolving nature of the Southern Ocean carbon flux, and/or changes to tropical and mid-latitude terrestrial sinks.
2. ASCENDS will substantially advance our understanding of the carbon cycle through improved flux estimates with reduced uncertainty at global to regional scales. Reduced flux uncertainties at regional scales are necessary for improved understanding of the processes controlling long-term carbon sinks.
3. ASCENDS measurements also have the potential to reduce biases due primarily to lower susceptibility to errors from atmospheric scattering and changes in illumination geometry. This can contribute significantly towards improving constraints on surface fluxes beyond passive sensors such as GOSAT and OCO-2.

During the past decade, NASA has invested in the development of several different Integrated Path Differential Absorption (IPDA) lidar approaches and associated technologies that are candidates for ASCENDS. The IPDA approach measures the range to the scattering surface, and the column abundance and average mixing ratio of atmospheric CO_2 with increased sensitivity

throughout the mid- and lower troposphere. Several aircraft field campaigns have already demonstrated that:

1. Accurate CO_2 column mixing ratios can be retrieved from airborne lidar data.
2. Evaluation against in situ aircraft observations show that CO_2 column absorption measurements can be made with high precision and low bias over a wide range of surface types and between scattered clouds.
3. High-quality observations can be made to cloud tops and through thin clouds and aerosol layers.

In addition, evaluation of the magnitude of errors in present atmospheric models has helped to clarify the need for ancillary measurements and to define the error budget for the ASCENDS measurements. Statistical analysis of meteorological products from three different atmospheric modeling centers shows that uncertainty in current surface pressure estimates from models is typically less than 0.1% except in high latitudes regions. These findings will be used to evaluate the need and required performance for a coincident oxygen lidar measurement to meet the desired CO_2 mixing ratio accuracy for ASCENDS.

These studies and field activities have greatly improved our understanding of the space-based capabilities required for ASCENDS, and represent significant progress toward meeting the demands of an active remote-sensing mission. Integrating results from the measurement campaigns and modeling studies, the ASCENDS SDT has developed a preliminary set of measurement requirements as well as a study of the ASCENDS mission that demonstrates the feasibility of deploying the observatory. The results of this study show that multiple commercially-available spacecraft buses should be able to accommodate an ASCENDS instrument with minor mission-specific modifications. In addition, the Falcon 9 or Atlas V (EELV) launch vehicles can accommodate an ASCENDS observatory with the parameters used in this study.

Finally, this report outlines areas where further research is needed. These include but are not limited to:

1. Modeling studies that incorporate error statistics from the OCO-2 mission, assess the impact of errors in meteorological parameters on flux estimates, and evaluate the impact of different orbit choices and vertical information on flux inference.
2. Aircraft campaigns targeting observations over high latitudes and forested areas, and also performed to coincide with OCO-2 overpasses.
3. Technology development focused on demonstrating the required laser power for space, and further improving O_2 lidar capabilities.

Such studies are needed to improve traceability from science questions to measurement requirements. The ASCENDS SDT plans to continue working on these activities to advance mission readiness in coordination with the carbon cycle research community.

1. Introduction

1.1 Justification and Key Science Questions

The fourth and fifth Assessment Reports of the Intergovernmental Panel on Climate Change (IPCC) conclude that warming of the global climate system is unequivocal, and anthropogenic emissions of greenhouse gases are responsible for most of the increase (IPCC, 2007 and IPCC, 2013). Additionally, the reports state that the interaction between the global carbon cycle and the physical climate system is still a substantial source of uncertainty in climate projections.

The difference between observed increases in atmospheric CO_2 concentrations and anthropogenic CO_2 emissions indicate that the natural terrestrial and oceanic sinks have absorbed approximately 55% of the CO_2 generated by human activities. There are, however, significant year to-year variations. Although these variations are attributed to changes in the terrestrial and oceanic sinks, the processes governing sink strengths and the relative partitioning of CO_2 between terrestrial, oceanic, and atmospheric reservoirs are poorly understood.

Errors in the representation of these processes in existing coupled carbon-climate models lead to large uncertainties in long-term climate projections. Therefore improving our understanding of carbon sink processes is critical to improving projections of atmospheric CO_2 levels and Earth's climate.

In order to address the gaps in our current understanding of atmospheric CO_2 and its relationship to climate change, three overarching needs have been defined (NASA, 2008). They are to:

- *Improve our understanding of the current magnitude and distribution of terrestrial and oceanic sources and sinks, distinguishing between natural and anthropogenic sources and sinks,*
- *Improve our understanding of the time scales of natural sources and sinks, from short (e.g. diurnal) to medium (seasonal/annual) to extended (climatological) time scales, including processes resulting from ecosystem/biosphere disturbances, and*
- *Improve our ability to predict/model long-term changes in the climate system due to natural variability of carbon sources and sinks, as well as the transport of carbon through the atmosphere.*

Globally distributed atmospheric CO_2 measurements are critical to address these needs. The fluxes of CO_2 from the surface vary in both space and time. The resulting gradients in concentration caused by the fluxes are small and are mixed and integrated by atmospheric transport. Sampling atmospheric CO_2 in time and space can be used, along with appropriate transport and inversion models, to quantify the surface fluxes. The remote sensing challenge is to provide the atmospheric CO_2 measurements with sufficient global coverage, accuracy and sampling frequency to allow inferring the locations and magnitudes of the sources and sinks.

1.2 CO_2 Measurements Near the Surface

The modern atmospheric CO_2 measurement record began in 1957 with flask measurements taken atop Mauna Loa. These provided samples of the global background concentration of atmospheric CO_2. Over the years, our understanding of the spatial and temporal variations in atmospheric CO_2 concentrations has improved via the establishment of additional ground measurement sites providing both surface and tower measurements, aircraft campaigns and routine airborne observations, and most recently, contributions from space-based remote sensing. Yet there remain

significant gaps in our understanding that result from limited measurements, particularly related to the distribution and variability of terrestrial and oceanic sinks and the processes controlling this variability.

1.3 Space Missions Using Passive Remote Sensing

The important first steps toward measuring greenhouse gases globally from space were demonstrated using spectrometers that viewed the Earth's thermal emission or reflected sunlight. The initial passive radiometer and spectrometer missions for GHG observations included SCIAMACHY on ENVISAT, AIRS, and IASI. Their observations have been critical in demonstrating using space-based spectrometers to address questions about atmospheric composition. However, all these early multi-purpose instruments had relatively coarse spectral resolution and large measurement footprints that limited their coverage and the precisions and accuracies of their retrievals.

Subsequently two satellite missions have been developed specifically for measuring atmospheric CO_2 and CH_4 using higher resolution passive spectrometers. The Japanese Greenhouse gas Observing Satellite (GOSAT) was launched in 2009. The precision of GOSAT's XCO_2 and XCH_4 measurements has been assessed by comparing its measurements to those from ground-based spectrometers, in particular those of the Total Column Concentration Observing Network (TCCON).

In order to extend CO_2 observations from space, NASA's OCO-2 mission was launched during July 2014. While it does not measure CH_4, the OCO-2 mission uses optical spectrometers with higher sensitivity detectors, and it views the Earth in smaller footprints. Preliminary OCO-2 data show higher precision XCO_2 observations from space, and it is hoped these will improve knowledge of CO_2 sources and sinks [5]. More details on these missions are in Chapter 2.

1.4 Potential Benefits of Active (Laser-Based) CO_2 Measurements

To date, observations of CO_2 from space have used passive remote sensing techniques. While their contributions to understanding the global carbon cycle are significant, passive measurement techniques have some inherent limitations. When conditions are favorable, these approaches allow accurate measurements of the atmospheric gases. However favorable conditions require sunlit scenes, cloud-free conditions, and accurate estimates of surface elevation within the spatial resolution elements.

The Earth's atmosphere is complex and optical scattering by clouds and aerosols is common. For passive sensors, this scattering causes variability in the optical path length and hence it contributes to spatially and temporally varying biases. There are also wide variations in surface elevation, due to topography and trees, which change the length of the measurement path and the CO_2 column. The accuracy of measurements at large solar zenith angles is also limited due to this scattering and by variability in surface reflectance. The resulting sparse coverage of passive spectrometers at high latitudes is a serious limitation, particularly for the Northern Hemisphere, since these regions exhibit substantial emissions during the winter as well as other times of year.

In contrast, an active (laser) remote sensing mission carries its illumination source whose characteristics have been carefully optimized for these measurements. It involves a simpler fixed observational geometry, with a common vertical illumination and observation path. The range - resolved laser measurements eliminate errors from atmospheric scattering. This approach allows measurements to be taken day and night, over ocean and land surfaces, at all latitudes, and at all

times of year. Active CO_2 remote sensing also enables enhanced sensitivity to CO_2 in the lower troposphere, where the atmospheric concentrations respond most strongly to surface fluxes. Over oceans, a lidar enables more frequent observations of the southern ocean, especially in the wintertime, where dark oceans are virtually inaccessible to shortwave passive systems.

The ability of active CO_2 sensors to measure during day and night provides for at least twice the coverage of shortwave passive systems that rely on reflected sunlight. Nocturnal measurements with atmospheric weighting toward the surface are desired for investigations of respiration and urban areas. Since lidar can make effective measurements regardless of local observation time, various non-Sun synchronous orbits also can be considered to provide additional information about diurnal cycles on different time scales.

Depending on the approach chosen, there are other potential benefits from lidar measurements. Higher spatial sampling, for example, would allow detection of strong, localized gradients in CO_2 concentration to facilitate investigations in complex terrain. It could also enable measurements through smaller gaps in clouds and to cloud tops, significantly improving the measurement density and coverage under these conditions.

1.5 Objectives for ASCENDS

To address these unmet needs, more accurate remote sensing measurements of atmospheric CO_2 are required with more complete global coverage. In the US, the NRC's 2007 Decadal Survey (NAP, 2007) recommended the Active Sensing of CO_2 Emissions over Nights, Days, and Seasons (ASCENDS) mission (NASA, n.d.). The objectives of ASCENDS are to:

1) Quantify the global spatial distribution of atmospheric CO_2 on scales of weather models in the 2010-2020 era;
2) Quantify the current global spatial distribution of terrestrial and oceanic sources and sinks of CO_2 on 1-degree grids at weekly resolution; and
3) Provide a scientific basis for future projections of CO_2 sources and sinks through data-driven enhancements of the Earth-system process modeling.

An important consideration for this mission is that the CO_2 fluxes from the surface cause only small changes in the spatial distributions of CO_2 concentrations in the lower troposphere. Hence the remote sensing challenge is to accurately measure these small changes in in CO_2 concentrations globally. The required levels of measurement uncertainty that must be attained over a wide range of atmospheric and surface conditions are typically <0.25% (< 1 ppm).

1.6 The ASCENDS Approach

A lidar utilizes its own specialized light source and use a common illumination and observation path. Greenhouse gas measurements can be made using a range-resolved integrated path differential absorption (IPDA) lidar approach. These measurements are independent of solar angle and of prior knowledge of scattering surface elevation. Measurements with high precision and low bias can be made under a wide variety of atmospheric and topographic conditions thus allowing extended spatial coverage. The lidar can sample a selected gas absorption line, measure the surface elevation, and retrieve the gas mixing ratio. The range resolving capability of the lidar enables accurate measurement of scattering surface elevation and atmospheric path length, as well as excluding biases due to the optical scatter by clouds and aerosols.

The basic approach for the ASCENDS measurements of CO_2 is shown in Figure 1.1. This example depicts a pulsed approach using the minimum of two wavelengths to sample the

absorption line. The figure shows two beams (red and blue) directed at nadir, corresponding to the laser pulses tuned on and off the absorption line. They pass through the atmospheric column containing an unknown concentration of CO_2 and illuminate nearly the same area on the scattering surface, either the Earth's surface or cloud top. The light reflected by the surface passes back through the atmosphere and a small fraction is collected by the receiver telescope. The lidar receiver measures the energies of the on- and off-line pulses (E_{on} and E_{off}) and the range to the surface.

The insert shows a sketch of the shape of the CO_2 line's transmission (top) and optical depth when measured from space. The maximum CO_2 absorption occurs for laser wavelengths tuned to the line's center. The wavelength of the laser's "on-line" pulse is usually selected to be offset from the peak of the CO_2 absorption line and is indicated by the red vertical line. The wavelength of the laser's "off-line" pulse, that undergoes negligible CO_2 absorption, is indicated by the blue line.

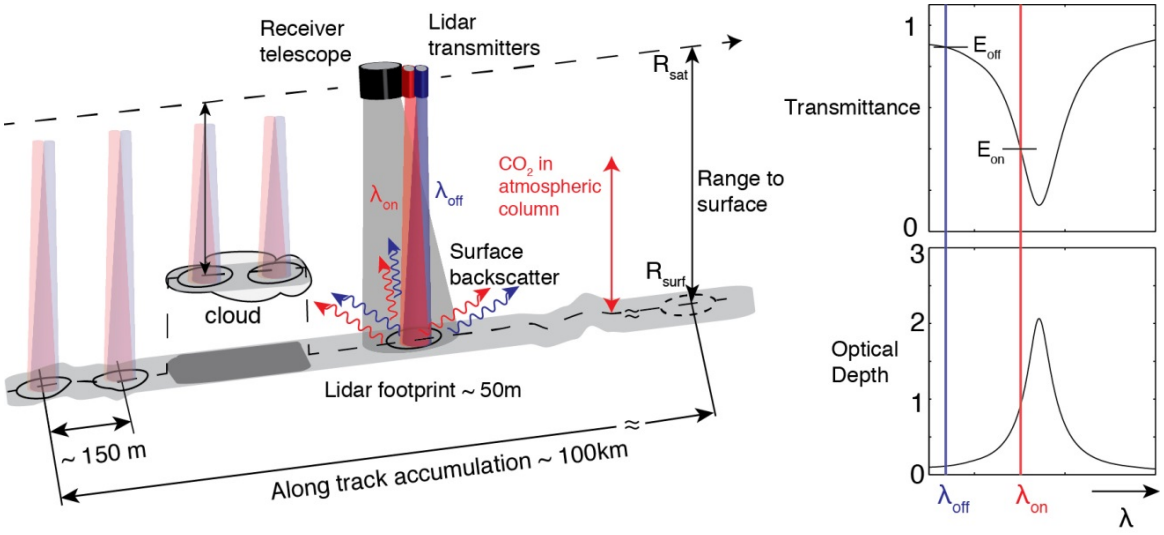

Figure 1-1 One approach for an Integrated Path Differential Absorption (IPDA) measurement from space to scattering surfaces on or near the Earth's surface. While there are several different IPDA measurement approaches, this drawing is for the two-wavelength pulsed approach that was considered for the ESA A-SCOPE Mission [8] Several IPDA approaches use more than two wavelengths to sample the absorption line shape to provide additional information.

The CO_2 column abundance is calculated from the lidar's measurement of range to the scattering surface and ratio of the energies in the on- and off-line echo pulse signals. The column integrated mixing ratio XCO_2 is calculated using additional information about the density of dry air in the same measurement column. In the present baseline approach for ASCENDS, a simultaneous O_2 lidar measurement is being considered as an additional capability of the instrument. Another option may be to use a numerical weather prediction model's estimate of surface pressure at the location and time of the CO_2 lidar measurement to calculate the CO_2 mixing ratio.

1.7 The Benefits of the ASCENDS Approach

The IPDA lidar approach offers a number of unique and important capabilities for ASCENDS, allowing accurate column measurements of CO_2 with extended coverage. These are summarized in Table 1.

For these reasons the ASCENDS approach, using an orbital IPDA lidar, will allow accurate measurements of greenhouse gas concentrations over a much wider variety of conditions than is possible with passive sensors. These more accurate measurements, with wider spatial coverage, are key to address important questions about the locations, strengths and evolution of the regional CO_2 fluxes needed for climate models.

Table 1-1 Unique capabilities of the ASCENDS approach

1. The lidar measurements work well in darkness and are independent of sun angle.
2. It measures in a single vertical column, using a common illumination and observation path.
3. The same nadir-zenith viewing geometry is also the "glint mode" for the ocean and water surfaces. This allows ocean and land measurements to be made continuously using the same spacecraft orientation.
4. The laser line-width is much smaller than the gas absorption line, and so the absorption lines measured are fully resolved. Using on-line measurements on the side of the gas line allows weighting of the column measurements preferentially in the lower troposphere, which contains a stronger signature from the surface fluxes. On-line measurements near the peak of the line also allow additional measurements weighted toward the upper atmosphere.
5. The laser can utilize gas absorption lines to minimize temperature sensitivity and contamination from other gases. The spectroscopic knowledge needed for accurate retrievals involves only the region around the single gas line sampled by the lidar, and is independent of the solar spectrum.
6. The small (typically 100m) lidar spot size also enables utilizing small gaps in clouds to obtain gas column measurements to the surface in partially cloudy scenes and through broken cloud fields.
7. The lidar measures range to the scattering surface simultaneously with column gas absorption. This provides accurate determination of the scattering surface elevation and column length. This also allows simple range gating to eliminate signals scattered by thin clouds and aerosols. The range measurements are particularly important when measuring over regions with varying topography and tree cover that cause the range to vary significantly.
8. The ranging information also enables accurate column measurements to the tops of some clouds, providing some vertical resolution in the column concentrations.

1.8 Overview of NASA's Development of ASCENDS Mission

Over the past decade NASA has been supporting the development of several lidar concepts and their associated technologies for its planned ASCENDS mission, as described in the 2007 US National Research Council's Decadal Survey for Earth Science [NAC, 2007]. The approaches all use the IPDA technique. An ASCENDS ad hoc science definition team leads the mission definition activities. Team members are from NASA Goddard, NASA Langley (LaRC) and NASA Jet Propulsion Laboratory (JPL) as well as the University of Oklahoma, Colorado State University, and others. Their work has focused on four areas, including developing the mission's science objectives and requirements, conducting science mission modeling studies (Observing System Simulation Experiments) for various parameters of the space mission, and carrying out initial engineering studies of potential lidar and spacecraft. NASA's Earth Science Technology Office has supported the development of the key lidar technologies used by the investigators.

A large fraction of the ASCENDS work has been directed at developing and demonstrating candidate lidar approaches from aircraft. Candidate lidar techniques that include two direct detection lidar approaches have been demonstrated that measure both range and a selected CO_2 lines near 1571 and 1572 nm. One uses sine-wave laser intensity modulation that is swept in modulation frequency. The other uses pulsed laser modulation that samples the absorption line at multiple wavelengths and uses a time resolved receiver to measure the laser backscatter profile and range to the surface. Two approaches have demonstrated measurements of the CO_2 line near 2051 nm. A CW heterodyne approach measures this line at two wavelengths, and a pulsed direct detection approach that measures both range and CO_2 absorption using the same line.

In parallel with the technique development and system-level demonstrations, Observing System Simulation Experiment (OSSE) studies are being conducted to assess the characteristics of the CO_2 fluxes that can be inferred from space-based lidar measurements with various levels of measurement precision and accuracy. The mission simulations have used a lidar measurement model with surface reflectivity maps from MODIS and information on cloud and aerosol heights and extinctions from the Calipso Mission (Cloud-Aerosol Lidar and Infrared Pathfinder Satellite Observations) [c.f. Winker et al. 2013]. OSSE analysis has identified some mission science tradeoffs and the formulation of an initial set of ASCENDS measurement requirements. Preliminary instrument and space mission engineering studies also have been conducted on lidar candidates that are suitable for the mission. The payload parameters are consistent with a medium-sized spacecraft bus to be flown in a polar ~400 km altitude orbit.

1.9 Remainder of Report

The remaining chapters of this report expand on the topics briefly introduced here. Chapter 2 summarizes the science of CO_2 and history of atmospheric CO_2 measurements. Chapter 3 summarizes present studies on the impact of Ascends Mission on carbon cycle science and Modeling. Chapter 4 assesses the influence from uncertainties in the atmospheric state on the space-based measurements. Chapter 5 provides a summary of the mission measurement requirements, along with an overview of the various lidar techniques that may be candidates for the mission. Several have demonstrated promising measurements during airborne campaigns. This chapter also has a brief overview of ongoing work and discusses scaling the approaches to space. Chapter 6 summarizes the result from an initial space mission engineering study. Finally Chapter 7 summarizes the report and discusses next steps.

2. Science of Atmospheric CO_2 and Measurement History

2.1 Introduction

At the beginning of the industrial era in the late 18th century, the atmospheric carbon dioxide (CO_2) concentration (or "dry air mole fraction") was about 280 parts per million (e.g. Etheridge et al., 1996). Since that time, fossil fuel combustion, deforestation, and other human activities have emitted more carbon dioxide (CO_2) into the atmosphere each decade, driving the weekly average atmospheric CO_2 mole fraction past the 400 ppm mark in May 2013. Recent estimates of fossil fuel emissions derived from fossil fuel inventories (Marland et al., 2009; Guan et al., 2012; Andres et al. 2012) show that this source alone was adding more than 36 billion tons (Gigatons or Gt) of CO_2 to the atmosphere each year (Peters et al., 2012; Le Quéré et al., 2013).

The CO_2 emissions from burning fossil fuels are superimposed on an active, global carbon cycle that regulates the exchange of carbon among reservoirs in the ocean, land biosphere, and atmosphere (SOCCR (State of the Carbon Cycle Report), 2008). Each year, the land biosphere absorbs and then re-emits over 440 Gt of CO_2 into the atmosphere through photosynthesis and respiration, respectively. The ocean is also a massive reservoir of carbon, exchanging about 330 Gt of CO_2 with the atmosphere each year, as CO_2 is exchanged across the air-sea interface. Because these natural fluxes of CO_2 are roughly balanced, ice core records show they have maintained atmospheric CO_2 mole fractions between ~180 and 300 ppm for at least the past several hundred thousand years (cf. Archer et al., 2009). The CO_2 emissions associated with human activities are still only about 1/20th as large as these natural fluxes, but they are not balanced, and are now pushing the atmospheric CO_2 mole fractions to levels not seen throughout the 800,000 year ice core record (Lüthi et al., 2008) and perhaps for as long ago as 3-4 million years (cf. Badger et al., 2013).

A precise, continuous, record of direct atmospheric CO_2 measurements was started in 1958, when Charles Keeling of Scripps Institute of Oceanography installed a CO_2 monitoring station on the flanks of the Mauna Loa volcano in in Hawaii (Keeling, 1960). The initial measurements showed CO_2 mole fractions near 315 ppm, about 35 ppm above the pre-industrial values of ~280 ppm. Within a couple of years, his measurements clearly documented the global atmospheric signature of photosynthesis and respiration by land plants. They showed a ~7 ppm CO_2 drawdown during the northern hemisphere spring and summer, when forests and grasslands were growing rapidly and a comparable CO_2 buildup during fall and winter when these plants dropped their leaves and went dormant or died. As this measurement record continued through the 1960's and 1970's, a clear trend emerged, revealing an increase in the background CO_2 mole fraction of over 1 ppm per year.

The National Oceanic and Atmospheric Administration (NOAA) joined the atmospheric CO_2 monitoring effort in 1974. The NOAA Earth System Research Laboratory Global Monitoring Division (ESRL GMD) now operates the Carbon Cycle Greenhouse Gas (CCGG) Cooperative Air Sampling Network, which currently includes 71 surface stations and 17 vertical profiling sites. This network has been incorporated into the World Meteorological Organization (WMO) Global Atmospheric Watch (GAW) Program, which now includes over 150 surface stations that report CO_2 mole fraction measurements on time scales varying from minutes to one week. These data are collected and distributed by the World Data Centre for Greenhouse Gases (WDCGG) at the Japan Meteorological Agency. Stringent quality control procedures and frequent, rigorous calibration efforts ensure that these measurements from these stations are not only extremely

precise, but also highly accurate, through comparisons to standards with accuracies of ~0.2 ppm (cf. Conway et al., 2009; Conway et al., 1994; Zhao and Tans, 2006; Dlugokencky et al. 2013; Tans and Keeling, n.d.).

Recent measurements from this surface-based greenhouse gas network show that the annual growth rate of CO_2 has increased by about a factor of two since the 1960's, and now exceeds 2 ppm (0.5%) each year. Comparisons of these measurements with CO_2 emission inventories reveal an intriguing puzzle. If all of the CO_2 emitted by human activities remains in the atmosphere, the atmospheric CO_2 abundance should be increasing at twice this rate. This apparent discrepancy was initially somewhat surprising because CO_2 is also a chemically stable atmospheric constituent, with an estimated atmospheric half-life of almost 900 years. The accuracies of both the CO_2 emissions estimated from fossil fuel inventory and the atmospheric measurements are more than adequate to resolve a deficit this large. Apparently, since the beginning of the industrial age, natural "sinks" in the ocean and land biosphere have kept pace with the rapidly growing emission rates, and are now absorbing slightly over half of the CO_2 emitted by human activities (cf. Le Quéré et al., 2013).

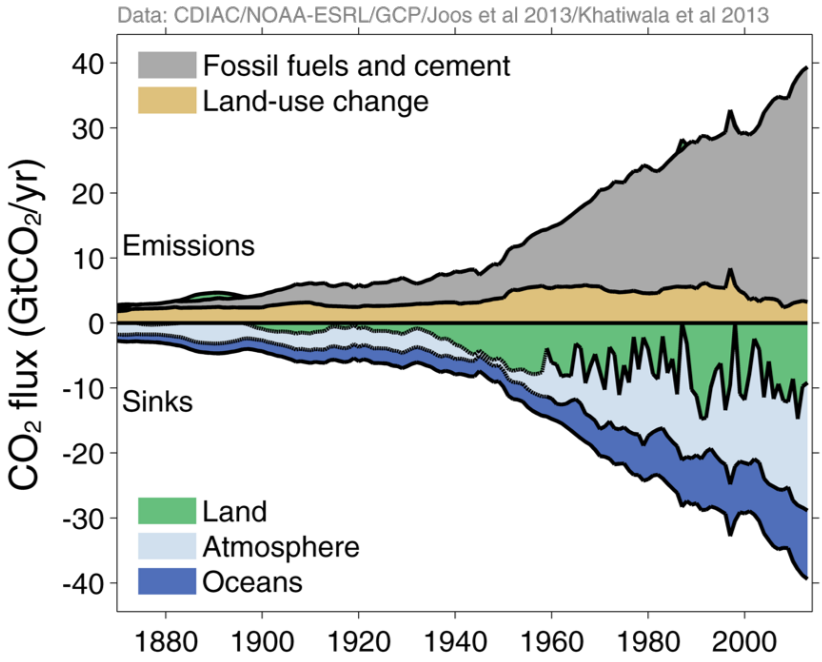

As atmospheric CO_2 is absorbed by the ocean, it produces carbonic acid, and recent measurements of increases in the ocean acidity indicate that the ocean has been absorbing about half of the "missing" CO_2. The rest (~ 9.6 Gt CO_2 / year) is apparently being absorbed by sinks in the terrestrial biosphere, whose identity, location, and driving mechanisms are still very poorly understood. While they absorb about half of the CO_2 emitted by human activities, when averaged over decadal time scales, their efficiency appears to vary dramatically from year to year. In some years, they absorb almost all of CO_2 emitted by human activities, while in others they absorb almost none (Dlugokencky et al. 2013; Tans and Keeling, n.d.). The processes responsible for modulating the efficiency of these sinks from year to year are largely unknown. There are also large uncertainties in the response of these natural sinks to climate change. Will they continue to

absorb roughly half of all the CO_2 emitted by human activities, or will they eventually saturate, or perhaps even become sources as the climate changes in response to greenhouse-gas-induced warming? An improved understanding of these natural sinks and the processes that control them is therefore critical for predictions of future atmospheric CO_2 increases and their impact on the climate.

An improved understanding of CO_2 emissions from human activities is also needed to predict future CO_2 growth rates. Until recently, these emissions were dominated by fossil fuel combustion in the developed world. The inventory-based CO_2 emission estimates have grown progressively more accurate for this particular source, with uncertainties as small as ~5% in Europe and North America (cf. EPA, 2010; Boden et al. 2013). However, since the turn of the 21st century, fossil fuel CO_2 emissions from China, India, the Russian Federation, and other developing nations have grown rapidly, and now account for more than 57% of all emissions from fossil fuel combustion (cf. Le Quéré et al., 2013). The uncertainties in these emissions are much higher than those for Europe and North America, and their future rate of increase (currently 5.9%/year for China) is difficult to predict. CO_2 emissions from other sources in the developing world, including biomass burning and other land use practices, are also less well known. When these uncertainties in CO_2 emission sources are combined with those associated with possible changes in natural CO_2 sinks, predictions of the atmospheric CO_2 concentration at the end of this century are uncertain by amounts exceeding the current atmospheric CO_2 abundance.

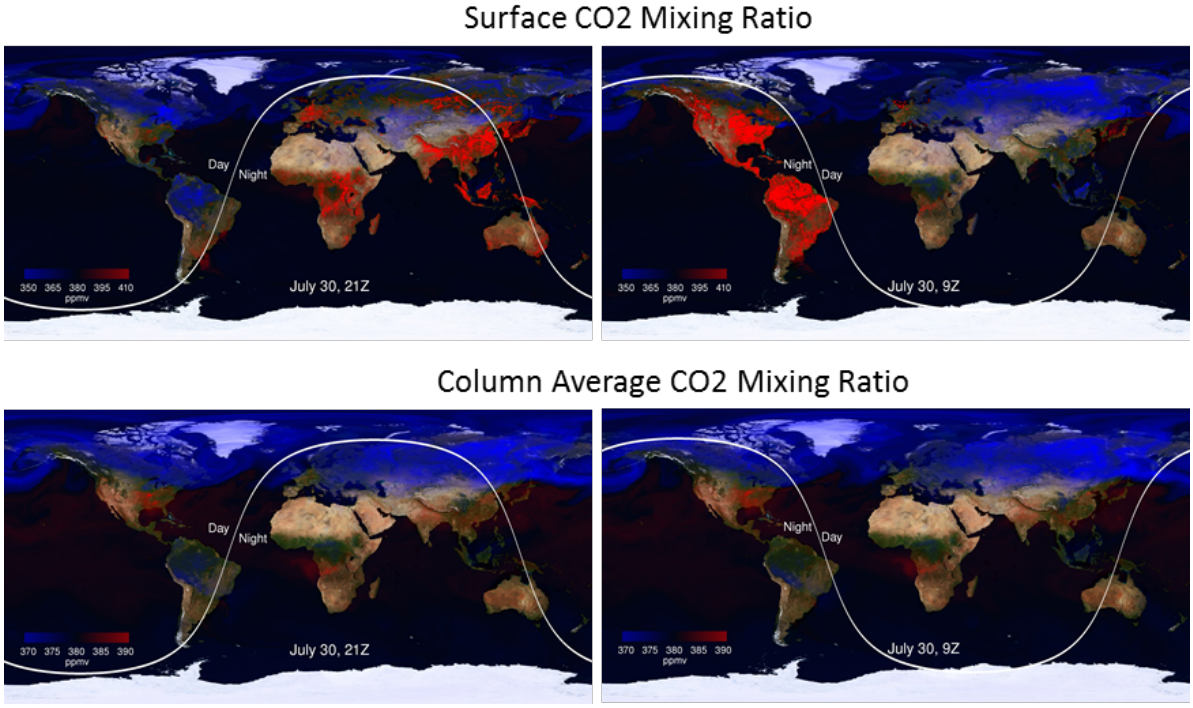

Figure 2-1 Simulated surface (top) and column average (bottom) CO_2 fields for July from the Goddard Earth Observing System Model, Version 5 (GEOS-5; Ott et al., 2014) illustrate the effects of diurnal variations in surface sources. The white line indicates the position of the terminator.

The quantity and accuracy of the measurements of CO_2 and other greenhouse gases from the surface-based greenhouse gas monitoring network have improved progressively since 1957, and now produce a highly accurate integral constraint on the global abundance of CO_2 and its rate of change. These precise atmospheric measurements have been augmented by CO_2 flux networks,

that quantify the exchange of CO_2 between the surface and atmosphere associated with natural processes. Ground-based remote sensing measurements of the column-average dry air mole fraction of CO_2, CH_4 (Methane), and other gases by the 21-station Total Carbon Column Observing Network (TCCON) are providing additional insight into the emission, absorption, and transport of the species (cf. Keppel-Aleks et al., 2012; Geibel et al., 2012; Wennberg et al., 2012; Messerschmidt et al., 2013; Wunch et al., 2013).

The existing ground based greenhouse gas network was not designed to quantify emissions from large point sources, such as cities or power plants. In fact, most of its stations were deployed away from large point sources, to record large-scale global trends. The simulation of the atmospheric CO_2 distribution shown in Figure 2.1 illustrates another reason why it has been impossible to identify and study these sinks with the existing ground-based network. As CO_2 is emitted into the atmosphere or absorbed by surface processes, the resulting CO_2-rich or CO_2-poor air is transported by the prevailing winds, mixing the CO_2 with the ambient air mass. To track these air masses, the measurement system must be able to resolve the wind field as well as the spatial scales of the sources and sinks. This is challenging because the atmosphere already contains a substantial amount of CO_2 (~400 ppm), such that even the largest sources rarely produce CO_2 perturbations larger than 10% near the surface, where their amplitudes are largest. The amplitude of these CO_2 anomalies decays rapidly with altitude, yielding column-integrated variations in the background CO_2 distribution that are almost always less than 2%, and typically no larger than a few tenths of a percent on local to regional scales.

2.2 History of CO_2 Measurements From Space

The ground based greenhouse gas monitoring network is reasonably dense in some areas (e.g. North America, Europe), but far more sparse elsewhere, especially over tropical and polar land masses and the ocean basins. A dramatic expansion of this network would be needed to identify and quantify sources and sinks of CO_2 on local to regional scales over the globe. One way to expand the spatial and temporal resolution and sampling of CO_2 observations is to acquire global measurements at high spatial resolution from space (Rayner and O'Brien 2001; O'Brien and Rayner, 2002; Rayner et al., 2002; Houweling et al., 2004; Chevallier et al., 2007; Hungershoefer et al., 2010). The principle challenge to this approach has been the need for precise measurements of CO_2 near the surface, where most sources and sinks are located. Thermal infrared (5 to 15 micron) temperature sounders such as the NASA Atmospheric Infrared Sounder (AIRS) and the CNES (Centre National d'Etudes Spatiales (French Space Agency)) Infrared Atmospheric Sounding Interferometer (IASI) routinely acquire measurements within atmospheric CO_2 bands, where CO_2 absorbs and emits thermal radiation. These measurements typically yield CO_2 mixing ratios with accuracies of ~1% at altitudes in the middle troposphere (~5 km), but have little or no sensitivity near the surface (Chevallier et al., 2009).

Estimates of the column averaged CO_2 dry air mole fraction, XCO_2, can be retrieved from space-based observations of reflected sunlight in near infrared CO_2 and O_2 bands. The European Space Agency's (ESA) EnviSAT (Environmental SATellite) SCIAMACHY (SCanning Imaging Absorption Spectrometer for Atmospheric CartograpHY) and Japanese Greenhouse gases Observing SATellite (GOSAT) TANSO-FTS (Thermal And Near infrared Sensor for carbon Observation-Fourier Transform Spectrometer) were the first two satellite instruments designed to use this approach. SCIAMACHY returned global maps of $XCO_2$and XCH_4 from 2002 – 2012. The precision of its measurements over land eventually approached ~1 to 2 percent. However, the

instrument's low sensitivity over dark surfaces precluded useful observations over the ocean and its large (30 km by 60 km) sounding footprints were often contaminated by clouds.

GOSAT was launched in January, 2009, and flies in a 666 km altitude, sun synchronous orbit with a 12:47 PM equator crossing time and a 3-day ground track repeat cycle. Its Thermal And Near infrared Sensor for carbon Observation (TANSO) Fourier Transform Spectrometer (FTS) has returns high resolution spectra of reflected sunlight in the CO_2 bands near 1.57, 1.61, and 2.06 microns, the CH_4 band near 1.67 microns, and O_2 A-band near 0.765 microns since April 2009. Groups in Japan, the U.S. and Europe are using these spectra to estimate XCO_2 and XCH_4. Due to strong collaboration among these groups on retrieval algorithms, validation techniques, and data screening methods the observational biases are being reduced. Random errors that are typically less than 0.5% (2 ppm) on regional scales over much of the Earth (cf. Yoshida et al., 2012; Inoue et al., 2013; Crisp et al., 2012).

As the biases and random errors have been reduced, the principal limitation of the GOSAT data set has been its coverage and resolution. The TANSO-FTS acquires about 10,000 soundings over the sunlit hemisphere each day. Over land, the ~10.5 km diameter surface footprints of these soundings are separated by ~253 km. With its relatively large sounding footprint (85 km^2), up to 90% of these soundings are too contaminated by clouds or optically-thick aerosols to yield accurate estimates of XCO_2 with the current retrieval algorithms. Persistent cloudiness over the tropics, south Asia (monsoons), and at high latitudes in the winter hemisphere further reduces the coverage there. Over the ocean, the TANSO-FTS coverage is restricted to ±20° of the sub-solar latitude, where its pointing mechanism can target the bright "glint spot," in which sunlight is specularly reflected from the surface. So, while GOSAT extends the coverage of the ground based network, it still leaves large regions with little or no sampling. In spite of these limitations in coverage and resolution, XCO_2 estimates from GOSAT TANSO-FTS are being used in flux inversion models and are beginning to improve our understanding of CO_2 sources and sinks in data poor regions, such as Africa and central Asia (Basu et al. 2013; Belikov et al., 2014; Guerlet et al. 2013).

The Orbiting Carbon Observatory-2 (OCO-2) is NASA's first satellite designed to retrieve estimates of XCO_2 over the sunlit hemisphere. OCO-2 was launched from Vandenberg Air Force Base in California in July 2014. It flies at the head of the 705-km Afternoon Constellation ("A-Train"), in an orbit tailored to yield nadir observations that overlap with those from CALIPSO (Cloud-Aerosol Lidar and Infrared Pathfinder Satellite Observations) and CloudSat. This sun-synchronous orbit has a 1:30 PM equatorial crossing time and a 16-day repeat cycle.

The OCO-2 spacecraft carries single instrument that incorporates three, co-bore-sighted high-resolution, imaging, grating spectrometers designed to measure reflected sunlight in the O_2 A-band, and within the CO_2 bands near 1.61 and 2.06 microns. Each spectrometer collects 24 XCO_2 soundings per second along a narrow (< 10.6 km), ground track, yielding up to one million soundings over the sunlit hemisphere each day. To yield more useful data in partially cloudy regions, the surface footprint of each OCO-2 sounding has an area of less than 3 km^2. With this small footprint, cloud screening studies indicate that 20 to 30% of these soundings should be sufficiently cloud free to yield full-column estimates of XCO_2. To detect CO_2 variations over dark, ocean or ice-covered surfaces, OCO-2 can point the instrument's field of view toward the bright ocean glint spot over almost 90% of the range of latitudes on the sunlit hemisphere. The baseline plan is to alternate between glint and nadir observations on alternate, 16-day ground-

track repeat cycles, to optimize the coverage of the sunlit hemisphere at monthly intervals. With these capabilities, OCO-2 provides substantially better coverage than previous missions.

3. Impact to Carbon Science and Modeling

3.1 Introduction

The overarching science goal of the ASCENDS Mission, as outlined above, is to establish quantitative constraints on terrestrial and oceanic CO_2 surface fluxes at both global and regional scales from measurements of CO_2 column concentration. In order to achieve this goal, it is critical to thoroughly understand the impact of measurement accuracy and precision on the flux estimates. Even the largest sources and sinks produce local perturbations in the background concentration of CO_2 no larger than a few percent. In addition, biases in the data are particularly problematic since their impact cannot be reduced via averaging.

This chapter outlines the ongoing modeling efforts undertaken by the ASCENDS ad hoc science definition team to assess the ability of expected ASCENDS measurements to constrain flux estimates. Under reasonable assumptions for ASCENDS technical performance, the modeling efforts consistently demonstrate the following major points:

- ASCENDS will resolve statistically-significant differences in total column CO_2 concentrations, resulting from foreseeable changes in surface flux, over the entire globe including high latitudes throughout the year.
- ASCENDS will substantially advance our understanding of the global carbon budget through improved flux estimates with reduced uncertainty at global to regional scales.
- ASCENDS measurements have the potential for lesser bias and greater representation that can contribute significantly to improved constraints on surface fluxes beyond what passive sensors such as GOSAT and OCO-2 can provide.

In this chapter, we elaborate on these points in detail through the use of three common, overlapping modeling approaches or Observing System Simulation Experiment (OSSE) frameworks. These approaches are: 1) Signal detection simulations that test the global measurement significance for perturbation flux scenarios of interest; 2) Inverse modeling OSSEs that quantify the reduction in flux uncertainty provided by the ASCENDS data at global and regional scales, and 3) OSSEs that compare the impact of ASCENDS data to that of current passive measurements from GOSAT and that expected from OCO-2 at the global scale. Most of the modeling is performed using a range of possible technology implementations and performance specifications for ASCENDS to bracket projected measurement error levels and ultimately to help guide requirements for the mission formulation.

3.2 Detection of Changes in Column CO_2 and Flux by ASCENDS

The ability of ASCENDS to detect changes in total column CO_2 resulting from variations in underlying fluxes is tested in the two-step methodology of Hammerling et al. (2015). First, a realistic baseline set of CO_2 sources and sinks is perturbed to generate a simulated atmosphere, which represents the science hypothesis in question. Second, the control and perturbed CO_2 fields are sampled according to the projected ASCENDS sampling and error characteristics, and the 'observed' differences are evaluated statistically. This procedure is carried out for three hypothetical flux scenarios (Hammerling et al., 2015): emissions from thawing permafrost (Section 3.2.1), a shift in fossil fuel emissions from Europe to China (Section 3.2.2), and simulated interannual variability in the Southern Oceans (Section 3.2.3). These scenarios are then

introduced into an inversion model framework to calculate the fluxes and uncertainties inferred from the pseudo data.

Box 3-1 Simulation of Random Errors

Prospective ASCENDS sampling and measurement error characteristics are derived in a realistic scheme from observations and model output using the Cloud-Aerosol Lidar and Infrared Pathfinder Satellite Observations (CALIPSO) orbital track for the ASCENDS orbit (Kawa et al., 2010, Kiemle et al., 2014). CALIPSO optical depth (OD) data are reported every 5 km along track and this forms our basic ASCENDS sample set. We have also tested sample error calculated using OD derived for a subset of single-shot 20-Hz CALIPSO data and found that the global statistics are very similar to those using the 5-km data.

Since ASCENDS laser measurements of atmospheric CO_2 (and O_2) will be made using the integrated path differential absorption (IPDA) technique, the dominant random error source is likely to be the shot noise in the signal, i.e., the statistical variability in the number of detected signal photons. Hence the measured signal to noise ratio (SNR) of the optical depth of the gas absorption depends on the square root of the received signal energy. In general, the SNR of an individual measurement of 2-way optical depth (SNR_i), can be related to that measured under reference conditions (SNR_0) by:

$$SNR_i = SNR_0 \left[\frac{\beta_i}{\beta_0} \frac{T_i^2}{T_0^2} \right]^{1/2} \quad (3\text{-}1)$$

Where β_i is the average backscatter factor (sr-1) of the measured surface, β_0 is the backscatter for the reference surface, T_i is the one-way atmospheric transmission to the surface due to aerosols and clouds for measurement i, and T_0 is the transmission for the reference measurement. For the reference conditions, we have chosen clear air with the high reflectivity of a desert like Railroad Valley, NV in summer and a 10-s sample integration time. The measurement at this reference location is assumed to be aerosol and cloud free, thus $T_0 = 1$. Using Equation **Error! Reference source not found.**, we estimate the random relative error (= $1/SNR_i$) globally from an estimate of the error under the reference conditions.

The transmission for each ASCENDS pseudo data sample is taken directly from the CALIPSO OD data: where τ_i is the one-way integrated aerosol and cloud OD to the surface reported by CALIPSO. The aerosol OD is taken from the 1064-nm channel and the cloud OD from the 532-nm, and these values are assumed to apply equally at each of the possible ASCENDS measurement wavelengths (i.e., 1.57 and 2.05 μm). Samples are excluded where CALIPSO cannot see to the surface due to thick clouds. Global backscatter estimates over land have been assembled for wavelength bands at 1.57 and 2.05 μm for CO_2, and 0.76 and 1.26 μm for O_2 measurement using MODIS bands 6, 7, 2, and 5, respectively, which are then interpolated to the CALIPSO-based sampling points. The details vary slightly from band to band. Backscatter over water is calculated according to Hu et al. (2008) using surface wind speeds from GEOS-5.

For the modeling studies, a range of nominal reference random error levels ($1/SNR_0$) is considered (0.5, 1.0, 2.0 ppmv) to represent a range of possible instrument precision levels. Global median errors scaled from these ideal/desert-like nominal values are 1.7, 3.3, 6.7 ppmv, respectively for the 1.57 μm case when screened for samples with optical depth less than 1.0. All of the models use the same sample distribution and measurement error scaling described here, however, different modeling teams employ somewhat different techniques to aggregate the pseudo data and determine the model-data mismatch errors that are ultimately used in the flux estimation experiments (Appendix C).

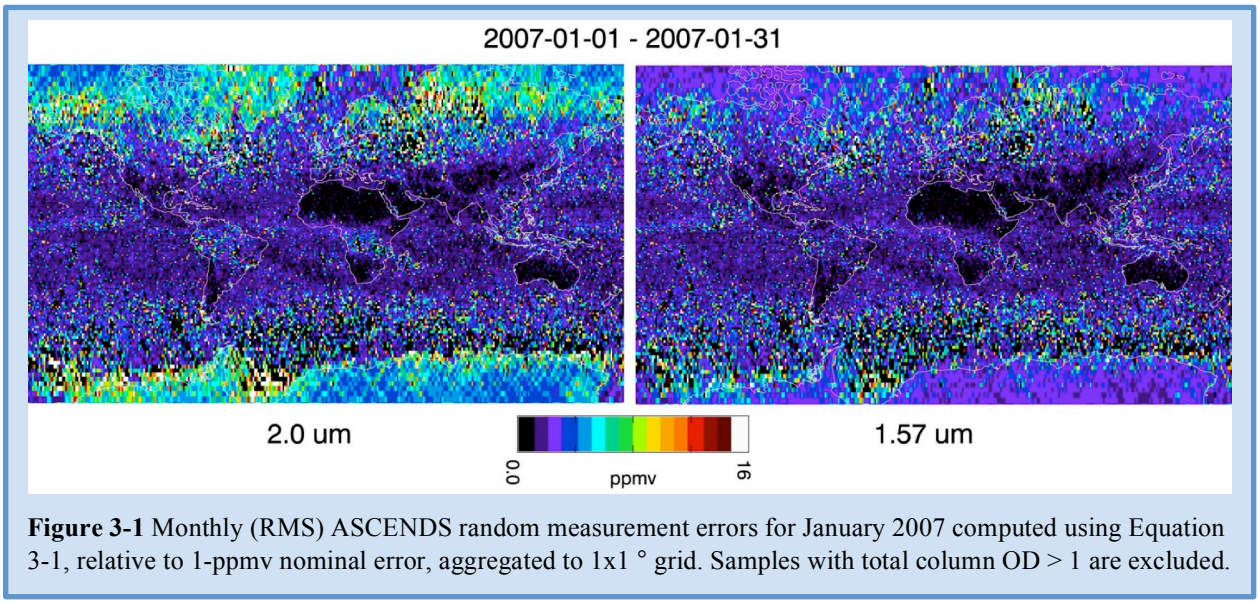

Figure 3-1 Monthly (RMS) ASCENDS random measurement errors for January 2007 computed using Equation 3-1, relative to 1-ppmv nominal error, aggregated to 1x1 ° grid. Samples with total column OD > 1 are excluded.

3.2.1 Arctic Permafrost Thawing Emissions

Permafrost soils occupy about 24% of the exposed land area in the high latitude Northern Hemisphere (Zhang et al., 1999) and contain approximately 1700 Gt of carbon in the form of frozen organic matter (Tarnocai et al., 2009). As temperatures increase and the permafrost thaws, the organic material begins to decay, releasing CO_2 and methane into the atmosphere, resulting in enhanced atmospheric concentrations of these greenhouse gases and further warming. The rate of this feedback is highly uncertain, however, prompting calls for enhanced pan-Arctic greenhouse gas monitoring including satellite observations (NRC, 2013). Measurements at high latitudes with required sensitivity near the surface are particularly difficult, if not often impossible, for passive sensors making this a unique area of contribution for the ASCENDS lidar approach.

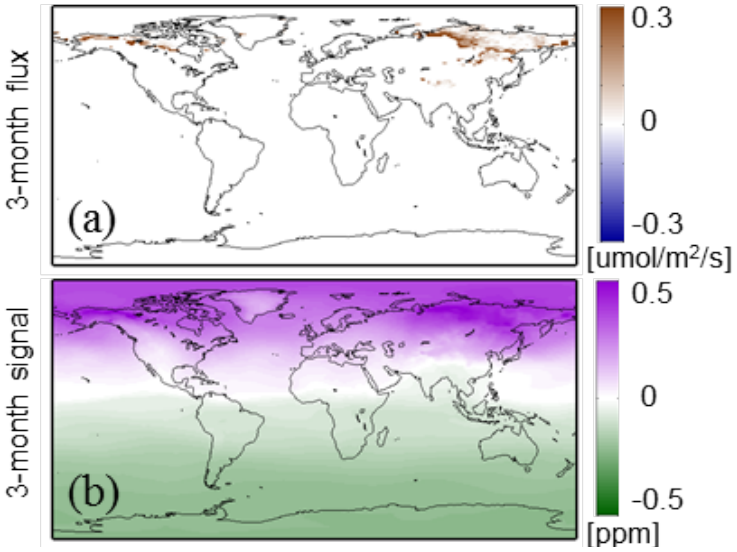

Figure 3-2 Perturbation flux and column average CO_2 mixing ratio for carbon release experiment (a) 3-month average (May – July) CO_2 flux for 2022 and (b) resulting 3-month average CO_2 perturbation. Negative mixing ratio values in the Southern hemisphere are a result of the global mean adjustment to create an overall flux neutral scenario (Hammerling et al., 2015).

The permafrost carbon emission scenario tested here derives from the simulations of Schaefer et al. (2011). Emission distributions are formed from the ensemble mean of CO_2 flux projections calculated in the Simple Biosphere/Carnegie-Ames-Stanford Approach (SiB-CASA) land biosphere model, driven by output from several General Circulation Models for the A1B scenario from the Intergovernmental Panel on Climate Change (IPCC) Fourth Assessment report (Lemke et al., 2007). The 2020 and 2021 fluxes were used to spin up the Parameterized Chemistry and Transport Model (PCTM, Kawa et al., 2004) and create corresponding atmospheric CO_2 concentrations. The atmosphere resulting from the 2022 fluxes was taken as the perturbation field. The 2022 permafrost fluxes and CO_2 perturbation are shown in Figure 3-2.

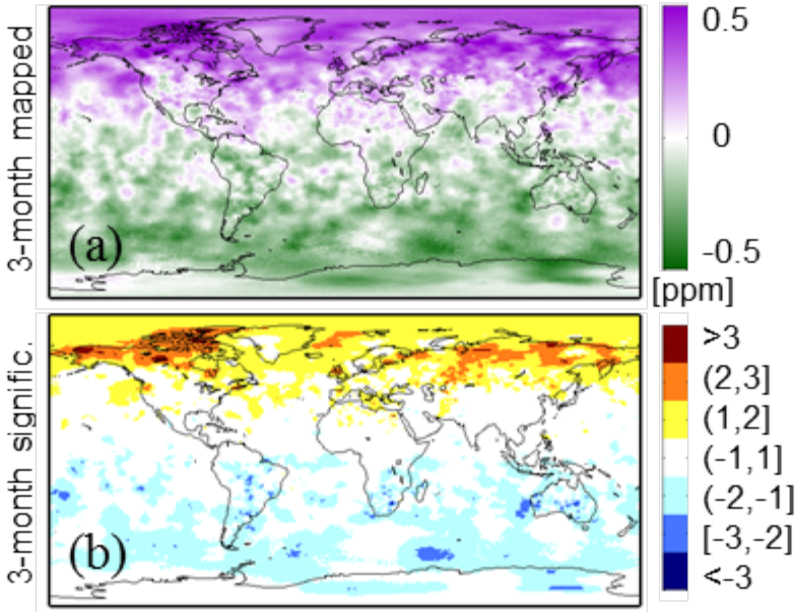

Figure 3-3 Results from the permafrost carbon release experiment (a) 3-month (May-July) ASCENDS-mapped CO_2 signal (perturbation minus baseline) and (b) significance level of the 3-month mapped signal. Significance is the mapped signal divided by the uncertainty of the mapped signal in units of standard deviations. The values are discretized for improved visualization. Yellow, orange and dark red (light, medium and dark blue) represent areas where the mapped CO_2 perturbation is larger (smaller) than the mapped baseline CO_2 concentration by more than one, two or three standard deviations, respectively, of the uncertainty of the mapped signal. This example uses the ASCENDS medium measurement noise (1 ppmv random error), 1.57 μm case (See Box 3-1 and Hammerling et al., 2015).

Signal Detection Significance

The detectability of a significant signal is relatively straightforward in the case of the anticipated permafrost carbon emissions (Figure 3-3). The challenge is in capturing longitudinal and latitudinal gradients, which can better attribute the increase to the permafrost thawing process. Because of the seasonality of the permafrost fluxes, the gradients in the atmospheric CO_2 distribution are most evident in the months following the start of the spring thaw. By August, atmospheric mixing, which occurs rapidly in the Arctic, spreads the spatial signature of the tundra thawing into a near-uniform zonal increase. While the concentration signal is highest around September, or even later in the year, when most of the seasonal melting has occurred, the diagnostic concentration signals are mostly indicative of the spatial pattern of the tundra thawing fluxes that occur in the late spring/early summer before the effects of atmospheric mixing take over. This phenomenon is caused by the specific combination of the temporal pattern of the

permafrost carbon release and rapid atmospheric mixing in the High Northern Latitudes. Overall, the permafrost thawing signal is readily detectable (i.e., SNR > 2-3) for either level of ASCENDS measurement noise considered (0.5, 1.0 ppmv, see Box 3-1), and spatial gradients are best detected using two to three month aggregation periods in the late spring/early summer.

Flux Estimation

Flux estimation experiments were conducted using the transport model TM5 (Krol et al, 2005) together with a 4DVAR inversion system (see Table 3-1, Box 3-2, and Basu et al, 2013). The prior (first guess) emissions are taken to be the baseline fluxes (with no permafrost thaw included), while the "true" fluxes are the prior plus the permafrost emissions described above, for the model year 2022. These true fluxes are used to drive TM5, whose output is sampled with the ASCENDS weighting functions for the two instrument wavelengths considered. The observation errors are as detailed in Appendix C. Two different prior error covariance assumptions were made. The first is that we would have no knowledge of the permafrost thaw, and so the prior covariance is taken to be the difference between two biosphere and ocean flux estimates, as described below in Section 3.3.3. The second assumption is that the community has some knowledge of the spatial pattern of the permafrost, but that its flux magnitude is uncertain. This is modeled by taking a prior covariance that is the sum of the general background covariance in the first experiment together with the permafrost emissions themselves. The spatial pattern is important to the 4DVAR assimilation system, because the optimization makes the largest corrections where the prior uncertainty is largest. In general including this uncertainty in the spatial pattern improved posterior errors.

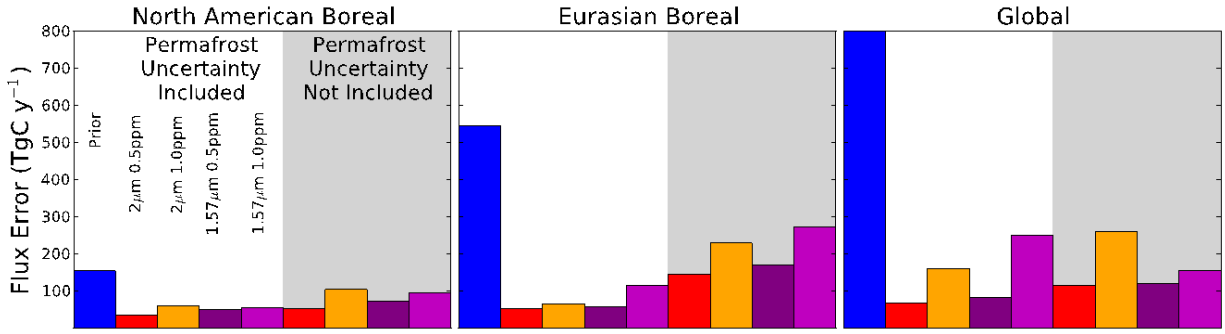

Figure 3-4 Regional inversion results from the permafrost carbon release experiment. Flux error is the RMSE of the monthly fluxes aggregated across each region scaled to an annual amount. The blue bar represents the prior and the red and orange bars represent the posterior fluxes using ASCENDS pseudo-data derived with the 2.05 μm weighting function and 0.5 ppm (red) and 1.0 ppm (orange) nominal errors (see Box 3-1). The purple and magenta bars represent the posterior flux error using the 1.57um weighting function and 0.5 ppm (purple) and 1.0 ppm (magenta) errors. The bars under the grey shaded background represent experiments in which the permafrost distribution uncertainty was not included in the prior covariance, while the other four bars represent the case in which the permafrost uncertainty was included.

The results are depicted in Figure 3-4. The optimized fluxes are found at the monthly time scale, at a global resolution of 6° longitude by 4° latitude, and the resulting fluxes are aggregated to regions that contain the permafrost flux signal of interest. The global value is also shown. For the boreal regions, ASCENDS reduces the monthly aggregate error significantly (40 to 90%) in all experiments. The cases with greater measurement precision resulted in greater uncertainty reductions. Especially for the 0.5 ppm nominal measurement precision, the high latitude monthly

fluxes are recoverable with relatively low error (10 to 30%) using ASCENDS. These results reinforce the signal detection experiment conclusions, which show detectability after a few months of observations. The lesser measurement time requirement in the inversion is expected, since the transport model and its adjoint provide source information in the identification problem, reducing the need for the temporal averaging in the signal detection.

Table 3-1 ASCENDS Inverse Models Summary

Modeling Approaches					
	4DVAR-TM5	**4DVAR-PCTM**	**EnKF-GEOS-Chem**	**Bayesian**	**GIM**
Team	OU/Melbourne	CSU-CIRA	CSU-CIRA	GSFC/AER	Stanford-Carnegie
Inversion Method	Four-dimensional variational data assimilation	Four-dimensional variational data assimilation	Ensemble Kalman filter	Batch Bayesian synthesis inversion	Batch geostatistical synthesis inversion
Transport Model	TM5 (Eulerian), ECMWF winds	PCTM (Eulerian), MERRA winds	GEOS-Chem (Eulerian), MERRA winds	STILT (Lagrangian), WRF winds	STILT (Lagrangian), WRF winds
Domain and Flux Resolution	Global, 6°x4°, monthly	Global, 6°x4.5°, weekly	Global, 2°x2.5°, two weeks	North America, 1°x1°, weekly	North America, 1°x1°, 3-hourly
Chapter Sections	3.2.1-3.2.3	3.3.3, 3.4.1-3.4.2	3.2.4	3.3.2	3.3.1
Reference	Basu et al. (2013); Krol et al. (2005)	Baker et al. (2006); Kawa et al. (2004)	Tippet et al. (2003); Bey et al. (2001)	Wang et al. (2014)	Shiga et al. (2014)

ASCENDS data will readily enable detection of realizable permafrost thawing CO_2 emissions at high latitudes on a monthly to seasonal time scale.

3.2.2 Fossil Fuel Emission Shift

As fossil fuel burning increases rapidly in the developing world and potentially decreases as a result of policy implementation in industrialized countries, more accurate and better-resolved emissions information is needed (Duren and Miller, 2012). Fossil fuel emissions from China have increased rapidly over the last decades (Olivier et al., 2012; Peters et al., 2011), while those from Europe decreased by 3% in 2011 relative to 2010 with an overall decline over the last two decades (Olivier et al., 2012). Satellite data, such as those available from the ASCENDS mission, increasingly play a role in both validating bottom-up estimates (e.g., Bovensman et al., 2010) and directly inferring fossil fuel emissions. In this section, we describe results from experiments to test the capability of the ASCENDS data to constrain fossil fuel distributions.

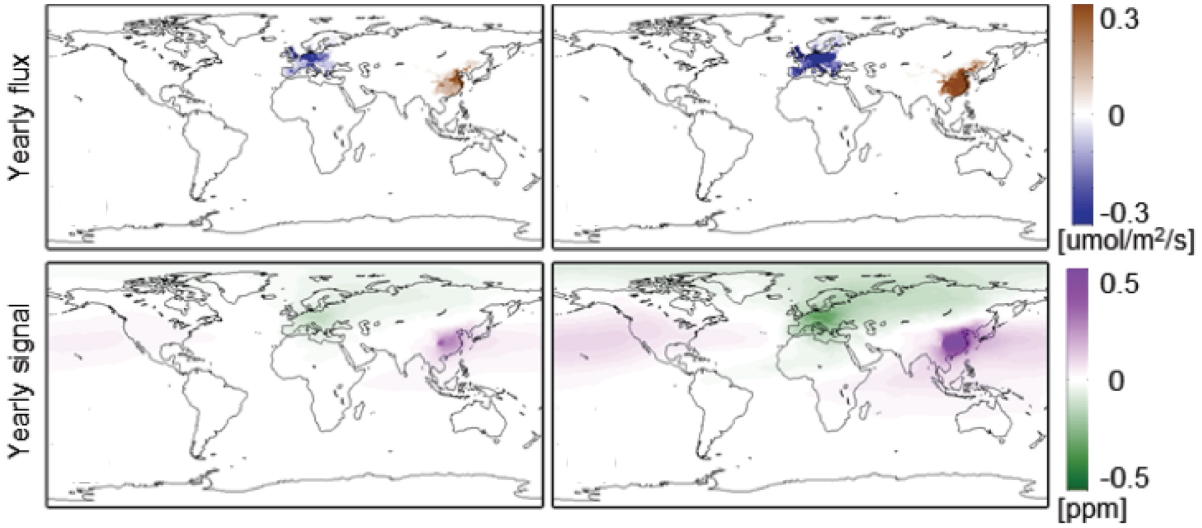

Figure 3-5 Perturbation flux and column CO_2 mixing ratio for the fossil fuel experiments. First row: Yearly average CO_2 flux shift. Second row: Yearly average column CO_2 concentration perturbation. Left (right) panels show the lower (higher) emission change case.

Two "flux neutral" emission scenarios valid around the year 2022 were derived to test ASCENDS ability to detect potential fossil fuel emissions changes (Hammerling et al., 2015). The emissions scenarios and corresponding CO_2 column average mixing ratio perturbation are depicted in Figure 3-5. The lower emission change scenario represents a 20% decrease (compared to 2007 Carbon Dioxide Information Analysis Center (CDIAC) levels (Andres et al., 2011)) of European emissions, with a corresponding 12% increase in China. The higher signal case includes a 50% decrease of emissions in Europe with a corresponding 30% increase in China, and is used for illustration purposes; a decrease of this size is not expected in Europe within a decade.

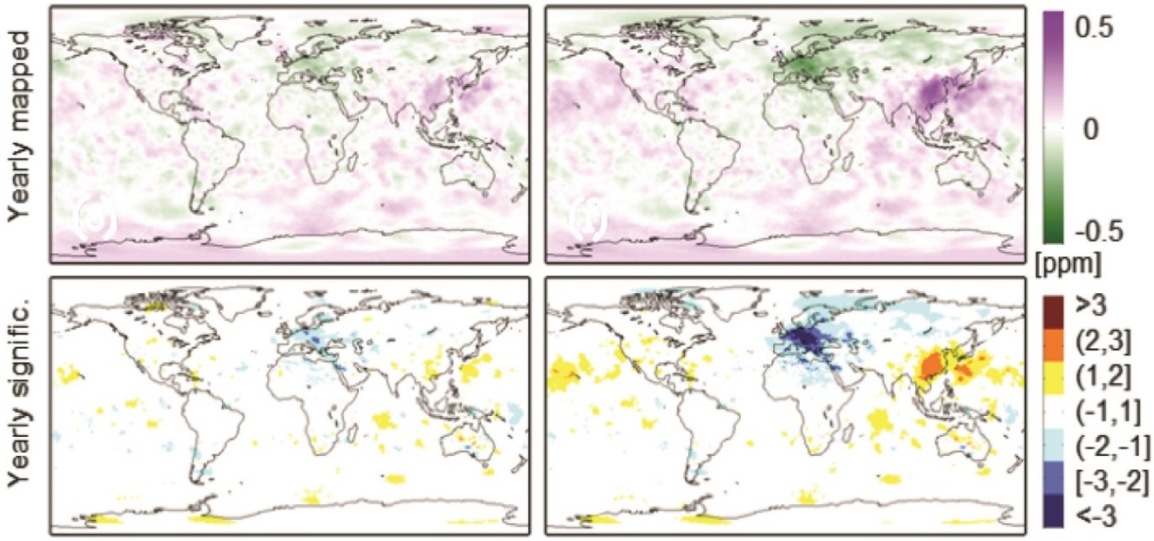

Figure 3-6 Significance results for the fossil fuel experiments for ASCENDS. Using nominal measurement noise at 1 ppmv and the 1.57 µm case (Box 3-1). First row: yearly mapped CO_2 signal. Second row: significance of the yearly mapped CO_2 signal. The mapped signal is calculated and plotted as described in Figure 3-3. Left (right) panels show the lower (higher) emission change case.

Signal Detection Significance

The imposed fossil fuel emissions perturbations lead to a pronounced CO_2 spatial signature that is localized over Europe and China (Figure 3-6). This is in contrast to other experiments at mid-to-high latitude, where the spatial signatures are largely diffused and the signals in atmospheric CO_2 are seen primarily as zonal increases. The magnitude of the lower fossil fuel perturbation signal, however, is very small, and likely to be difficult to detect

Given the relative lack of seasonality in the imposed fossil fuel perturbation scenarios, averaging over longer periods of time leads to better detectability, i.e., the annual signals are greater than those aggregated for 3 months. Although the diffusive nature of the atmospheric transport clearly plays a role, the atmospheric signal still localizes the source region of the perturbation flux throughout all the seasons. The effect of varying measurement noise levels on the detectability is as expected: increasing measurement noise leads to decreased significance in the results and requires in turn longer averaging periods. For the higher signal case, however, all three considered instrument noise levels (0.5, 1.0, 2.0 ppmv, Box 3-1) capture the signal in the annual results. Overall, these findings imply that ASCENDS can detect changes in fossil fuel emissions, but depending on the strength of the signal, detection may require multiple years of observations.

Flux Estimation

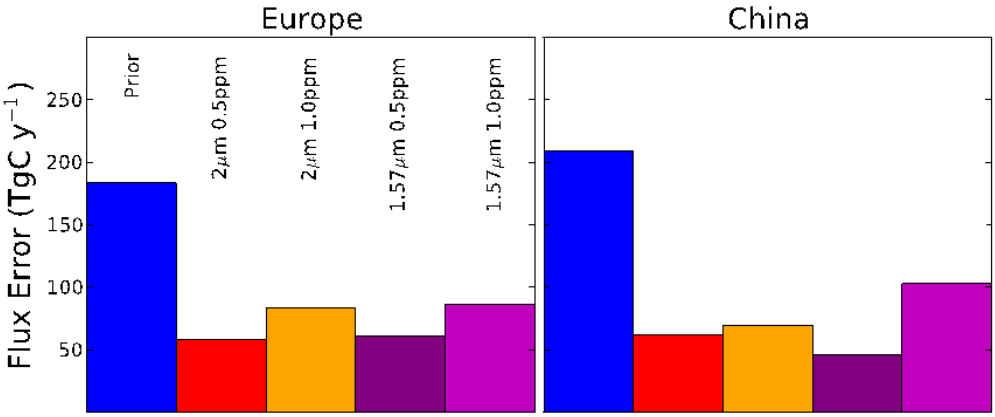

Figure 3-7 Regional flux errors for the 20% European fossil fuel emission shift scenario as in Figure 3-4. The prior errors for each region are about 200 TgC, and each of the ASCENDS instruments reduces that significantly. The flux errors are monthly RMSE, scaled to an annual amount.

For the TM5-4DVAR inverse experiment, the true fluxes are the baseline emissions together with the low fossil fuel shift scenario pictured in the left panels of Figure 3-5. The perturbation adds about 0.2 PgC for Europe and subtracts the same from China. The prior uncertainty was taken to be the biospheric uncertainty described in Section 3.3.4 together with 20% of the CDIAC emissions for 2010. This small value for the fossil fuel emissions is enough to provide the 4DVAR system with some spatial information on the location of the sources. Results for the flux estimation are shown in Figure 3-7. These figures suggest that ASCENDS is able to reduce errors in the prior emissions by at least 50% at the monthly time scale. In addition, aggregating to annual numbers yielded even larger reductions in the fossil fuel emissions errors. This greatly strengthens the results of the signal detection experiment. Again, this is due to the inclusion of the transport model adjoint, which is able to correctly trace concentration differences back to source regions as large as Europe and China. Though not shown here, similar experiments that did not

include a fossil fuel prior uncertainty term yielded promising results, though with smaller reductions in the posterior error.

ASCENDS will be able to identify a foreseeable shift in monthly fossil fuel emissions at the scale of Europe and China, presuming an accurate model for transport.

3.2.3 Flux Changes in the Southern Oceans

The Southern Ocean is a very sparsely sampled region that represents a key uncertainty in the carbon cycle. This region has an apparent high sensitivity to climate change (Le Quéré et al., 2009), and understanding its regional carbon-climate feedback has implications for quantifying the region's future as a carbon sink. Studies have shown that the southern oceans contributes half of the ocean uptake of anthropogenic CO_2 (e.g., Le Quéré et al., 2009; Meredith et al., 2012), although uncertainties on the magnitude of this uptake and its trend over time are high. Given that the Southern Ocean is also very difficult to monitor *in situ*, the ability of the ASCENDS mission to observe in this region could provide invaluable insights into changes in the ocean carbon sink.

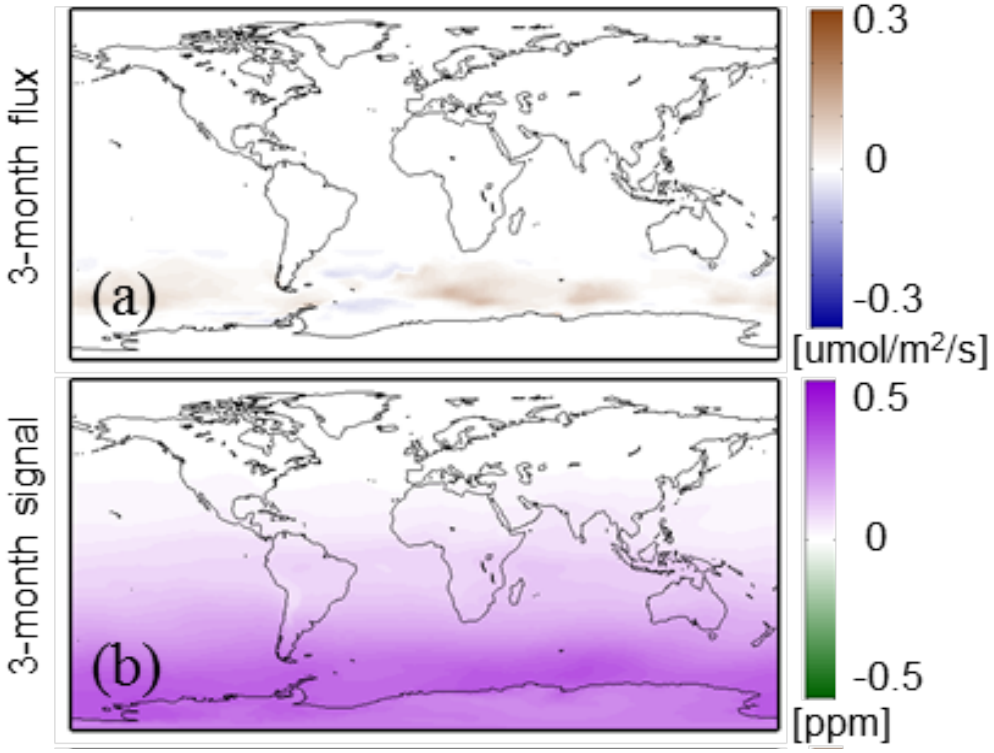

Figure 3-8 Southern Ocean experiment flux difference and column average CO_2 mixing ratio perturbation using the 1-ppmv, 1.57 µm nominal ASCENDS error case. (a) 3-month (April – June) average CO_2 flux and (b) 3-month average CO_2 concentration.

Variations in climatic modes, such as the El Nino-Southern Oscillation (ENSO), are key drivers of interannual variability in ocean carbon exchange. For this reason, scenarios for opposing ENSO modes were chosen to test detectability of Southern Hemisphere (SH) ocean flux changes that ASCENDS expects to encounter. The Southern ocean fluxes used for this scenario are based on a hindcast simulation of the Community Climate System Model (CCSM) Ocean

Biogeochemical Elemental Cycle model as described by Doney et al. (2009). Fluxes were obtained at one degree spatial and monthly temporal resolution. The years 1977 and 1979 were chosen as prototypical example flux patterns, as they represent large differences in ocean fluxes due to variations in climatic modes. The simulated air-sea CO_2 flux in 1979 was about half of that for 1977 averaged across the Southern ocean. The flux difference between 1977 and 1979 in the Southern Ocean is used for the perturbation scenario. Figure 3-8 shows the average fluxes and column mixing ratio change for April through June (from Hammerling et al. (2015)).

Signal Detection Significance

The detection of changes in the Southern Ocean source/sink characteristics is the most challenging of the three signal detection scenarios considered for several reasons. The overall magnitude of the CO_2 difference signal in the Southern Oceans is weak, with an absolute value never exceeding 0.4 ppm in the column. In addition, this scenario contains sub-seasonal and sub-regional-scale flux variability, superimposed on the seasonal pattern in the fluxes, which makes the perturbation more difficult to distinguish. Atmospheric mixing also plays a role in obscuring the longitudinal fingerprint of the Southern Ocean as the origin of the signal, similar to what was observed in the permafrost carbon release scenario described above.

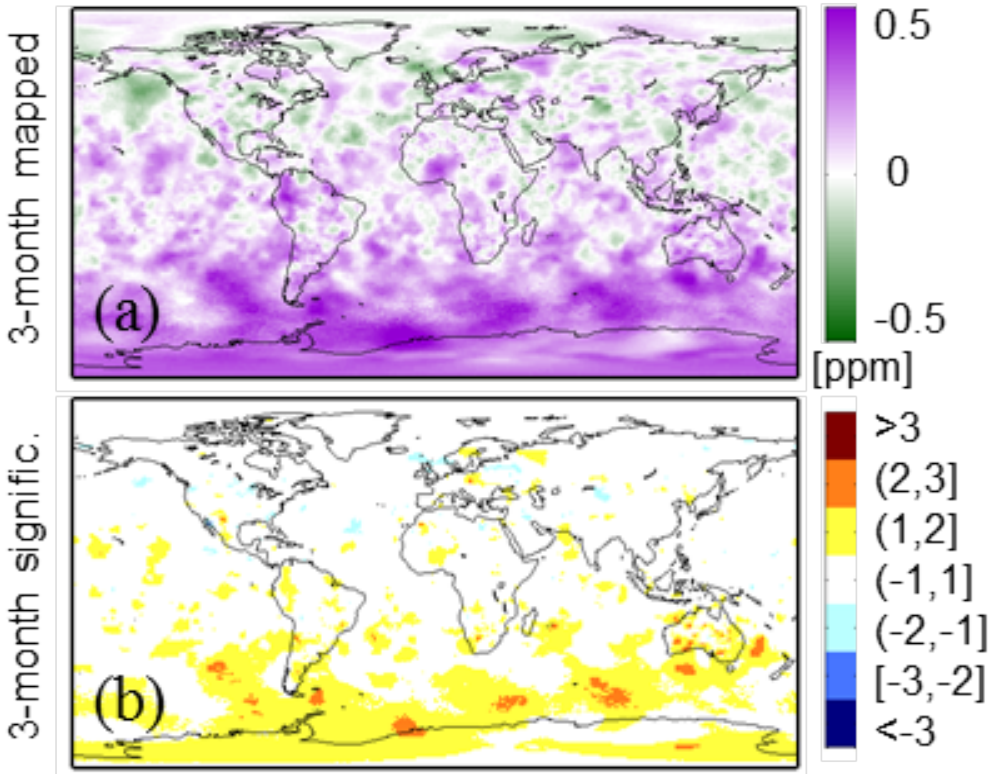

Figure 3-9 Significance results for Southern Ocean experiment for medium measurement noise (1 ppmv, 1.57 µm case, Box 3-1). (a) 3-month mapped CO_2 signal, (b) Significance of the 3-month mapped CO_2 signal as described in Figure 3-4.

Figure 3-9 shows areas of the SH ocean are distinguishable at the 2 to 3 sigma level for 3-month aggregated ASCENDS sampling with 1-ppmv nominal random error levels, but the signal is not strong. For annually aggregated measurements (not shown), the yearly results clearly indicate a

zonal increase in the High Southern Latitudes, however, the pattern indicative of the Southern Ocean flux difference within the zonal band is less clear.

Flux Estimation

A surface flux estimation experiment was performed, similar to those described in Sections 3.2.1 and 3.2.2, where the true flux was taken to be the ocean flux from 1979 (and zero for the rest of the globe), while the prior was the flux from 1977. The prior covariance was as described in Section 3.3.3 below, which for the Southern Ocean is the difference between the NCAR Ocean Model and Takahashi et al. (1999) for the reference year 2000.

The prior and posterior errors aggregated for the Southern Ocean are shown in

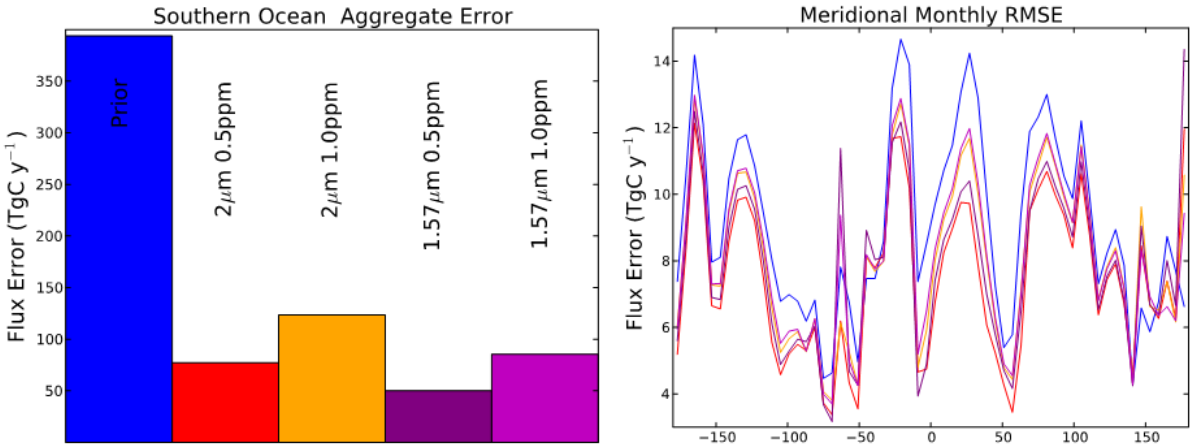

Figure 3-10 Inversion results from the Southern Ocean interannual variability experiment. Colors represent the different instrument concepts as described in Figure 3-4. In the left panel, the bars represent the monthly RMSE aggregated to Southern Ocean taken as a whole. In the right panel, the latitudinally averaged errors are plotted as a function of longitude, with the line color denoting the experiment as labeled in the left panel. Southern Ocean is treated here as south of 40S, and excluding landmasses.

ASCENDS observations, coupled with an accurate transport model, have potential to substantially reduce uncertainty in Southern Ocean fluxes and provide some constraint on their spatial and temporal variability.

Despite the weak signal strength, ASCENDS would be able to estimate at least 65% of the tested interannual variability in the emissions of the Southern Ocean. Furthermore, we assess the ability of ASCENDS to give information about the spatial gradient from east to west in the Southern Ocean by aggregating along lines of longitude in the Southern Ocean and plotting the resulting meridional errors (Figure 3-10). Note that ASCENDS is able to reduce the errors for nearly every longitude across the Southern Ocean by about 1 TgC mon^{-1} (6 deg longitude)$^{-1}$, despite the weak magnitude of the spatial gradient across the region. In addition, though the RMSE for the 1.57 μm instrument was lower for the region as a whole, the flux error for the 2.05 μm instrument is smaller than for 1.57 μm when the spatial dimension is considered, which is evident from the red line in Figure 3-10 being lower than the purple for most of the longitude bins. This type of spatial information would be unavailable using the current surface network, which could only provide a few pieces of information that would represent local flux variations only.

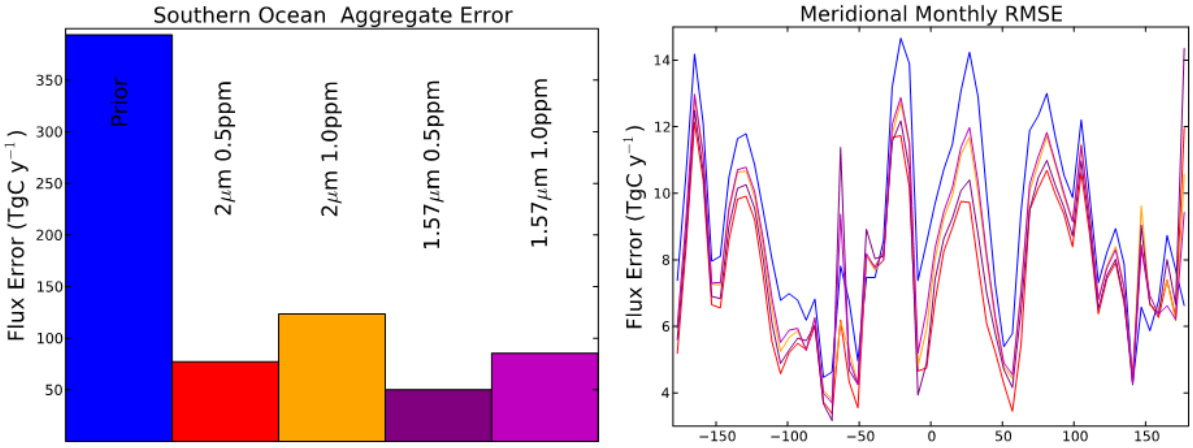

Figure 3-10 Inversion results from the Southern Ocean interannual variability experiment. Colors represent the different instrument concepts as described in Figure 3-4. In the left panel, the bars represent the monthly RMSE aggregated to Southern Ocean taken as a whole. In the right panel, the latitudinally averaged errors are plotted as a function of longitude, with the line color denoting the experiment as labeled in the left panel. Southern Ocean is treated here as south of 40S, and excluding landmasses.

ASCENDS observations, coupled with an accurate transport model, have potential to substantially reduce uncertainty in Southern Ocean fluxes and provide some constraint on their spatial and temporal variability.

3.2.4 Enhanced Sink Due to Carbon Fertilization

The previous experiments examine realistic perturbations to one aspect of the carbon cycle. In reality, CO_2 datasets and models will be used to examine multiple possible perturbations to land and ocean fluxes occurring simultaneously. Here, we create a more complex signal detection experiment by combining several realistic perturbations to test the ability of the ASCENDS data to constrain net ecosystem carbon exchange (NEE) over different times and locations. These perturbations include:

- Respiration reduced by 5% over Northeastern U.S. forests to simulate forest regrowth after land use change. There is strong evidence (Houghton et al., 1999; SOCCR, 2007; Pan et al., 2011) to support an enhanced carbon sink as forests re-grow after centuries of clearing for agriculture.
- Forest Gross Primary Production (GPP) increased by up to 10% over regions of Western Europe and the Central U.S. as a function of nitrogen deposition, with peak effect over areas of known industrial nitrogen emissions.
- GPP amplified by 5% over tropical broadleaf forest regions between 30°S and 30°N to account for a CO_2 fertilization effect in tropical forests. Both basic plant physiology, as well as experimentation (Oren et al., 2001) support the idea that increased atmospheric carbon dioxide levels should lead to increased plant uptake.
- A reduction of overall atmospheric-ocean exchange (as might result from decreasing winds) imposed by providing a zonal variation to the flux, from a 5% reduction in flux

over the Northern Oceans to a 15% reduction over the Tropical Oceans, to a 25% reduction over the Southern Oceans (e.g., Le Quéré et al., 2009).

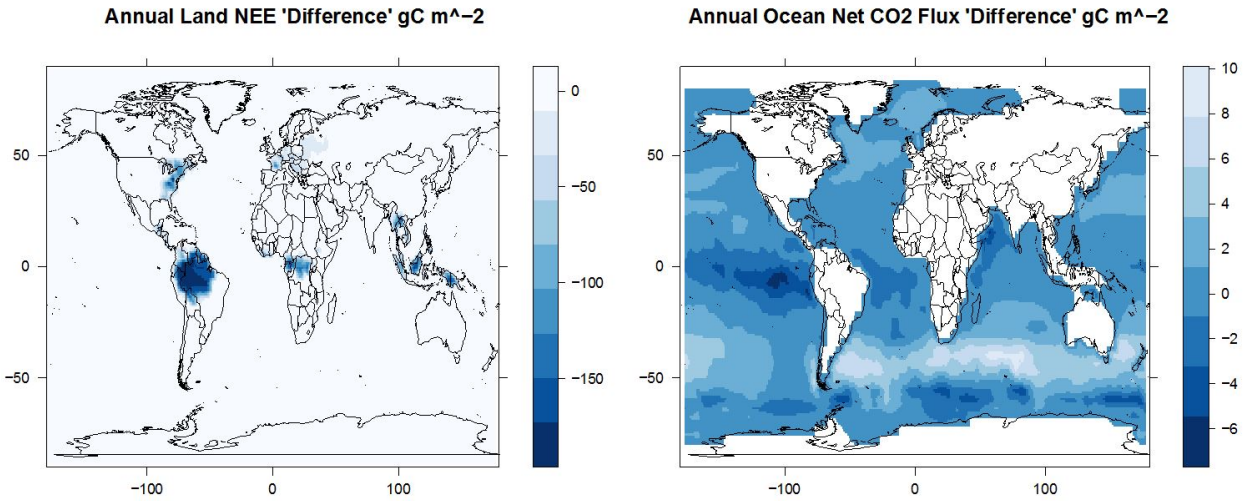

Figure 3-11 The simulated net CO_2 flux anomalies that arise from the GPP and ocean flux perturbations used in the multiple signal detection exercise and inversions. Note the dominance of Amazon GPP sink enhancement.

The flux perturbations shown in Figure 3-11 were used to drive GEOS-Chem for 2006 and 2007 to produce 3-D CO_2 anomaly fields for 2007. The fields were then sampled using the ASCENDS weighting functions resulting in XCO_2. The mean zonal gradient for each month was then subtracted from the monthly perturbation XCO_2 fields in order to isolate the local effects of sinks on XCO_2. Finally, this average perturbation field was divided by the expected ASCENDS errors. The absolute perturbation signal-to-noise of the ASCENDS pseudo measurements (Figure 3-12) is often greater than 0.5 for *individual* retrievals at 1-ppmv nominal error (Box 3-1), with slightly stronger signals during the Amazonian wet season. These results suggest that the strong Amazon drawdown would be evident from ASCENDS by carefully aggregating individual satellite retrievals. While the weakened surface exchange of CO_2 in the oceans seems unlikely to be detectable from individual ASCENDS retrievals, the combined effect of reduced respiration and N fertilization effects on regrowing Northeastern U.S. forests, most evident in the late spring and summer, is evident, although at much lower signal to noise than the Amazon.

Flux Estimation

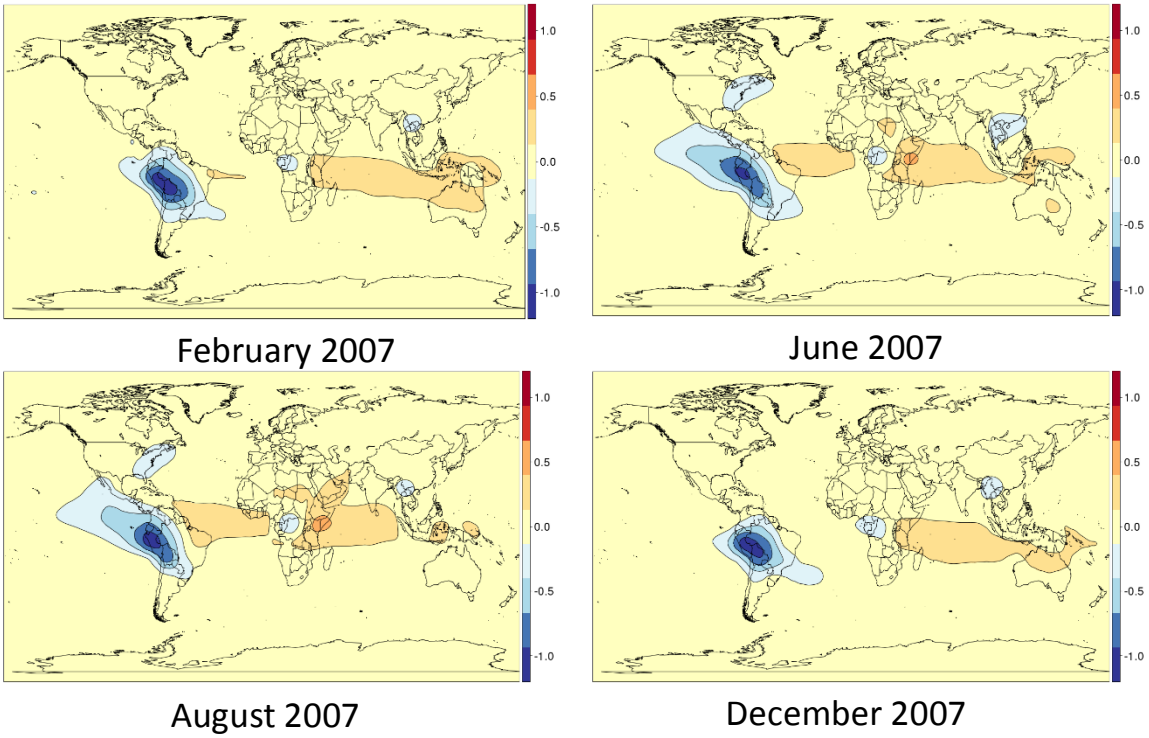

Figure 3-12 Simulated perturbation signal-to-noise for XCO_2 with 2.05 µm weighting function (See Box 3-1 and Figure 5-2) for the multiple flux perturbations of Figure 3-11.

The results above suggest the ability of individual retrievals to detect realistic flux perturbations. An EnKF-based inversion (Table 3-1, Box 3-2, Appendix C) was run on the perturbed CO_2 field to determine to what degree the true perturbed fluxes could be estimated using ASCENDS observations. Figure 3-13 shows the true and the posterior estimated fluxes: their similarity indicates that large perturbations in land fluxes, such as the Amazon, will be attributable via inversions of atmospheric CO_2 measurements from ASCENDS. Figure 3-14 shows that the difference between the ensemble mean CO_2 flux estimate for the Tropical South American region (Transcom, Gurney et al., 2002) and the "truth" is approximately 100 TgC/year with a standard deviation (uncertainty) of the posterior estimate at approximately the same magnitude. The recovered sink is approximately 18 times that, indicating a strong recovery by the inversion system.

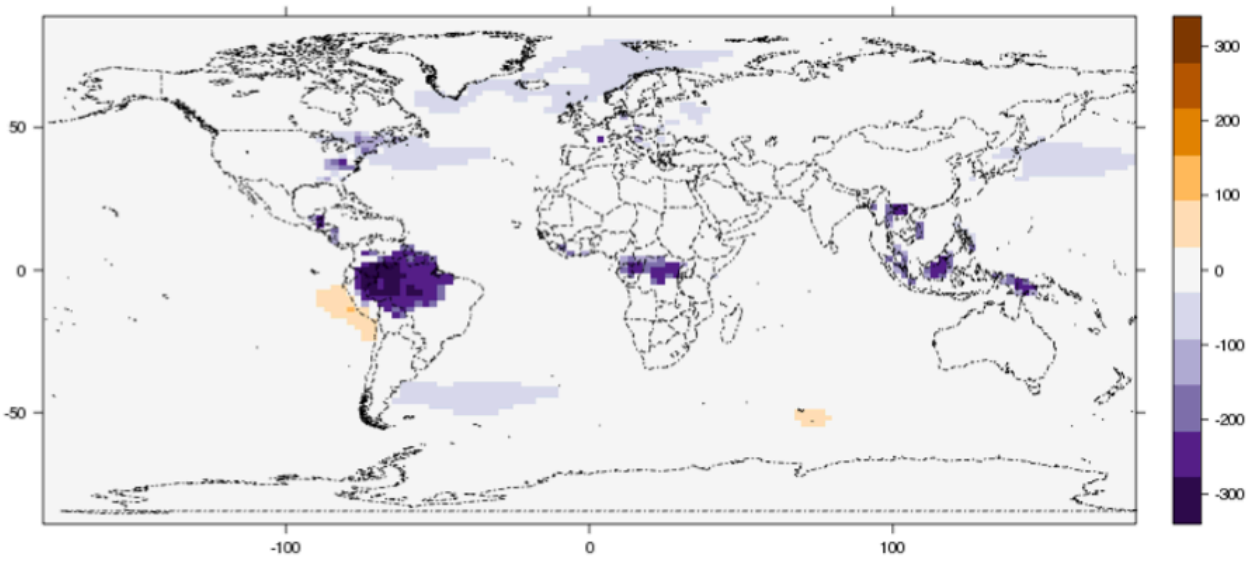

(a)

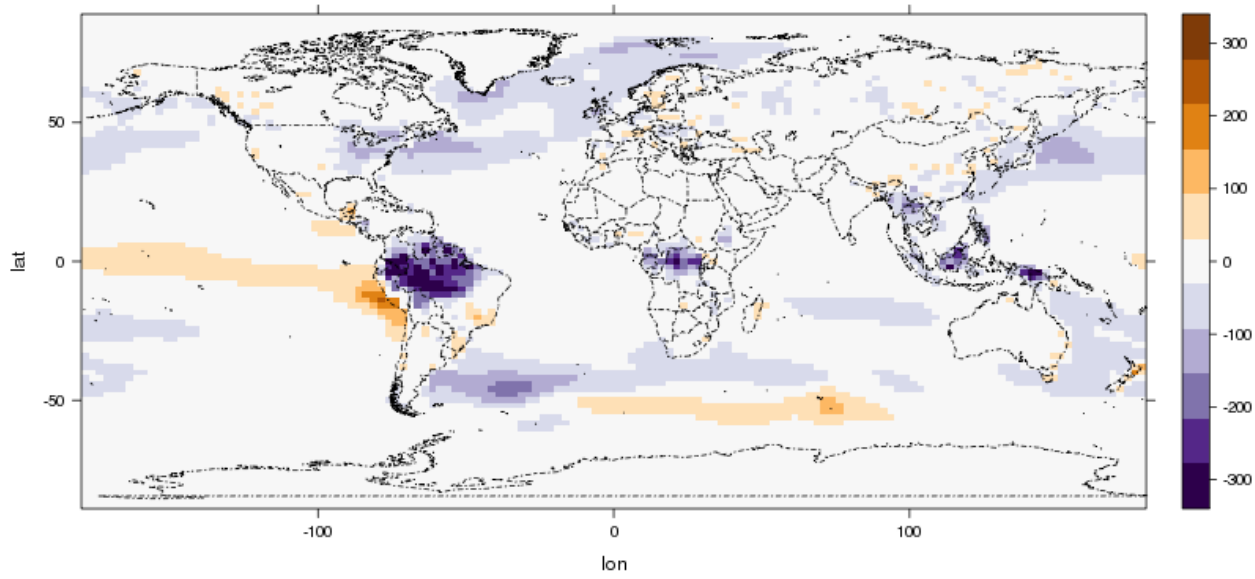

(b)

Figure 3-13 Comparison of 'truth' and model annual Net Ecosystem Exchange (NEE, gC m-2 yr-1) (a) the 'truth' representing the sum of the two sets of perturbations shown in Figure 3-11 and (b) model estimated posterior mean NEE from the atmospheric inversion. Posterior uncertainty can be seen below in Figure 3-14.

Weaker land signals such as those generated by regrowth of forests in the northeastern U.S. and nitrogen fertilization of Europe are also generally improved by the inversion system, although the pattern is more diffuse than that specified in the "true" fluxes. The difference between the ensemble mean CO_2 flux estimate for the Temperate North American region and the "truth" is approximately 38 TgC/year with the standard deviation of the estimate at approximately 40 TgC/year, significantly smaller than the recovered sink (~200 TgC/year). Spatial differences of up to 100 gC/m^{-2} within the region are seen (Figure 3-13) although the integrated average

difference is much smaller. Ocean perturbations are not seen well by the inversion system, which could be due to a misspecification of the prior covariance for the ocean fluxes in the simulations, weaker magnitudes of the ocean flux perturbations, or likely some combination of the two.

ASCENDS will provide data sufficient to constrain large tropical land sinks as well as some weaker Northern mid-latitude regional land sinks.

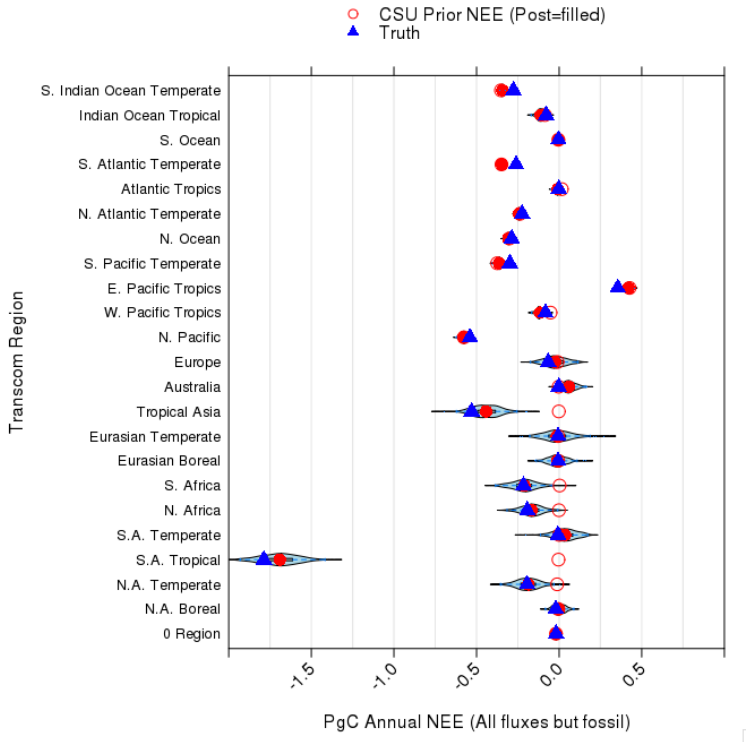

Figure 3-14 Regional integrated annual NEE for atmospheric inversion test. The blue shaded area can be interpreted as the probability density function estimate for the ENKF ensemble (Hintze et al., 1998).

3.3 Improved Flux Estimates at Global and Regional Scales

The experiments in Section 3.2 evaluated the ability of ASCENDS measurements to address specific science hypotheses posed as realistic perturbations to carbon fluxes. Here, we broaden this approach to test the general impact of prospective ASCENDS data on flux inversions at both regional and global scales. A major goal of this exercise is to test the impact of a range of possible mission and instrument implementation options (Chapter 5) on the ability of ASCENDS to reduce uncertainty in our knowledge of the carbon budget. Some of these parameter explorations were already exhibited in the inversions in Sections 3.2. A variety of modeling approaches is used in order to bolster the robustness of the findings from any individual model, whose flux retrieval performance may well depend on model-specific methods and assumptions (Table 3-1). The general Bayesian inverse modeling approach, and its variants, employed for these experiments are briefly outlined in Box 3-2, and in more detail in Appendix C. The instrument models that are tested include sampling with vertical weighting functions applicable to

measurement wavelengths of 1.57 and 2.05 μm (Figure 5.2), three levels of nominal random error (0.5, 1.0, and 2.0 ppmv) scaled globally (Box 3.1), and several possible forms of bias error (in the global inverse model only).

Box 3-2 Flux Estimation Techniques

The basic premise of the inverse modeling approaches is that, given a set of atmospheric concentration observations and using a model of atmospheric transport and chemistry, it is possible to infer information on the distribution of sources and sinks at the surface of the Earth (Enting, 2002). The approach most commonly adopted in atmospheric inverse modeling of CO_2 sources and sinks is based on Bayesian inverse modeling, in which one seeks the optimal flux estimate $\hat{\mathbf{s}}$ that minimizes:

$$J(\mathbf{s}) = (\mathbf{s}-\mathbf{s_o})^{\mathrm{T}}\mathbf{B}^{-1}(\mathbf{s}-\mathbf{s_o}) + (\boldsymbol{h}(\mathbf{s})-\mathbf{y})^{\mathrm{T}}\mathbf{R}^{-1}(\mathbf{h}(\mathbf{s})-\mathbf{y}) \quad (3\text{-}2)$$

where y is a vector of atmospheric CO_2 observations, **h** represents an atmospheric transport model, s is a vector of the discretized unknown surface flux distribution, **R** is the model-data mismatch covariance, s0 is the prior estimate of the flux distribution **s**, and **B** is the covariance of errors in the prior estimate s0. The final solution in the form of a posteriori means and covariances is given by:

$$\hat{\mathbf{s}} = \mathbf{s}_0 + \mathbf{B}\mathbf{H}^T\left(\mathbf{H}\mathbf{B}\mathbf{H}^T + \mathbf{R}\right)^{-1}\left(\mathbf{y} - \mathbf{H}\mathbf{s}_0\right) \quad (3\text{-}3)$$

$$\mathbf{V}_{\hat{\mathbf{s}}} = \mathbf{B} - \mathbf{B}\mathbf{H}^T\left(\mathbf{H}\mathbf{B}\mathbf{H}^T + \mathbf{R}\right)^{-1}\mathbf{H}\mathbf{B} \quad (3\text{-}4)$$

where is the posterior best estimate of the surface flux distribution and is the a posteriori covariance of that best estimate, where the diagonal elements represent the predicted error variance () of individual elements in s. H (a.k.a. the sensitivity matrix) is calculated by sampling the atmospheric transport model and represents the sensitivity of the observations y to the fluxes s (i.e.,). Participating modeling groups (Table 3-1) have employed different techniques to find the solution to the atmospheric inverse problem posed in the equations above. Further detailed information can be found in Appendix C.

3.3.1 North American Regional Flux Estimates

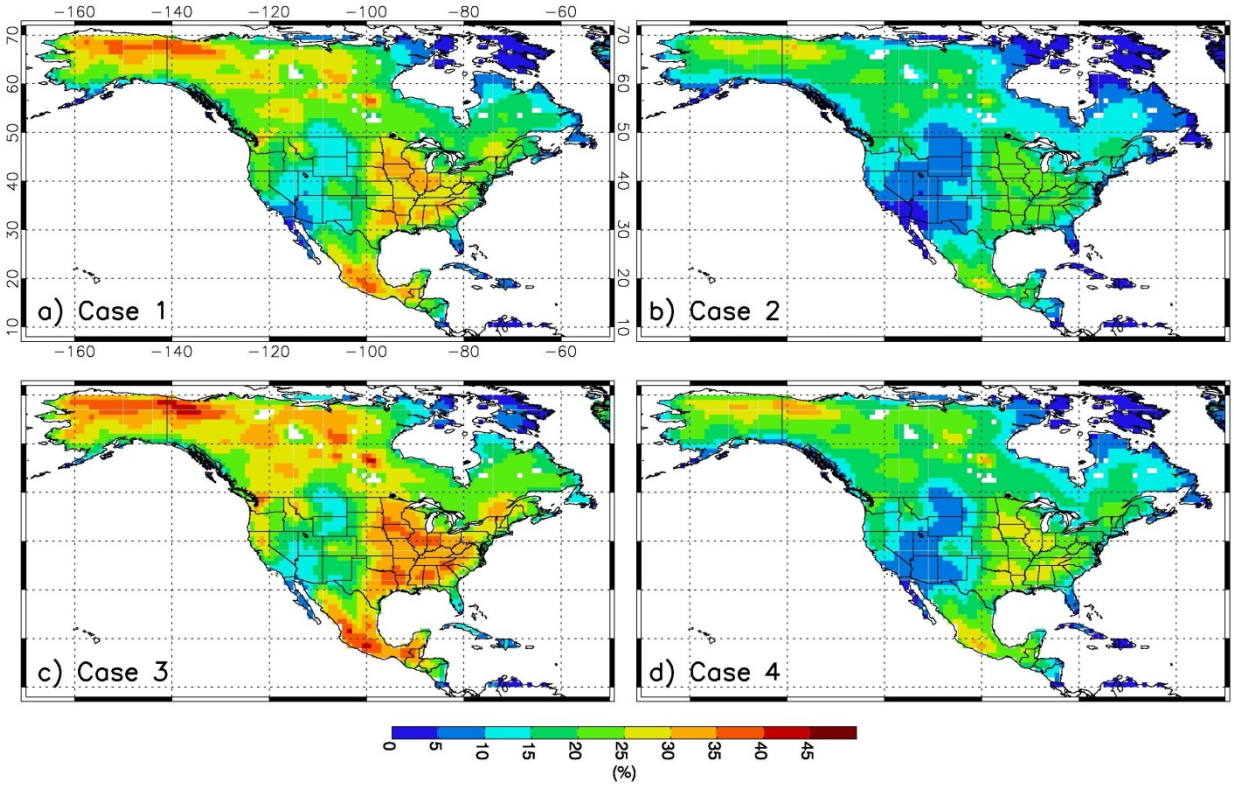

Figure 3-15 Weekly flux uncertainty reduction (RMS over the 4 months) over North America for a) Case 1 (1.57 µm and 0.5 ppm nominal error), b) Case 2 (1.57 µm and 1.0 ppm), c) Case 3 (2.05 µm and 0.5 ppm), and d) Case 4 (2.05 µm and 1.0 ppm).

Bayesian synthesis (batch) inversions are used to quantify the precision with which ASCENDS measurements can constrain land carbon sinks and sources at relatively high spatial resolution over a region such as North America (Wang et al., 2014). We consider four possible instrument configurations, including two weighting functions (for the 1.57 µm and 2.05 µm wavelengths) and two nominal random error levels (0.5 ppm and 1.0 ppm, see Box 3-1). ASCENDS observations in this modeling framework reduce flux uncertainties substantially at fine scales. At 1° x 1° resolution, weekly uncertainty reductions up to 30-45% (averaged over the year) are achieved depending on the instrument configuration (Figure 3-15). Relatively large uncertainty reductions occur year-round in southern Mexico and the U.S. Pacific Northwest and seasonally over the southeastern and mid-western U.S. and parts of Canada and Alaska. The magnitude of uncertainty reduction is dependent on the observational coverage, the specified model-data mismatch and the prior flux errors. Uncertainty reductions at the annual, biome scale range from ~40% (desert) to ~75% (eastern temperate forest and temperate grassland/shrubland) over the four experimental cases, and from ~65% to ~85% for the continent as a whole (Figure 3-16). The uncertainty reductions for the 1.57 µm candidate wavelength are on average 8% smaller than those for 2.05 µm, and for 0.5 ppm reference error are on average ~15% larger than those for 1.0 ppm error.

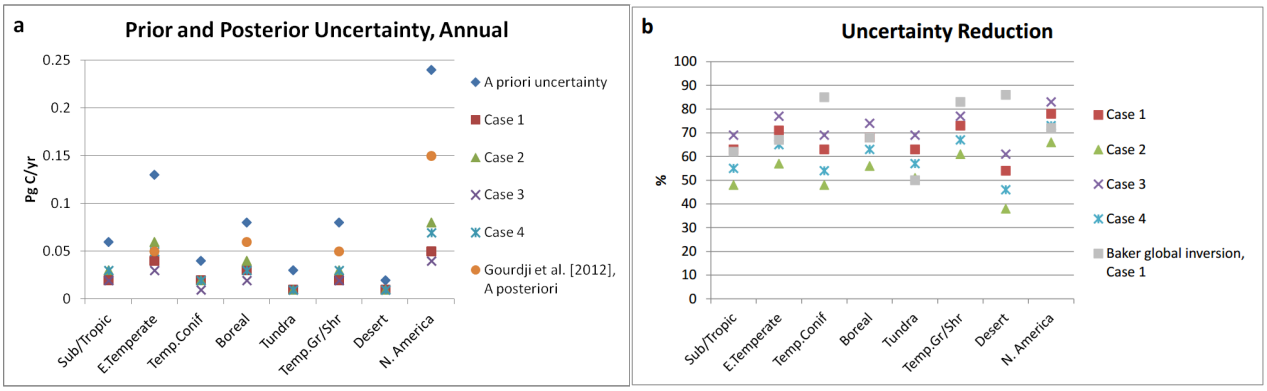

Figure 3-16 Results aggregated to biomes and continent, and compared with other studies a) A priori and a posteriori uncertainties for the year, including results from Gourdji et al. (2012). b) Fractional uncertainty reductions, including results from the CSU-PCTM OSSE described in Section 3.3.3. Gourdji et al. reported results for only the three biomes that were well constrained by their in situ observation network, along with results aggregated over the full continent; we show the approximate average of their "Simple" and "NARR" inversions. The Gourdji et al. method does not rely on prior flux estimates.

The uncertainty reductions in this regional OSSE are similar in magnitude on average to those of the global ASCENDS inversion detailed in Section 3.3.3.1 when aggregated to the latter's coarser 4.5° x 6° model grid and to the biome and continent scales (Figure 3-16).

Based on the flux precision level suggested by Hungershoefer et al. (2010), ASCENDS observations would meet the threshold requirement (flux uncertainty of less than 0.1 Pg C yr^{-1} at the annual, biome scale) for all biomes within the range of measurement designs considered here (Figure 3-16). The observations constrain *a posteriori* flux uncertainties to a level of 0.01-0.06 Pg C yr^{-1}, and could thus help identify the location and magnitude of long-term carbon sinks. With regard to the more stringent target requirement (less than 0.02 Pg C yr^{-1}), a subset of the instrument designs would meet the target for a majority of biomes.

These results represent a best-case scenario, as measurement biases and other sources of systematic errors not considered here (e.g., transport model, boundary condition) degrade inverse flux estimates. However, abundant concentration measurements by ASCENDS can be expected to mitigate the impact of boundary condition uncertainties on regional flux estimates (Wang et al., 2014).

ASCENDS observations could reduce flux uncertainties substantially at biome and finer (e.g. approximately 100 km by 100 km) scales, meeting requirements for improved understanding of long-term carbon sinks.

3.3.2 Regional Fossil Fuel Emissions

In this experiment, we explore the ability of ASCENDS CO_2 measurements to distinguish between fossil fuel and natural biospheric fluxes. This analysis is performed with a regional geostatistical inverse modeling (GIM) framework over North America (NA) that examines fluxes at a 1° by 1° spatial and 3-hourly temporal resolution (Table 3-1). We examine the potential of ASCENDS measurements to detect and attribute variations in the spatio-temporal patterns of fossil fuel CO_2 ($FFCO_2$) emissions from sub-continental regions in NA during January. January is selected because it represents a time when the confounding effects of biospheric CO_2 flux are at a

minimum. Simulated CO_2 observations are created using biospheric fluxes from CASA-GFEDv2 (Randerson et al., 1997), $FFCO_2$ emission from the Vulcan Project (Gurney et al., 2009) over the continental U.S. and Open-source Data Inventory of Anthropogenic CO_2 emission (ODIAC) (Oda and Maksyutov, 2011) over Alaska, Canada and Mexico, and various levels of random error. Detection is evaluated by the ability to attribute variations in three-hourly ASCENDS CO_2 observations to patterns consistent with the simulated $FFCO_2$ emissions. A more detailed description of the $FFCO_2$ emissions pattern detection methodology can be found in Shiga et al. (2014).

Four cases representing different instrument configurations are explored using the two weighting functions (1.57 µm and 2.05 µm) and two random error levels (0.5 ppm and 1.0 ppm) as in the previous section. For the 1 ppm nominal error cases, both 1.57 µm and 2.05 µm instrument configurations could detect the $FFCO_2$ emissions from only one region, i.e., the Northeast US region (Figure 3-17a). For the 1.57 µm instrument case, reducing errors to the 0.5 ppm nominal error level did not improve detectability. However, for the 2.05 µm instrument case, when reducing errors to the 0.5 ppm nominal error level, detection of the $FFCO_2$ emissions patterns from the Midwest and Southeast US regions becomes possible (Figure 3-17b). This result shows that the impact of reducing errors for the 2.05 µm instrument are greater with regards to detecting $FFCO_2$ emissions than for the 1.57 µm instrument configuration. For all configurations, the ASCENDS CO_2 observations, in the absence of in-situ observations, will be able to detect the $FFCO_2$ emissions patterns of the largest emitting sub-continental regions over NA.

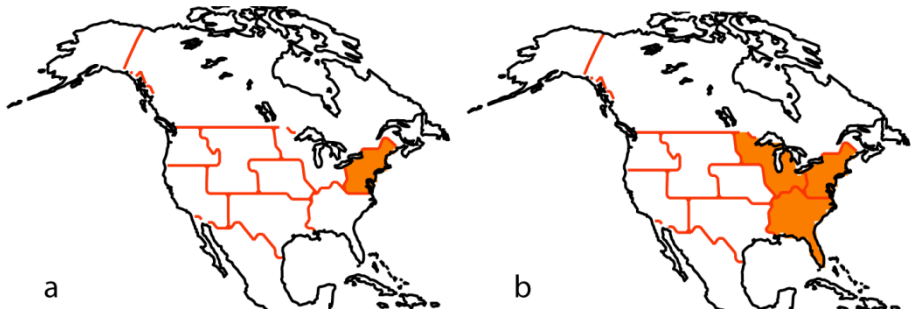

Figure 3-17 The regions where fossil fuel CO_2 emissions are detected for January (in orange) using ASCENDS 2.05µm weighting function with (a) 1 ppm nominal error and (b) 0.5 ppm nominal error. Detection results for the 1.57 µm weighting function for both error levels mirror panel (a).

ASCENDS will be able to discern the $FFCO_2$ emissions patterns from the largest emitting sub-continental regions over North America, particularly with the 2.05 µm weighting function.

3.3.3 Global Flux Estimation with ASCENDS

In this section we quantify the reduction in the uncertainty in the flux estimates globally that is possible by using CO_2 measurements from ASCENDS. The flux errors are constructed by selecting two reasonable models of global land biospheric fluxes and air-sea fluxes, each set having the seasonal variability of a representative year (Table 3-1, Box 3-2, Baker et al., 2010). Net fluxes from the Lund–Potsdam–Jena (LPJ) land biosphere model (Sitch, et al., 2003) plus

ocean fluxes from a run of the National Center for Atmospheric Research (NCAR) ocean model that captures the impact of rising anthropogenic CO_2 concentrations (Doney et al., 2006; Najjar et al., 2007) are assigned the role of the "true" fluxes. Net CASA land biospheric flux from Randerson et al. (1997) plus air-sea fluxes from Takahashi et al. (1999) are used as the prior flux estimate. The difference between the two can be thought of as a global net CO_2 flux error "signal" to be estimated in the assimilation, analogous to the sum of process-based signals like those used in Section 3.2. The difference is that this "signal" is perhaps more representative of the actual flux error we expect to encounter in the real world. Insofar as the inversion problem is made more difficult by having to distinguish between large fluxes in close proximity to each other, this simulation should provide a more general test of the ability of ASCENDS data to constrain fluxes. Other than not having errors due to uncertainties in the fossil fuel flux distribution (which are relatively small except over the strongest fossil emission areas), this case should provide flux estimation errors similar to what would be obtained using real ASCENDS data.

3.3.3.1 Impact of Random Observational Errors

To test the flux impact of different instrument design possibilities, weekly fluxes for a full year were estimated at 4.5º x 6º resolution (lat/long) for four ASCENDS cases: the 2.05 and 1.57 μm weighting functions with nominal random measurement errors at two levels, 0.5 and 1.0 ppm (Box 3-1). In this model setup, measurement uncertainties across the globe were estimated by multiplying the spatial patterns like those in Figure 3-1 by a given error value (e.g., 0.5 ppm) on a monthly basis (see Appendix C).

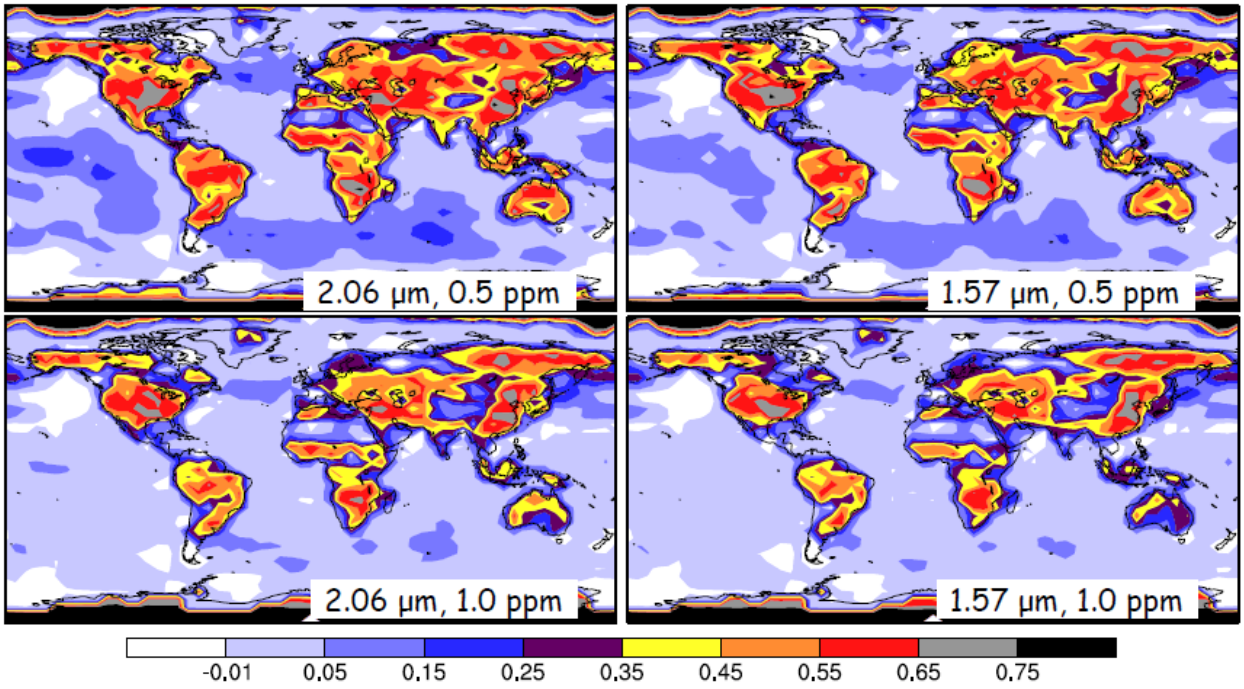

Figure 3-18 Fractional error reduction in weekly flux at 4.5ºx6º resolution (lat/long) for four cases: using the 2.05 μm and 1.57 μm vertical weighting and measurement uncertainties at 0.5 and 1.0 ppm.

Figure 3-18 shows the fractional error reduction with respect to the prior for the four cases. Substantial improvements in the flux estimates are obtained in all cases (Table 3-2). At 0.5 ppm

nominal measurement error, flux uncertainty reductions of 50% or better are obtained over most of the vegetated land areas. As expected, reducing the measurement error from 1.0 to 0.5 ppm, reduces flux error over both land and ocean areas. The improvements obtained for the 2.05 μm case, whose vertical sensitivity (Figure 5-2) peaks nearer the surface, are generally slightly larger than for the 1.57 μm case. This is true despite the fact that the measurement uncertainties for the 2.05 μm case are somewhat higher over land (Figure 3-1**)**: the stronger near-surface vertical sensitivity outweighs the impact of the higher errors.

The *a posteriori* flux uncertainties obtained here should be applicable to localized fluxes from any part of the globe, since they primarily reflect the constraint provided by the measurements rather than the prior flux uncertainties. To compare these results to those of the signal detection experiments in Section 3.2, we sample the grid-scale errors for the regions of interest. Fluxes north of 65ºN are retrieved here with a precision of 0.38 gC/m^2/day (1σ) during June-August, and to 0.26 gC/m^2/day across the full year, using ASCENDS data at the 0.5 ppm nominal measurement uncertainty. This corresponds to a weekly flux uncertainty of ~200 TgC/year. Uncertainty totals for the North American and Siberian areas are ~80 and ~180 TgC/year, respectively. These numbers give the precision of the estimate of net CO_2 flux coming from the permafrost region – that is, the combined impact of photosynthesis, respiration, fire, and any other permafrost-related emissions (e.g. methane oxidized to CO_2) – but cannot say how much is due strictly to permafrost-related emissions. The magnitude of the permafrost emission perturbation is 613 to 752 TgC/y for 2020 to 2022 (Hammerling et al., 2015), which should be readily attributable, consistent with the findings from Section 3.2 above.

Table 3-2 Flux Inversion Fractional Error Reduction*

Mission Sampling	ASCENDS 1.57 um		ASCENDS 2.05 um		In situ + TCCON	GOSAT ACOS	OCO-2 estimated
Mmt Error (ppmv)	0.5	1.0	0.5	1.0			
Land	0.49	0.41	0.51	0.44	0.22	0.30	0.59
Ocean	0.21	0.14	0.24	0.17	0.09	0.10	0.31

* Reduction is equal to (prior-posterior)/prior error where the prior error is the grid-scale RMS flux difference between two carbon models and the posterior error is the flux difference after assimilating each data stream separately. Values are the RMS of 52 weekly flux differences. Global prior errors are 2.84 and 0.33 (10^{-8} $kgCO_2$ m^{-2} s^{-1}) for land and ocean, respectively.

In the Southern Ocean (taken as south of 47ºS), weekly net CO_2 fluxes at the scale of the 4.5ºx6º grid boxes used here may be retrieved with a precision of ~0.05 gC/m^2/day using ASCENDS data at the 0.5 ppm measurement uncertainty. This is accurate enough to track strong local spatial and temporal variability. In terms of the precision of the flux integrated across the full extent of the Southern Ocean, the measurements can constrain fluxes with an uncertainty of ~300 TgC/year, a precision that is not sensitive to the time-scale of the solution (weekly to seasonal). The magnitude of the flux perturbation for this case in Section 3.2 is +/- 180 TgC/y (Hammerling et al., 2015), which is near the detection limit if taken to be at signal to noise of 1, again consistent with the prior assessments.

Substantial flux uncertainty reductions are obtained for all tested cases of ASCENDS measurement error and vertical weighting function. Simulations with the 2.05 µm weighting function are slightly better than for 1.57 µm at the same nominal errors levels.

3.3.3.2 Impact of Systematic Measurement Errors

In addition to the impact of random measurement errors on the uncertainty in the estimated fluxes, systematic errors in remote sensing CO_2 measurements can lead to serious flux errors even at relatively small magnitudes (Chevallier et al., 2014) because the systematic errors can be correlated with geophysical variations related to flux, e.g., land/ocean, solar zenith, surface reflectance, clouds, etc. For satellite CO_2 measurements, systematic measurement errors can be of a similar magnitude to random measurement errors, as is thought to be the case with GOSAT data (O'Dell et al., 2012, Kulawik et al., 2015). The impact of systematic errors on flux estimation is assessed in the same OSSE setup as used above, where systematic errors are added to the simulated measurements in parallel with the random errors. Although systematic errors are by their nature hard to foresee (if we knew them, we could calibrate them out), we have derived a set of potential bias cases for ASCENDS that can be scaled and used in flux OSSEs to help guide bias requirements for the instrument development based on their impact in flux estimation.

Table 3-3 ASCENDS Bias Cases

Case #	Bias Error Dependence	Rationale	Initial Error Scaling	Comments
1	Error varies with Sun angle on spacecraft	Instrument temperature changes can cause errors. Sun illumination is a heat source and heating usually depends on angle of the sun relative to the instrument.	Error (x) = 1 ppm * COS (solar zenith angle) for SZA < 95.	Instruments usually cool in shadow.
2	Error depends on received signal strength	Plausible to expect small degree of non-linear instrument response, or small offset	Error (x) = -1 ppm * ((1-r) / (1+50*r) + r^2) where r = 0.33 * signal strength (x) / nominal desert signal	Error scaling formula is for a small offset in readings.
3	Error varies with cloud backscatter (i.e., cloud optical depth)	Possible "leakage" of cloud scattered light into signal. Usually, cloud scatter has a shorter path length resulting in negative bias.	Error (x) = -1 ppm * (cloud OD(x)) for OD cutoff < 1	Mixed cloud and ground scattering (i.e., cloud OD is not too high)

The ASCENDS measurement teams formulated three possible bias cases based on sources of systematic error that could conceivably be present in actual lidar CO_2 measurements on-orbit (Table 3-3). The maximum magnitudes of the biases were arbitrarily set at 1 ppm. The biases in Table 3-3 were then added to the simulated true CO_2 concentrations in separate OSSEs, in addition to the 0.5 ppm nominal random errors added above. The magnitude of the shift in the

flux estimates caused by the measurement biases was then compared to the magnitude of the random flux errors computed before.

The impact of these biases on the fluxes at seasonal time scales is significant (Figure 3-19). They cause a bias in the flux estimates that is generally 25-50% of the magnitude of the a posteriori random errors over land, with a smaller impact over the oceans. Bias case #2 (the signal strength-dependent bias) caused the largest impact at these longer time scales. A fourth case (not shown), which tested snow under northern trees biasing the apparent surface height, had a much smaller impact on the fluxes.

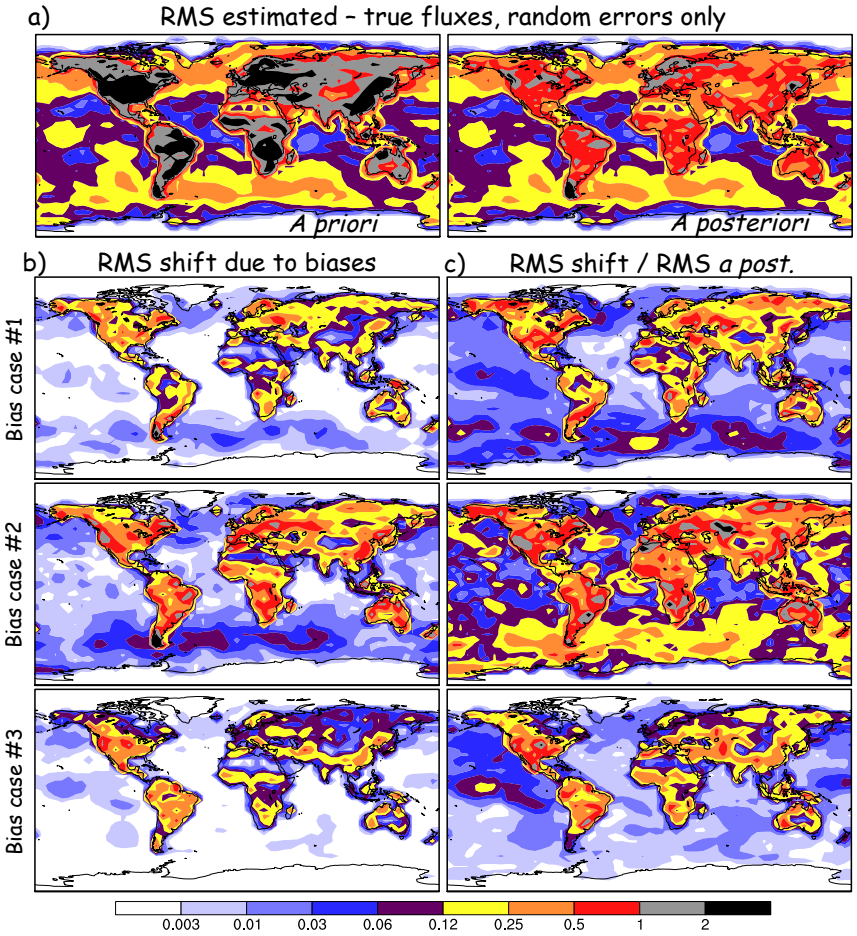

Figure 3-19 Seasonal RMS shift or bias cases compared to a priori and a posteriori errors b) The RMS of the shift or bias in the seasonal fluxes caused by the three ASCENDS bias cases from **Error! Reference source not found.**3 at the ±1 ppm level, compared to a) the a priori and a posteriori RMS seasonal flux errors [10-8 $kgCO_2/m^2/s$] caused by random errors only. c) The ratio of the RMS flux bias to the RMS a posteriori random errors is also given according to the same color scale (unitless). All results are for the 1.57 μm, 0.50 ppm random error case.

These experiments illustrate the importance of considering the impact of systematic errors when assessing the scientific return of a space mission like ASCENDS. Systematic errors are thought to be significant for CO_2 measurements of current satellites (e.g. GOSAT, AIRS) and will likely play a significant role for future satellites such as OCO-2 and ASCENDS. They are considered further below in assessing the value of ASCENDS in comparison with other measurements.

3.4 ASCENDS in the Context of Other CO_2 Observing Systems

In this section we compare the impact on flux estimates of using simulated ASCENDS data to that of using current in situ plus TCCON data, GOSAT, and projected OCO-2 data. The global flux estimation OSSEs are well-suited to answer these questions because they can be constructed to estimate the flux uncertainty reduction provided by any hypothetical set of measurements. Two sets of experiments were run, one using only random measurement errors, the other including systematic errors as well. Passive sensors such as OCO-2 and GOSAT are expected to be more susceptible to bias errors than ASCENDS due to the greater difficulty in determining the atmospheric path length and influence of scattering, as has been seen with GOSAT (O'Dell et al., 2012). The measurement capabilities of GOSAT are based on its current performance, while those for OCO-2 are based on its expected performance using prelaunch calibration data and the experience of GOSAT as a guide.

3.4.1 Comparison in Terms of Random Errors

Together with the ASCENDS OSSE results discussed above (Section 3.3.3.1), Table 3-2 includes aggregate flux uncertainty reductions for a case using CO_2 from the current NOAA *in situ* network (flasks, observatories, tall towers, and routine light aircraft profiles) plus the TCCON network, as well as that using the GOSAT satellite in 3-point cross-scan mode. For weekly fluxes at the scale of (~500km^2), the existing ground network provides only a weak constraint, except over certain well-instrumented areas like Temperate North America. The GOSAT satellite improves upon this, but due to its relatively large FOV (~100 km^2) and consequent sensitivity to clouds, the additional constraint is not great. We have assumed measurement uncertainties of 1.7, 1.5, and 1.0 ppm (1σ) for GOSAT high-gain land, medium-gain land, and ocean glint data, respectively, based on its currently estimated capabilities (ACOS b3.4 retrieval, ACOS Level 2). GOSAT data add the most value in areas that are poorly constrained by the ground-based measurements. Aggregating results into TRANSCOM regions (not shown) produces rank-order results consistent with those given for global land and ocean. ASCENDS data for any of the tested instrument configurations provide a major improvement in flux uncertainty reduction compared to current observations.

Flux estimates have also been made using projections for random errors from OCO-2. OCO-2 nominal uncertainties in the 0.5-1.0 ppm range are obtained by multiplying the uncertainties of Bösch et al. (2011), by a factor of two to account for errors not captured by their analysis. The Bösch et al. measurement uncertainties and averaging kernels are computed as a function of solar zenith angle, aerosol optical depth, and surface type. According to these simulations, OCO-2 provides a much stronger constraint than either GOSAT or the ground-based measurements (Table 3.2). This is a result of OCO-2's much greater sampling density. The smaller OCO-2 field of view (~3 km^2), should allow more frequent cloud-free shots, improving data yield fraction by as much as a factor of two compared to GOSAT (Miller et al., 2007). OCO-2 also has greater measurement frequency: with roughly 24x60 possible measurements per minute, compared to ~30 for GOSAT, the OCO-2 satellite should provide substantially more CO_2 information than GOSAT, even if the two satellite instruments were to have similar precision levels.

Considering only random errors, ASCENDS measurements with a nominal precision equivalent to 0.5 ppm provide a somewhat weaker constraint on the fluxes globally at weekly time scales than expected from OCO-2 (Table 3-2). By these global metrics, the denser OCO-2 sampling more than compensates for the extra coverage provided by ASCENDS on the night side of the

orbit and at high latitudes. ASCENDS would have to push nominal random errors as low as 0.25 ppm (not shown) to equal or improve upon OCO-2 in these random error OSSE results. Random errors of 0.25 ppm, however, are outside the current ASCENDS design envelope.

ASCENDS data will provide a major improvement in flux uncertainty compared to current observations including in situ, TCCON, and GOSAT. Globally, flux estimates from ASCENDS will be similar to or slightly worse than those projected for OCO-2 if only random errors are considered.

3.4.2 Comparison Considering Systematic Errors

Systematic errors can greatly degrade the flux constraints as calculated above and, based on GOSAT experience, are suspected to have a larger impact on the flux estimates from satellite data than random errors at this point in time (Chevallier et al., 2014). GOSAT measurements currently suffer from significant and poorly-characterized systematic errors, up to about 0.7 ppm even after the standard bias correction is applied (Kulawik *et al.*, 2015). OCO-2 will be subject to similar possible systematic errors (though perhaps of a lower magnitude due to its improved ability to avoid clouds.) ASCENDS can be expected to provide measurements with significantly lower biases than the passive missions as a result of the laser measurement approach (Section 1.4). Flux OSSEs are used here to demonstrate the impact of systematic errors, based on plausible systematic error patterns added to the random measurement errors.

Box 3-3 Simulation of Systematic Errors

One approach to estimating the systematic errors that will affect the OCO-2 measurements is to pattern them after the biases currently affecting the GOSAT measurements (the best source of near-infrared (IR) CO_2 measurements currently available). The raw column CO_2 mixing ratios retrieved by the Atmospheric CO_2 Observations from Space (ACOS) team for GOSAT have been compared to column CO_2 measurements from the TCCON network, as well as to CO_2 from a suite of atmospheric models; the differences were then correlated with a variety of parameters used in the CO_2 retrieval (O'Dell et al., 2012). Assuming the differences are due to instrument retrieval problems, an XCO_2 bias correction is derived by regressing the differences on a subset of these parameters. Since it is not always clear that the parameters used in the regression are uncorrelated with the desired XCO_2 values in the real atmosphere, it is unclear how aggressive a bias correction to make. Using more parameters in the bias fit increases the likelihood that actual flux information (or signal) will be removed instead of measurement bias. For the results presented in Section 3.4.2 the biases are constructed by regressing the difference between actual raw GOSAT XCO_2 values (ACOS B2.10 retrievals) and the XCO_2 values from a forward run of the PCTM atmospheric transport model on (1) aerosol optical depth derived from CALIPSO, (2) the ratio of the signal in the weak CO_2 band to that in the O_2 band (referred to as S31, which is related to the albedo in the two bands as well as the signal strength in each), and (3) the solar zenith angle. The parameters used in this bias correction curve fit are different than those used in the official ACOS XCO_2 bias correction (based on O'Dell et al., 2012), in order to provide global values outside the current GOSAT ground track. The patterns produced with this correction are similar to those in Deng et al. (2014), though the magnitudes in Figure 3-20 are about 25% larger, which makes them a fair prediction of the biases expected from OCO-2 retrieved XCO_2. The biases varied by month; their annual average is shown in Figure 3-20.

Realistic bias patterns that might affect OCO-2 are obtained from estimates of such biases currently being calculated for GOSAT by the ACOS project (Box 3-3). These biases were then added on top of the OCO-2 random measurement errors assumed in Section 3.4.1. For ASCENDS, we added scaled multiples of the hypothetical bias distributions given by Table 3-**Error! Reference source not found.**3.

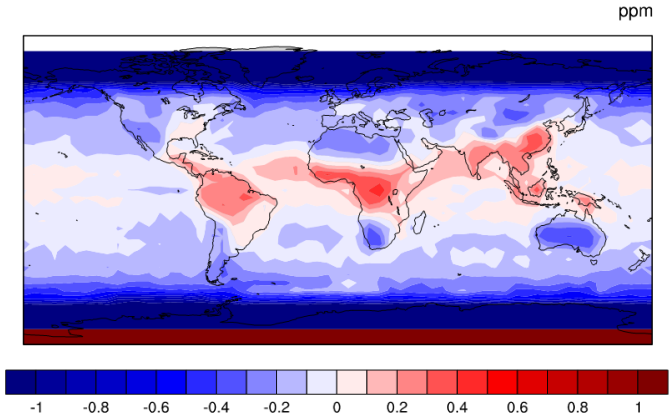

Figure 3-20 The annual-mean measurement bias [ppm] derived from a comparison of raw ACOS B2.10 GOSAT XCO_2 values to modeled values, used to approximate OCO-2 bias.

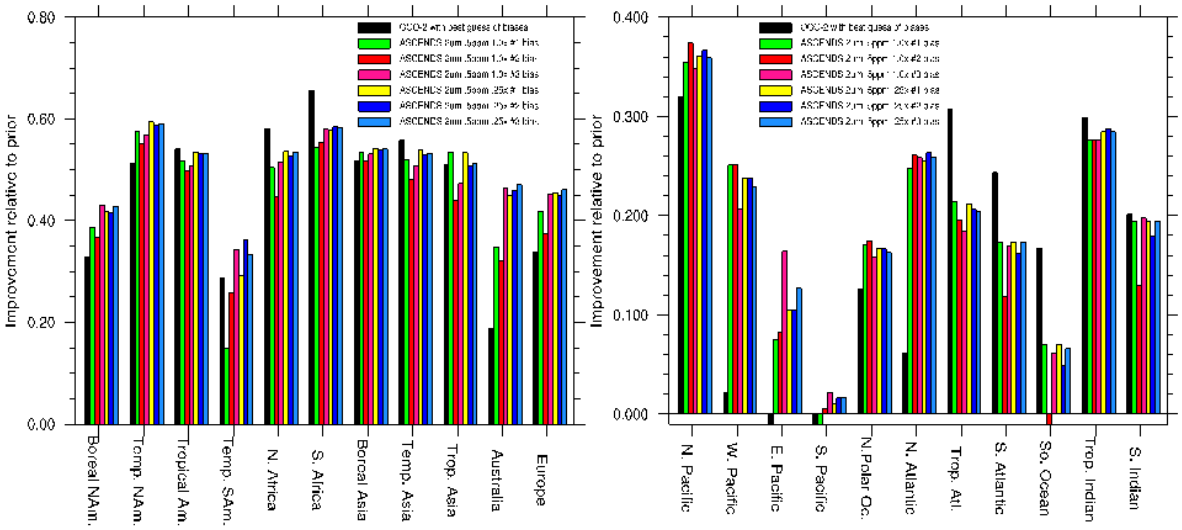

Figure 3-21 Uncertainty reductions for weekly 4.5x6° fluxes aggregated to TRANSCOM regions produced by assimilating CO_2 measurements from OCO-2 and ASCENDS, accounting for both random and systematic measurement errors of different forms and magnitudes. The biases from Figure 3-20 were applied to the OCO-2 sampling, while the biases from Table 3-3 were applied to the ASCENDS cases at two levels of scaling (1 and 0.25). Random errors were as in Table 3-2 for OCO-2 and the ASCENDS 2.05 μm, 0.5 ppmv nominal error case. Note different y-axis scales.

Figure 3-21 shows the flux uncertainty reductions that result when biased measurements are used to infer fluxes. When the biases are added into the glint-mode OCO-2 OSSE, most of the improvement in the fluxes over the oceans seen in the random error OSSEs (c.f., Table 3-2) disappears: the relatively low-magnitude ocean fluxes are the first to be thrown off by the systematic errors. The improvements over land are also degraded to a lesser extent. When these degraded OCO-2 estimates are compared to the ASCENDS results, it is seen that ASCENDS can

equal or exceed OCO-2's performance for almost all regions, if the tested systematic errors can be kept under about 1 ppmv. This is true especially over some ocean regions, even though OCO-2 has lower random flux errors there when looking in sun glint mode. For many regions, ASCENDS does not even need to reduce its systematic errors below OCO-2's to achieve better results, e.g., Boreal NA. The benefit of not experiencing SZA-dependent biases is significant. The 1.57 μm case flux improvement is similar although less pronounced, especially over ocean (not shown).

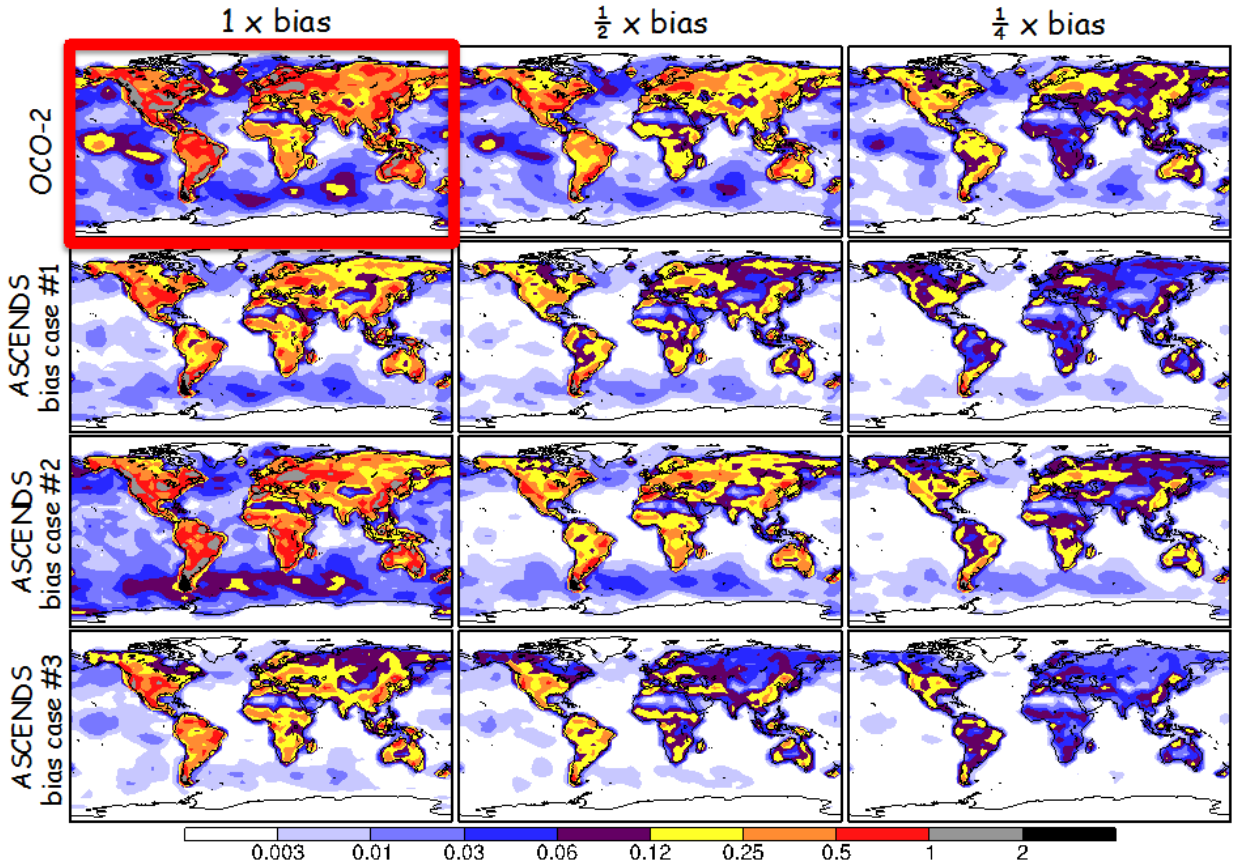

Figure 3-22 The shift in the weekly flux estimates caused by the addition of measurement biases of three different magnitudes (1x, 0.5x, & 0.25x) for OCO-2 and for the three different forms of ASCENDS bias given in Table 3-3. The RMS of 52 weekly flux shifts [10^{-8} $kgCO_2/m^2/s$] is shown for each case. The case in the red box is thought to be the most realistic guess of OCO-2 biases: ASCENDS can improve upon this by limiting biases to the ±0.5 ppm level.

The impact of the measurement biases can be seen more directly by comparing the magnitude of the shift in fluxes globally caused by the bias, as is done in Figure 3-22. Relatively speaking, ASCENDS would need to keep its systematic errors to about half of those shown in Table 3-3 (i.e. to the ±0.50 ppm level or better) to achieve a flux estimate with significantly lower error than that projected for OCO-2 (highlighted in Figure 3-22 with the red box). This is thought to be a realistic design goal for ASCENDS. Since biases in the CO_2 retrievals of passive missions such as GOSAT are currently thought to be the limiting factor in the usability of their data, not the random errors, reducing these biases is of primary interest for future CO_2 missions such as ASCENDS.

Reducing systematic errors in ASCENDS CO_2 measurements compared to prior CO_2 missions will lead to significantly smaller errors in inferred fluxes.

3.5 Summary

A series of modeling tests is used to explore the impact of prospective ASCENDS observations in inferring surface sources and sinks of CO_2. A fairly realistic representation of expected random and systematic measurement errors for ASCENDS has been constructed to test the impact of instrument implementation alternatives on the models' ability to infer fluxes and, thus, to begin to establish measurement performance requirements for the mission. A variety of modeling approaches has been employed to bolster the findings from any individual model, given that flux retrieval performance typically depends on model-specific methods and assumptions. The results show: 1) ASCENDS will resolve statistically significant differences in total column CO_2 concentrations, resulting from foreseeable changes in surface flux, over the entire globe including high latitudes throughout the year; 2) it will advance our understanding of the carbon cycle through improved flux estimates with reduced uncertainty at global to regional scales; and 3) ASCENDS data have potential for reduced bias and improved representation that can contribute significantly improved constraints on surface fluxes beyond passive sensors such as GOSAT and OCO-2. In summary, the modeling tests consistently demonstrate that, under reasonable assumptions for instrument technical performance, ASCENDS will provide accurate, precise, and representative data to address key carbon cycle science problems and hypotheses, i.e., ASCENDS can provide new science, better science, and continuity of global CO_2 observations from space.

The mission formulation for ASCENDS is currently a work in progress and several modeling exercises are planned to further explore its potential. For example, we expect to further study the impact of including O_2 measurement errors in calculating CO_2 dry air mixing ratio versus using surface pressure from weather analyses. We also plan to explore the impact on flux estimates of using ASCENDS data retrieved above clouds or vertical multi-layer CO_2 retrievals. Simulations using alternate orbital parameters, e.g., dawn/dusk or precessing, will be tested to see if additional information on vegetation respiration and photosynthesis fluxes can be extracted. Finally, as the performance of OCO-2 is now starting to come to light, we plan to further refine our random and bias error comparisons using real OCO-2 data and to test the impact of combining active and passive measurements in obtaining robust estimates of the carbon budget at a variety of spatiotemporal scales.

4. Impact of Uncertainties in Atmospheric State on ASCENDS Measurements

4.1 Introduction

This section addresses two critical elements that span mission requirements and general instrument design space. They are: 1) The assessment of uncertainties in ancillary knowledge of the atmospheric state and 2) The general impact of these uncertainties on measurement error. Special attention is given to the assessment of uncertainty in surface pressure estimates from meteorological reanalyzes to determine the necessity of an O_2 lidar measurement and, potentially, target requirements. ASCENDS provides Column XCO_2 amounts derived from active differential absorption measurements along CO_2 spectral features, in conjunction with collocated estimates of the atmospheric state provided by meteorological analyses. Understanding the propagation of errors in the atmospheric state into XCO_2 measurement errors is necessary to define a rigorous error budget and ensure a high quality measurement.

Measurement error terms are not only driven by the instrument design, but also the ancillary meteorological data employed in the retrieval process, and the interplay between the two. The observed CO_2 differential optical depth, $\Delta\tau$, associated with a given CO_2 spectral feature, is given by

$$\Delta\tau = \int_0^{P_{sfc}} \Delta\sigma(\lambda_{on}, \lambda_{off}, T, p) \cdot \eta(T, WV, p) dp \quad (4\text{-}1)$$

where $\Delta\sigma$ is the CO_2 differential absorption cross section, η is the dry air CO_2 number density, p_{sfc} is the surface pressure, and $\lambda_{on}/\lambda_{off}$ represent the on/off-line wavelengths. XCO_2 is given by

$$XCO_2 = \frac{\Delta\tau}{\int_0^{P_{sfc}} \Delta\sigma(\lambda_{on}, \lambda_{off}, T, p) dp} \quad (4\text{-}2)$$

Both $\Delta\sigma$ and η vary as a function of pressure (P) and temperature (T). In addition, absorption due to other trace gas features (including water vapor), which are not considered in this simplified formulation, may also impact the observed $\Delta\tau$. As illustrated by these equations, the accuracy of retrieved XCO_2 values depends not only on the error characteristics of the observed $\Delta\tau$, but also the ability to accurately characterize the P, T, and water vapor (WV) concentration along the observed path. In the case of global space-based monitoring systems, retrievals typically rely on values derived from meteorological analyses that combine atmospheric general circulation models (GCMs) with assimilation of both conventional and satellite observations to estimate the atmospheric state globally.

The work summary below provides a baseline assessment of these uncertainties in atmospheric state variables (vertical temperature and moisture, plus surface pressure), and their impact on a generic instrument implementation for a selected set of spectral lines/features. While it does not address the end-to-end performance of a fixed-point baseline ASCENDS solution, it does provide a common parametric baseline that will evolve over time as the design matures. The assessment will aid in instrument and mission definition, design and potential future source selection activities, as well as provide a systematic mechanism for comparing proposed solutions and a foundation for assessing end-to-end mission performance throughout the ASCENDS mission life-

cycle. In addition, these analyses will help guide the mission requirements for potential additional space-based measurements, e.g. the necessity for an O_2 based surface pressure measurement, and provide a single common set of vetted sources of ancillary data that may be incorporated into the procurement phase to aid in source selection. Section 0 provides a summary of the uncertainty analysis of expected atmospheric state and Section 4.3 summarizes a baseline analysis of potential impact due to these uncertainties on retrieved XCO_2 column amounts.

4.2 Uncertainties in Observed Atmospheric State

Current pre-phase A investigations focus on gathering current state-of-the-art model analysis and forecast fields as a proxy for future ancillary mission data to develop a comprehensive set of statistically-based estimates that bound the expected uncertainties in surface pressure and vertical temperature and moisture profiles. A variety of methods are employed to develop these bounds, including:

1. Comparison of in situ observations and meteorological analysis data to assess model errors.
2. Comparison of reanalysis products with independent (not assimilated) datasets, where available.
3. Inter-comparison of multiple reanalysis products to inform error estimates in poorly observed regions

Comparing analysis fields to prior short-term forecasts for the same period constrains the error introduced into an operational retrieval relying on forecast fields and the temporal interpolation error that may occur when meteorological information from a different time is assumed during the retrieval process. Differences that arise in comparisons of fields from different modeling systems are due in part to errors in the Numerical Weather Prediction (NWP) model physics, spatial scales, and other implementation differences; such analysis is also valuable in estimating model error in data poor regions. Comparisons of NWP fields to observations is challenging because the majority of high quality, operationally available in situ data are assimilated to produce meteorological analyses. Truly independent observations are limited in number and distribution, and indeed often are near operational sites. Standard in situ observations also have limited precision due to instrument limitations or through data collection procedures (Sun et al., 2010) (U.S. DOC/NOAA Office of the Federal Coordinator for Meteorology (OFCM), Washington, D.C., 2005; NOAA, Washington, D.C., 2003; Developmental Testbed Center (DTC), n.d.) (Salstein et al., 2008). Despite these limitations, the collective statistics provide a semi-unbiased assessment of expected uncertainties in atmospheric state knowledge, and a consistent set of benchmarks that can be used to assess potential mission design solutions.

4.2.1 Uncertainties in Surface Pressure

ASCENDS requires both a precise knowledge of the surface pressure on a fine scale grid and a comprehensive understanding of the associated errors. While state-of-the-art mesoscale NWP models currently have horizontal grid spacings of at least several kilometers, with global-scale models an order of magnitude larger, surface pressure must be characterized on a spatial scale comparable to the measurement of interest. Space-based estimates of surface pressure normally require a separate sensor, thereby increasing the overall size, weight, power and complexity of the satellite payload. The use of meteorological analyses presents an alternative approach for estimating surface pressure, but implementation depends on the quality of the analyses and the ability to adjust relatively coarse resolution grid-based information to precise measurement

locations. A comprehensive understanding of the errors associated with each of these approaches is a critical part of the design characterization of a remote-sensing system whose measurement accuracy depends on knowledge of surface pressure. Current capabilities of O_2 measurement techniques are addressed in Sections 5.2 and 5.3.3.5 while errors in surface pressure derived from meteorological analyses are addressed here.

4.2.1.1 Comparison of Surface Pressure Model Values and Observations

In this study we compared global in situ measurements with estimates of surface pressure derived from the Global Forecast System (GFS) and the North American Mesoscale Model (NAM) NWP analyses and short-term forecast data. Surface observations were obtained from National Climatic Data Center (NCDC's) Integrated Surface Database (ISD) (NCDC, n.d.). In order to compare measured surface pressure to model fields, a correction must be applied to the surface pressure of the model to account for the altitude difference between the model surface height and the actual terrain height of the station. In this work, the standard lapse rate equation

$$P_{adj} = P_s \cdot exp\left(\frac{-g \cdot dz}{R\left(T_m + L_r \cdot {dZ}/{2}\right)}\right) \quad (4\text{-}3)$$

where P_s is the model surface pressure, dZ is the difference between the model terrain height of the two resolutions, R is the dry gas constant**,** T_m is the model two-meter air temperature, and L_r is the lapse rate of 0.0065 K/m, was employed to account for these height differences. This adjustment was also applied, where required based on database values, to convert surface observations of sea-level pressure to station pressure. ISD surface pressure observations were converted from sea-level pressure to station pressure and co-located with model estimates that had been corrected for model height error. The results shown in this work are based on data retained every fifth day from the thirteen-month period between January 2012 and August 2013 (inclusive). Observations in the matched pair database are comprised of observations valid at 0000 and 1200 Coordinated Universal Time (UTC). Model data are either analyses valid at 0000 and 1200 UTC or 6-h forecasts from the prior 1800 and 0600 UTC model cycles. The choice of a 6-hour forecast was selected to match the time interval between typical synoptic model runs. In a real-time environment, surface pressure estimates would be computed from both spatially and temporally interpolated NWP data to match the satellite measurement. This approach requires not only the most recent NWP analysis, but also a forecast or set of forecasts that span the observation times. In non-real-time environments, where data are not required to be processed as they are received, one could consider temporally interpolating between analyses or data from alternative applications that provide non-forecast fields on a more frequent basis.

Figure 4-1 illustrates the overall small bias and Root Mean Square Error (RMSE) values at most observing sites. Errors are typically larger in regions with complex topography or at high elevations as evident over the Alps. Model values in these regions are heavily influenced by the veracity of the underlying model initial conditions whose effects are most strongly felt at such short forecast lengths. It is also in these regions that the failures in the corrections using the standard atmospheric lapse rate are most apparent. Figure 4-2 illustrates that even at a 90% confidence level, the majority of stations sampled have 1σ values below 2 mb. The cumulative distribution functions (CDFs) in this figure illustrate the distribution of RMSE values for selected sets of surface station observations. The minimum annual RMSE for all station approaches 0.25mb and the maximum exceeds 3mb for a handful of outlier stations as illustrated in Figure 4-

1. Errors for the 6-h forecasts are slightly larger (not shown). Table 4-1 shows biases binned by latitude band for the GFS global analysis typically are small and negative, while RMSE values for (approximately) 1, 2 and 3 standard deviations for a normally-distributed sample are to first order 1, 2 and 3 mb.

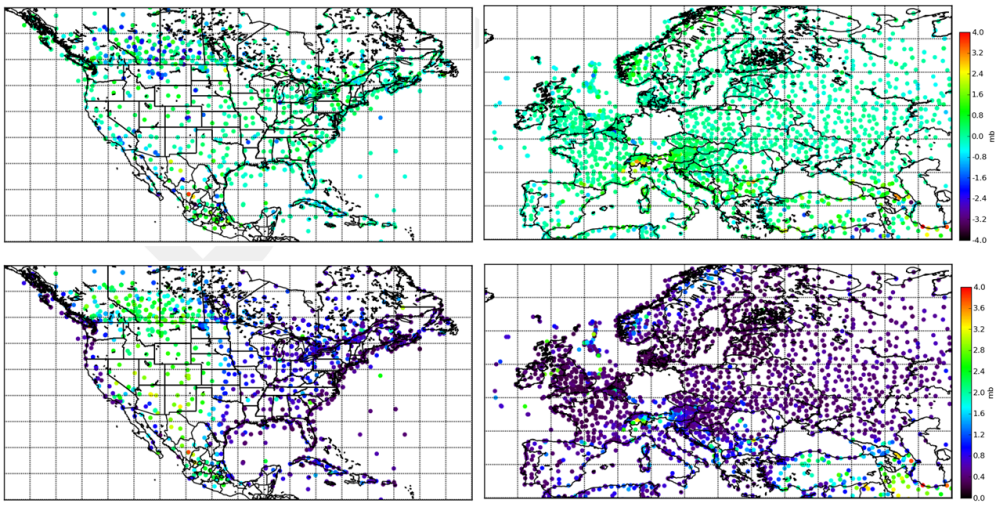

Figure 4-1 Estimated surface pressure biases and RMS errors for the U.S. and Europe. Estimated surface pressure biases (top row) and root-mean-square errors (bottom row) for the U.S. (left column) and Europe (right column). Units are in mb. Model data are the NAM regional model and GFS global model for the U.S. and Europe, respectively.

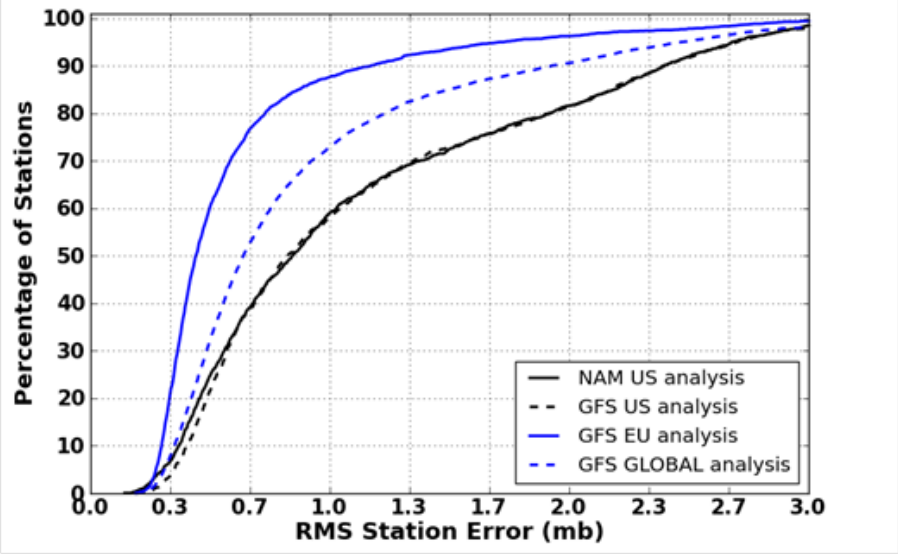

Figure 4-2 RMS differences in surface pressure observations vs fraction of stations with annual RMSE less than defined error. Cumulative distribution functions for the number of stations whose RMSE surface pressure errors, the RMS difference between NAM/GFS analysis values and surface observations for the U.S. (US), Europe (EU), and global regions. The percent of observation denotes the fraction of stations who yearly average RMSE is less than or equal to the defined error in mb.

Table 4-1 Regional differences mean bias and RMSE, and inter-modal range RMSE thresholds (in mb) for GFS analysis.

Region	Mean Bias	Mean RMSE	65%	90%	95%	99%
NH High Latitudes	-0.14	0.74	0.67	1.19	1.67	2.57
NH Mid Latitudes	-0.01	0.88	0.70	2.02	2.47	3.24
Tropics	-0.13	1.02	0.91	1.86	2.52	3.78
SH Mid Latitudes	0.02	0.86	0.80	1.35	1.84	2.83
SH High Latitudes	-0.41	1.25	1.27	1.93	2.12	2.65
All Latitudes	-0.06	0.90	0.75	1.86	2.40	3.31

4.2.1.2 Inter-model Comparison of Surface Pressure Differences

While comparisons with available observations provide the best assessment of errors in meteorological analyses, large areas of the globe remain unobserved including high latitude regions of both hemispheres, southern hemisphere oceans, South America, Africa, and Siberia. In these regions, comparisons of different meteorological analyses provide the only possible estimate of uncertainty. To characterize uncertainty in these regions, we compared surface pressure fields from the Modern Era Retrospective-analysis for Research and Applications (MERRA) (Rienecker et al., 2011), the European Centre for Medium-Range Weather Forecasts' (ECMWF) ERA-Interim reanalysis (Dee et al., 2011), and NOAA's Climate Forecast System Reanalysis (CFSR) (Saha et al., 2010). The range of reanalysis surface pressure estimates was computed every 6 hours during January, April, July, and October 2009. All reanalysis fields were re-gridded to MERRA's nominal half-degree resolution. The lapse rate altitude correction discussed above is applied to reduce effects of underlying topography differences. While this correction reduces intermodal differences due to topography, it does not entirely remove them. Annual mean surface pressure differences are subtracted as a type of bias correction because we assume that persistent errors in surface pressure from analyses will be successfully diagnosed and adjusted for as part of the ASCENDS retrieval process. Monthly means and standard deviations of the instantaneous range were computed. Standard deviations of the surface pressure range are shown in Figure 4-3.

In most regions, intermodal differences are less than 1 hPa, consistent with the analysis based on surface pressure observations. Largest differences among analyses exist in data poor regions where Atmospheric General Circulation Model (AGCM) model physics dominate pressure estimates rather than data constraints, which are fairly consistent among models. In particular, large errors are evident in the southern ocean translating to 0.5-0.8 ppm in XCO_2. Not only is this area virtually unobserved by conventional observations (radiosonde, aircraft, and automated land and ocean stations), but assimilation of satellite observations of other meteorological state

variables, which provide some constraint on surface pressure, is obstructed by persistent cloudiness.

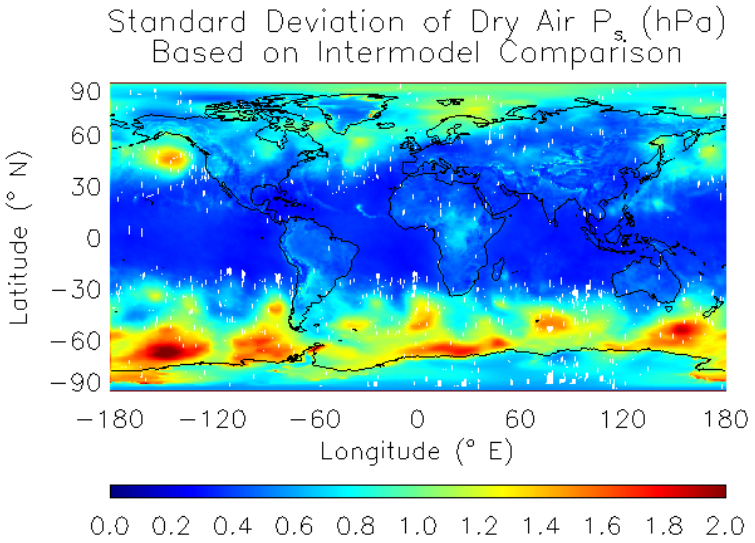

Figure 4-3 Model comparison between reanalysis surface pressure estimates for dry air. Comparison provides insight into model error in data poor regions. Instantaneous ranges were computed between three reanalysis datasets for 2009 to determine the standard deviation.

4.2.1.3 Spatial Interpolation Errors in Surface Pressure

In addition to errors in the surface pressure provided by meteorological re-analyses, further error can be introduced when surface pressure is adjusted to the measurement location as part of an XCO_2 calculation. To estimate the magnitude of such errors, we use a combination of MERRA surface pressure estimates and the United States Geological Survey (USGS) GTOPO30 digital elevation model map that provides estimates of surface elevation at 1km resolution. We use the lapse rate based correction discussed above to adjust from MERRA's ~50 km grid-based surface pressure estimates to calculate the 'true' surface pressure at all GTOPO30 elevations. To estimate potential errors, we perform the same calculation assuming a 1 K temperature error and then calculate the difference in surface pressure from the 'truth.' Figure 4-4 shows the standard deviation of surface pressure errors within each 50 km grid cell. Over most of the world, the topographic correction assuming a realistic error in temperature introduces a small error less than 0.1 hPa. Over regions with large topography gradients, errors are still ~0.2 hPa. Even in areas with significant topographic variation, adjustment errors are much smaller by an order of magnitude than the errors shown in section 0 and 0. This analysis assumes that ASCENDS will have perfect information about the elevation associated with a particular measurement based on the altimeter. Errors in altimetry, pointing location, or low level temperature errors greater than 1 K could all lead to errors larger than those shown in Figure 4-4, but are still likely to be smaller inherent uncertainty in surface pressure reanalysis.

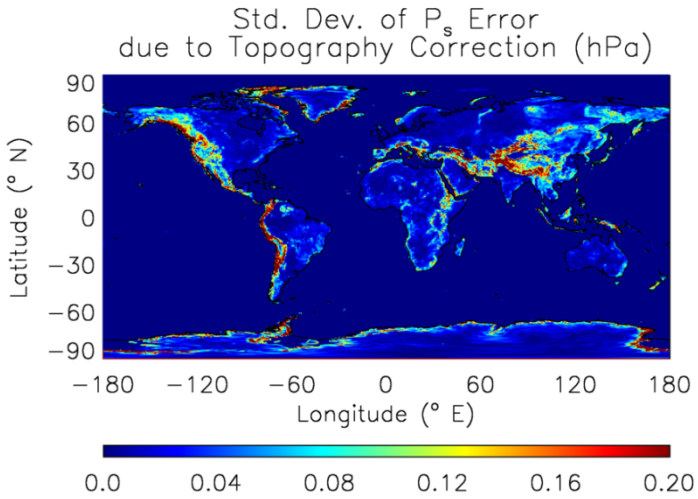

Figure 4-4 Effects of grid scale on surface pressure errors. Errors induced when relatively coarse resolution reanalysis surface pressure fields are adjusted to represent subgrid-scale topographic variations.

The data described in this section and section 4.2.1 provide confidence that the values derived in section 4.1 and presented in Table 4-1 are with in reason. The long-term goal is to employ these spatially resolved global distributions of surface pressure errors due to both model limitation and/or terrain height differences as a mechanism for constructing globally representative spatially varying maps of expected errors in retrieved XCO2 that can enhance the inverse model results described in chapter 3.

4.2.2 Uncertainties in Temperature and Water Vapor Profiles

The error characteristics of above ground-level model profiles of temperature and moisture were examined by comparing against radiosondes (Figure 4-5). The largest temperature errors appear in the lowest 50 mb of the troposphere and again at high altitudes near the tropopause and in the stratosphere. Moisture errors are largest near the surface in the boundary layer where water vapor content is most abundant.

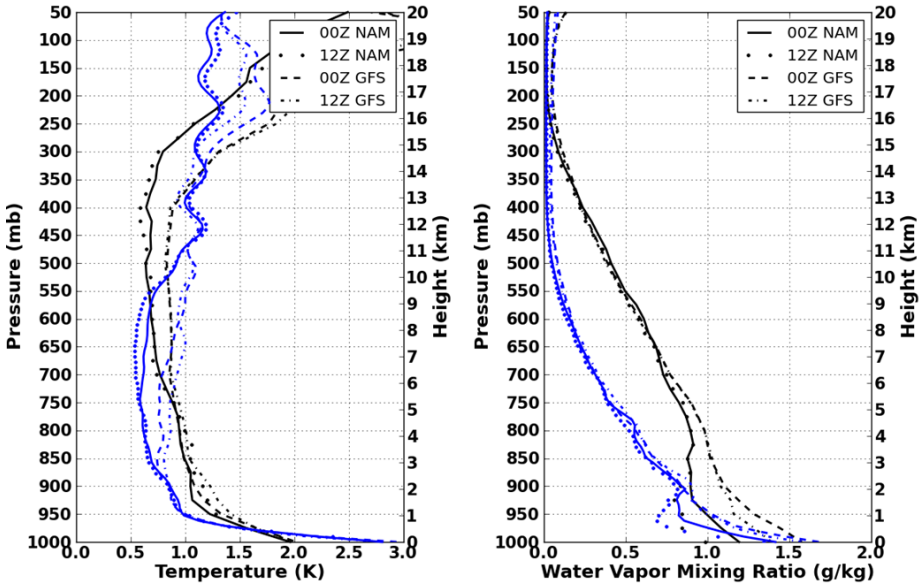

Figure 4-5 Ensemble RMS differences for radiosonde soundings in upper air observations for 5000 randomly selected soundings and corresponding 0000 and 1200 UTC NAM and GFS NWP analyses for temperature (left) and water vapor mixing ratio (right). The black traces are plotted as a function of pressure and blue traces are plotted as a function of height above surface.

4.3 Impact of Uncertainty in Knowledge of Atmospheric State on Retrieved XCO_2

The atmospheric state vector analysis described above was combined with a notional vertical CO_2 profile with a constant concentration of 385 ppm, and input into the Line-By-Line Radiative Transfer Model (LBLRTM) (Clough et al., 2005) to construct sets of simulated optical depths (ODs) over a predefined range of wave numbers. LBLRTM optical depths are computed from Voigt line shape functions at atmospheric levels and with a continuum model that includes self- and foreign-broadened water vapor as well as continua for carbon dioxide, oxygen, nitrogen, ozone and extinction due to Rayleigh scattering. The version used in the study included 2012 updates to the CO_2 line parameters and coupling coefficients based on the work of Devi et al. (2007a,b), the O_2 line parameters based on HITRAN (Rothman et al., 2009) and additional quadrupole parameters between 7571 - 8171 cm^{-1}.

For each of 5000 profile pairs discussed in section 4.2.2 a set of simulated truth, signal and model ODs were computed. The Radiosonde Observation (RAOB) data were used to simulate the "true" optical depths observed by the sensor and the model profiles were used construct the "model" optical depths that would be used in the retrieval approach given an estimate of the atmospheric state. In addition, a set of "signal" τs were constructed based on the "truth" profiles and either an augmented CO_2 profile or a change in surface pressure. In the CO_2 case, the nominal CO_2 profile was augmented by adding a pre-defined concentration to each layer between the surface and simulated observation height. In the O_2 case, the surface pressure was adjusted by modifying the surface height to match the desired surface pressure. In this case, the signal pressure values were assumed to be less than the observed or model values to prevent the use of sub-surface profile values. In the O_2 cases, the observed path length, i.e. the height between the observer and the surface, were held fixed to eliminate changes in optical depths due to path length.

These simulated optical depth values (truth, model, and signal) were then employed to generate spectrally dependent noise and average signal values given a defined set of differential

wavelength pairs. This work assumes that retrieved CO_2 column or surface pressure values are derived from the difference in optical depths between the absorption at an "off-line" wavelength whose absorption is dominated by the continuum or constituents other than the feature of interest, and the absorption at an "on-line" wavelength whose absorption is primarily driven by the feature of interest. While this approach does not address all retrieval methods or observational techniques that employ multiple measurements along a given absorption feature, it does provide metric values that can in general be used to constrain the fit between the observed data and Radiative Transfer (RT) modeled values. This Monte Carlo based approach provides a mechanism for computing an ensemble-based estimate of the biases and variances associated with retrieved XCO2 values for a variety of simple line combinations. The inclusion of a high-fidelity RT model enables these results to capture the errors due to both correlated and uncorrelated uncertainties in temperature, water vapor and pressure on the dry-air mixing ratio of CO2, an input the RT model.

The noise at each spectral location in the given simulated waveband was computed as the RMS error associated with the differences between the simulated true (τ_{signal}) and noise (τ_{noise}) values. In general, these differences in optical depths, for a given off-line wavelength (λ_{off}), are described as

$$\Delta\tau(\lambda) = \left(\tau_b\left(\lambda_{off}\right) - \tau_b(\lambda)\right) - \left(\tau_x\left(\lambda_{off}\right) - \tau_x(\lambda)\right) \tag{4-4}$$

where $\tau_b(\lambda)$ is the observed or true optical depths derived from RAOB data, and $\tau_x(\lambda)$ are the optical depths associated with atmospheric state of interest. In the noise case, $\Delta\tau_{noise}(\lambda)$, is computed based on $\tau_x(\lambda)s$ derived from NWP model data, and estimated noise values as a function of wavelength are given as the RMS error

$$noise(\lambda) = \sqrt{\frac{1}{N}\sum_{N}(\Delta\tau_{noise}(\lambda))^2} \tag{4-5}$$

where N is the number of profiles in the match pair dataset. In the signal case, the $\tau_x(\lambda)s$ values were those derived from atmospheric state variables derived from the RAOB data plus an augmented CO_2 column or surface pressure value. The resulting signal term is then given as the absolute average over the ensemble set

$$signal(\lambda) = \frac{1}{N}\left|\sum_{N}\Delta\tau_{signal}\,(\lambda)\right| \tag{4-6}$$

In this study, the differential signal and noise spectra are computed for four CO_2 and two O_2 bands of interest. Each band is 300 pm wide and has center wavelengths at approximately

1.5711, 1.5723, 1.5805, and 2.0510 µm (6364.92203, 6359.96733, 6327.06095, and 4875.59 cm^{-1}) for the CO_2 bands. The O_2 bands are centered at approximately 0.76468 and 1.2625 µm (13077.29386 and 7920.5976 cm^{-1}). In addition, a single observational scenario is constructed to evaluate the performance of observations from a space-based mission based on a nadir viewing geometry. The space-based scenario is based on a 20 km fixed path length. While it is well understood that the space-based scenario covers only a fraction of path associated with any proposed viewing geometry, the length selected bounds the limits of the observed and NWP data, and represents the fraction of the atmosphere that has the most severe impact on these measurement techniques.

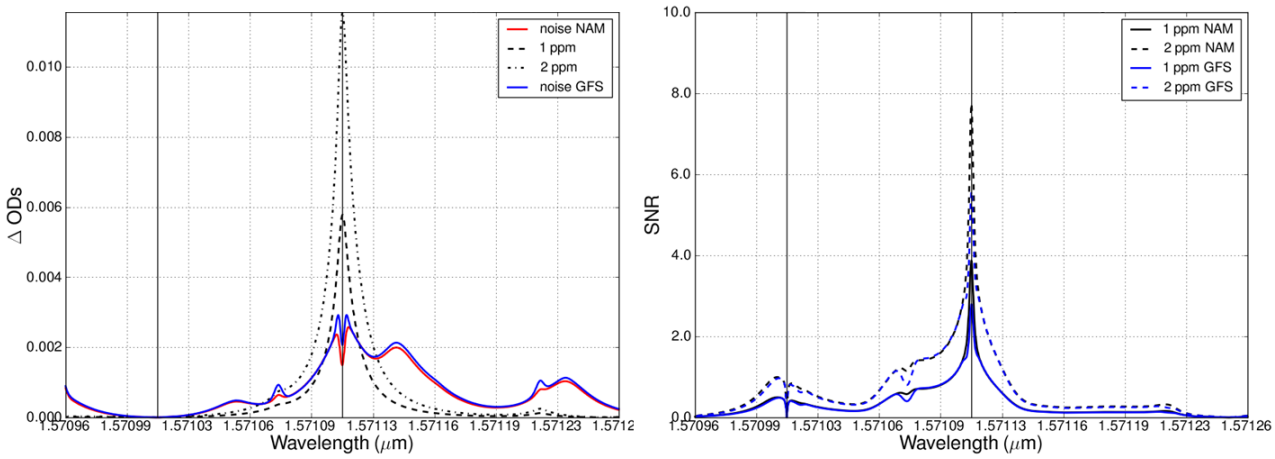

Figure 4-6 Representative signal/noise for 20 km nadir sensor to ground path length. Plots show values (left) and ratios (right).

An example set of computed signal and noise values and the associated signal to noise ratios (SNRs) as a function of wavelength for select off-line locations are provided in Figure 4-6 for a representative CO_2 case. These signal and noise terms form the basis for a number of analyses designed to assess and quantify the impact of uncertainties in atmospheric state knowledge on estimated CO_2 column amounts. The left plot illustrates signal and noise values for a representative CO_2 line for absorption feature centered at 1.5711 µm. The solid lines represent the simulated noise values as a function of wavelength derived from both the Contiguous United States (CONUS) NAM data (red) and the global GFS data (blue). In this CO_2 case, an additional 2.40 mb uncertainty in surface pressure was also introduced. The dashed and dotted lines in the left hand plot represent the average signal given by a 1 and 2 ppm change in column amount. The on-line (1.5711 µm) and selected off-line (-100 pm) positions are illustrated in the graphs as solid vertical lines. The right plot shows representative SNRs constructed for a 1 and 2 ppm signal derived from CONUS NAM data (black) and global GFS data (blue). An example two-dimensional representation of associated noise equivalent signal for the CO_2 line at 1.5711 µm and 20 km nadir viewing geometry is shown in Figure 4-7. The noise equivalent signals are constructed by interpolating noise ΔOD to signal values for all on/off-line combinations ±150 pm from line center.

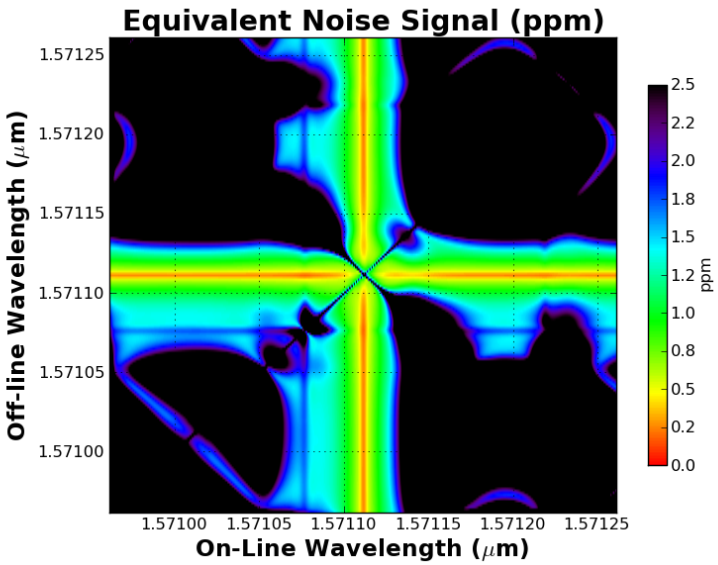

Figure 4-7 Two-dimensional representation of noise equivalent signal for CO_2 line at 1.5711 μm and 20 km nadir viewing geometry.

Figure 4-8 illustrates the minimum equivalent noise for on-line positions ±20 pm from line center for the same sample CO_2 line and geometry. Shown is the minimum equivalent noise associated with uncertainties in vertical temperature and water vapor (T/WV) only, and T/WV uncertainties combined with 0.75, 2.40, and 4.31 mb uncertainties in surface pressure derived from both CONUS NAM data (black) and global GFS (blue). These surface pressure uncertainty values were chosen based on table 4-1 and the analyses described in section 4.2.1.1, and provide three global surface pressure uncertainty regimes at the 65%, 95% and 99% confidence levels. Finally, Figure 4-9 shows minimum equivalent noise signals for CO_2 lines centered at 1.5711, 1.5723, 1.5805 and 2.0510 μm given uncertainties in vertical T/WV, a 2.40 mb uncertainty in surface pressure, and a 20 km nadir viewing geometry derived from CONUS NAM NWP data (black) and the global GFS data (blue). The 2.0510 μm center line is chosen in the wing of the 2 μm absorption feature due to the high absorption of CO_2 in this band, which results in low SNR and smooth equivalent noise signal across the ±20 pm region plotted.

The profile database, simulated optical depths and resulting uncertainties outlined above are more formally presented in (Zaccheo, et al. 2014), and utilized in (Crowell, et al. 2015) to assess the impacts of atmospheric state uncertainty on O2 measurement requirements for the ASCENDS mission.

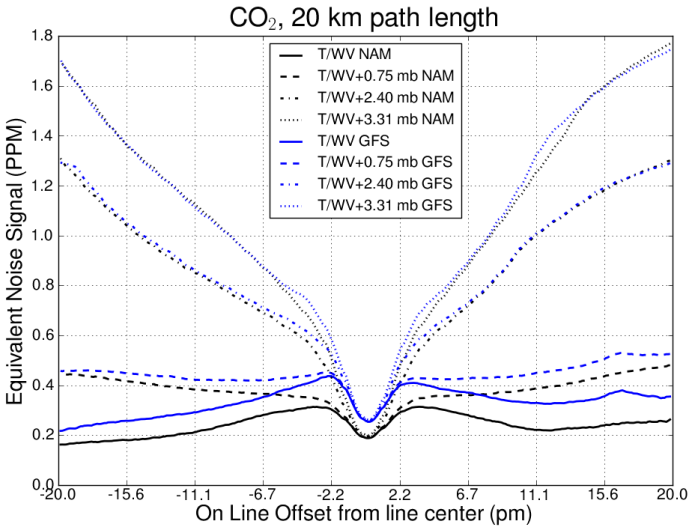

Figure 4-8 Equivalent noise signal errors for sample CO_2 line at1.5711 µm. Minimum equivalent noise for on-line positions ±20 pm from line center for CO_2 line at 1.5711 µm and 20 km nadir viewing geometry.

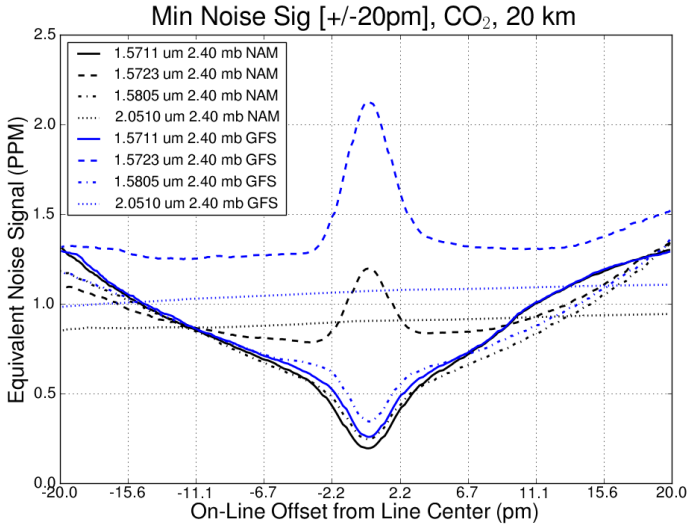

Figure 4-9 Sample set of minimum equivalent noise errors for CO_2 lines between 1.57 and 2.05 CO_2 lines centered at 1.5711, 1.5723, 1.5805 and 2.0510 µm and a 20 km nadir viewing geometry.

ASCENDS XCO_2 measurements require both state of the art instrument design and precise knowledge of the atmospheric state (temperature, moisture and surface pressure) to ensure desired precision and accuracy.

4.4 Summary

A baseline assessment of uncertainties in atmospheric state variables (vertical temperature, vertical moisture, and surface pressure) and their impact on a generic instrument implementation for a selected set of spectral lines/features is provided. This assessment provides a common parametric baseline that will evolve over time as the ASCENDS design matures, and will aid in instrument and mission definition, design and potential future source selection activities. In addition, these analyses will help guide the mission requirements for potential additional space-based measurements, e.g. the necessity for an O_2 based surface pressure measurement, and provide a single common set of vetted sources of ancillary data that may be incorporated into the procurement phase to aid in source selection.

5. Technical Feasibility

5.1 Introduction – Lidar Measurements for the ASCENDS Mission

The ASCENDS lidar uses the Integrated Path Differential Absorption (IPDA) lidar approach to measure the column abundance and mixing ratio of atmospheric CO_2. Various IPDA lidar approaches may be used to sample the CO_2 line, measure range, and estimate CO_2 mixing ratio. The simplest approach to describe is shown in Figure 5-1 and uses a pulsed approach with the minimum of two wavelengths to sample the absorption line.

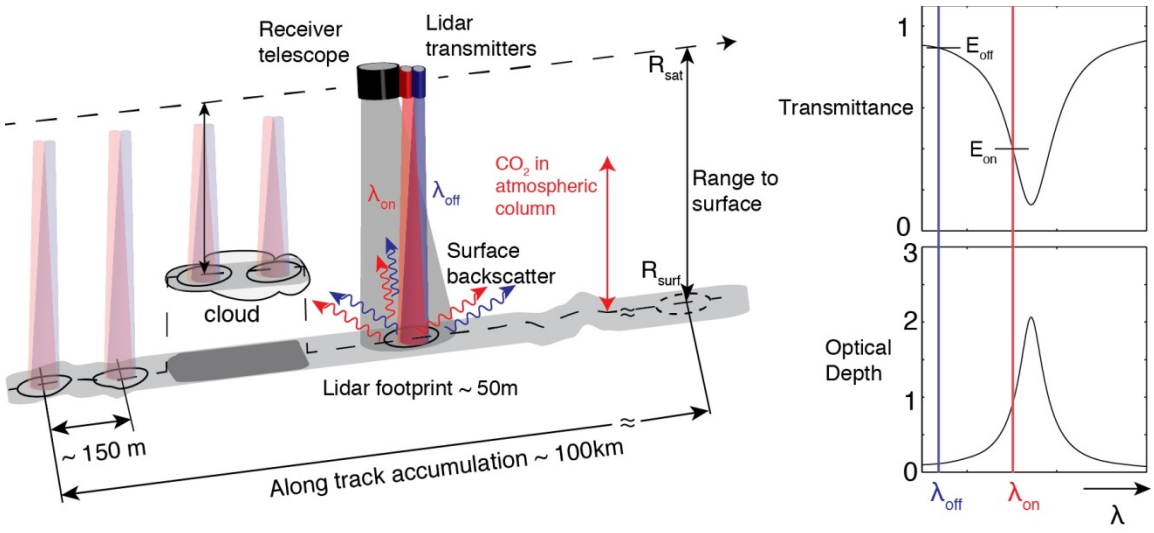

Figure 5-1 Illustration of one approach for an Integrated Path Differential Absorption (IPDA) measurement from space to scattering surfaces on or near the Earth's surface.

While there are several somewhat different candidate measurement approaches for ASCENDS, this drawing is for the two-wavelength pulsed approach considered for the ESA A-SCOPE Mission. Several candidate approaches for ASCENDS use more than two λ_{on} wavelengths to gain some additional information on the vertical distribution of CO_2 and to control biases.

5.1.1 Overview of Measurement Approach

The pulsed two-wavelength lidar approach transmits two laser pulses of slightly different wavelengths in quick succession for every IPDA lidar measurement. Figure 5-1 shows two beams (red and blue) directed at nadir corresponding to the laser pulses tuned onto and off the CO_2 absorption line. They pass through the atmospheric column containing an unknown concentration of CO_2 and illuminate nearly the same area on the scattering surface, either the Earth's surface or cloud top. The light reflected by the surface passes back through the atmosphere, and a small fraction of the light is collected by the receiver telescope. The lidar receiver measures the energies of the on- and off-line pulses (E_{on} and E_{off}) and the range to the scattering surface.

Figure 5-1 right insert shows a sketch of the shape of the CO_2 line's transmission (top) and optical depth (bottom) when measured from space. The maximum CO_2 absorption occurs for laser wavelengths tuned to the line's center. The wavelength of the laser's "on-line" pulse is usually selected to be offset from the peak of the CO_2 absorption line and is indicated by the red vertical line. The wavelength of the laser's "off-line" pulse, that undergoes negligible CO_2 absorption, is

indicated by the blue line. The wavelengths λ_{on} and λ_{off} are sufficiently close that the scattering and absorption by atmospheric aerosols, clouds, and the illuminated scattering surface are the same for both.

The CO_2 column abundance is calculated from the lidar's measurement of range to the surface and ratio of the energies in the on- and off-line return pulse signals. In the IPDA lidar designs considered for ASCENDS, averaging of multiple lidar measurements is planned, so the column abundance specification is for the average of measurements made (typically for 50-100 km) along the orbit's ground track. The column average mixing ratio XCO_2 is calculated using additional information about the density of dry air in the same measurement column. In the baseline approach for ASCENDS, a simultaneous O_2 lidar measurement is included as part of the instrument. A sufficiently accurate atmospheric model evaluated at the location and time of the CO_2 lidar measurement, may be used as an alternative.

The IPDA lidar approach offers a number of unique and important capabilities for column measurements of greenhouse gases. A summary is given in Table 5-1.

Table 5-1 Unique capabilities of the ASCENDS Lidar

Unique capabilities of the ASCENDS Lidar
The light source (the laser) is in the instrument measuring consistently in a nadir path. This enables day and night measurements at all latitudes in all seasons.
The measurements to the surface are range resolved. This allows accurate, bias-free column CO_2 measurements to the scattering surface through thin clouds and aerosol layers.
The lidar directly measures range, thus the estimates of the scattering surface elevation needed to infer CO_2 column mixing ratio are accurate and not impacted by height errors in DEM's, variable heights of trees and other above-surface scatterers, and/or reflectance variability within the footprint.
The laser footprint and spatial scale of sampling (~ 100 m) are small. This enables more frequent measurements to the surface in small gaps between optically thick clouds.
Many sources of potential bias are eliminated since the lidar interacts with the atmosphere and surface consistently in a nadir path. Other than causing signal attenuation, atmospheric aerosol scattering does not impact the lidar CO_2 measurement.
The laser's spectral width is a small fraction of the atmospheric CO_2 absorption linewidth, and it is tunable. Sampling the pressure-broadened CO_2 absorption line at an appropriate offset from its absorption line center enables preferential weighting to the CO_2 molecules in the lower troposphere, where the CO_2 source and sink "signals" are the strongest.
The absorption line can be sampled at a several different offsets from line center wavelength, potentially enabling determination of column concentrations with separate weightings toward both the lower and upper troposphere.
The lidar samples only one selected atmospheric line instead of an entire band. This minimizes errors from interfering gas species. It also greatly reduces the quantity of accurate spectroscopic information needed, and so reduces the potential for spectroscopy-dependent errors.

5.1.2 General Measurement Principle

For the two-wavelength approach, the column averaged CO_2 mixing ratio measured from space to the scattering surface can be calculated from (Menzies and Tratt, 2003; Ehret et al., 2008; Browell et al., 2012)

$$X_{CO_2}(R_{surf}) \equiv \frac{N_{CO2}(R_{surf})}{N_{air}(R_{surf})} = \frac{\int_{R_{surf}}^{R_{sat}} n_{CO2}(r)\left[\sigma_{on}(r) - \sigma_{off}(r)\right]dr}{\int_{R_{surf}}^{R_{sat}} n_{air}(r)dr} \propto \frac{\ln(E_{off}/E_{on})}{2N_{air}(R_{surf})} \qquad (5\text{-}1)$$

Here R_{surf} is the elevation of the scattering surface, R_{sat} is the elevation of the satellite, $n_{CO2}(r)$ is the altitude dependent CO_2 number density, and $n_{air}(r)$ is the altitude dependent dry air number density. At an elevation r, $n_{CO2}(r) = X_{CO2}(r)n_{air}(r)$ and the CO_2 line's absorption cross-sections are $\sigma_{on}(r)$ and $\sigma_{off}(r)$ at the on- and off-line wavelengths respectively. Equation (5-1) assumes that there is no other absorption from other gas species (such as water vapor) at the CO_2 measurement wavelengths. If other gas species absorb there, then their additional absorption effects must be accounted for.

The lidar receiver measures the return pulse energies, E_{on} and E_{off} measured for the on- and off-line pulses reflected from the surface at elevation R_{surf}. The satellite's elevation (its distance from the Earth's center of mass) can be determined with meter-level or better accuracy by using an orbit model with inputs from the satellite's on-board GPS receiver. Given the lidar's measurement of range R to the scattering surface, the elevation of the scattering surface is computed from

$$R_{surf} = R_{sat} - \mathrm{R} \qquad (5\text{-}2)$$

The total dry air column density to the scattering surface, N_{air}, can be estimated either from a simultaneous O_2 lidar measurement made to the same surface, or by evaluating a sufficiently accurate atmospheric model at the lidar's spatial position and measurement time.

Because the width of the CO_2 line is broadened by atmospheric pressure, the line narrows at higher altitudes. This causes the off-set line's absorption cross section to decrease with increasing altitude. The measurement's area normalized weighting function, $W'(r)$ gives the measurement's relative sensitivity to CO_2 at different geometric altitudes. (See Equation (5-3) below.)

$$W'(r) = \frac{n_{air}\left[\sigma_{on}(r) - \sigma_{off}(r)\right]}{\int_{R_{surf}}^{R_{sat}} n_{air}\left[\sigma_{on}(r) - \sigma_{off}(r)\right]dr} \qquad (5\text{-}3)$$

Figure 5-2 shows an example of a CO_2 line's cross sectional shape and weighting function vs pressure altitude. The weighting function's dependence on altitude depends on the absorption line strength, the displacement of the "online" frequency from line center, and dry air density.

Most candidate IPDA lidar approaches exploit the weighting function to enhance the column measurement's sensitivity in the lower atmosphere. By choosing a suitable λ_{on}, the laser signals are preferentially absorbed by the CO_2 molecules in the lower troposphere, where the ambient pressure is higher. This allows $W'(r)$ to be strongest in the lower troposphere. Thus the lidar measurement can be more sensitive to the lower tropospheric CO_2 than that of a passive reflected solar instrument, by as much as a factor of two.

From equation (5-1), the one-way differential absorption optical depth (DAOD) measured by the lidar can be defined as

$$DAOD \equiv \frac{1}{2}\ln(E_{off}/E_{on}) \tag{5-4}$$

The accurate measurements of XCO_2 needed for ASCENDS require accurate lidar measurements of *DAOD* and *R*, as well as of N_{air}. The conditions for measuring gas column densities to the Earth's surface from orbit can be complex. There can be variability in R_{surf}, surface reflectivity, as well as in the spatial coverage, altitude distribution and strength of cloud and aerosol scattering. Generally there are potential error sources from the instrument, spectroscopy of the CO_2 line, and platform altitude and pointing angle (*measurement errors*) as well as potential errors from the knowledge of the parameters of the atmospheric column (*environmental errors*). There are similar potential errors for an O_2 lidar if one is used to estimate N_{air}. All these factors must be considered when defining the measurement requirements for the ASCENDS lidar. A major strength of the lidar approach is providing accurate and high-resolution measurements under widely varying conditions.

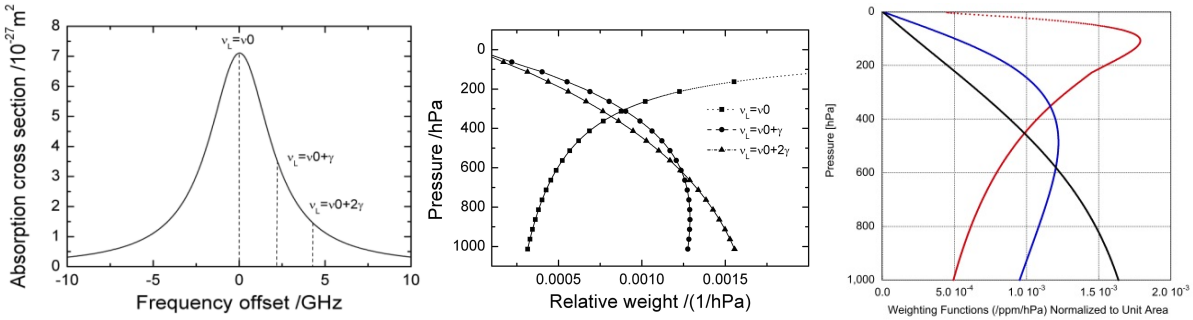

Figure 5-2 Absorption cross section and relative weight by pressure for an example CO_2 line. (Left) Example of the molecular absorption cross section of the 6348 cm^{-1} CO_2 line near 1575 nm, as function of frequency offset of the on-line laser frequency from line centre for typical near surface conditions (T= 288 K and P = 1013 hPa). The dashed lines indicate the on-line laser frequency detuned off line center at one and two collisional halfwidths γ. As the atmospheric pressure decreases with increasing altitude, γ decreases and the CO_2 absorption line narrows. *(Middle)* Relative weight of the CO_2 column content as a function of pressure level for the same example on-line laser frequency positions (ν_L) with respect to the center of the absorption line (ν_0) (Ehret et al., 2008)). (*Right*) Weighting Functions calculated for some CO_2 line candidates for ASCENDS at different on-line wavelength offsets from line center (*Red* – 1572-nm line with 3-pm offset, *Blue* – 1572-nm line with 10-pm offset, *Black* – 2051-nm line with 42-nm offset). These are all normalized to unit area.

The various lidar approaches demonstrated as candidates for ASCENDS have used somewhat different methods for their IPDA measurements. They have sampled different CO_2 and O_2 lines, used different absorption line sampling strategies with different numbers of wavelength samples, and different ways of measuring the elevation of the scattering surface. All CO_2 lidar demonstrations to date have estimated N_{air} using atmospheric models. The details on their

approaches are described in their respective sections. However, the operation of all the lidar candidates generally follow the measurement concept described above.

5.1.3 Measurement Section Overview

The measurement group of the ASCENDS ad hoc science definition team has developed a preliminary set of ten requirements for the lidar measurements on the ASCENDS Mission. They are described in Section 5.2. These requirements are the consensus view of the measurement group and are intended to be generic and independent of the measurement approach.

During the past decade, NASA has invested in the development of several different lidar approaches and technologies which may be candidates for ASCENDS. With the support of the Earth Science Technology Office (ESTO), the ASCENDS ad hoc science definition activity, NASA centers and some industry investments, the NASA lidar teams have made a number of advances in developing candidate lidar approaches, in demonstrating their measurement capabilities from aircraft, and in demonstrating data analysis (retrieval) approaches. These are summarized in Section 5.3. Work on other approaches has also been pursued and their status is summarized in Section 5.4. Several activities are recommended in the near term to improve the definition, enhance the performance, and reduce the risk of the ASCENDS mission. Those are summarized in Section 5.5.

Although the airborne lidar have been quite valuable in demonstrating capability of candidate lidar approaches, a space version requires some additional technology development to allow similar measurements for an extended time from orbit. Some teams have also conducted analysis on the capabilities needed for a space lidar and made progress in addressing some key technologies for it. This work is summarized in Section 5.6. Some general needs for lidar development for the ASCENDS space mission are summarized in Section 5.7.

5.2 ASCENDS Lidar Measurement Requirements

During 2013, the measurement group of the ASCENDS ad hoc science definition team developed a preliminary set of measurement requirements for the ASCENDS lidar. These requirements were developed based on the team member's prior lidar experience as well as that gained from the numerous ASCENDS airborne campaigns that used different candidate lidar measurement techniques. These represent the consensus view of the present best understanding of the lidar measurement needs for the space mission. The requirements are also consistent with the initial mission simulation studies performed by Kawa et al. (2010).

The preliminary requirements are provided in this section with a justification for each. The preliminary set of requirements is summarized in Table 5-2, including one requirement that is applicable to the ground segment. Each individual lidar requirement ("R-#") is stated subsequently, along with its rationale and a discussion of the relevant issues and questions.

Table 5-2 Summary of Measurement Requirements needed for ASCENDS

Summary of Measurement Requirements needed for ASCENDS
1. Measure & report the 6 lidar measurements stated below with a spatial resolution equivalent to a sampling rate of at least 50 Hz. (This implies a compatible laser footprint diameter). This spatial resolution is related to (a) the ability to measure scattering surface elevation (SSE) with sufficient accuracy over sloping terrain (R-7), and (b) the ability to obtain data in scattered cloud conditions (R-4, R-8). These six measurements are: (1) CO_2 differential absorption optical depth (DAOD), (2) Range to the surface at an "offline" wavelength within the CO_2 absorption band, to allow determination of column length and SSE of CO_2 column density measurement, (3) Range spreading (i.e., variability of SSE) at the "offline" CO_2 wavelength within the spatial resolution element (R-6, R-7) , (4) O_2 DAOD, (5) Range to the surface at an "offline" wavelength within the O_2 absorption band, to allow determination of column length and SSE of O_2 column density or surface pressure measurement in the O_2 wavelength region, and (6) Range spreading at the "offline" O_2 wavelength. The uncertainties in these measurements, as stated in the ten individual requirements, must enable computing XCO_2, the column average CO_2 mixing ratio, consistent with the random error and bias requirements, R-1 and R-2. The altitude sensitivity (or the weighting function) of XCO_2 must have ≥ 50% of its response (or sensitivity) below 5 km.
2. The CO_2 & O_2 lidar measurements must be co-aligned spatially
3. The CO_2 & O_2 measurements must have sufficient resolution and precision to enable computing CO_2 dry air mixing ratio over a virtual bright flat reference surface (with lidar reflectance equivalent to that of Railroad Valley NV) in a clear atmosphere to ≤ ~10 ppm at a 50-Hz rate, or ≤ 0.5 ppm using 10-second averaging.
4. The bias in XCO_2 determined from the lidar measurements must be < 2 ppm pre-launch. There must be a credible path to reduce the biases as the mission progresses to < 0.5 ppm, 1 year after launch. See R-2.
5. Measurements made under reduced atmospheric transmission due to thin clouds and to darker surfaces must also be reported, but can have correspondingly reduced precision. See R-3 and R-5 for more information.
6. The lidar must be capable of making CO_2 & O_2 measurements to surfaces whose lidar reflectivity may vary widely (more than 100x) from one measurement sample to the next.
7. The lidar must provide measurements at the lidar-reporting rate when orbiting over rapid changes in height of the reflecting surface of up to 5 km (e.g., to accommodate transitions between cloud tops and the surface).
8. The lidar must provide measurements when orbiting over surfaces that have up to 40 m of range spreading within the sampling interval, such as sloping terrain in mountains and forests with tall trees.
9. The lidar must provide measurements through thin clouds and aerosol layers with performance metrics as stated in R-3 and R-5.
10. The lidar instrument or spacecraft must provide measurements of its orbit position and pointing angle to allow post processing to determine its radial orbit altitude to ≤ 1 m in order to enable conversion of range into scattering surface elevation.
11. The lidar measurements must be processed using adaptable algorithms ("measurement models") that allow the algorithm parameters and computations to be updated post-launch, for the purpose of improving the processed measurement data accuracy and coverage by incorporating improved knowledge of instrument behavior from on-orbit calibrations, etc.

These requirements are intended to be as general as possible and to be independent of individual lidar measurement approaches. These requirements are also preliminary, and the intent is that they will be updated as the understanding of the mission's required measurements improve. For example, one question still being evaluated is whether the expected improvements in meteorological models will be adequate for the dry air mass estimates and thus obviate the need for the O_2 lidar measurements.

The requirements take into account the high precision and high degree of stability (or low measurement bias) needed for the ASCENDS lidar. They also take into account the complexity of making precise measurement of atmospheric gas columns when viewing the Earth from space. Some of the complicating factors include the widely varying reflectance and topographic heights of the Earth's land and ocean surfaces, the wide variety of cloud types, and the large variations in cloud and aerosol attenuation and scattering in the atmosphere. The physics of the IPDA lidar approach uniquely enables retrieving CO_2 mixing ratios with high precision and low bias in the midst of these complications. Several of the listed requirements relate to essential attributes of the lidar system that has these capabilities, as discussed briefly here.

5.2.1 Why Are Ranging Measurements Important?

Ranging, which allows linking the backscattered online/offline signals with their round-trip time-of-flight, provides accurate determination of the column length and enables effective filtering of aerosols and optically thin clouds. It is well known that atmospheric scattering, if not accurately accounted for or eliminated, is a source of bias in passive optical measurements of CO_2 columns (see for example Aben et al. (2007)). For example, a high-altitude cirrus layer having optical depth of 0.03 can produce a bias of as much as ~10 ppmv (Menzies et al., 2014). Along-track sampling resolution of ~ 100-150 m also provides capability to take advantage of gaps in thick clouds to obtain CO_2 data in the lower troposphere to the surface. Requirements R-4 and R-5 are relevant to this capability.

Accurate measurements of the column length to the scattering surface are also important. The weighting function depends on the pressure of the scattering surface, which is derived from its elevation (SSE, scattering surface elevation) together with pressure surface data from atmospheric models and the O_2 lidar. A small lidar footprint, or spatial sampling resolution element, has significant advantages when measuring over regions with varying topography and/or with tall trees, causing the range to vary significantly. This is further justification for along-track sampling resolution of 150 m or better (i.e., a sampling rate of at least 50 Hz). There are limitations to the use of a Digital Elevation Model (DEM). For example, the DEM is not an accurate indicator of the SSE over forests.

Finally it is important to note that the reflectance of surface materials vary for different gas absorption bands. For some important cases (snow beneath trees) this can cause the SSE to be different for CO_2 and O_2 measurements. Requirements R-4, R-6, and R-7 are relevant to this discussion.

5.2.2 Discussion of Requirement Elements

The ad hoc science definition team has summarized ten specific requirements for the ASCENDS lidar. They are discussed in this section. Many of the requirements need some additional work to resolve questions, and those needs are summarized under the Discussion headings. The value of

some parameters needed for accurate retrievals will need to improve after launch by using calibration/validation (cal/val) activities and campaigns.

R-1: XCO_2 Random Error

Baseline: ~ 0.5 ppm, for 10-sec averaging, over a surface with a lidar directional reflectance equivalent to the Railroad Valley, NV (RRV) surface, with clear atmosphere, and effective weighting function with over 50% of its response (or sensitivity) below 5 km.

Rationale: Observational System Simulation Experiments (OSSE's) performed by the ASCENDS Modeling team indicate that 0.5-ppm XCO_2 precision for a 10-second average over a surface with a lidar directional reflectance equivalent to RRV, will yield adequate precision over a wide range of surface types (ocean, forests, snow, ice) (c.f., Kawa et al., 2010).

Comments: This requirement assumes that individual samples are averaging over 10 seconds (70 km along track with no gaps), over a surface with a lidar directional reflectance or "backscatter" of $\beta = 0.176$ sr^{-1} (typical RRV playa value), with negligible atmospheric attenuation by clouds and aerosols. See R-3 for more surface information.

Discussion: This is weighting function dependent, i.e., the lower in altitude the weighting function is peaked; the greater the sensitivity to surfaces sources and sinks. See the modeling chapter for examples of this effect.

The requirement is on XCO_2, and the apportionment of the errors/uncertainties that contribute is not specified. Uncertainties in surface pressure, water vapor, and temperature profiles will contribute. We estimate roughly half of the mission-required error budget is due to the lidar CO_2 column measurement error.

R-2: XCO_2 Biases

Baseline: Instrument must have sufficient stability so that its "Residual biases" can be reduced over the first year of the mission by adding additional instrument characterization & on-orbit calibrations and validations. They should be:

$\leq$ 2 ppm pre-launch, $\leq$ 1 ppm 6 months after launch; $\leq$ 0.5 ppm, one year after launch

Rationale: Results from Modeling team simulations.

Comments: The main emphasis is on "residual spatially- or temporally-varying biases" (i.e., biases that are likely to vary over spatial and/or time scales which remain after measurement bias model corrections). The residuals will decrease as the on-orbit instrument calibration and retrieval algorithms improve during the mission (as for GOSAT).

Discussion: Biases could be introduced by variable surface spectral reflectivities; pathlength uncertainties; low received signal levels due to aerosol/cloud scattering, calibration errors, instrument thermal environment; uncompensated non-linearities in detector response; or errors or uncertainties in the spectroscopy of CO_2, O_2, or interfering gases. Two simple categories for these are "environmental errors" and "instrument errors."

Determining an acceptable level of residual bias for the ASCENDS is complex activity. Although important progress has been made, more work is needed. The "forward runs" (i.e., detection

experiments) offer the simplest approach to determine. More study of bias impacts on different space and time scales is needed.

R-3: Return Signal Dynamic Range & Measurement Precision

Baseline: To provide global coverage, the lidar must make and record measurements to a wide variety of surface types and through atmospheres with some thin cloud and/or aerosol attenuation. These will present a wide range of signal strengths to the lidar receiver.

Table 5-3 Return Signal Dynamic Range for 1570-nm CO_2 lidar

Case:		Surface beta(pi) (ster^-1)	Effective Lambertian Albedo	Atm Optical Depth	Beta(pi)* atm trans^2	Received Signal Relative to RRV clear	Received signal as Percent of RRV Clear	Measurement Error Mult*
Clear	RRV	0.176	0.553	0.0	0.18	1.00	100	1.00
Clear	Snow**	0.016	0.050	0.0	1.60E-02	9.09E-02	9.09	3.32
Clear	Calm ocean	0.528		0.0	0.53	3.00E+00	300.00	0.58
Thin clouds &	RRV	0.176	0.553	0.7	4.34E-02	2.47E-01	24.66	2.01
Polar clouds &	Snow**	0.016	0.050	0.2	1.07E-02	6.09E-02	6.09	4.05
Thin clouds &	Rough ocean	0.025		0.7	6.16E-03	3.50E-02	3.50	5.34
Thin clouds &	Calm ocean	0.528		0.7	0.13	7.40E-01	73.98	1.16
** Snow albedo from Aoki (2000)				Total Signal Dynamic Range (Ratio Strongest to Weakest)				86
Rough Ocean ~ 12 m/sec wind speeds				* based on an ideal signal shot-noise limited lidar receiver				

Calculations for candidate CO_2 lidar that measure in the 1570-nm and 2051-nm bands shown in the following two tables. These are followed by calculations for candidate O_2 lidar that operate in the 760-nm O_2 A-band and 1270-nm singlet-delta band. These estimates are based on limiting cases with one-way extinction optical depth (OD) $\leq$ 0.7 at the strong return signal end of the range, and one-way OD $\leq$ 0.2 (1570 nm) or OD $\leq$ 0.1 (2051 nm) at the weak signal end. The upper limit cutoff for the signal is (about 3 times that from Railroad Valley) for measurements to smooth water surfaces (i.e., surface wind speed less than ~ 3 m/sec). The instrument CO_2 measurement precision must meet or exceed the precision multiplier estimates shown in the last column for various signal measurement conditions. This includes allowing for noise from detector and optical background.

Table 5-4 Return Signal Dynamic Range for 2051-nm CO_2 Lidar

Case:	Surface beta(pi) (ster^-1)	Effective Lambertian Albedo	Atm Optical Depth	Beta(pi)* atm trans^2	Received Signal Relative to RRV clear	Received signal as Percent of RRV Clear	Measurement Error Mult*
Reference case RRV	1.61E-01	0.506	0.0	0.16	1.00	100	1.00
Clear atm & Snow**	6.40E-03	0.020	0.0	6.40E-03	3.98E-02	3.98	5.02
Clear atm & Calm ocean	5.28E-01		0.0	0.53	3.28E+00	327.95	0.55
Reference case RRV	1.61E-01	0.506	0.7	3.97E-02	2.47E-01	24.66	2.01
Polar clouds & Snow**	6.40E-03	0.020	0.2	4.29E-03	2.66E-02	2.66	6.13
Thin clouds & Rough ocean	2.50E-02		0.7	6.16E-03	3.83E-02	3.83	5.11
Thin clouds & Calm ocean	5.28E-01		0.7	0.13	8.09E-01	80.87	1.11
** Snow albedo from Aoki (2000)			Total Signal Dynamic Range (Ratio Strongest to Weakest)				123
Rough Ocean ~ 12 m/sec wind speeds			* based on an ideal signal shot-noise limited lidar receiver				

Table 5-5 Return Signal Dynamic Range for 765-nm O_2 Lidar

Case:	Surface beta(pi) (ster^-1)	Effective Lambertian Albedo	Atm Optical Depth	Beta(pi)* atm trans^2	Received Signal Relative to RRV clear	Received signal as Percent of RRV Clear	Measurement Error Mult*
Reference case RRV	0.168	0.53	0.0	0.17	1.00	100	1.00
Clear Snow**	0.271	0.85	0.0	2.71E-01	1.61E+00	161.05	0.79
Clear Calm ocean	0.528		0.0	0.53	3.14E+00	314.29	0.56
Thin clouds RRV	0.168	0.53	0.7	4.14E-02	2.47E-01	24.66	2.01
Polar clouds Snow**	0.271	0.85	0.2	1.81E-01	1.08E+00	107.95	0.96
Thin clouds Rough ocean	0.025		0.7	6.16E-03	3.67E-02	3.67	5.22
Thin clouds Calm ocean	0.528		0.7	0.13	7.75E-01	77.50	1.14
** Snow albedo from Aoki (2000)			Total Signal Dynamic Range (Ratio Strongest to Weakest)				85.6
Rough Ocean ~ 12 m/sec wind speeds			* based on an ideal signal shot-noise limited lidar receiver				

Table 5-6 Return Signal Dynamic Range for 1262-nm O_2 Lidar

Case:		Surface beta(pi) (ster^-1)	Effective Lambertian Albedo	Atm Optical Depth	Beta(pi)* atm trans^2	Received Signal Relative to RRV clear	Received signal as Percent of RRV Clear	Measurement Error Mult*
Clear	RRV	0.168	0.528	0.0	0.17	1.00	100	1.00
Clear	Snow**	0.175	0.550	0.0	1.75E-01	1.04E+00	104.21	0.98
Clear	Calm ocean	0.528		0.0	0.53	3.14E+00	314.29	0.56
Thin clouds	RRV	0.168	0.528	0.7	4.14E-02	2.47E-01	24.66	2.01
Polar clouds	Snow**	0.175	0.550	0.2	1.17E-01	6.99E-01	69.85	1.20
Thin clouds	Rough ocean	0.025		0.7	6.16E-03	3.67E-02	3.67	5.22
Thin clouds	Calm ocean	0.528		0.7	0.13	7.75E-01	77.50	1.14
** Snow albedo from Aoki (2000)				Total Signal Dynamic Range (Ratio Strongest to Weakest)				85.6
Rough Ocean ~ 12 m/sec wind speeds				* based on an ideal signal shot-noise limited lidar receiver				

Rationale: ASCENDS must record data over a variety of surface types (including snow & water) to get global measurements (including high latitude winter).

R-4: Along Track Sampling Resolution

Baseline: ≤ 150 m, (≥ 50 Hz sampling). This sampling rate is driven by the need for measurements over cloudy atmospheres and over regions of rapidly changing surface topography & reflectance.

The lidar measured parameters that need to be reported at this rate are:

Mean CO_2 DAOD (or column density), Mean Range (or scattering surface elevation) in CO_2 wavelength region, Range Spread*

Mean O_2 DAOD (or column density), Mean Range (or scattering surface elevation) in O_2 wavelength region, Range Spread*

Rationale: The ASCENDS capability in "seeing" through breaks in cloud cover diminishes with laser footprint sizes > 150m. ASCENDS also needs to measure to terrain surfaces that rapidly vary in elevation and reflectance. A smaller laser footprint reduces error in determination/assignment of "effective scattering surface elevation".

Discussion: This requirement relates to the maximum laser footprint size and along-track spatial scale of sampling. One driver for this requirement is to require measurements through scattered clouds. Estimates of cloud gap size were obtained from analyzing from laser altimeter measurements over Iowa during 2011 ASCENDS airborne campaign (Browell et al., 2012). More

data from the 2011 airborne campaigns are also available. Over mountainous terrain the rapidly varying column length causes the measurement to degrade with poorer along-track resolution.

* See discussion of range spreading in R-7

R-5: Measurements through atmospheric scatter (thin clouds & aerosols)

Baseline: To ensure adequate coverage of the globe, the lidar DAOD and range measurements must be made through scattering & attenuating aerosol layers and partially transmissive cloud layers.

The bias requirements (R-2) must be met under these conditions.

The measurement precision is allowed to degrade at the lower received signal levels as given in the last columns of the Tables in R-3 (Table 5-3 to Table 5-6).

Rationale: Thin clouds are quite prevalent in the Earth's atmosphere. An important benefit of ASCENDS is to allow accurate measurements in regions covered by thin clouds. The random errors will increase due to attenuation of energy of surface backscatter signal. Extensive airborne measurements of aerosol layer optical properties indicate that atmospheric aerosol OD is < 0.1 at 2051 nm and < 0.2 at 1570 nm, even for dust layers from Asia and the Sahara that have been transported from their source regions (Srivastava et al., 2001; Winker et al., 2010). From these results we conclude that aerosol layers alone will not seriously impact ASCENDS global coverage.

R-6: Measurements over forests & over sloped or rough bare terrain

Baseline: Measurements meeting R-1 & R-2 over forests and over surfaces with height variations of up to 40 m over a horizontal distance of 150 m are required.

Rationale: Forests are a large fraction of Earth's land surface and are an important part of carbon cycle. (Simard et al., 2011) report spatially-resolved tree heights over the globe, based on analysis of ICESat/GLAS measurements. Their results showed maximum tree heights of ~ 40 m. The ASCENDS lidar also must measure over bare terrain, rough or sloped, whose surface has similar range spreading over 175-m distances.

R-7.1: Range (Scattering Surface Elevation) measurement: Precision

Baseline:

a. Mean Range measurement precision: Baseline: ≤ 20 m (at 50-Hz rate) for all cases included in the R-3 tables (Table 5-3 to Table 5-6) and range spreading cases in R-6, and ≤ 2 m for a 10-s average over a RRV equivalent surface.

b. The Lidar must report range at both the CO_2 and O_2 measurement wavelength regions, both on the same spatial scale (see R-4).

c. Range Spread measurement: Baseline ≤ 20 m (at 50-Hz rate) for all cases included in the R-3 tables and range spreading cases in R-6, for both CO_2 and O_2 wavelength regions.

d. Rate of change in range: The lidar needs to accommodate changes in range of ≥ 5 km for adjacent footprints, to allow for measurements from cloud tops to the ground through holes in clouds.

e. Spacecraft radial orbit height**: < 1 m at a rate sufficient to model orbit to < 1-m radial error

Discussion: A summary of the rationale for measuring range at both CO_2 and O_2 lidar wavelengths is below.

a. Some surfaces (e.g., conifers with snow underneath) can have different average scattering surface elevations (SSE) at CO_2 & O_2 wavelengths, due to the variability in snow reflectivity with wavelength. Snow is quite dark at the CO_2 wavelengths but is much brighter at the O_2 wavelengths. In this case, there is a difference in the return signal from the snow surface (CO_2 is dim, O_2 is brighter). Consequently the mean range (i.e., the SSE) for these wavelengths will be different when there are spatial variations in snow cover across the footprint (e.g., coniferous forests with snow on the ground). Reporting SSE for both wavelengths will allow analysis to accurately estimate CO_2 mixing ratios.

b. In order to maximize the number of CO_2 retrievals over, e.g., patchy/broken cloud cover, range measurements are required at the 50-Hz reporting interval, with the precision requirement stated above. The 20-m uncertainty is equivalent to approximately 1 ppm of CO_2. This uncertainty should decrease with additional along-track samples, although the rate of decrease of the uncertainty depends on the cloud structure and the underlying surface topography.

c. Some reflecting surfaces (i.e., trees) will have range spreads within the footprint that can be 20-40 m. Also large surface slopes can occur over mountains. Range spread measurements at the 50-Hz sampling rate enable estimates of tree heights and slope magnitudes. Range spread with above-stated precision at both CO_2 and O_2 wavelength regions enable mitigation of bias over surfaces discussed in (a) above.

** Need to know the spacecraft's radial orbit height to compute the scattering surface elevation from the lidar measured range.

R-7.2: Range (SSE) measurements: Bias

Baseline:

a. Baseline for ranging measurements: ≤ 2 m per footprint for all cases included in the R-3 tables (Table 5-3 to Table 5-6) and satisfying R-4 range spreading. The lidar must also report range at both the CO_2 & O_2 offline wavelengths, both on the same spatial scale (see R-4).

b. Baseline for Spacecraft radial orbit height**: < 1 m

Discussion: The SSE needs to be measured at 50 Hz for both CO_2 and O_2 lidar wavelengths to minimize the bias inherent in rapidly changing terrain. Bias occurs under conditions described in R-7.1, due to spectrally varying reflectivity of various surface types. Large changes in, e.g., snow cover, can occur over distances of 150 m (the required sampling interval). Measurements are

made though "holes" for conditions of patchy/broken cloud cover, creating rapid changes from cloud top to ground.

In addition, over hills/mountains large changes in elevation also occur over km-scale distances. Due to the inherent reflectance weighting of the samples, correlations between elevation and surface type (and surface reflectivity) could produce bias if using km-scale averaging. Hence reporting the range to the SSE at 50-Hz rate, with sufficient precision (< 20-m uncertainty) and low bias (< 2 m) is required.

** Need to know the spacecraft's radial orbit height to compute the scattering surface elevation from the lidar measured range.

R-8: Measurements over Cloud Tops and Decks

Baseline: "Report" measurements over optically-thick cloud tops that meet the other signal requirements. (i.e., roughness, signal strength, etc.).

Rationale: These measurements are expected to be useful for future analysis, but currently it is judged that they do not have to be of the same measurement quality as those to the surface. Further studies are required to better quantify the requirement.

Discussion: Initial Airborne measurements in 2011 over stratus cloud decks show promise toward useful values. Some improvement can be expected with additional algorithm development. Cloud tops are diffuse scatters, and laser penetration depths may vary from ~ 10 m to > 100 m; consequently accurate measurements over cloud decks is more difficult than for solid surfaces.

R-9: Uncertainty in Measurement Footprint's* Surface Location (pointing control and knowledge)

Nadir angle offset*: 6 - 20 mrad (TBR)

Baseline Knowledge: ~ 100 m (TBR)

Baseline Control: ~500 m

Rationale: Measurement analysis needs knowledge of measurement locations for use in models, cal/val correlative measurements, control of systematic errors/biases due to terrain variability, above-ground variability, and effective use of digital elevation models (DEM's). The mission will also need control of measurement locations for effective cal/val (e.g., TCCON intercomparisons). See R-10.

Discussion: This requirement applies to both the CO_2 & O_2 beams and assumes that they are co-aligned (co-boresighted). Co-alignment requirements are lidar-design specific, consequently not quantified here. It is important to recognize that sharp ground-track transitions (e.g., land-to-water transitions) must be accommodated in meeting the XCO_2 precision and bias requirements.

The ASCENDS lidar must be pointed slightly offset from local nadir, to allow measurements to smooth water and certain flat ice crystals, while avoiding the strongest part of the specular reflections from it. ICESat results indicate that we need to stay > 6 mrad from local nadir. The maximum angle is uncertain but likely < 20 mrad. The final operational angle will need to be found on-orbit.

This requirement is also associated with accurate location of the measurement footprint on the surface for improved modeling accuracy. These numbers are consistent with maintaining the path length error (SSE estimate error) below a value that compromises the overall error budget. Studies using ASCENDS airborne lidar measurement indicate that slopes < 15 degrees over 100-m scales occur with ~ 50% probability over mountains ranges such as the Sierra Nevada. Any aspect of ground spot location uncertainty that affects bias error should be derived from the bias requirement stated earlier. Knowledge of spatial location of the column end-point is more important for smaller-scale sources. Typical pointing knowledge for the requirements above is 200 μrad, or 40 arcsec.

* See discussion of range spreading in R-7

R-10: Laser Beam Pointing Off-nadir Limits

Off nadir operating limits: < +/- 15 degree of nadir

Rationale: Need to allow a finite range of pointing angles away from nadir to permit a useful frequency of pointing to TCCON (or other ground-based calibration) sites over land areas.

Discussion: This specifies how far away from the nadir-pointing angle that ASCENDS is required to measure. The further off nadir, the more frequently ASCENDS can access (i.e., be "within range of") ground-based cal/val sites. In regular operation, ASCENDS will need to point off-nadir (cross-track) to locate footprints near ground-based cal/val sites (e.g., TCCON). Cal/val measurements are expected to be important to assess and minimize residual biases. It needs to be determined how frequently ASCENDS will needs to measure off nadir, to a TCCON site, for example. The larger the allowable off-nadir angle, the more frequently a ground based site can be sampled.

An additional complication for the CO_2 measurement is the Doppler shift. When pointed off nadir, the Doppler effects from the spacecraft's velocity, Earth's rotation, and atmospheric winds may shift the absorption line relative to the spacecraft and possibly change its shape. The above off-nadir pointing limitations were arrived at from an analysis provided to the ASCENDS ad hoc science definition team by Spiers and Menzies. Some aspects (spacecraft velocity & Earth's rotation) are predictable. Estimates of atmospheric wind velocity fields are available from NWP models.

5.3 Lidar Development and Measurement Demonstrations

During the past decade, NASA has invested in the development of several different lidar approaches and technologies which are candidates for ASCENDS. With the support of ESTO, the ASCENDS ad hoc science definition activity, and NASA Center and corporate investments, several NASA lidar teams have made substantial advances in developing suitable lidar systems, demonstrating lidar capabilities from aircraft, improving the understanding of the characteristics needed in the measurements, and reducing the risk for developing the technology for the space lidar.

The operating principles for different IPDA lidar approaches have been discussed in detail in many publications. Some examples are given by Ehret et al. (2008), Abshire et al. (2010a, 2013),

Spiers et al. (2011a), Browell et al. (2012), Dobler et al. (2013), Menzies et al. (2014) and others. A signal to noise analysis is also discussed by Sun and Abshire (2012).

Here we summarize NASA's experimental demonstrations and the results to date. This section gives a summary of the work demonstrating capabilities of candidate CO_2 and O_2 lidar techniques. Each candidate approach is described along with a description of the instrument and its type of measurements. Many have examples of atmospheric measurements from aircraft.

5.3.1 CO_2 Sounder Approach and Lidar

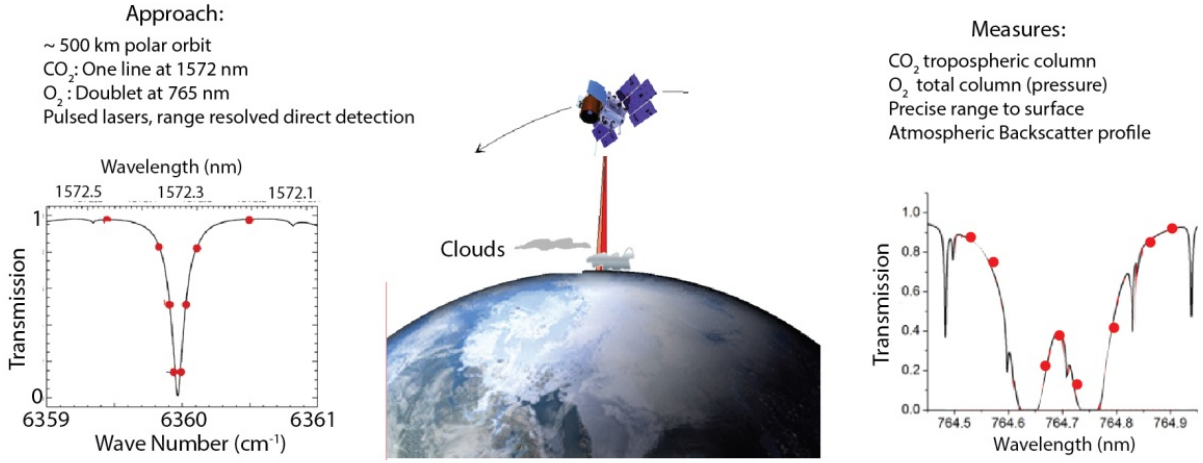

Figure 5-3 The CO_2 Laser Sounder measures column CO_2 & O_2 absorption and range to surface. (Left) Nominal CO_2 line (1572.33 nm) targeted for use for 2-way pass to surface from space. The laser sounder measures the shape and depth of this CO_2 line and the absorption of a line doublet near 764.7 nm in the O_2 A-band *(Right)*. The absorption lines are scanned at a 300 Hz rate from aircraft, and ~1 KHz rate from space.

A team at Goddard has developed the CO_2 Laser Sounder approach to enable space-based lidar measurements of CO_2 concentrations like those needed for ASCENDS. Given the high (< 1 ppm) accuracies required and the many potential error sources, the design of the measurement approach and the lidar instrument are critical (Kawa et al., 2010). The CO_2 Sounder Team has developed and demonstrated a pulsed lidar approach (Riris et al., 2007; Allan et al., 2008; Abshire et al., 2010a,b, 2011, 2014; Amediek et al., 2013), shown in Figure 5-3 to address the needed CO_2 column concentration measurements. It measures the range, line shapes and column abundance of CO_2 and O_2 via the integrated path differential absorption (IPDA) technique (Measures, 1992).

The team performed surveys of the spectroscopy (Mao and Kawa, 2004; Mao et al., 2007) and selected gas absorption lines with minimum interference from other species and with small temperature sensitivity. The CO_2 line at 1572.33 nm and O_2 doublet near 764.7 nm best fit the requirements. Another important consideration is the number of wavelength sampling points per measurement. The team found that using only a minimum two lines (on- and off-line) makes the measurement susceptible to small spectroscopic shifts and instrument errors. For airborne measurements, the team has used 20 and 30 samples across the lines, to allow for sampling experiments via deletion. For space the CO_2 Sounder approach plans to sample the CO_2 and O_2 line shapes with 8 wavelengths. This allows solving for and correcting for both environmental and instrument errors. Analysis of airborne lidar measurements shows this approach is quite robust.

The team's approach has been to analyze the science and measurement requirements (Kawa et al., 2010) and then to pursue the measurement approach and technologies that directly support a path toward space (Sun et al., 2013). The team has demonstrated increasingly accurate airborne measurements of CO_2 column abundance and range to 13 km in campaigns during 2009, 2010, 2011 and 2013. The team also demonstrated measurements of O_2 column absorption in the O_2 A-band (Stephen et al., 2007; Riris et al., 2011) during the 2011 and 2013 flights. The lidar development has been supported by the NASA ESTO Instrument Incubator program and summaries of papers and conference presentations are available (NASA Goddard, 2015).

5.3.1.1 CO_2 Sounder Measurement Approach and Lidar Description

The team developed its airborne lidar as a precursor/pathfinder for ASCENDS, using lower laser energies and a less sensitive CO_2 detector than planned for space. Photographs of the aircraft and instrument are shown in Figure 5-4.

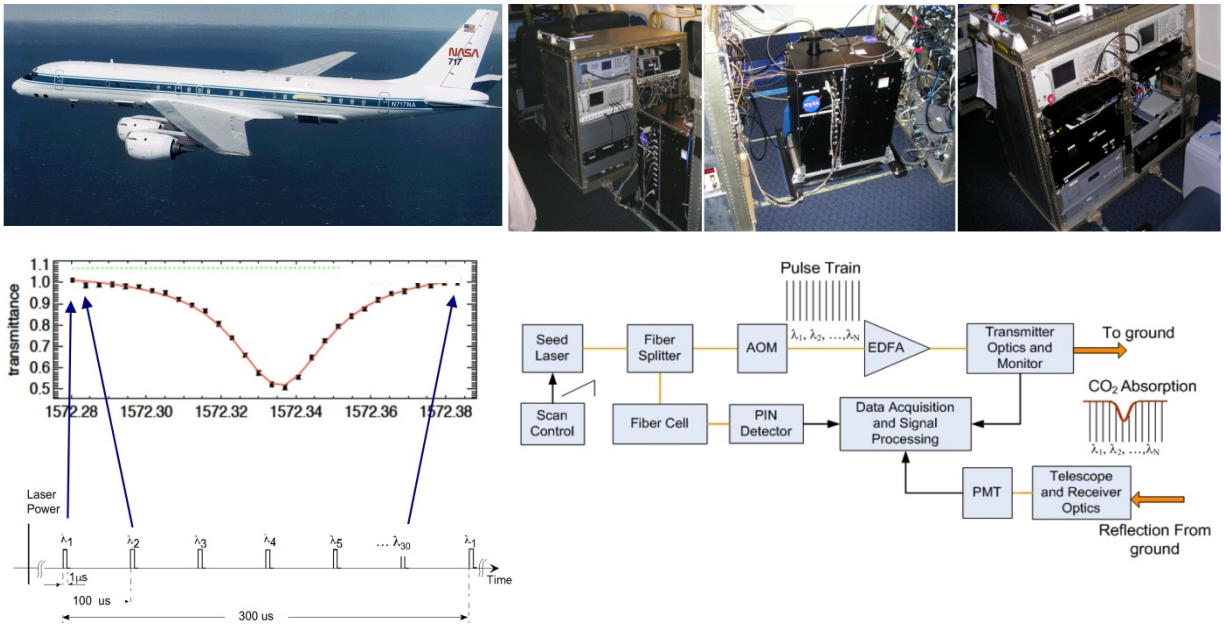

CO_2 line center wavelength:	1572.33 nm	Laser beam divergence:	100 urad	Detector quantum efficiency:	10%
Wavelength scan # across line:	30	Telescope diameter:	20 cm	PMT dark count rate:	~500 KHz
CO_2 line scan rate:	300 Hz	Receiver FOV diameter:	200 urad	Receiver time bin width:	8 nsec
Laser pulse energy & rate:	25 uJ, 10 KHz	Receiver optical bandwidth:	800 pm	Rcvr integr time / record:	0.9 sec

Figure 5-4 Airborne CO_2 Sounder lidar installation, line sampling approach and parameters. (Top) Photos of the NASA DC-8 aircraft and CO_2 Sounder lidar installed inside. The transmitter and receiver telescopes are in the black box mounted over the aircraft's aft-most nadir opening and views nadir through a dual optical window assembly. *(Middle left)* Line sampling approach showing the 30 wavelength samples across the line used in the airborne lidar, allowing robustness and diagnostic capability. *(Middle right)* Block diagram of the airborne lidar. *(Bottom)* Some parameters of the airborne CO_2 lidar.

The laser uses a Master Oscillator Power Amplifier (MOPA) approach with single frequency DFB diode laser followed by a pulsed acousto-optic modulator (AOM) and a commercial Erbium Doped Fiber Amplifier (EDFA). For flights after 2009, the airborne lidar steps the diode laser's

wavelength across the selected CO_2 line at a rate of 300 Hz with 30 steps per scan. The airborne lidar uses more wavelength samples than proposed for space, to allow evaluation of tradeoffs from the additional information. The time resolved laser backscatter profile is collected by the telescope, detected by a photomultiplier, and recorded by a multi-channel scalar.

The column concentration of atmospheric CO_2 must be measured accurately (< 1ppm) to be useful for carbon cycle science studies (NRC, 2007; NASA, 2008). The random error level (precision) can be determined from analysis by scaling the transmitted laser energy to the level needed (i.e. the SNR) to overcome the noise from the detector and detected solar background.

Systematic errors or "drifts" usually limit the accuracies of laser absorption spectrometers (Werle et al., 1993, 2004). Sampling the absorption line shape allows solving for a number of parameters in the data analysis, including baseline transmission, baseline tilt, line center wavelength, linewidth, peak transmission, best-fit line shape, and error in the fitted line. This approach allows retrieval and signal processing approaches to measure, model, and minimize systematic instrumental errors from etalon fringes and other sources (Abshire et al., 2014) and this analysis substantially reduces the magnitude of instrumental errors. It also accommodates environmental effects such as the spectral shift of the line with changing atmospheric pressure (Ramanathan et al., 2013).

5.3.1.2 Airborne Measurements of CO_2 Column Concentration and Range:

The CO_2 Sounder team made initial airborne CO_2 column measurements in 2008 (Abshire et al., 2010b). In 2009, additional measurements were taken at altitudes stepped from 3-13 km over a variety of locations. These flight data show the precision in CO_2 estimates follow predicted values (Abshire et al., 2013), and that the altimetry measurements had an uncertainty of about 3 m (Amediek et al., 2013). The team demonstrated improved airborne measurements of CO_2 and O_2 column abundance and inferred the mixing ratio in flights on the DC-8 during the 2011 (Abshire et al., 2014) and 2013 airborne campaigns. Some examples are shown in Figure 5-5 – Figure 5-11. These demonstrate the accuracy and precision that the airborne lidar has achieved to date when measuring to a variety of land surfaces, to cloud tops and through thin clouds.

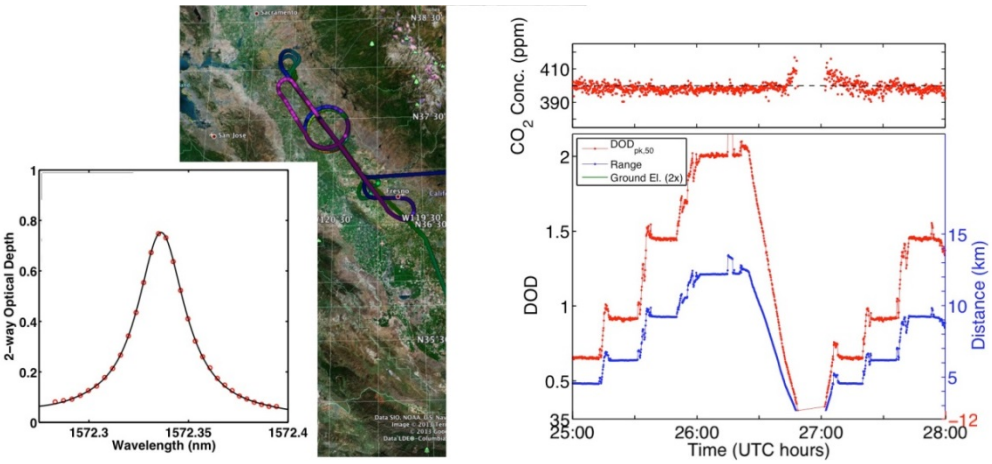

Figure 5-5 Results from CO_2 Sounder lidar measurements over a flat Central Valley CA. Data taken with a uniform atmosphere on 2/27/13. *(Left)* The lidar measured absorption lineshapes fit calculations quite well. The differential absorption optical depth (DAOD) reported is calculated from the fitted lineshape. *(Middle)* Ground track of flight. *(Right)* The results (10 sec average, Measured concentration = 394 ppm, Std dev = 1.5 ppm for 12 km altitudes) show the retrieved column averaged CO_2 concentration agree very well with in-situ measurements for an atmosphere with CO_2 =396 ppm.

These also demonstrate retrievals and progress toward the space lidar. These flights also demonstrated accurate CO_2 concentration measurements over varying topography, to cloud tops and through thin clouds, conditions that are challenging for passive optical CO_2 sensors.

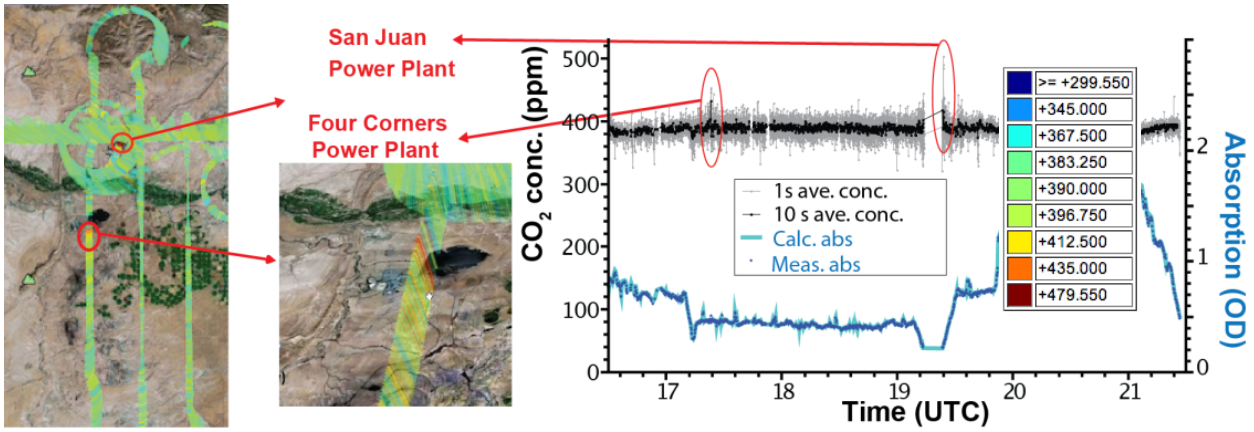

Figure 5-6 Detection of power plant plumes using the CO_2 Sounder lidar. In this flight segment over Four Corners, New Mexico (NM) on 8/9/11, our measurements detect elevated CO_2 in the plumes from power plants. *(Left)* measurement ground track geolocated on Google Earth, with concentrations color encoded, with color-scale in the inset at right. *(Right)* the total column measured concentration as a function of time. The two elevated CO_2 spots are seen directly over the two power plants. The CO_2 concentration is nearly constant at 390 ppm elsewhere, as expected.

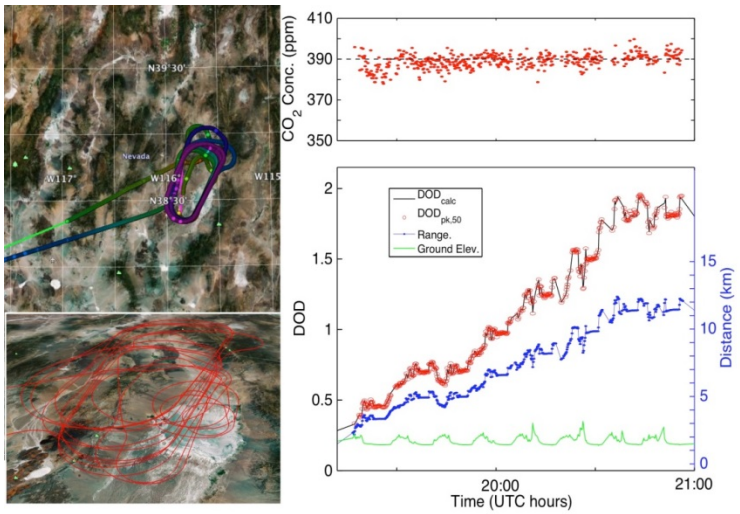

Figure 5-7 Measurements from the 2011 flight over Railroad Valley NV. This area is a flat playa surrounded by mountains, creating a flight track over rapidly varying ground elevation. The bottom plot shows the measured range to surface in blue, the measured Differential Absorption Optical Depth (DAOD) (pk, 50) in red, and the calculated surface elevation height in green. The DAOD is calculated from the fitted lineshape. The highly variable range and DAOD are due to the varying topography, aircraft banked turns over the mountains and the increasing aircraft altitude in successive passes over the ground track. The measured and calculated DAODs follow each other closely, even as they both vary rapidly during passes over the mountains. The top plot shows the CO_2 concentrations retrieved from the lidar measurements of lineshape. All points are for 10 second averages. The retrieved concentration closely follows the predicted column average value of 390 ppm calculated from the Atmospheric Vertical Observations of Carbon Dioxide in the Earth's Troposphere (AVOCET) measurements.

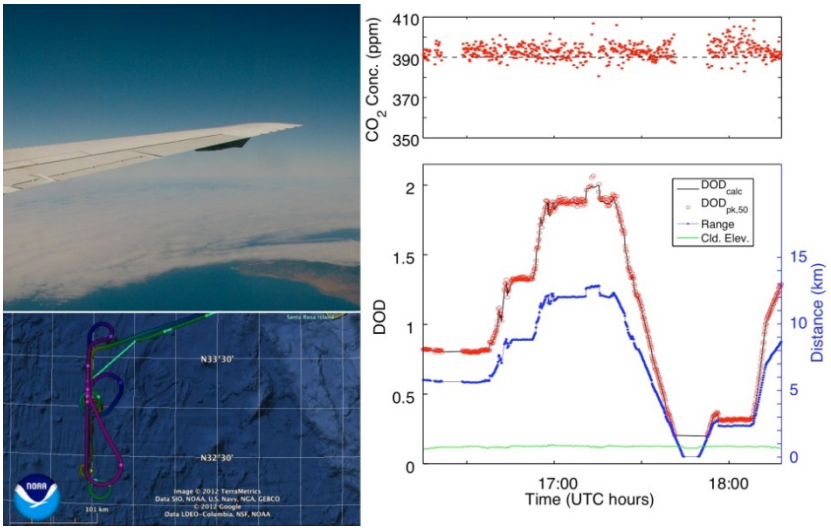

Figure 5-8 CO_2 Measurements made to the tops of marine stratus clouds. (Left) The ground track of a flight made over to the top of marine stratus cloud layer over the Pacific Ocean on August 2, 2011. The laser return pulses from the top of the stratus clouds allowed accurate CO_2 retrieval measurements. *(Right)* The retrievals from the lidar's plane-cloud column averaged CO_2 concentration are in very good agreement with calculated averages based measurements of outside air made by the in-situ Picarro instrument. The cloud tops vary more in range than over land and hence they slightly broaden the errors in the lidar's measurements.

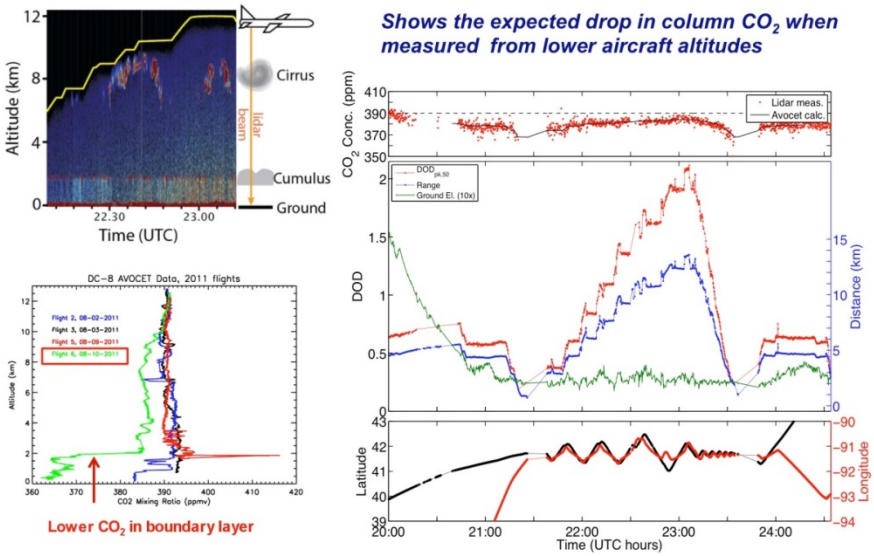

Figure 5-9 Measurements made to the ground through thin cirrus and gaps in cumulus clouds. Data was taken on flights over Iowa on August 10, 2011. *(Top Left)* Color coded backscatter profiles (vertical vs time (horizontal) showing scattering from the ground, the boundary layer, cumulus cloud tops and cirrus clouds *(Bottom Left)* In-situ measurements of CO_2 concentrations for 2011 flights at spiral down locations. The Iowa flight is in green and shows significant drop in concentrations within the boundary layer, from ground to ~2 km. *(Right)* The retrievals from the lidar for the flight segment from Colorado to Iowa. The range to the surface is in blue, the derived surface elevation is in green, the measured DOD (pk, 50) is in red in the lower plot, and retrieved CO_2 concentration is in red at the top plot. The CO_2 drawdown in the boundary layer from the growing crops reduced the concentration in the plane-ground column compared to plane to cloud, and the draw down in clearly evident in the lidar measurements. This is important since the air in the boundary layer is the most influenced by CO_2 fluxes from the surface.

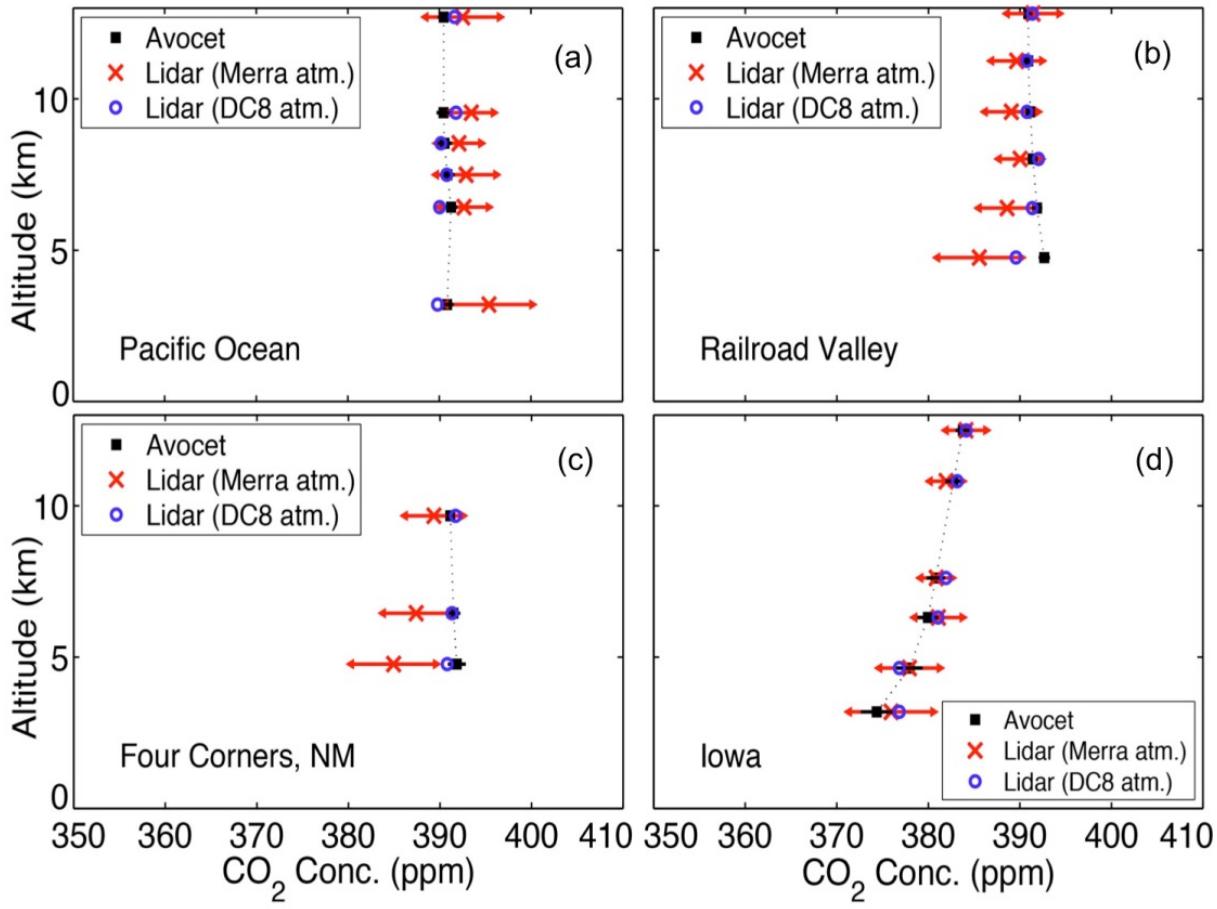

Figure 5-10 Comparison of single column average retrievals from airborne lidar versus altitude. Comparison (Abshire et al., 2014) for flights above the (a) Pacific Ocean, (b) Railroad Valley, (c) Four Corners NM and (d) Iowa. The plot shows lidar retrievals using the atmospheric profiles from the MERRA model *(red),* and those using the atmosphere sampled by the DC-8 during the spiral down *(blue),* and the column average CO_2 values from the AVOCET in-situ sensor *(black)*. The lidar measurement error bars are +/- 1 standard deviation for a 10 second average, and they apply to retrievals based on MERRA and DC-8 based atmospheres. The impact of the lower CO_2 concentration in the Iowa boundary layer is evident as the trend toward smaller CO_2 column densities for measurements made from lower flight altitudes. The lidar retrievals based on the actual atmospheric conditions measured by the DC-8 in the spiral show a close match to those measured by the in-situ sensor. The lidar retrievals based on the actual atmosphere are in quite good agreement with the in-situ measurements, and within 1.4 ppm for those made at 6 km and higher altitudes.

5.3.1.3 Near Term Plans for the CO_2 Sounder

Several components have been developed via support of the ESTO IIP-10 program in work that was conducted in parallel with demonstrating and improving the airborne lidar. These include developing a dynamically step- locked laser diode seed source for CO_2, developing a power amplifier for the O_2 lidar, developing high sensitivity Mercury Cadmium Telluride (HgCdTe) electron Avalanche Photodiode Detector (eAPD) detector assemblies for the O_2 and CO_2 measurement channels and adding analog signal recording. The present plans are to integrate them into the airborne instrument during the spring of 2014 and demonstrate them in the flight campaigns planned for August 2014. These new components should improve the measurements of both CO_2 and O_2. Laboratory tests show the sensitivity of HgCdTe APD detector is ~16 times higher at CO_2 wavelengths than the photomultiplier previously used in the airborne CO_2 receiver.

This added sensitivity should reduce the random errors in the airborne measurements by a factor of 4, or to ~0.5 ppm over most land surfaces.

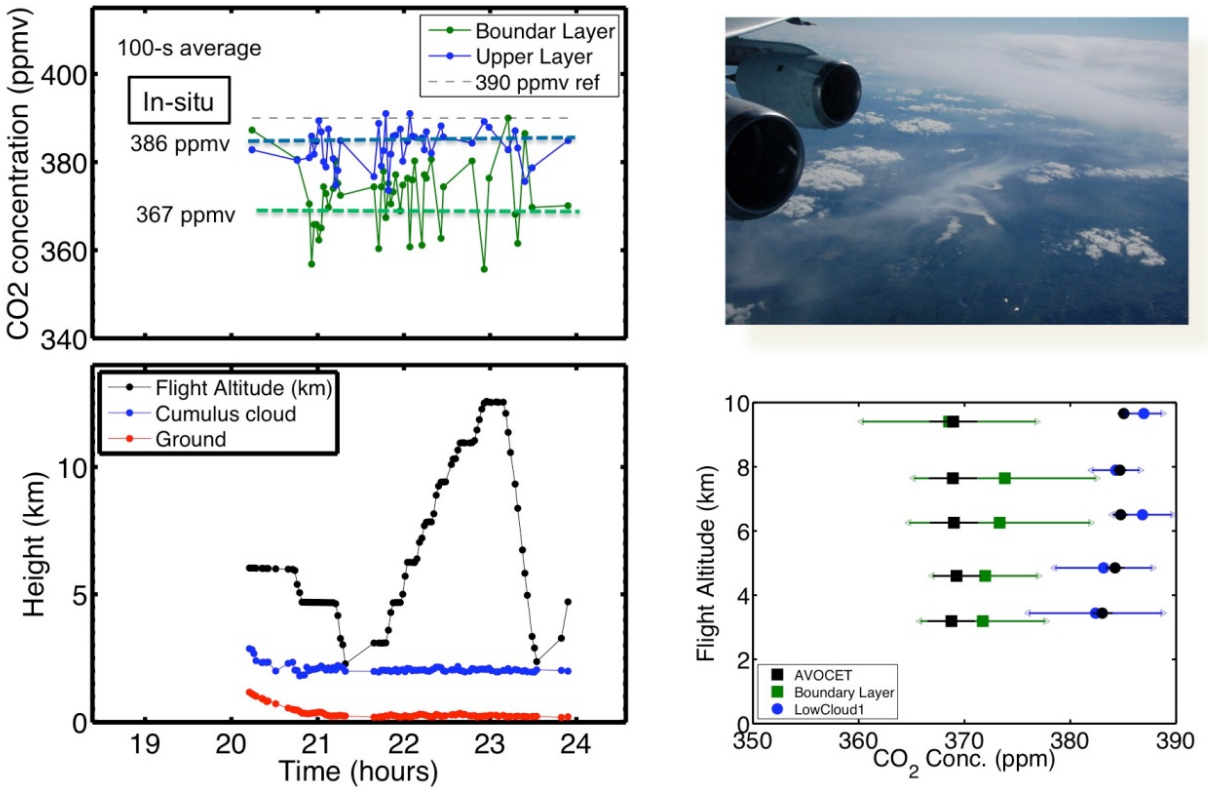

Figure 5-11 An initial example of a two-altitude level retrieval from the 2011 flight over Iowa. This demonstrated lidar measurements to the ground and to cumulus cloud tops, or "lidar cloud slicing" (Ramanathan et al., 2015). This approach separately solves for the best-fit CO_2 line shapes in the column to the ground and in the column to cloud tops, subtracts them to infer the CO_2 line shape from the ground to the cloud top, and then retrieves the CO_2 column in this lower column, which in this example was in the boundary layer. The demonstration showed the measurement worked for these flights and detected the lower concentration of CO_2 in the boundary layer. The best performance was from the highest aircraft measurement altitude of 9 km. The error bars in the retrieved boundary layer concentration are larger than those for the full column, due to its smaller CO_2 optical depth and that it is being solved for by differencing the two different column measurements.

5.3.2 Pulsed IPDA Lidar for Measurements of Atmospheric Density Using the Oxygen A-Band

In North America and most of Eurasia accurate estimates of the dry atmospheric column density can be obtained from meteorological sensors and models. However, global accuracy of these models is not sufficient to meet the ASCENDS requirements in sparsely populated areas. Since Oxygen (O_2) is a stable and uniformly mixed molecule in the atmosphere at 20.95%, the measurement of oxygen absorption can be used to infer the dry air density of CO_2 provided the water vapor mixing ratio is known or can be obtained by additional observations. Initial analysis for our approach shows that in order to keep the XCO_2 error below 1 ppm, a differential optical depth (DOD) error of ~0.2% will be needed.

Our approach uses the pulsed IPDA approach to measure the transmittance through the atmospheric column of a pair of Oxygen A-band lines at 764.7 nm, as shown in Figure 5-12. As for CO_2, our technique uses multiple wavelengths to sample these lines. For the O_2 lines we

selected, the peak of the absorption is optically thick (i.e. the optical depth is greater than 100 or the transmittance is near zero) so it is not suitable to use as an "on" wavelength. Instead, the trough between the two lines at 764.684 nm, which is not optically thick and it is sensitive to pressure changes, is used as the "on" wavelength. For the "off" wavelength we use the average OD value at the beginning and the end of our scan (764.5 and 764.9 nm respectively).

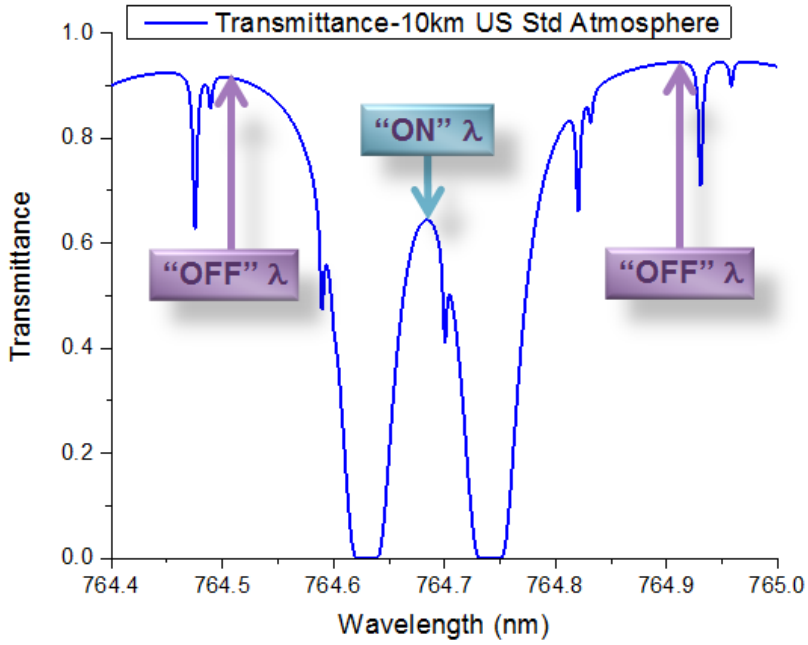

Figure 5-12 Atmospheric transmittance calculated from a 10 km altitude to the surface showing the Oxygen A-band absorption line at 764.7 nm based on a US standard atmosphere.

Our instrument (Figure 5-13) uses a continuous wave (CW) distributed feedback (DFB) diode laser operating at 1529.4 nm whose current and temperature are controlled by a commercial laser driver. The diode laser wavelength is rapidly scanned (at 250 Hertz (Hz)) over the O_2 absorptions by applying a voltage ramp waveform to the drive current. The frequency, amplitude, and shape of the wavelength scan waveform are adjusted using a computer-controlled waveform generator. The output of the diode laser is externally modulated (chopped) with a fiber-coupled acousto-optic modulator (AOM) to yield relatively short (~250 ns Full Width at Half Maximum (FWHM)) laser pulses. A master trigger, from a Global Positioning System (GPS) receiver 1 pulse per second (pps) signal, initiates a wavelength scan with a series of laser pulses separated by 100 µs (~0.011 nm) that are used to sample the oxygen absorption lines. The 100 µs time separation between pulses (equivalent to a range of 15 km) ensures that all wavelengths are sufficiently separated in time to avoid smearing due to atmospheric scattering so that only one wavelength is detected by the receiver at a time. Physically, the O_2 lidar subsystem is packaged as part of the CO_2 Sounder, shown in Figure 5.4.

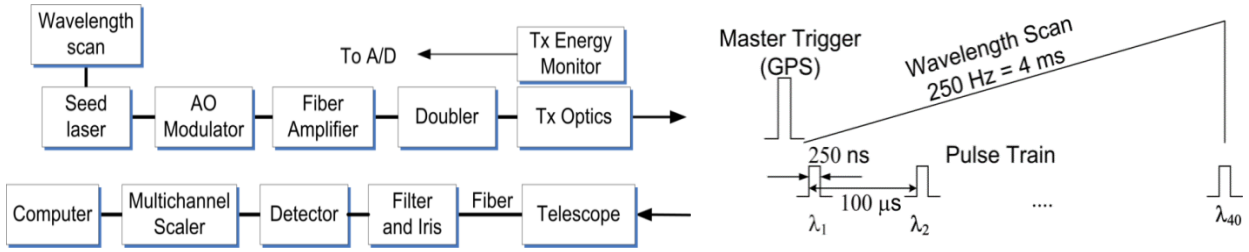

Figure 5-13 Block diagram (left) and the timing sequence (right) of the O_2 IPDA Lidar. The optical pulses from the AOM are amplified by an Erbium Doped Fiber Amplifier (EDFA) and then fiber-coupled into a periodically poled Potassium Titanyl Phosphate (KTP) crystal assembly which frequency doubles the 1529.4 nm laser radiation to 764.7 nm. The free-space output from the doubling crystal is directed to the transmit optics assembly and through the aircraft nadir port to the ground. The reflected ground returns are collected by a commercial 20 cm diameter receiver telescope and are fiber-coupled onto a single photon counting module. A multi-channel scaler produces a histogram of the return pulses as a function of time (or range) over the entire atmospheric column with a 1 second averaging time. The parameters of the airborne lidar are summarized in Table 5-7.

5.3.2.1 Airborne Campaigns and Data Analysis

We have demonstrated O_2 measurements using the multi-wavelength IPDA technique from the ground and from NASA's DC-8 airborne laboratory based in Palmdale, CA. In 2010, 2011 and 2013 we participated in a multi-instrument airborne campaign sponsored by the NASA ASCENDS program to measure CO_2 and O_2 fluxes in the United States.

Table 5-7 O_2 Sounder Lidar Parameters

Parameter	Value	Parameter	Value
Center ("on") Wavelength	764.685 nm	Histogram Bin width	32 ns
"off" wavelengths	764.5 & 764.9 nm	Divergence	110 µrad
Pulse Rate	10 kHz	Rcvr Diameter	20 cm
Pulse Width	250 ns	Rcvr Field of view	200 µrad
Energy/pulse	~2.0 µJ	Receiver band pass	0.5 nm (FWHM)
Scan rate	250 Hz	Averaging period	1 s
Wavelength Spacing	~0.011 nm		

The flights typically included multiple segments at increasing altitudes from 3 to 13.5 km over varying topography, type and atmospheric conditions. In addition, for most flights, a spiral descent from ~13.5 km to near the surface (30-70 m) was included in the flight plan in order to sample vertical profiles of meteorological parameters (pressure, temperature, humidity, etc.) using the aircraft's data acquisition system.

Our retrieval algorithm estimates the column average O_2 transmittance of the atmosphere by integrating the pulse returns from the surface return signals at each wavelength, after normalizing by the transmitted pulse energy, the filter transmission, and other instrument calibrations. The

algorithm then compares the experimental with the theoretically calculated transmittance values and adjusts the fit parameters to minimize the error. For the analysis to date, the theoretical calculations use a vertical profile of atmospheric information (measured during a flight segment or from a model) the lineshape parameters from the High Resolution Transmission (HITRAN) 2008 database (Dufour and Bréon, 2003) and line-by-line radiative transfer calculations (ESA, 2008). Although a Voigt profile was used for these calculations, recent spectroscopic studies suggest that more complex profiles and line mixing should be considered for more accurate retrievals (Mao et al., 2007; Kawa et al., 2010; Long et al., 2011).

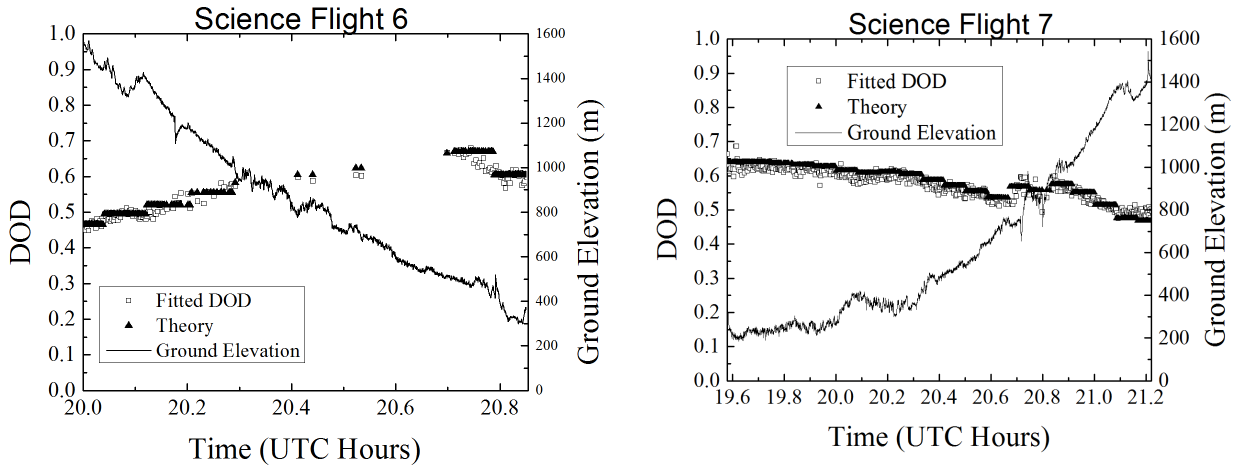

Figure 5-14 Plots of the results from the O_2 IPDA lidar flights for 2011. Flight 6 (left) and Flight 7 (right). The plots show the measured DOAD ("fitted") and those predicted DOD ("theory") along with ground elevation, as a function of time of day and hence location. The flight segments traverse approximately the region between Davenport, Iowa to Denver, Colorado where the ground elevation changes gradually. The ground elevation was calculated from the aircraft radar altimeter and the GPS readings. The predicted DOD was calculated using GMAO data with 5 minute intervals.

The range from the aircraft to the surface is determined from the laser pulse time of flight following the approach by (Amediek et al., 2013), correlating the first return pulse with the outgoing energy monitor pulse and measuring the time delay of the correlation peak. The meteorological data for the vertical profile of the atmosphere beneath the aircraft was obtained in two different ways. For flight segments near the spiral down point, it was obtained from in-situ measurements made from the aircraft. For flight segments distant from the spiral down points, our analysis used data from the Goddard Modeling and Assimilation Office (GMAO) Modern Era Retrospective –Analysis for Research and Applications (MERRA) along the flight paths with a sampling/interpolating interval of 5-minutes and using the 42 lowest atmospheric levels.

For the 2011 ASCENDS campaign, Flights 6 and 7 (from Palmdale, CA to Iowa, and from Wisconsin and back) provided the best opportunity to test the O_2 lidar measurements. The surface elevation from central Colorado to the plains of eastern Iowa changes gradually from ~1600 m to ~200 m. In the absence of significant weather that can change the local meteorological conditions, the changes in surface elevation produce a corresponding change in surface pressure. Figure 5-14 shows the DOD comparison and the ground elevation change, for the flight segment from Davenport, Iowa to Denver, Colorado for Flights 6 and 7. The agreement between the O_2 IPDA lidar measurements of optical depth and the theoretical predictions was good, and the averaged lidar measurements tracked the pressure change due to the changes in surface elevation.

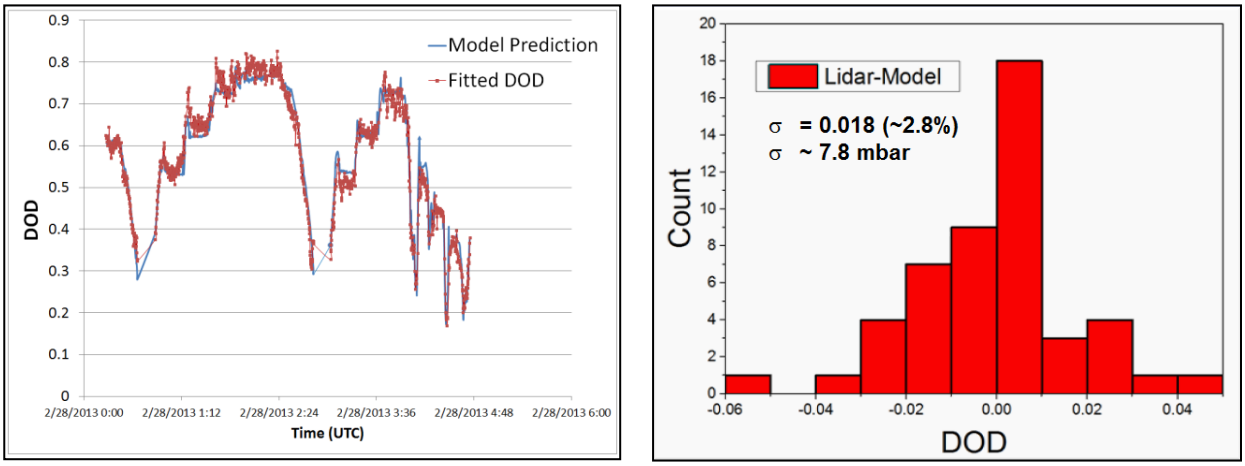

Figure 5-15 Results for the O_2 laser from the 2013 flight 2 over California's Central Valley. (Left) Plot of measured and predicted DOD versus flight time, showing they track one another over the flight altitude changes. *(Right)* The corresponding standard deviation of DOD (and pressure in the inset) for the 8 km segment of the same flight. The measurement precision is consistent with that expected from the low (~20 mW) average power laser transmitter.

During the 2013 ASCENDS campaign, Flight 2 was made over California's Central Valley. Since the meteorological conditions did not change significantly in the Valley, the atmospheric data measuring during the spiral down segment of this flight provided a good representation of the atmosphere for the entire flight. Figure 5-15 (left panel) shows the experimental and predicted DOD time series. The fitted data agreed well with predictions for all flight altitudes. Using data from the 8 km altitude segment of the flight we estimated that the standard deviation of the fitted DOD minus the model (predicted) DOD values was 2.8% that is equivalent to 7.8 mbar. This measurement precision is consistent with that expected with low (~20 mW) average power of the present O_2 lidar transmitter.

5.3.2.2 Summary

We have demonstrated airborne IPDA lidar measurements of O_2 column absorption using the Oxygen A-band at 765 nm. Measurements were made over varying surface elevations and up to altitudes of 13 km. Although this version of the lidar has significant limits in laser power, the results from several flights show good agreement between the measured differential optical depth with the theoretical predictions for aircraft altitudes from 3 to 13 km. Our primary random error sources are the low laser signal levels and the high solar background. We expect that, with a new higher power laser amplifier, we will increase the average laser power by ~10 times and reduce the random noise component by a factor of 3. We are also in the process of increasing the dynamic range of our receiver by increasing the number of Single Photon Counting Module (SPCM) detectors.

5.3.2.3 Near-Term Plans for O_2 Lidar

In work being conducted in parallel with the airborne lidar, several new components for the O_2 lidar are being developed as part of the ESTO Instrument Incubator Program (IIP)-10 program. These include new a power amplifier for the O_2 lidar, improving the O_2 detector's dynamic range, and adding analog signal recording to increase the receiver's dynamic range. The present plans are to integrate these improvements into the airborne instrument and to demonstrate them in the

summer 2014 ASCENDS flight campaigns. These new components are expected to increase the O_2 measurement precision by a factor of 3 or more.

5.3.3 Overview of the IM-CW Measurement Approach

The NASA Langley Research Center (LaRC) in collaboration with ITT Exelis, Inc. (Exelis) has been developing and testing advanced lidar technologies for application to the ASCENDS space mission. The critical aspect of these activities is the development of a prototype Intensity-Modulated Continuous-Wave (IM-CW) Laser Absorption Spectrometer (LAS) for high-precision, CO_2 column mixing ratio (XCO_2) measurements using the Integrated Path Differential Absorption (IPDA) approach. Airborne flight campaigns demonstrate that the CO_2 measurements of the current IM-CW LAS systems meet the accuracy and precision requirements of the ASCENDS mission. Also, model simulations have shown that this IM-CW LAS technology and approach can be used for the space ASCENDS mission to reach its science goals.

The first IM-CW LAS system, called the Multifunctional Fiber Laser Lidar (MFLL) and developed by Exelis (Dobbs et al., 2007, 2008; Dobler et al., 2013), demonstrated the capability of CO_2 column measurements from several aircraft under a variety of atmospheric and surface conditions (Browell et al., 2008, 2009a, 2009b, 2010, 2012; Dobler et al., 2013). More recently, MFLL has been modified to measure O_2 column amounts. O_2 column amounts are used to retrieve the surface dry-air pressure which is needed in the calculation of XCO_2 from CO_2 column amounts. Extensive demonstrations of this capability were conducted in laboratory and horizontal ground test range environments and in flight campaigns. The MFLL CO_2 column measurements over desert and vegetated surfaces are found to agree with those calculated from in-situ measurements of atmospheric meteorological and CO_2 profiles to within an average of 0.17% or ~0.65 ppmv. A measurement precision of ~0.3 ppmv for a 10-s average over these surfaces has also been achieved (Browell et al., 2009a, 2009b; Dobler et al., 2013).

5.3.3.1 Basic Characteristics of IM-CW LAS System

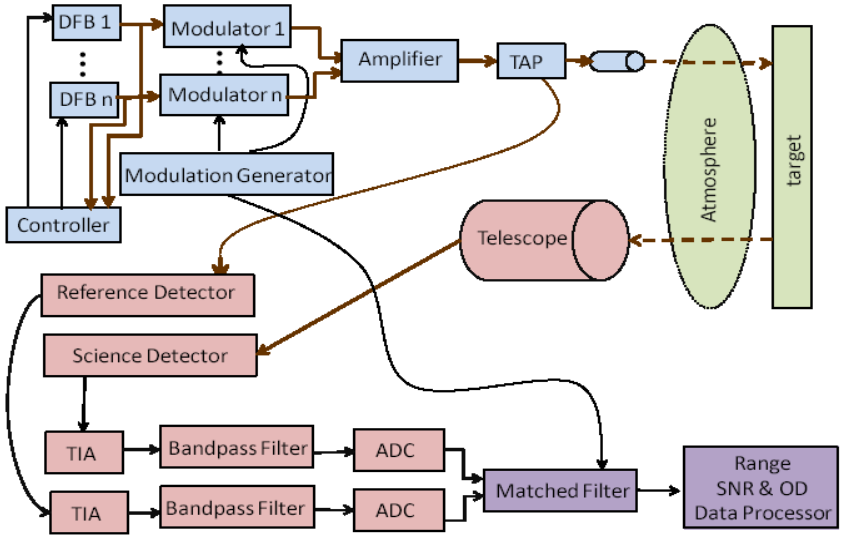

Figure 5-16 Architecture of the airborne prototype MFLL lidar.

The lidar discussed here is based on the airborne prototype LAS system, MFLL (Dobbs et al., 2007, 2008; Dobler et al., 2013; Lin et al., 2013). Figure 5-16 shows the lidar design.

The LAS system incorporates CO_2 and O_2 laser transmitters, a receiving telescope, a data acquisition system, and a signal-processing unit. The CO_2 and O_2 subsystems are all similar in form and function except they use a 5-W Erbium-Doped Fiber Amplifier (EDFA) and a 1.6-W fiber Raman amplifier (Dobler et al., 2011), respectively. The CO_2 subsystem has one laser wavelength positioned at the center of the CO_2 absorption line at 1571.112 nm ("online") and two other laser wavelengths in the distant wings of the absorption line at offsets of ±50 pm ("offlines") for the CO_2 IPDA measurements, as shown in Figure 5-17. Additional lasers operating at an online of 1262.531 nm and an offline of 1262.578 nm are used for O_2 IPDA measurements. All the CO_2 and O_2 wavelengths were selected to minimize water vapor and other trace gas interference effects on the IPDA measurements and to simultaneously maximize the signal-to-noise ratio (SNR) of the differential absorption optical depth (DAOD) measurements (Ismail and Browell, 1989; Remsberg and Gordley, 1978). Other major considerations in the laser line selection include the altitude-dependent gas absorption weighting function; the DAOD sensitivity to knowledge of the laser wavelength and line-width; and the wavelength stability of the laser spectra (Menzies and Tratt, 2003; Ehret et al., 2008; Kameyama et al., 2010; Lin et al., 2013).

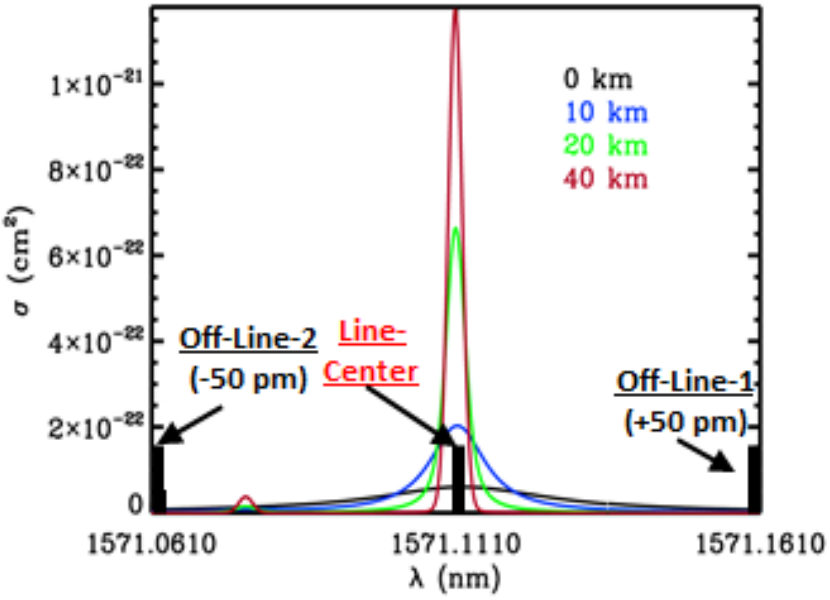

Figure 5-17 The wavelength sampling approach for the airborne MFLL lidar and the altitude dependence of the CO_2 absorption cross section (σ).

An essential capability to achieve high accuracy XCO_2 measurements is to apply a range-encoded intensity-modulation technique to the IM-CW lidar system for CO_2 and O_2 column measurements and range determination. The use of range encoding with a phase sensitive detection subsystem clearly discriminates the magnitude and timing/range of laser signals reflected from surface against those from other intermediate backscatters. A commonly used technique in the detection subsystem for the signal discrimination is a matched filter that correlates the range-encoded modulation waveforms with the recorded signals. Figure 5-18 illustrates the modeled capability of a range-encoded IM system using a swept frequency technique with three measurement channels. The illustration is for an idealized case of a target at 12-km range with an intermediate backscatterer at 6 km to represent the presence of a cloud/aerosol layer. Fractional intensity units

are used as the return power is normalized by the output power. The DC components for all signals were removed after the detector. The sampling rate, swept frequency bandwidth of the IM waveform, and unambiguous range (UR) are set to be 2 MHz, 500 KHz and 15 km, respectively, which are consistent with current airborne systems. The sampling rate and UR lead to a 75-m range per sample and 200 samples per IM cycle, respectively. Although the range sampling rate is 75 m, considerably smaller range errors of about 3 m can be achieved by applying curve-fitting techniques to the shape of correlation power of the matched filter outputs. The IM bandwidth dictates the sharpness of the main-lobe peaks of the correlation power of the matched filter.

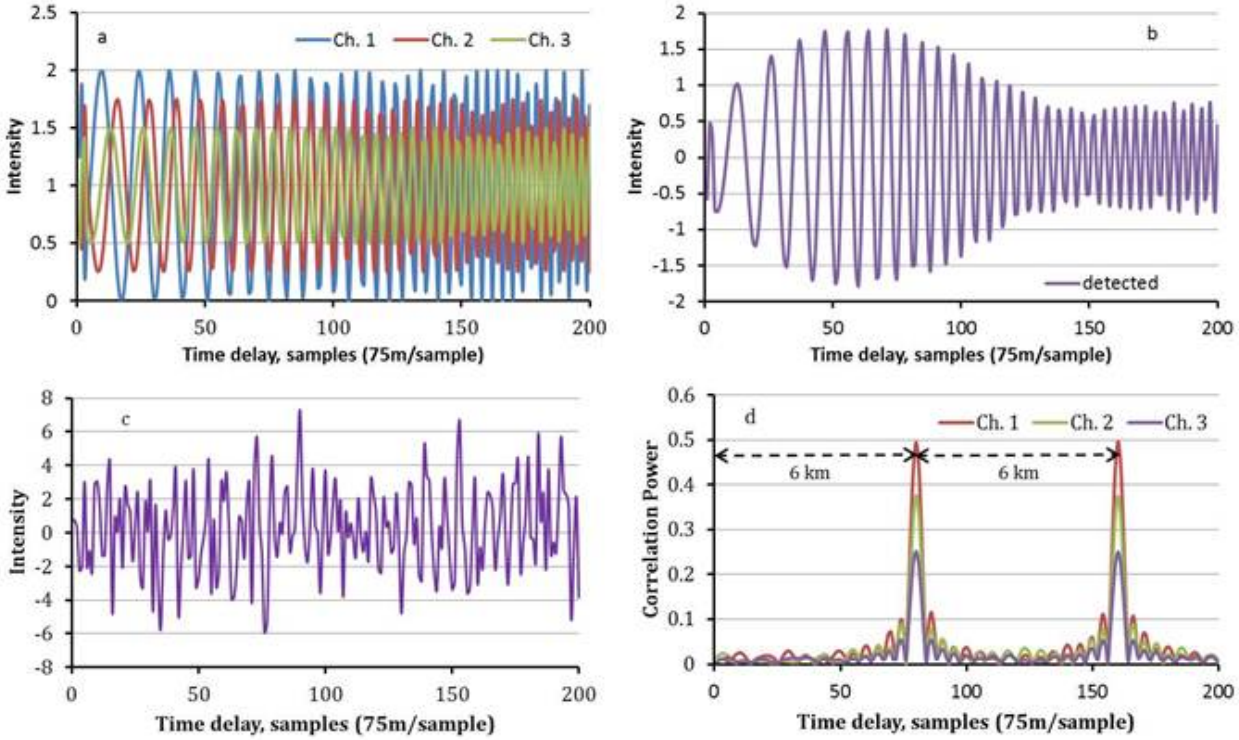

Figure 5-18 Sample laser signals detected by the airborne MFLL lidar.

In Figure 5-18, Panel A shows the individual laser signals that are combined to yield the modulated signal shown in panel b. The beat frequencies among the three channels are clearly shown in the variations of the signal power with the time delay due to the IM scheme used. The detector receives the combined signal, including noise, and this is then passed through an electronic bandpass filter to reduce background noise and to avoid spectral aliasing. The bandpass filter also removes the DC component of the signal. To show the importance of intermediate scatterers, the received signal power from the intermediate scatterer is assumed to be equal to that of the target, and the noise level is as high as the return signal power from both scatterers. Compared to candidate IM waveforms (panels a & b), the signature of the received signal (panel c) appears be very weak due to 3 channel signal mixing, a combination of signals from target and intermediate backscatter with different time delays, and noises. Even in this case, the matched filter technique with 0.1-s integration period clearly demonstrates the capabilities of detecting weak target signals and minimizing the effects of intermediate scatterers and noise. The outputs of the matched filter show two distinct correlation peaks corresponding the target and intermediate scatterer (panel d). The wider the IM bandwidth, the narrower the peaks and the easier it is to differentiate between two closely spaced scattering objects. Besides the detection of

target signals, panel d also illustrates that the target range can be estimated by measuring the time delay of the peak power of the target or intermediate reflection. The range capability and CO_2 column measurements to both surface and cloud tops under cloudy conditions are clearly illustrated by this figure.

The panels show: a) Range-encoded lidar signals from the target without noises for individual channels coming onto detector; b) The intensity modulated lidar signals of the three channels produce a single time series at the detector; c) Recorded lidar return, which is a combination of lidar signals from the target and intermediate backscatterer as well as of all noises; d) Lidar signal power as a function of range obtained by the correlation of the matched filter of lidar system.

A photograph of the MFLL lidar onboard the NASA DC-8 aircraft is shown in Figure 5-19. The onboard data processing and onboard display unit, detection system, and CO_2 transmitter subsystems are in the front while the O_2 subsystems are in the two racks in the back. The telescope and transmit optics are housed under the black laser curtain in the middle. Table 5-8 lists the key parameters of the lidar system. The CO_2 and O_2 subsystems of the LAS have been implemented using similar IM-CW techniques that include both sine wave and rolling tone frequencies, and more recently a swept frequency IM approach. The swept frequency IM provides ranging and capabilities to discriminate clouds and aerosols. After the receiver and data acquisition subsystems record lidar return signals, a matched filter that correlates the transmitted IM waveforms with the received IM waveforms reflected from the surface and clouds. The location and magnitude of correlation peak power values are estimated from the matched filter output. The peak magnitudes of individual channels are proportional to the powers received for their corresponding channels and used in the retrievals of CO_2 and O_2 column amounts. Thus, they lead to the calculation of the two DAOD values, while the location of the peaks and shape of the entire correlation functions are used to determine the range. From flight campaign and range testing, the accuracy and precision of the calculated range was found to be better than 3 m (Dobler et al., 2013; Lin et al., 2013) that is equivalent to a XCO_2 error of about 0.12 ppmv. Details on the instrument and data processing can be found in Dobler et al. (2013) and Lin et al. (2013).

Figure 5-19 Photograph of the MFLL lidar mounted inside the NASA DC-8 aircraft.

Table 5-8 Airborne MFLL Lidar Parameters

Airborne MFLL Lidar Parameters	
Seed laser type:	DFB diode laser
Line width	< 6 MHz each wavelength
Side mode suppression	Ratio > 45 dB
CO_2 lines: (vacuum)	1.571112 μm (On), 1.571061 μm (Off 1), 1.571161 μm (Off 2)
O_2 lines: (vacuum)	1.262531 μm (On), 1.262578 μm (Off)
Modulator:	Semiconductor Optical Amplifier
Modulation type:	Intensity-modulated continuous-wave (IM-CW)
Optical amplifier:	CO_2: EDFA, O_2: Raman Amplifier
Output power:	5 Watts for CO_2 ; 1.6 Watts for O_2
Optical bandpass filter:	2.4 nm
Telescope	Cassegrain, 8 in. diameter.
Receiver optical throughput	8.5%
Detectors	DRS; HgCdTe APD gain: ~940; Excess noise factor ~1.3, 77 K as operated
Transimpedance amplifier	Gain: 10^6
Sample rate of digitizer	2 MHz
Encoding scheme:	Swept-frequency; ~350 ± 250 KHz; Rolling tone; ~50 ± 3 KHz
Max unambiguous range:	15-km (or 200 samples); 30-km (or 400 samples)
Laser divergence angle:	190 urad (half angle)
Receiver FOV:	240 urad (half angle)
Receiver duty cycle:	100%
Reporting interval:	100 msec (10 Hz)

5.3.3.2 Approach for Determining CO_2 Column Differential Absorption Optical Depth

To evaluate the accuracy and precision of the MFLL remotely-sensed CO_2 column measurements, actual CO_2 DAOD values are needed. These DAOD values are derived based on the knowledge

of the in-situ observed vertical profiles of XCO_2 and meteorological conditions; the altitude- and meteorologically-dependent spectroscopy of CO_2 and interfering gases, such as water vapor; the path length from the aircraft to the surface; and the off-nadir pointing of the laser beam (Browell et al., 2008, 2009, 2010, 2012; Dobler et al., 2013; Lin et al., 2013). High-quality in-situ measurements of XCO_2 (Choi et al., 2008; Vay et al., 2003), temperature (T), pressure (P), and relative humidity (q) profiles and other meteorological conditions were obtained from onboard instruments during aircraft spirals and collocated with contemporaneous radiosonde launches. A laser altimeter was also included as a part of the MFLL suite of subsystems to make an independent measurement of the range to the surface or cloud tops. A GPS receiver and the aircraft navigation system provided additional aircraft location including altitude and attitude information. Comparisons of MFLL and in-situ-derived DAOD values were typically limited to a horizontal distance of less than 10 km of the aircraft spiral and radiosonde comparison locations. When multiple in-situ spirals were conducted during a flight, the spiral data corresponding to the closest MFLL overpass time was used.

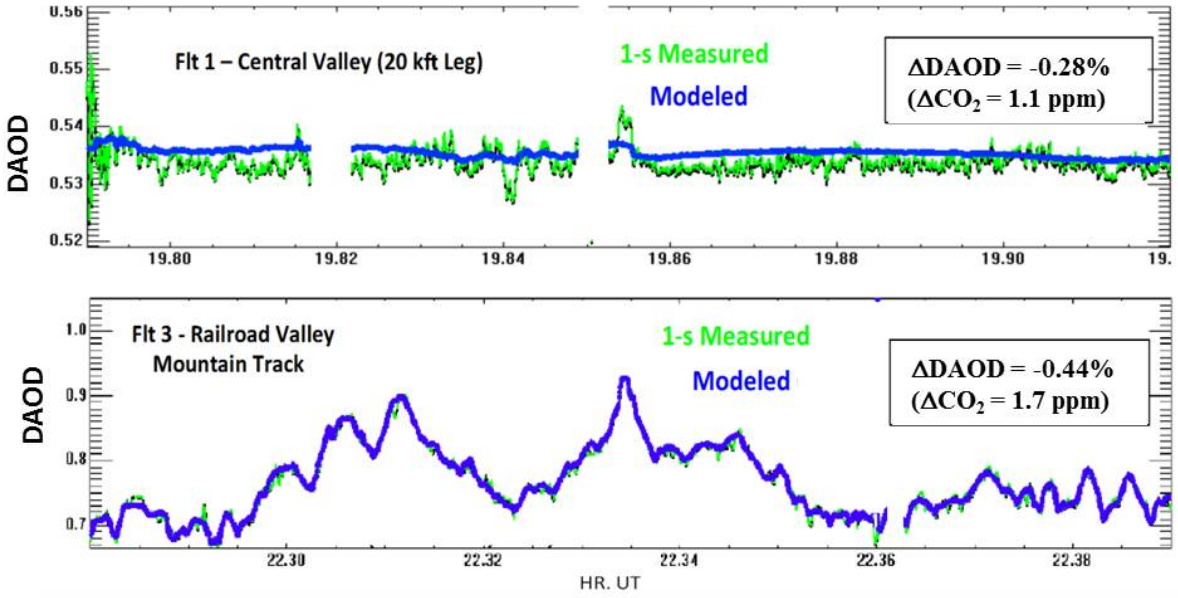

Figure 5-20 Comparison of airborne measured and modeled CO_2 DAODs. The figure shows flights over California's Central Valley (top) and the Rocky Mountains (bottom) in route to Railroad Valley, NV.

5.3.3.3 Airborne CO_2 Column Measurements

The LaRC ASCENDS team conducted a total of 13 flight campaigns with various aircraft such as NASA UC-12 and DC-8 since May 2005 to evaluate the capability in making remote CO_2 and XCO_2 column measurements for the ASCENDS mission. Accurate CO_2 column measurements have been demonstrated by these comprehensive aircraft flight tests. For example, 1-s averaged CO_2 column measurements over desert regions resulted in high precision measurements with SNR of DAOD (SNR_{DAOD}) higher than 600 (Browell et al., 2012; Dobler et al., 2013). Figure 5-20 shows two comparison examples of 1-s MFLL CO_2 DAOD measurements and in-situ-derived (modeled) values in drastically different geographic regions.

The top panel of Figure 5-20 shows the CO_2 measurements on a constant altitude flight leg over the Central Valley, CA in comparison to modeled DAOD values derived from in-situ CO_2 data of a DC-8 spiral at the center of the leg and radiosonde data obtained within about 1 hour of the

over-flight. The small variations in the in-situ-derived (i.e., modeled) DAOD across the flight leg were due to small changes in the range from the aircraft to the surface. The resulting difference of 1-s averages between the measured and modeled DAOD values on the Central Valley flight leg was found to be -0.28% or the equivalent of ~1.1 ppmv. The bottom panel shows the DAOD comparison while transiting across the Rocky Mountains. The in-situ data (spiral and radiosonde) came from Railroad Valley, NV, and the variation in DAOD values across the mountains was almost entirely due to surface elevation changes as the aircraft was at a constant altitude. The comparison of 1-s measured and modeled DAOD values demonstrated a high level of agreement (ΔDAOD = -0.44% or ~1.7 ppmv) even when one expects some change in CO_2 across the mountains that could not be captured in the modeled DAOD due to the lack of in-situ data. Flight tests of the current LAS instrument have demonstrated very high-precision CO_2 DAOD measurements (SNR_{DAOD} >1300) with a 10-s averaging interval (Browell et al., 2012; Dobler et al., 2013).

5.3.3.4 Surface Reflectance, Thin Cloud Discrimination, and Range Measurements

Since variations in surface types and reflectance can significantly affect lidar return powers and thus CO_2 column retrievals, different surface conditions were analyzed from MFLL flight data. For farm fields and deserts, moderate to high reflectance values were observed, and strong signals for CO_2 column retrievals were received. For some surfaces especially snow, ice, and rough water surfaces, very low reflectance was expected and was observed. From MFLL data, the measured surface reflectance of snow and ice was as low as about 0.02/sr. Fresh snow (less than 1-2 days old) was found to have even significantly lower reflectance (about ~ 0.01/sr). Even in these low reflectance cases, MFLL received enough backscattered signal for CO_2 column retrievals from high altitude flight legs. The variability in the surface reflectance for complete snow covered terrain was found to be relatively homogeneous, however the magnitude of the surface reflectivity for both snow covered mountainous and farmland terrain was observed to vary by more than an order of magnitude over distances of less than 10-20 meters from the nominal snow and ice surface reflectance values.

In addition to surface types, the presence of thin clouds and aerosol layers are an important factor that can affect the accuracy of CO_2 and O_2 column measurements. The capability for discrimination of cloud returns from ground returns is achieved using the swept frequency IM-CW approach as shown in Figure 5-21. The data were obtained from the DC-8 flight on 04 August 2011 over Railroad Valley, NV. Distinct altitudes and reflectances of the surface and clouds were clearly derived from the swept-frequency measurements. The presence of intermediate thin clouds and aerosols will definitely reduce the lidar return signals and likewise reduce the precision of CO_2 column estimates, but the CO_2 measurements will still satisfy the mission requirements when cloud attenuation scaling is considered (c.f., Section 1.2, R-3; Lin et al. 2013). Ranging accuracies of about 3 m for these surfaces and clouds have also been achieved (Dobler et al. 2013; Lin et al. 2013).

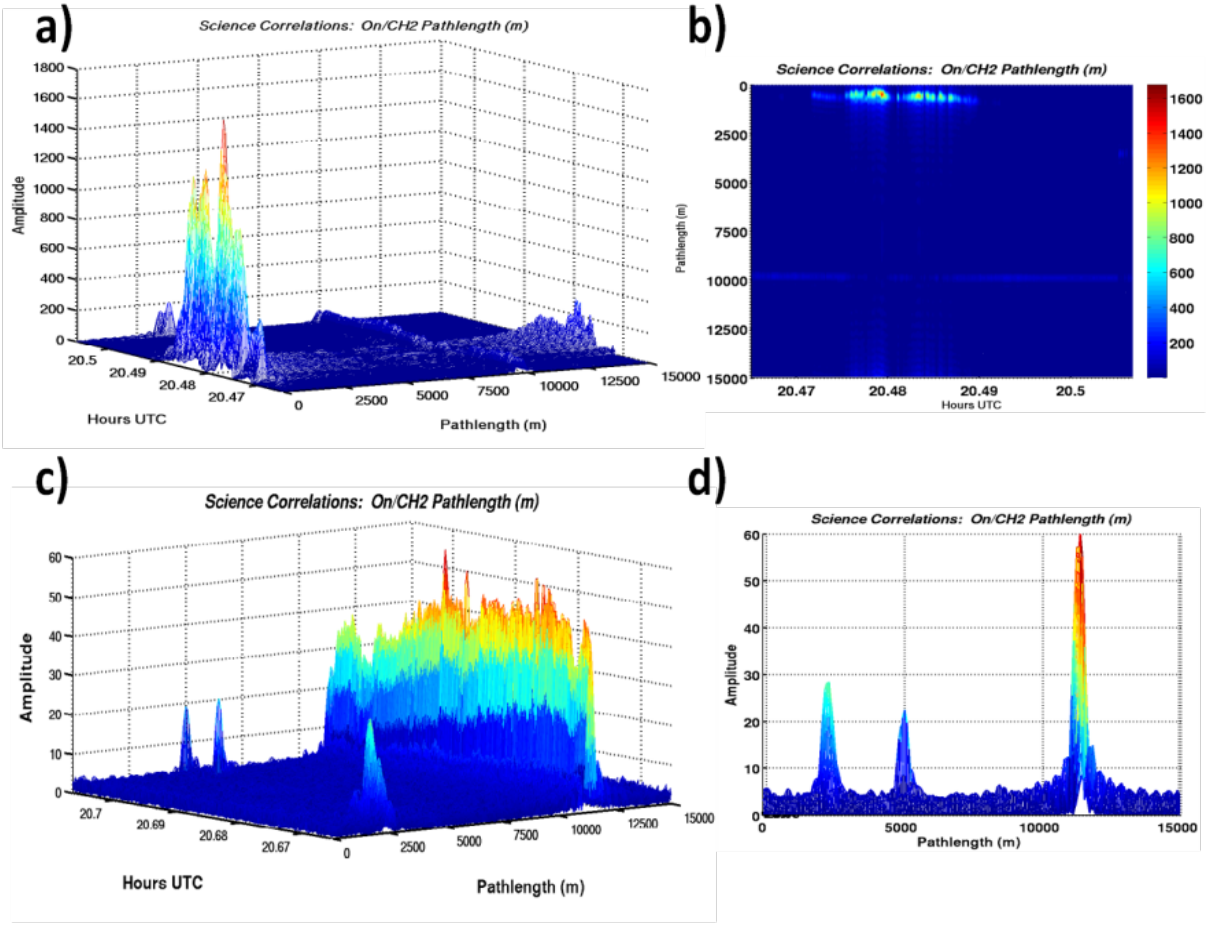

Figure 5-21 Range discrimination of cloud returns from ground returns using the swept frequency IM-CW approach.

Panels a) and b) show 3-D and 2-D, respectively, representation of a large cloud return above a small ground return; panel c) shows the distribution of signals from weak clouds and strong ground return signals, and panel d) is a superposition of data from c) on a signal vs. path length.

5.3.3.5 Airborne O_2 Column Measurements

The capability to measure O_2 column amounts was added to MFLL for the 2011 flight campaign. O_2 column amounts are needed to determine surface dry air pressure and then to calculate XCO_2 from CO_2 column amounts. The spectral lines in the 1.26-μm O_2 absorption band are selected for IPDA measurements of O_2 column. The O_2 IPDA lidar operates with the same IM-CW LAS approach as the CO_2 instrument on the MFLL. The major difference is that the O_2 lidar uses a low-power 1.6-W fiber Raman amplifier rather than an EDFA to amplify the combined O_2 on-line and off-line laser signals at 1.26 μm before transmission. Figure 5-22 shows the placement of on-line and off-line laser beams transmitted with respect to the O_2 absorption lines used in the MFLL IPDA O_2 measurements. The key line parameters of the 1.26 μm O_2 absorption lines are summarized in Table 5-9.

The 2011 flight campaign provided the proof of concept demonstration of the O_2 lidar subsystem and utilized a standard PIN diode as the detector. The low gain of the PIN detector and low transmitted power at the O_2 wavelengths resulted in lower O_2 SNR_{DAOD} than that for CO_2

SNR_{DAOD} during the same measurement period. The PIN detector was replaced by the DRS HgCdTe APD detector cited in Table 5-8 during the March 2013 DC-8 flight campaign. A rolling tone modulation scheme was used for O_2 transmitted laser beams during the 2011 campaigns. This modulation scheme had four discrete frequencies in the 50-kHz region and allowed independent detection and discrimination of the O_2 on-line and off-line backscatter signals. During the 2013 campaign, the swept frequency IM scheme was used. Besides the CO_2 and O_2 lidars, a Pseudorandom Noise (PN) code laser altimeter was used during the flight campaigns to determine the reference range to compare to the swept-frequency-derived range.

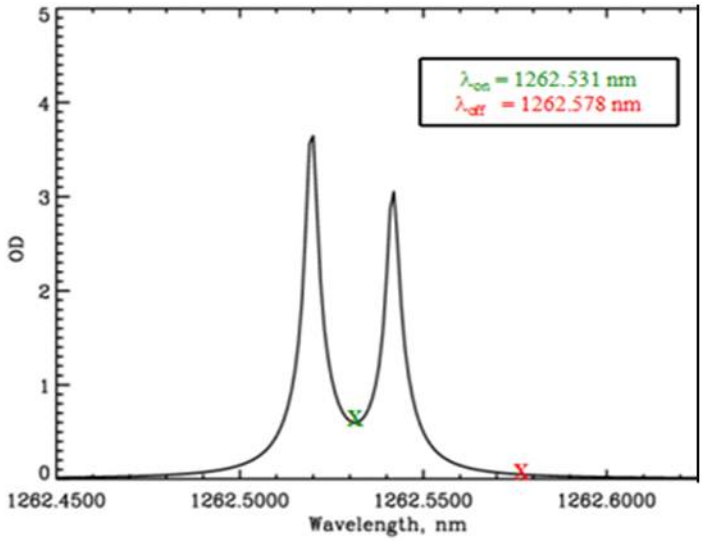

Figure 5-22 Calculated spectral profile of the O_2 absorption line doublet at 1262.52195 and 1262.5416 nm (c.f., Table 5-9) and the spectral locations of the on- and off-line laser beams.

The plotted values represent the vertically integrated optical depth (OD) of the O_2 absorption lines.

Table 5-9 Line parameters of the O_2 absorption lines

	Line center (μm)	ID	Line strength (cm/mol.)	Linewidth (cm^{-1})	Energy of lower state (E") (cm^{-1})
O_2 (1)	1.2625195	RQ5	4.99E-26	0.047	260.50
O_2 (2)	1.2625416	SR5	4.63E-26	0.052	42.224

Figure 5-23 shows a rapid spectral scan of the O_2 doublet measured from 6-km altitude on 7 August 2011 with approximately the same spectral coverage as the O_2 doublet spectra shown in Figure 5-22. It illustrates the ability to tune across the absorption feature resulting from the O_2 absorption lines with high spectral resolution (Browell et al., 2012). Column O_2 optical depths were calculated using the IPDA approach, and Figure 5-24 shows the variation of O_2 SNR_{DAOD} as a function of range to the surface. The data with diamond points in Figure 5-24 were collected on two flights (27 July, 20011 and 3 August, 2011) that each operated from several altitudes. No background subtraction was included in the calculations, but the data were screened to remove

cloudy regions. The 10-s O_2 SNR_{DAOD} values were estimated using the 10-Hz O_2 SNR_{DAOD} statistics.

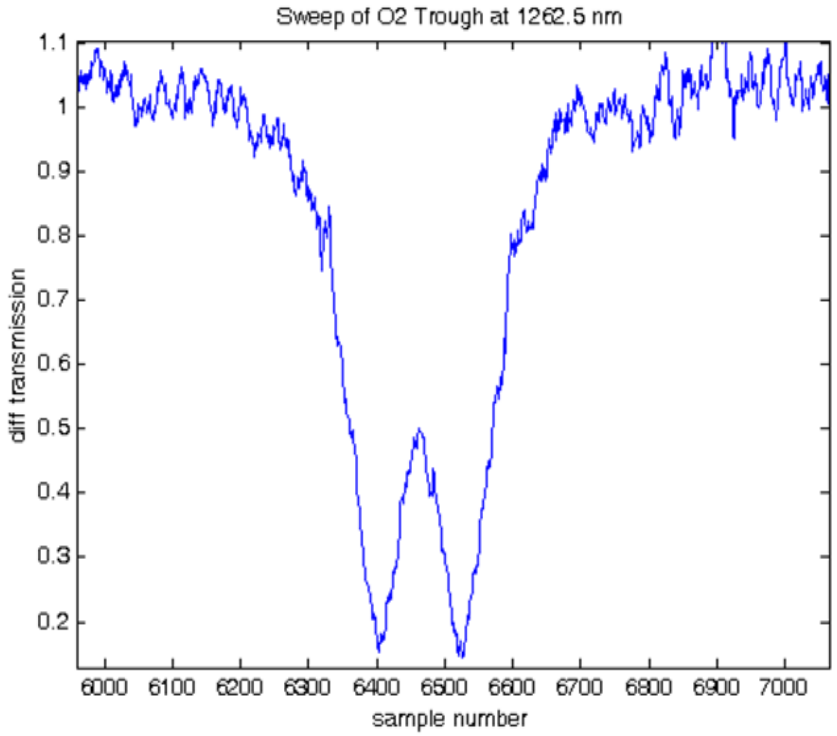

Figure 5-23 A lidar spectral sweep across the O_2 doublet from 6 km altitude on 7 August 2011.

Figure 5-24 shows that the O_2 SNR_{DAOD} varied as the inverse of the range squared, as expected from shot noise limited performance, in the presence of daytime background. Initial analysis of the measurements from the March 2013 flight campaign shows significant improvement in O_2 SNR_{DAOD} as shown by the triangle data points in Figure 5-24. These data were collected from several altitude levels in a single flight on 26 March 2013 over similar terrain as that of the 2011 data. More than an order of magnitude improvement in SNR over long ranges (6-12 km) has been found. This improvement is the result of the incorporation of the DRS HqCdTe detector in place of the PIN diode detector used in the 2011 campaign. This demonstrates the capability of airborne retrieval of O_2 column amounts in the presence of high solar background conditions. Figure 5-25 shows a comparison between the measured and in-situ derived column O_2 DAOD to the surface from a range of about 3.5 km (Browell et al., 2012). These data were taken from a flight to Castle, CA on 27 July 2011. In situ measurements were used within 10 km of the MFLL DAOD measurement region. A 10-s signal averaging was done prior to DAOD calculation, and in-situ derived DAODs were calculated using a procedure similar to that for the CO_2 DAODs. The 1-standard deviation difference between the in situ and measured DAODs was 1.26% and the average difference of the DAODs was < 0.5% (Browell et al., 2012). These measurements show an encouraging result that an O_2 SNR_{DAOD} of 700 or higher can be achieved by the technology development.

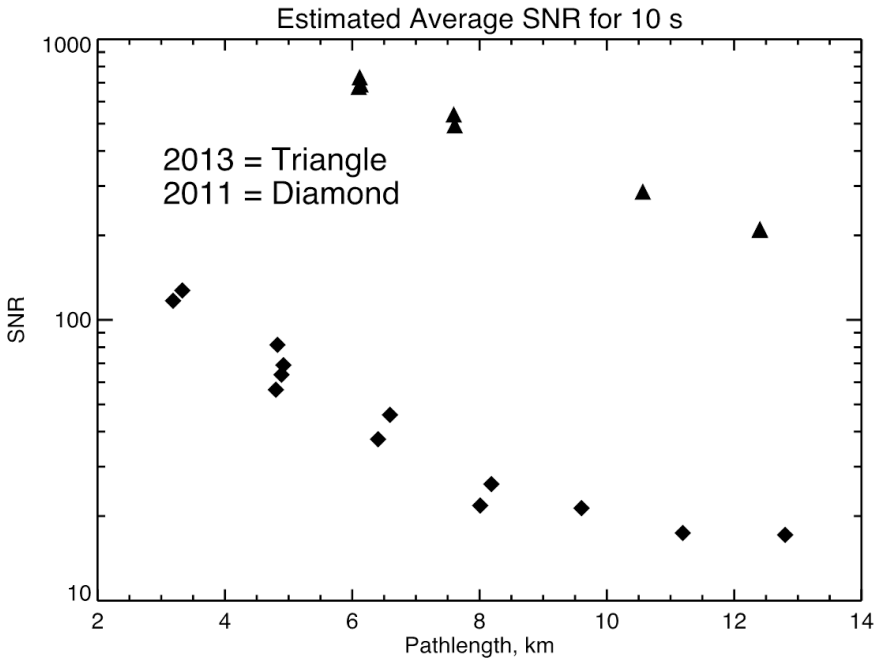

Figure 5-24 Variation of SNR in the measurements of O_2 SNR_{DAOD} with range from the DC-8 on 27 July and 3 August 2011(diamonds) compared with measurements from the 26 March 2013 flight with an improved detector (triangles).

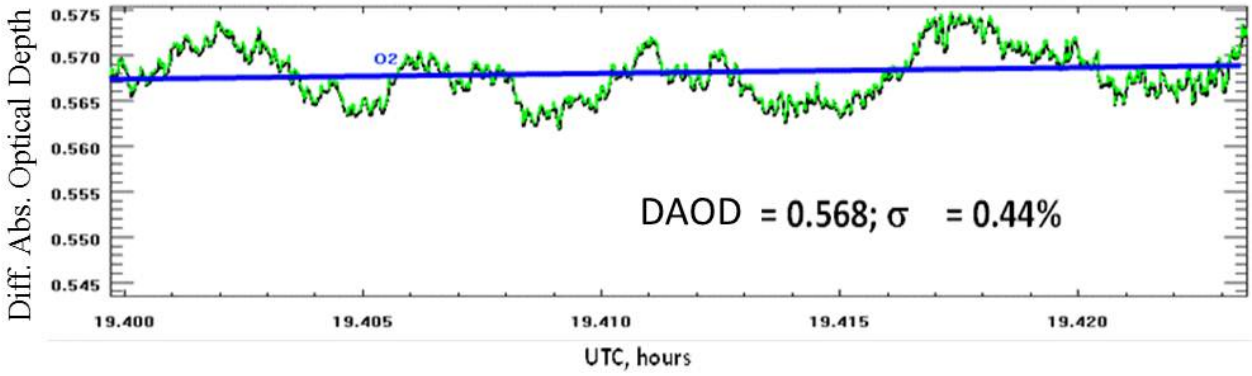

Figure 5-25 Comparison of measured and in-situ derived O_2 DAOD from the DC-8 on 27 July 2011. Measured values (green line) and in-situ derived values (blue line) are plotted. It illustrates high precision measurements of O_2 DAODs.

5.3.3.6 Laboratory and Ground-Based Measurements

Many efforts have been made for the demonstration of the IM-CW IPDA approach and towards the development of technologies for a future space-based LAS system. In a typical example, the LaRC team conducted a comprehensive MFLL ground test on an 860-m horizontal test range at NASA LaRC during July-August 2012 (Lin et al. 2013). Several surface targets covering a wide range of reflection were tested and calibrated using standard diffuse reflectance products. Very good agreement between model predictions and LAS signal measurements for the tested albedos was obtained, which significantly enhances the scaling and evaluation capabilities for space missions (Lin et al. 2013).

5.3.3.7 Near-term Plans

The key areas for the LaRC team near-term measurement development and demonstration plan include maturing low-mass, high-power high-efficiency lasers, optical receiver subsystems, and electronics required for the ASCENDS space mission via the ASCENDS CarbonHawk Experiment Simulator (ACES; Obland et al., 2012, 2013) program and further demonstrating the capabilities of CO_2 column measurements in various environmental conditions. The LaRC team conducted ACES ground tests at LaRC's lidar test range in April 2014 with flight tests in July 2014. Initial results are very encouraging because of significantly increased transmitted power. Additional flight tests are planned for August 2015 to further demonstrate the CO_2 column measurement capability of the ACES instrument. The LaRC team is close to achieving the laser power required for the space mission through the ACES program and has developed an achievable path to meet the ASCENDS mission requirements on the relevant time scale. A DC-8 flight campaign for making measurements of CO_2 drawdown over cornfields was conducted during summer 2014 and flights to examine CO_2 during the cold season are planned during winter 2016. CO_2 column measurements over snow and ice surfaces will be analyzed extensively from existing and future flight data. The CO_2 measurement accuracy and precision over low reflectance rough ocean surfaces and the length of integration period to increase SNR_{DAOD} to required level will be tested through open ocean flight campaigns. The accuracy and systematic errors in the retrievals of CO_2 column amounts from low and high thin clouds will be further assessed using summer 2011, winter 2013 and future flight campaign data sets.

The cloud slicing technique, which is enabled by the ranging-encoded lidar approach, such as the swept-frequency IM-CW, will be investigated from various airborne data sets. This should provide the capability to determine CO_2 columns across both the free troposphere and the planetary boundary layer. Further improvements on the atmospheric slicing capability will be achieved by using sideline wavelengths that are considered for space applications (Lin et al., 2013) because of the differences in atmospheric weighting functions. Furthermore, advanced lidar intensity modulation algorithms that eliminate cloud impacts on lidar surface returns when clouds are very close to the surface are developed (Campbell et al., 2013) and will be tested. Along with these efforts, modeling of LAS atmospheric CO_2 column measurements is also a key part of the measurement development and demonstration plan (Lin et al., 2013).

5.3.4 CO_2 Laser Absorption Spectrometer (LAS)

A team at JPL developed an airborne CO_2 Laser Absorption Spectrometer (JPL CO_2LAS) in the 2002-2006 time frame to demonstrate the airborne IPDA lidar technique as a stepping stone to an Earth-orbiting capability for global-scale measurements of CO_2 concentrations. The first airborne measurements were conducted in summer, 2006 on a Twin Otter aircraft. The JPL CO_2LAS has flown on the NASA DC-8 since summer, 2010. This instrument utilizes the 2.05μm CO_2 band, which has a band-strength nearly an order of magnitude larger than the 1.57 μm band. This enables probing CO_2 at frequencies suitably displaced from line center such that the IPDA measurement preferentially weights the lower tropospheric CO_2 molecules, while maintaining a differential absorption optical depth (DAOD) at its optimum value for maximizing the DAOD signal (Bruneau et al., 2006) and simultaneously minimizing the impacts of sources of bias. The instrument uses a heterodyne detection receiver, which provides optimum photon detection efficiency.

5.3.4.1 JPL CO_2 LAS Instrument Description and Data Processing

The CO_2 LAS instrument developed jointly by JPL and Coherent Technologies, Inc. (later Lockheed Martin Coherent Technologies) (Spiers et al., 2002; Spiers et al., 2011a) consists of five key subsystems: (1) the optical assembly, (2) the control electronics unit, (3) the control software unit, (4) the thermal management assembly, and (5) the signal processing / data acquisition electronics. In operation, the optical assembly is completely autonomous, no adjustments are required. The optics alignment has not been adjusted since the instrument integration and tested in 2004.

The CO_2 LAS transceiver approach utilizes heterodyne detection, implementing a narrow bandwidth receiver, with frequency-stabilized narrow-linewidth laser transmitters and local oscillators. The lasers are diode-pumped Tm/Ho-doped YLF crystal lasers (McGuckin and Menzies, 1992), that emit in the 2.05 μm spectral region. The transceiver consists of two separate transmit/receive channels for the on-line and off-line measurements. The off-axis beam expanding telescopes for each channel are identical in size and configuration. The transmitter frequencies are stabilized with respect to a selected CO_2 absorption line. Each channel has a dedicated heterodyne detector, and a continuous-wave (cw) single frequency laser which acts both as the transmit laser and the local oscillator for heterodyne detection of the return signal. The transceiver also includes a separate low-power cw laser that provides a reference for frequency offset-locking of the on-line and off-line lasers.

A comprehensive study of candidate CO_2 absorption lines was conducted considering (1) minimizing interference from water vapor lines, (2) minimizing susceptibility to atmospheric temperature profile uncertainty, (3) optimizing line strength (Menzies and Tratt, 2003). The R(30) line of the (2001)III $\leftarrow$ (0000) band, with line center at 4875.749 cm^{-1}, was selected based on this evaluation. The choice of R(30) as the optimum line in the 2.05-μm band has been validated in recent more comprehensive wavelength optimization studies (Caron and Durand, 2009). The instrument contains an onboard low pressure CO_2 gas absorption cell for locking the reference laser to the CO_2 R(30) line. The on-line laser is tunable over a range of several GHz with respect to the fixed reference laser frequency. A few mW from the on-line laser is tapped off to act as the local oscillator (LO) for heterodyne detection of the return on-line signal.) The offline laser channel configuration is similar.

Offset locking is accomplished using wide-band photomixers that monitor the beat frequencies between the outputs of the on-line and off-line lasers with respect to the reference laser. Dating from the time of first integrated performance tests, the on-line and off-line lasers have been tuned to the same offset frequencies with respect to the CO_2 R(30) line center, namely +4.00 GHz and -15.72 GHz respectively.

A frequency offset is required between the return signals and their corresponding local oscillators for heterodyne detection. By pointing the transmit beams at a known offset from nadir, the return signals are Doppler shifted by the aircraft velocity, eliminating the need for a frequency shifting device in the instrument. The aircraft pitch angle adds to the fixed off-nadir pointing angle and is taken into account both in mounting hardware and retrieval software.

The transceiver assembly is mounted to a 2-sided optical bench, with custom-designed mounts for the optical components. This optical bench is edge-mounted to a base plate, as pictured in Figure 5-26. In operational configuration, the optical bench is in a near-vertical plane, and a cover is fastened to the base plate. Thus the assembly is contained within an enclosure with electrical

feed-throughs and optical windows. (See Figure 5-27.) The baseplate/enclosure assembly includes vibration isolation. With the cover in place, the transceiver subsystem is ready to be mounted to an aircraft interface frame. In the DC-8, it is mounted in the rear cargo bay.

The key airborne LAS instrument parameters are summarized in Table 5-10 below**.**

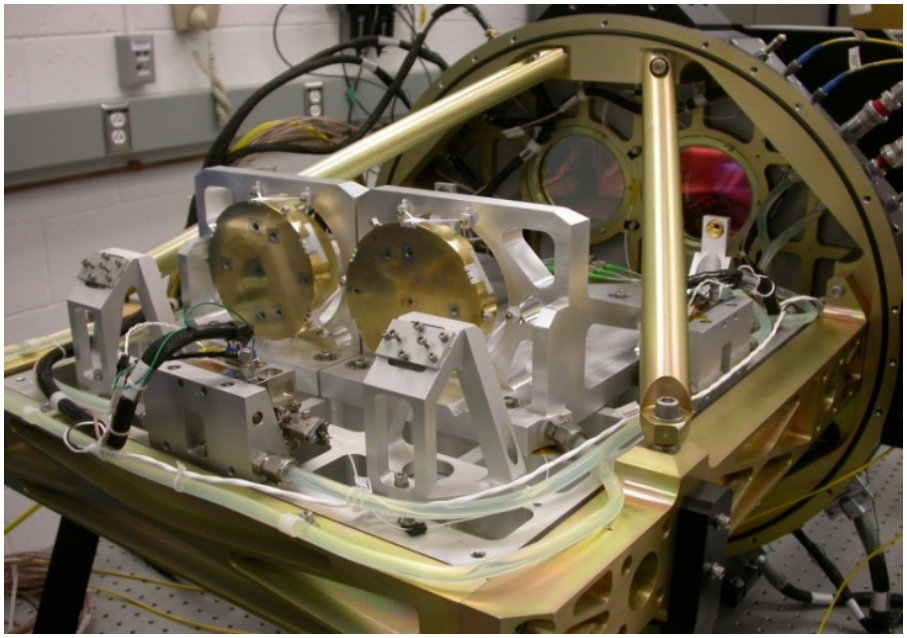

Figure 5-26 LAS with optical bench horizontal, telescope side up, base plate in background.

5.3.4.2 Signal Processing and Data Analysis

The approach to data analysis and CO_2 retrieval is as follows. The LAS on-line and off-line signals are sampled, stored, and processed as described below, to calculate for various atmospheric layers the values of

$$ln\,(P_{off}/P_{on}) = (2\,DAOD) \qquad (5\text{-}5)$$

The P_{off} and P_{on} are the estimates of return power at the off-line and on-line frequencies, properly normalized by the transmitted laser powers at these two frequencies. Then these results, derived from the measurements, are compared with forward model predictions of *DAOD*. We use the LBLRTM (Line-By-Line Radiative Transfer Model) provided by the Atmospheric and Environmental Research Inc. (AER), modified to include a merged line parameter database in the 5 cm^{-1} region centered at 4875.5 cm^{-1}. The forward model is based on this modified LBLRTM code, plus the atmospheric meteorological data needed to provide the altitude-dependent weighting function. The on-board GPS system provides the aircraft position knowledge (including altitude with respect to the geoid). Lacking an on-board co-aligned laser altimeter, the surface elevation is obtained using the Shuttle Radar Topography Mission (SRTM) digital elevation database along with the laser pointing angle, updated at 10 Hz rate.

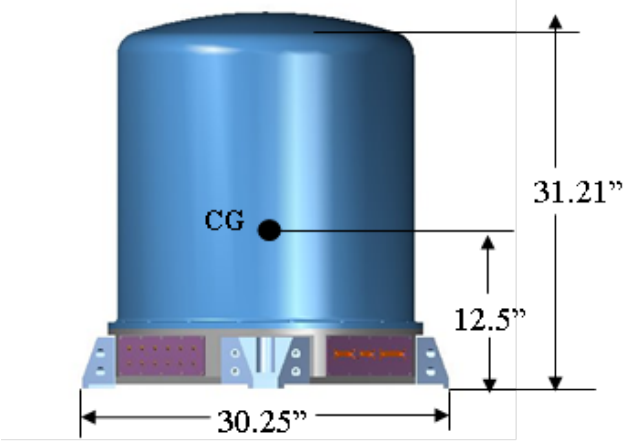

Figure 5-27 LAS transceiver in hermetically sealed enclosure.

Table 5-10 JPL airborne LAS instrument parameters

Parameter	Value
CO_2 line center frequency	4875.749 cm^{-1}
JPL LAS ON frequency JPL LAS OFF frequency	4875.882 cm^{-1} 4875.225 cm^{-1}
Laser output power	100 mW
Transmit/Receive Telescope apertures	10 cm diameter
Receiver FOV (diffraction limited)	60 μrad
Photomixer type	InGaAs
Receiver heterodyne frequency window	9-21 MHz
Signal Digitization	14 bits / 50 MHz

The normalized return signal power values are determined as follows. The Intermediate Frequency (IF) photomixer signals from the on-line and off-line channels are amplified and are bandwidth limited to a nominal 9-21 MHz window. The signals from each channel are digitized with a 50 Msamples/sec, 14-bit digitizer. The samples are transformed into the spectral domain using a Fast Fourier Transform (FFT) operation followed by conversion to periodograms. The return power is proportional to the size of the signal in the frequency space of the periodogram. On-line and off-line signal power calculations are performed, followed by normalization steps to account for variations in slant path length between instrument and footprint on the surface, small variations in laser power, or other small drifts in ch1, ch2 overall system gain. System stability is quantified through the use of “validation” data collection periods, when an on-board

backscattering Validator subsystem is inserted into the instrument field-of-view, intercepting the transmitter beams.

5.3.4.3 Cloud Detection and Filtering

To obtain adequate coverage, (weighted) column CO_2 mole fractions must be collected in the presence of broken clouds. Clouds in the FOV reduce the path length, and if not recognized, bias the CO_2 retrieval. In cases of scattered cloud cover, breaks or holes permit soundings down to the surface some fraction of the time. The small transmitter footprint of the lidar provides an inherent capability to acquire retrievals in such circumstances. If the lidar provides time-of-flight to the backscatter source (e.g. a range-gated pulsed system, or a Frequency-Modulated/Continuous Wave (FM/CW) system), any sources of backscatter other than that which occurs at the expected delay time corresponding to range to the surface can be set aside or filtered out. With the current implementation of our airborne system, we do not have this capability. We do not chirp (frequency modulate) our transmitters. However we do employ alternative methods to detect and filter out the backscatter signals that are due to clouds in the FOV (field of view). The following methods are very effective in identifying a large variety of clouds.

- Heterodyne detection provides capability to see both intensity and spectral properties of backscatter signal;
- Cloud motion provides a discriminating tool, both broadening and shifting the backscatter signal in the spectral/frequency domain;
- Clouds in FOV also cause shortening of atmospheric sounding path length – reduced values of retrieved CO_2 column;

The heterodyne signals backscattered from the surface are sufficiently narrow to permit identification of cloud backscatter if the cloud movement relative to the surface, along the line-of-sight, exceeds 0.5 m/s. Since the typical point-ahead angle in the DC-8 is ~ 0.1 rad, this corresponds to a threshold horizontal motion of 5 m/s. However, in practice, the backscatter signals from cumulus and stratocumulus are also spectrally broadened, compared with the ~ 200 kHz FWHM (full width at half maximum) signals backscattered from the surface in clear air conditions. This provides another filtering method. This spectral broadening is typical of backscatter from cumulus and also stratocumulus (Spiers et al., 2012).

5.3.4.4 Observation of CO_2 Drawdown

The August 10, 2011 flight's primary objective was the upper Midwest, arriving over the target area (Iowa) near mid-day, with the expectation that CO_2 drawdown in the boundary layer would be observed due to the photosynthetic assimilation by crops over this large-scale agricultural region. The JPL LAS data clearly indicated a steady decrease in CO_2 weighted column mole fraction (or mixing ratio) en route to Iowa beginning with the overflight of the Eastern Colorado high plains (Spiers et al., 2011b; Spiers et al., 2012; Menzies et al., 2014). After arriving in the vicinity of the West Branch Iowa (WBI) tall tower (Miles et al., 2012), a spiral was implemented in order to profile the CO_2 mole fraction using an on-board cavity ring-down spectroscopy sensor [Picarro, Inc.], and several fixed-altitude "tower transits" were conducted at different altitudes. (The NASA DC-8 also has on-board sensors providing atmospheric temperature, pressure, and relative humidity data to the investigator teams.)

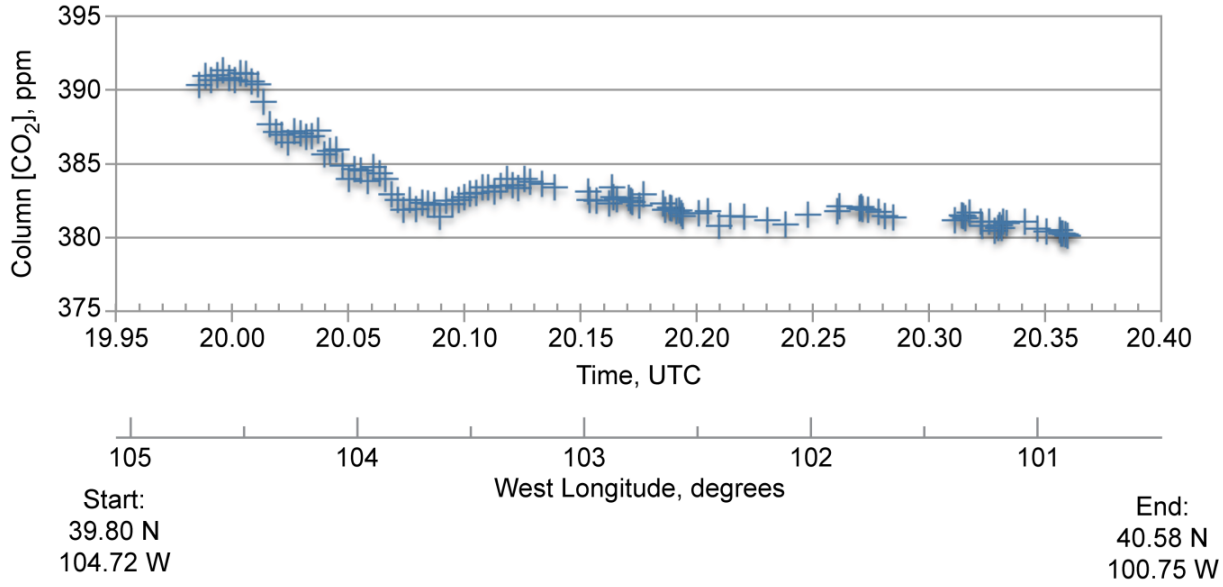

Figure 5-28 LAS weighted column CO_2 mole fraction retrievals during flight over Central US. The segment from Denver, Colorado vicinity to middle of Nebraska, was flown on August 10, 2011. (Locations: 39.80 N / 104.72 W at 19.98 UTC; 40.58 N / 100.75 W at 20.37 UTC. Distance travelled: 310 km.) The 1-sigma precision level for this retrieval is equivalent to 1.1 ppm. The steady decrease in column CO_2 is due to mid-day drawdown in the atmospheric boundary layer.

The flight to the Midwest included a long transit at fixed pressure altitude starting near Denver, CO and continuing to the vicinity of the WBI Tower in Iowa. We encountered clear atmosphere over the Denver area, with scattered fair weather cumulus appearing over the eastern Colorado plains. Cloud fraction steadily increased as the flight ground track moved into Nebraska. The observed weighted-column CO_2 mixing ratio decreased during this time period as shown in Figure 5-28. The aircraft flew at a constant 15 kft pressure altitude during this transit. The SRTM DEM data were used to obtain the along-track elevation. The atmospheric meteorological data that were incorporated into our retrieval algorithm came from the MERRA (Modern Era Retrospective Analysis for Research and Applications) products available from the NASA Goddard Space Flight Center GMAO (Global Modeling and Assimilation Office) (MERRA, 2012). For example, the surface pressure from MERRA, interpolated along this ground track and "corrected" using the higher resolution topographical data along the ground track, was used in the CO_2 retrieval algorithm.

The Figure 5-28 record starts a few km south of the Denver International Airport, and the distance covered from left to right is 340 km. The along-track averaging corresponds to about 4 km along-track resolution for the plotted data. The flight altitude CO_2 readings from the in situ Picarro instrument measurements trended lower over a narrow range from approximately 389.5 to 387.5 ppmv during the period of time plotted. The column is likely sampling urban-influenced regional boundary layer air at the beginning. Nadir camera imagery shows a transition to agricultural activity (occasional crop circles) beginning at 20.02 UTC, with increasing land use for agricultural activity occurring as the ground track continues eastward. Crossing into Nebraska occurred near 20 hr 13 min UTC. Gaps in the data are due to presence of fair weather cumulus. The ground track is in the middle of Nebraska at the end of the plotted data. By this time the cumulus coverage had increased, with corresponding decrease in the durations of the clear air gaps between clouds, precluding the continuation of the high precision retrievals.

The conclusion that the observed steady decrease in column CO_2 abundance is due to drawdown is supported by later measurements in Iowa during a traverse over the West Branch Iowa (WBI) tower at 10 km altitude, where in situ vertical profile data obtained near the WBI tower from the on-board Picarro instrument indicated boundary layer CO_2 mole fraction values ~ 365 ppm, and free troposphere values averaging 382 ppm. The magnitude of this mid-day decrease in the boundary layer mixing ratio is consistent with other reported measurements and simulations (Miles et al., 2012; Denning et al., 1996). Regional-scale simulations of the CO_2 exchange between the atmosphere and the terrestrial ecosystems (Denning et al., 1996) and measurements at the U.S. upper Midwest tall towers (Miles et al., 2012) show peak daytime NEE (Net Ecosystem Exchange) flux values of -50 to -60 μmol m^{-2} s^{-1} in the summertime, corresponding to mid-day boundary layer CO_2 mole fractions in the 360-365 ppm range at corn dominated sites such as the WBI tower site and the Mead tower site in western Nebraska. Mid-day CO_2 levels in this region during early August are among the lowest in North America due to strong uptake by corn and other crops.

Figure 5-29 Four-Corners Power Plant, New Mexico, U.S showing 3 main clusters of stacks. From left to right, starting with the tall stack (cluster #1): Clusters #1 - #2 separation ~ 400 m; Clusters #2 - #3 separation ~ 150-200 m.

5.3.4.5 Observation of Power Plant CO_2 Plume and CO_2 Emission Rate Calculation

On August 9, 2011, the DC-8 flew a northward flight segment at 15,000 foot pressure altitude whose ground track was downwind of the 4-Corners Power Plant, located in San Juan County, New Mexico (36.690 N, 108.483 W). The JPL LAS data indicated multiple spatially distinct plumes emanating from the power plant complex (Spiers et al., 2012; Menzies et al., 2014). The ground track was within a few hundred meters of the plant site. The plant has five coal-fired units, with spacing such that the emissions appear to originate from three sources. The source encountered first during this flight leg (leftmost in Figure 5-29) is the tall stack. Approximately 400 m from this source are a pair of stacks, and approximately 200 m from this pair is a third stack cluster, dark in appearance from the camera imagery. Figure 5-30 is a plot of the weighted column CO_2 mole fraction during the pass, with variable along-track resolution. The along-track resolution is 15 m during the 1-km segment immediately downwind of the plant, which is clearly sufficient to resolve plumes from the various stacks or stack clusters.

A simple box model estimate of the power plant CO_2 emission rate during the mid-day time of this flight leg can be made by calculating the CO_2 mass crossing a plane of height equal to the aircraft height above ground (3135 m) and ground track segment length of 1.0 km for which the mole fraction is above the background or baseline value. The speed of the wind carrying the CO_2 plume across the plane at this time, 2.15 m s^{-1}, is obtained from the MERRA reanalysis (MERRA,

2013). The atmospheric temperature in the lowest MERRA layer at this time was 299 K. Taking the weighting function into account, and assuming the plume is within the first 200 m above the surface, where the weighting function is nearly constant, a source of 470 kg s^{-1} emission rate is derived, based on the observed integrated weighted column increment (Menzies et al., 2014).

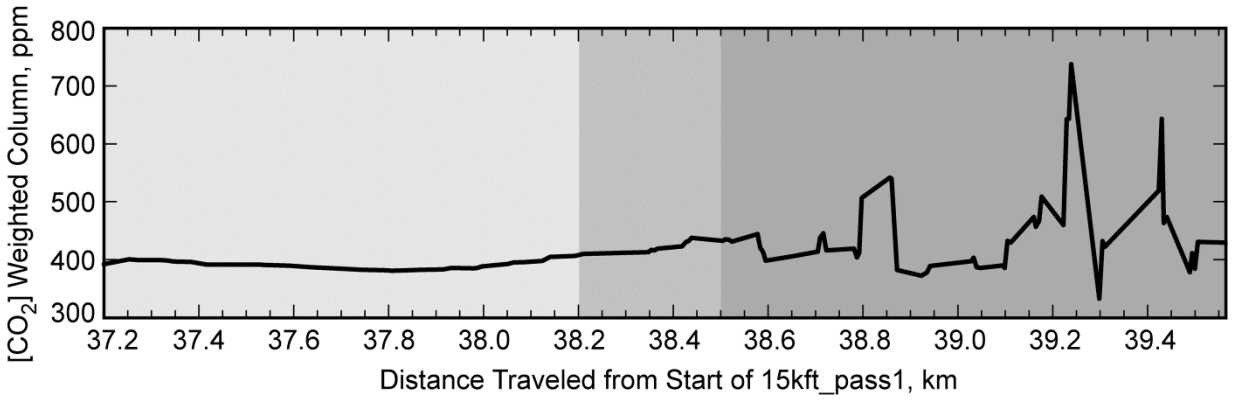

Figure 5-30 Weighted column CO_2 retrievals during flyby of the Four-Corners Power Plant at 15 kft pressure altitude along a south-to-north track and a few hundred meters downwind. The shading corresponds to three spatial resolution segments: (1) 37.2 – 38.2: 150 m along track resolution; (2) 38.2 – 38.5: 50 m resolution; (3) 38.5 – 39.5: 15 m resolution.

The Four Corners Power Plant complex emits in the neighborhood of 14 x 10^6 metric tons of CO_2 annually, according to a 2011 study prepared by RMT, Inc. for the California Public Utilities Commission (RMT, 2011). (A pdf of this document is available.) This corresponds to an average CO_2 emission of 440 kg s^{-1}. Surely there is some temporal variability in the emission rate – on daily, weekly, or monthly time scales, but we do not have that information. However we do have a measurement that corresponds closely with the average emission rate. This demonstrates the potential capability of the IPDA measurement method.

5.3.4.6 CO_2 Retrievals over Snow-Covered Surfaces: Evidence of Plumes from Developments

Assessment of the capability to retrieve CO_2 weighted column mole fraction over snow-covered surfaces is an important objective in ASCENDS planning. Snow reflectance at the 1.57 and 2.05 μm wavelengths is relatively low (Aoki et al., 2000), but quantitative values of lidar directional reflectance at these wavelengths did not exist prior to the ASCENDS campaigns of 2011 and 2013. These campaigns offered the opportunity to measure reflectances of a variety of snow-covered surfaces. The basis of our 2.05 μm snow reflectance derivation is the linkage that we have to ocean surface reflectance as measured over the clear Pacific Ocean off the coast of California. The CALIPSO mission provides by far the largest study of lidar backscatter from the ocean surface, and we rely on data from Hu et al. (2008) for determination of the surface directional reflectance (backscatter) over this region of the Pacific Ocean, given the estimated surface wind. (Correction was made for the wavelength-dependence of water refractive index between 1.06 and 2.05 μm.) We are able to take advantage of the fact that at the JPL LAS nominal 5-degree off-nadir angle, the surface backscatter is only weakly dependent on surface wind speed in the range from ~ 2.5-12 m/s (Menzies et al., 1998). Comparison were made of range-corrected off-line return signal values from the Pacific Ocean flight and the 8/07/2011 flight values over the snow-capped British Columbia coastal mountains. The LAS instrument radiometric stability is good to within 10% from flight-to-flight, and flight-to-flight and in-flight

variations are monitored with the internal Validator. This allows the determination of surface reflectance during the flight segment over the BC coastal mountains, as in Figure 5-31. In this case the snow backscatter averaged over the ground track is ~ 0.012 sr^{-1} (Menzies et al., 2014).

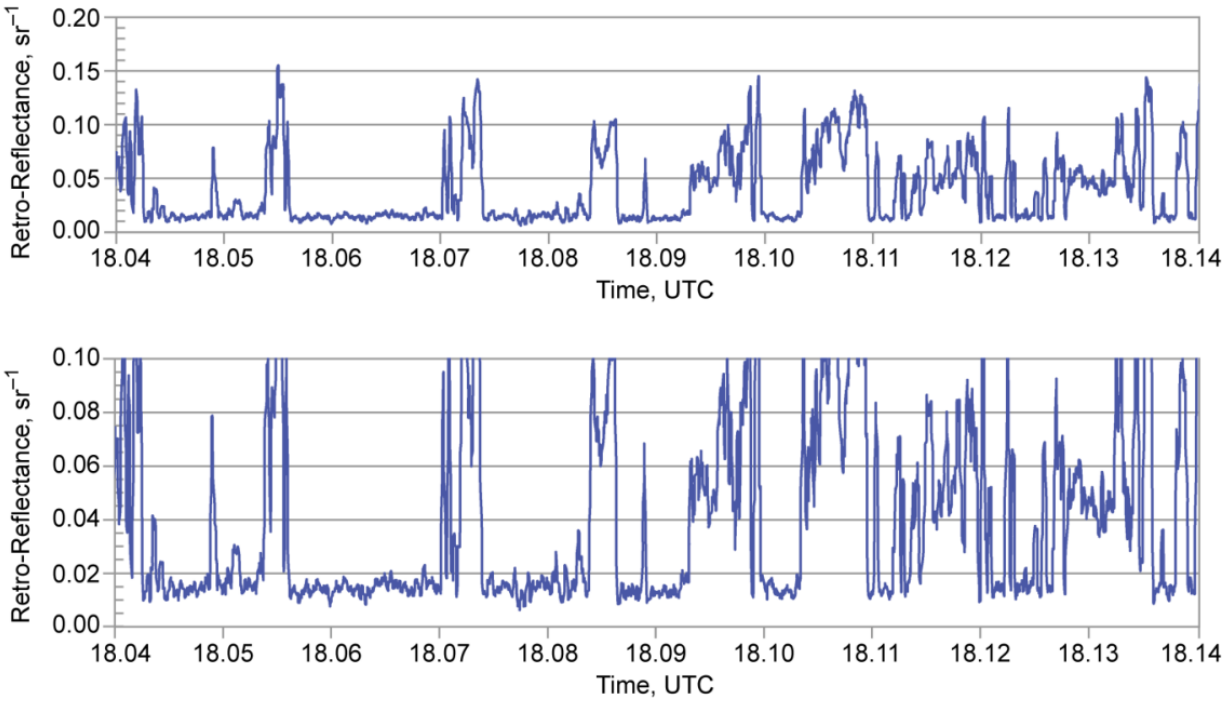

Figure 5-31 LAS measured surface reflectance during a portion of the "snowline out" flight segment over the British Columbia Coastal Mountains, August 7, 2011 at 2.05 µm wavelength (in units of sr-1). Snow covered areas (low backscatter) were mixed with patches of bare rock, dirt, alpine flora. Time duration from left to right: 0.1 hr (6 min). The two panels differ only in scale.

Snow-covered terrain was also encountered on the March 7, 2013 flight to the upper Midwest. The low reflectance over snow-covered land was often interrupted by road crossings, structures, and patches of bare land that show larger reflectances. We found during this flight and the March 5 flight that targeted the Colorado Rocky Mountains a range of values for snow reflectance (i.e., lidar directional reflectance), with values at the 2.05 µm lidar wavelength from 0.07 to 0.2 sr^{-1}.

The CO_2 retrievals over the upper Midwest flight tracks show bulges or plumes that appear to be associated with developed areas, e.g. cities in the vicinity of the ground tracks. Through the use of the combination of nadir camera imagery, MERRA wind direction, and Google Earth, we observe cases when ground tracks are over urban areas, developments near cities, or downwind of nearby urban areas. Figure 5-32 shows an example. In this case, the wind direction was primarily westward, with a small northward component. Space heating in cold winter weather may be the primary source of these CO_2 plumes from populated areas.

The flights of the JPL CO_2 Laser Absorption Spectrometer have enabled us to assess and demonstrate the performance of a 2.05 µm IPDA lidar using a heterodyne detection receiver to obtain CO_2 retrievals for a variety of atmospheric and surface conditions. Measurements made during a mid-day flight over the U.S. Upper Midwest clearly indicate that we can observe the CO_2 drawdown due to photosynthesis at the surface. Measurements made in the vicinity of the Four Corners power plant demonstrate the capability to resolve the plumes with high spatial resolution and estimate the source emission rate. We demonstrated the capability to measure CO_2 over

snow-covered surfaces in the Upper Mid-West during winter, 2013, and we observed CO_2 bulges/plumes that appear to be associated with developed areas that were encountered along the flight tracks. The 2-μm weighting function, which gives added weight to the atmospheric boundary layer (ABL), enables enhanced sensitivity to sources and sinks that alter the CO_2 mole fraction in the ABL.

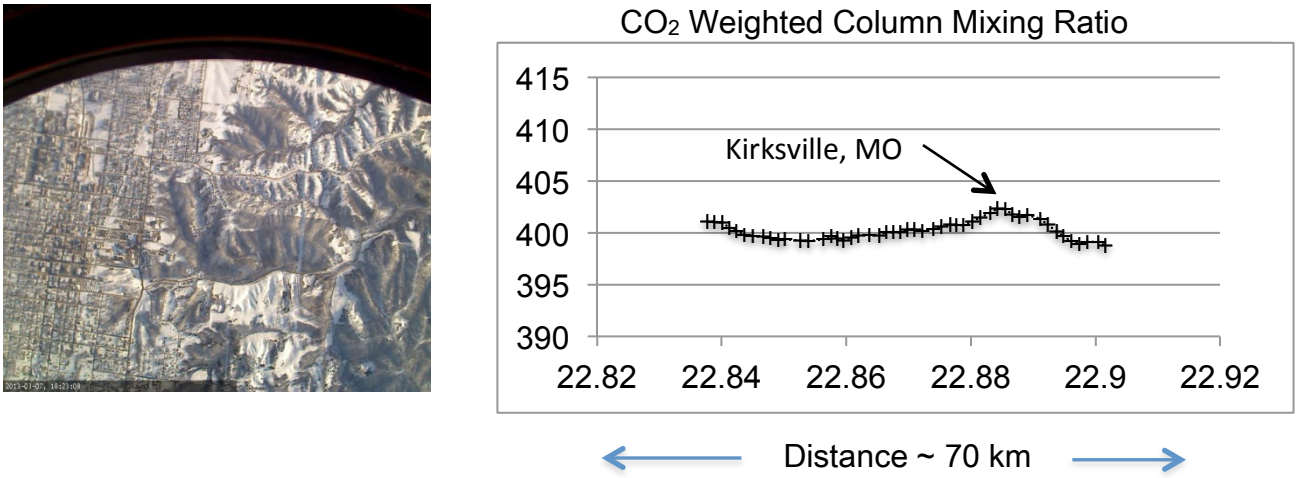

Figure 5-32 CO_2 retrieval in vicinity of Kirksville, Missouri on March 7, 2013 (Left) JPL nadir camera image of partially snow-covered landscape in Kirksville vicinity, taken from the DC-8 rear cargo bay at 22.886 (22:53:08) UTC. (Right) Weighted column CO_2 along a 70 km length flight segment heading south, near 92.5° west longitude. The time is UTC, covering 6 min from left to right. The track went over the west edge of Kirksville, downwind side, showing a plume that is associated with the city.

5.3.4.7 Near-term Plans for the LAS

Improvements to the airborne system were implemented in 2014, and more are planned in 2015. The most significant 2014 modification included (1) installation of a faster data acquisition system in the airborne LAS instrument, in order to increase the speckle-limited sensitivity on short time scales; (2) replacement of 10-yr old RF electronics with current commercially available electronics. The 2015 planned improvements include installation of a fiber amplifier in the online channel to boost the online transmit power output, and the addition of a laser altimetric capability. Improvements in ground-based data processing and analysis algorithms are continuing. Goals are (1) to decrease the data latency between in-flight acquisition and availability of CO_2 products; (2) to utilize digital noise filtering and contrast enhancement techniques in order to reduce the impacts of speckle noise on the CO_2 retrievals.

5.4 Development of Additional Lidar Measurement Approaches

NASA has also supported the development of two additional lidar approaches to measure the CO_2 column. These use CO_2 column lidar measurement using different approaches than those described earlier. They are earlier in their evolution and so have not been fully demonstrated in airborne campaigns.

5.4.1 Broad Band Lidar Approach

There are two principal elements involved in the IPDA measurement: the source and the detector. Most laser-based instruments use tunable laser sources to provide different wavelengths needed to sample the selected CO_2 line. The Broad Band Lidar (BBL) uses an alternative approach. It

transmits a spectrally wide (~ 1 nm) laser pulse and uses a spectrally (wavelength) resolved detector to differentiate the wavelengths on a finer scale. Thus the broadband lidar uses a combination of active illumination with a receiver similar to those in passive sensors. In fact, the BBL detector was originally developed as a passive sensor for measuring CO_2 using reflected sunlight. The BBL approach is made possible by the use of new broadband laser sources that can emit over several nanometers of continuous bandwidth rather than single, narrowly defined wavelengths. This permits a differential absorption measurement employing a single source with all wavelength differentiation done in the detector.

Several versions of the BBL have been developed. A ground based version employing a superluminescent diode (SLED) source was demonstrated in 2010 as well as at 2.05 μm employing a fiber laser source. A 1.57 μm version using an Optical Parametric Amplifier (OPA) source was flown in the 2011 ASCENDS intercomparison and a second lidar operating at 1.57 μm employing an array detector was flown in the 2013 campaign. Performance has been quite limited in the aircraft tests because of the unfortunate location of the instrument in the DC-8 cargo pit where it is subjected to temperature extremes that tend to drive it off wavelength and out of alignment. Figure 5-33 shows the instrument responding to changing CO_2 column density with altitude early in a test flight before the change in temperature detuned the laser and the receiver.

5.4.1.1 BBL Fabry-Perot Interferometer and Detector

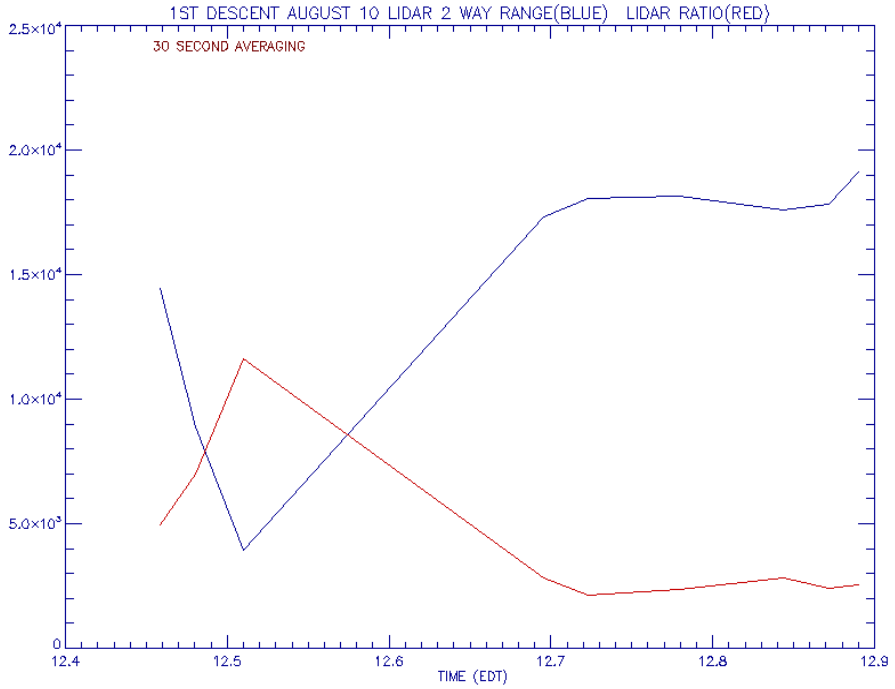

Figure 5-33 BBL measurements made shortly after takeoff on August 10 test flight. The anti-correlation of total absorption (aircraft to ground) in red versus altitude in blue shows that the Broad Band Lidar is responding to CO_2 along the changing path length.

The BBL receiver uses a Fabry-Perot (FP) interferometer as the wavelength selective element for its detector. Aligning multiple adjacent passbands of the FP with several CO_2 absorption lines increases the lidar signal and permits selection of absorption lines that respond to temperature changes in opposite directions, reducing the overall instrument sensitivity to atmospheric temperature change. The width of the Fabry-Perot passbands can be adjusted with very high

fidelity by changing the reflectivity of the coatings used in its manufacture. Passbands can be selected to surround the full widths of the various CO_2 absorption features reducing the sensitivity of the instrument to slight changes in line position and width caused by changing atmospheric pressure. The fine alignment between etalon fringes and CO_2 absorption lines is achieved by temperature tuning of the Fabry–Perot. The passive Fabry-Perot detector was developed at GSFC from 2003-2006 as a sensor to measure atmospheric CO_2 column using scattered solar flux in the 1.57-μm region. It was tested during two successful flight campaigns. It demonstrated very high sensitivity to changes in the CO_2 column abundance, but was subject to errors arising from atmospheric scattering of the sunlight, a problem that lidar instruments eliminate (Georgieva et al., 2006, 2008; Wilson et al., 2007; Heaps et al., 2008).

5.4.1.2 BBL Receiver Design.

The detector in an IPDA lidar performs two functions simultaneously. It determines the length of the atmospheric column by measuring the amount of time that elapses between the emission of the laser light pulse into the atmosphere and its subsequent return. It also measures the intensity of the returning light pulse. This intensity measurement is then used to determine the magnitude of the atmospheric absorption in the path.

Our previous version of the Broad Band lidar used an avalanche photodiode detector (APD) both for ranging and for signal level measurement, but its performance was not sutiable for space. More recently we have built a lidar receiver that uses an two different detectors to perform the receiver functions. In this design an APD was used to make precise measurements of range. An InGaAs camera was used to measure signal intensities. The camera is not range resolved. However it is very sensitive to photons (it can count single photons) and it generates very little noise during the measurement process. Our simulations of this receiver design indicate that a system based on this configuration could meet the requirements for the ASCENDS lidar.

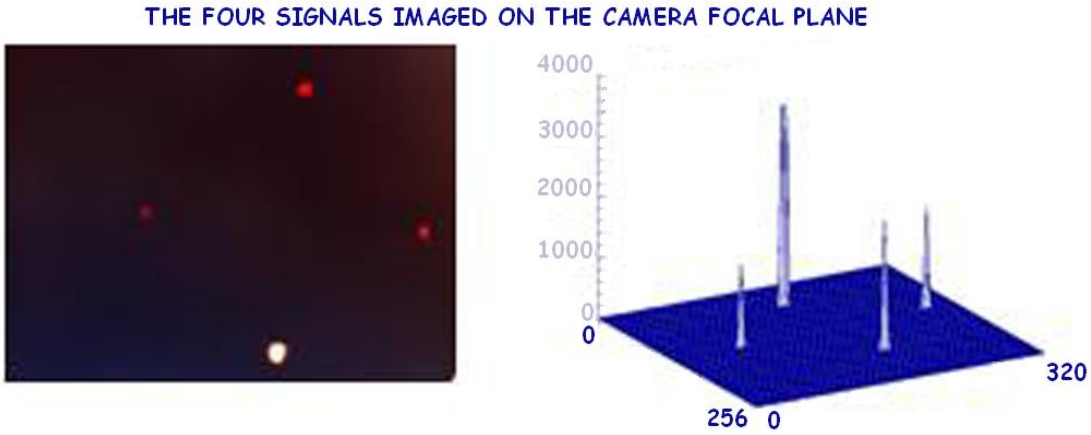

Figure 5-34 Image and plot of the four signals represented in the InGaAs camera focal plane.

Figure 5-34 shows the focal plane of the InGaAs camera and a plot of the signals measured during a recent airborne flight test campaign. The four dots represent the “on-line” and “off-line” intensity for the transmitted beam and for the reflected signal. A receiver for the ASCENDS space mission would use three Fabry-Perots and so would have three “on line” spots and one “off-line” spot each for the transmitted and return measurement—eight spots in all.

Figure 5-35 shows the arrangement of the detector for the lidar. Beams from the receiver telescope and the outgoing laser sampling system are fiber coupled into the receiver. Polarizing beam splitters and quarter wave plates are used to introduce light into 3 individual Fabry-Perots (FP) that are tuned to sample different portions of the broad-band signal. And a 4th channel that uses no FP representing the "off-line" of "reference" channel. Two outputs each (one from the receiver telescope and one from the laser sampler) from the 4 channels are imaged onto the focal plane of the single camera resulting in 8 measurement spots from which the CO_2 absorption can be determined.

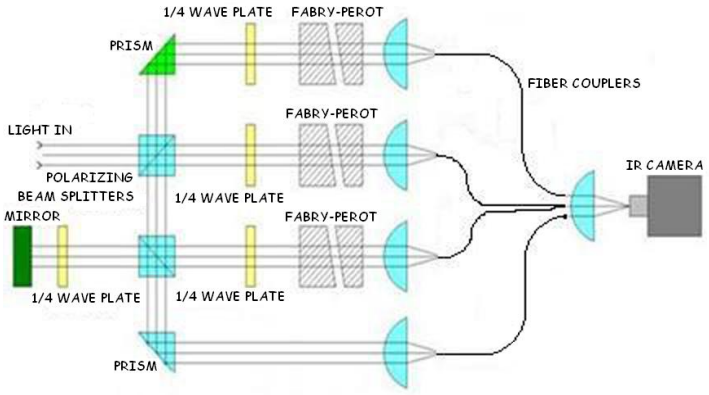

Figure 5-35 Drawing showing light path in instrument to reach 3 FPs and reference channel. Light reflecting from the FPs has its polarization rotated by the combination of ¼ wave plates so if it reflected from a beamsplitter at first incidence it passes through at the 2nd incidence. All signals are collected by fibers then recorded on the focal plane of a single camera.

Figure 5-36 shows how a multiple FP receiver system operating in the 1.57-μm region can remotely sense CO_2 columns.

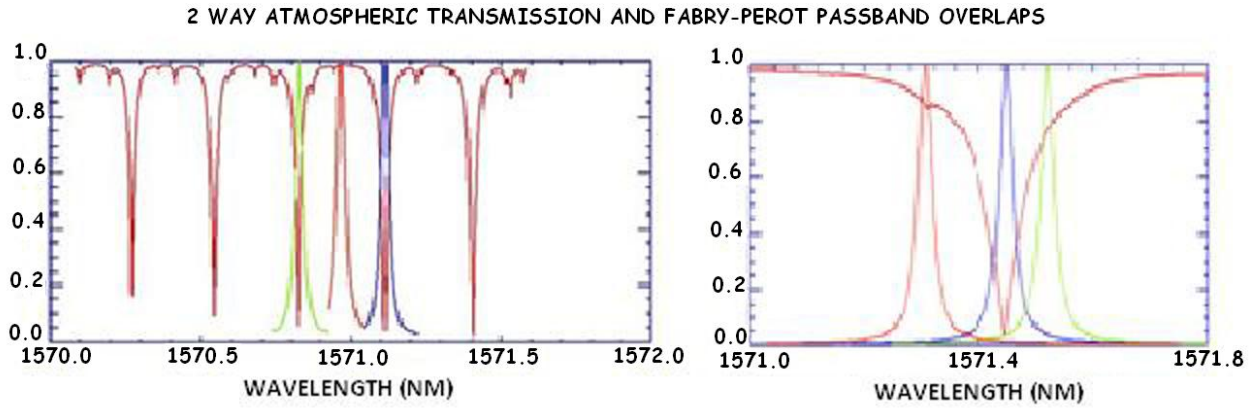

Figure 5-36 Two possible ways that the Multiple FP detector can investigate CO_2 absorptions. The approach on the left samples two separate CO_2 lines providing information that can be used to correct for atmospheric temperature effects.

5.4.1.3 Laser for BBL:

In 2011 Northrop Grumman Aerospace (NGA) delivered a prototype Tm-fiber laser to Goddard. Output power was 3 W and pulses were spectrally and temporally stable over several hours of

continuous operation during the laboratory demonstration. The system was used to test and develop the 2.05 μm broadband CO_2 lidar concept. Fiber lasers are a proven method for producing photons at high efficiency in compact, robust packages.

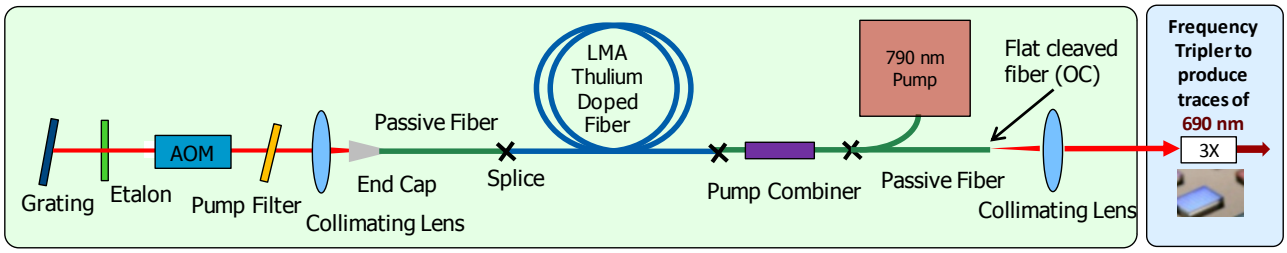

Figure 5-37 A Q-switched fiber laser architecture is used to generate multi-line broadband wavelengths near 2.05 μm.

The BBL version of the ASCENDS mission will use a Tm-fiber laser operating at 2.05 μm. The choice of a fiber laser inherently mitigates several risks associated with other types of lasers. The fiber nature of the system allows simply achieved mechanically robust operation in a compact footprint. Thulium's 2.05 μm wavelength enables the use of larger diameter fiber cores without loss in beam quality compared to other fiber lasers. This reduces the risk of catastrophic optical fiber damage and the onset of deleterious nonlinear effects enabling higher pulse energies and peak powers since damage and nonlinear effects scale down with increase in core area. The Efficiency of thulium fiber lasers can also be very high due to a cross relaxation process in thulium's energy levels whereby one pump photon can create two laser photons, leading to potential laser slope efficiencies approaching 70% (Jackson, 2004; Ehrenreich et al., 2010; Goodno et al., 2009; Creeden et al., 2008). For a space-based lidar the laser power would be scaled to the 30-40 Watt level. Our work shows it will be capable of wall plug efficiencies >15%.

5.4.2 Pulsed 2-μm Differential Absorption Lidar (DIAL)/IPDA Lidar

Pulsed 2-μm lasers have narrow linewidths and can have high energies that make them suitable for a CO_2 IPDA lidar. The strong 2.0-μm CO_2 lines also have weighting functions that are strongly peaked near the surface. NASA Langley Research Center (LaRC) has been involved for over 15 years in developing pulsed 2-μm lasers and lidar technologies. Recently we have applied them to the measurement objectives of ASCENDS (Koch et al., 2008; Refaat et al., 2010, 2011; Yu et al., 2003, 2012). This section describes the development of ground-based DIAL and airborne IPDA systems for CO_2 measurements.

5.4.2.1 Single-Pulsed 2-μm CO_2 DIAL Demonstration

Range Resolved CO_2 DIAL measurement using single-pulse 2-μm laser have been demonstrated by NASA LaRC (Koch et al., 2008; Refaat et al., 2010, 2011). For these initial demonstrations, the wavelength of the output laser pulses alternated between on-line and off-line positions at a 5-10 Hz rate. Using heterodyne detection, CO_2 DIAL measurements were attempted with a 90 mJ, 140 ns, 5 Hz pulsed Ho:Tm:LuLiF laser transmitter (Koch et al., 2008). The laser used a wavelength control to precisely tune and lock the operating wavelength at any desired offset, up to 2.9 GHz, from the center of a CO_2 absorption line. Once detuned from the line center the laser wavelength is actively locked to keep the wavelength within 1.9 MHz. The laser transmitter has been coupled with a coherent heterodyne receiver for measurements of CO_2 concentration using aerosol backscatter.

Detector technology usually limits the CO_2 DIAL profiling capability at 2 μm. Therefore, 2-μm phototransistors have been developed and integrated for the first time in lidar applications and using direct detection, another 2-μm CO_2 DIAL system was developed at NASA LaRC using the same transmitter (Refaat et al., 2010, 2011). Field experiments were conducted at West Branch, Iowa, for evaluating the system for CO_2 measurement by comparing with NOAA in-situ sensors located on the WBI tower at 31, 99 and 379 m altitudes. Results demonstrated the capabilities of the DIAL system in profiling atmospheric CO_2 using the 2-μm wavelength with both range resolved and integrated column content (Refaat et al., 2010).

The results from single-pulse 2-μm CO_2 DIAL experiments highlight several desirable improvements to enhance their measurement capability. First, the selected and demonstrated target CO_2 R22 line includes high water vapor interference that coexists at the same operating wavelength. Operating on the CO_2 R30 line potentially increases the lidar sensitivity while reducing the impact of water vapor interference. These improvements require upgrading the 2-μm laser transmitter. The laser pulse repetition rate also must be increased. With single-pulse, 5-Hz transmitter, the on-line and off-line pulses are separated by a long period resulting in inconsistent volume sampling between the two wavelengths. This led to the adoption of the higher pulse rate double-pulsed 2-μm laser transmitter. In the double-pulse operation, two pulses are generated, which are separated by 150 to 200 μs, and thus requires only one laser to generate the on-line and off-line pulses for DIAL/IPDA profile or column measurement of CO_2.

5.4.2.2 Double-Pulsed CO_2 IPDA Lidar for Aircraft

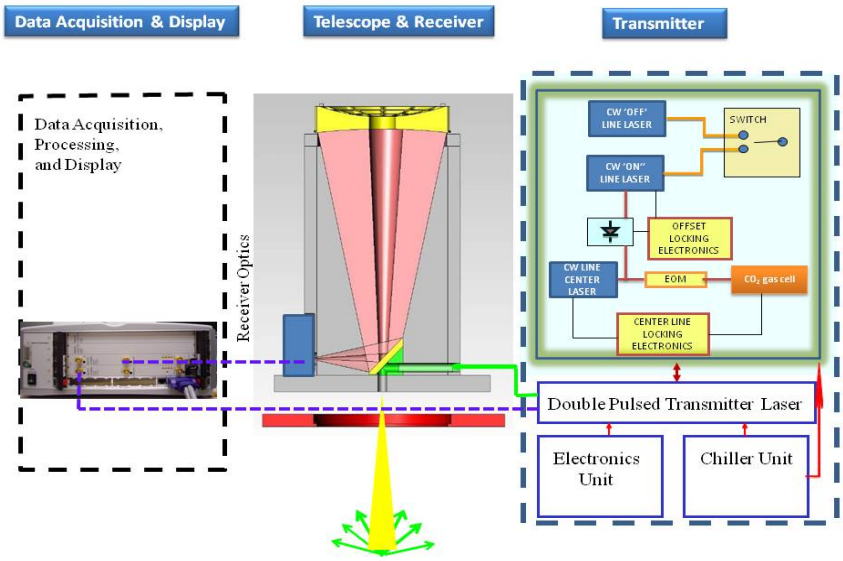

Figure 5-38 Schematic of the 2-μm, double-pulsed, CO_2 IPDA lidar. Given an estimate of the O_2 column, a weighted-average dry-air volume mixing ratio of the target gas can be retrieved from this measurement by using the CO_2 weighting function, defined by the differential absorption cross section and the dry air mass. Figure 5-39 shows the total integrated vertical optical depth variation with wavelength for atmospheric CO_2 and H_2O, the dominant interfering molecule. Optical depth calculations were conducted using the US Standard model for metrological profiles and gases mixing ratios and HITRAN for line parameters. IPDA operation is achieved by proper selection of the wavelengths of the laser pulses that are transmitted sequentially within the short time interval. The principle of wavelength selection in this technique is shown in Figure 5-39. The figure shows the normalized CO_2 pressure-based weighting functions at selected spectral positions for nadir IPDA measurement from an airborne platform versus altitude. The weighting function defines the altitude sensitivity of the measurement.

Because it uses the strong reflection from hard targets, the IPDA lidar approach provides higher signal-to-noise ratio measurement compared to the range-resolved DIAL that depends on atmospheric backscatter. If the online wavelength setting is changed, then it will change the column weighting function. Therefore, the transmitter could be tuned to weight the column measurement near the surface for optimum CO_2 interaction studies or closer to line center for measurements of the free troposphere. Currently, NASA LaRC is developing a double-pulsed 2-μm direct detection IPDA lidar for CO_2 column measurement from an airborne platform (Singh et al., 2013) shown in Figure 5-38.

By tuning the on-line position different weighting can be achieved. For example, tuning the on-line to $\lambda_{on,1}$ weights the measurement toward the surface where CO_2 sources and sinks interactions take place. Tuning the on-line to $\lambda_{on,2}$ weights the measurements toward the free troposphere. System simulations resulted of 0.2% total CO_2 optical depth error for $\lambda_{on,1}$ operation, for 8 km flight altitude and 10 sec average. The corresponding signal-to-noise ratios for the on-line and off-line ocean return signals are 1.1×10^4 and 4.1×10^3, respectively.

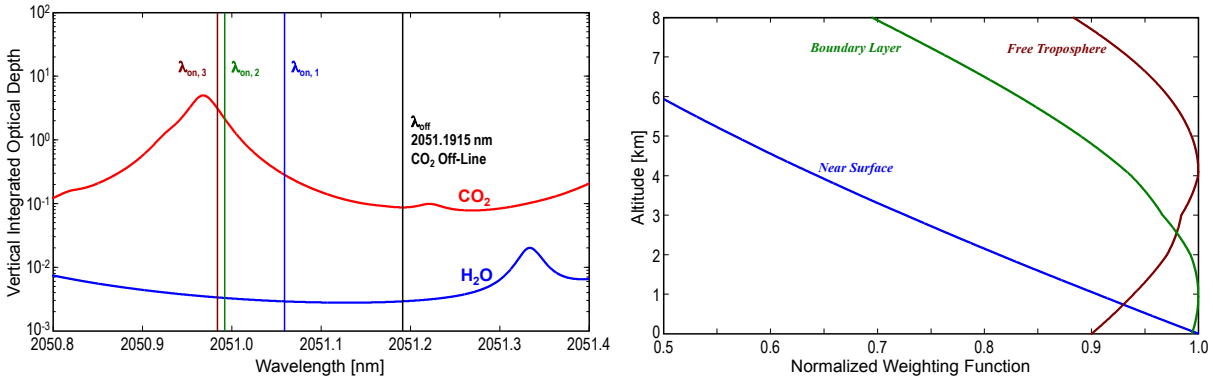

Figure 5-39 Comparison of the CO_2 and H2O integrated optical depths. (Left) Comparison derived using the HITRAN 2008 database for line parameters and US Standard model for meteorological profiles. The vertical lines indicate wavelengths for the three laser pulses, for simultaneous CO_2 measurements with two different weighting functions *(Right)*.

5.4.2.3 Laser and Receiver Development

Double-pulsed 2-μm lasers have been demonstrated with energy as high as 600 mJ and up to 10-Hz repetition rate (Yu et al., 2003). The two laser pulses are separated by 150 μs and can be tuned and locked separately. The CO_2 IPDA laser transmitter is based on the Ho:Tm:YLF high-energy 2-μm pulsed laser technology. This laser transmitter is side pumped by AlGaAs diode arrays at 792 nm. It is capable of generating two pulses with 100-mJ and 30-mJ energies at 10 Hz. For airborne use, the double-pulse operation allows maximizing the overlap between the on-line and off-line footprint on the ground resulting in sampling the same atmospheric volume. This feature enhances the IPDA measurement by reducing the sampling error. The emission wavelengths of the pulsed laser are determined by the wavelength control unit. The first pulse and the second pulse are injection seeded alternately by the on-line frequency and the off-line frequency, respectively. The laser transmitter is 29 x 67.3 x 16.5 cm in size, and weighs less than 70 lbs.

The receiver telescope is a custom designed Newtonian with 40-cm diameter aluminum primary mirror. The shape of the primary mirror is hyperbolic allowing the returning signal can be focused to a spot with a diameter < 300 micron. A 300-μm diameter InGaAs pin photodiode detector has

selected. Detector characterization showed a Noise-Equivalent Power (NEP) of 6.8×10^{-14} W/Hz$^{0.5}$ at 30°C. After amplification the lidar signals are digitized and stored by a data acquisition unit. The data acquisition unit is based on two 200-MHz, 12-bit digitizers, where one monitors the laser energy and the other for the lidar return.

5.4.2.4 Plans for Ground and Aircraft Testing

The IPDA lidar is designed for integration into a small research aircraft such as the NASA B-200. The mechanical design of the CO_2 IPDA lidar is compact and light weighted to meet the payload requirements for the aircraft, simultaneously with any CO_2 validation instruments. **Error! Reference source not found.** shows a preliminary design concept of the Transmitter-Telescope-Receiver Integrating Structure of the CO_2 IPDA Lidar system as installed in a B-200 aircraft. The optical portal has already been modified and installed to readily accept the lidar system.

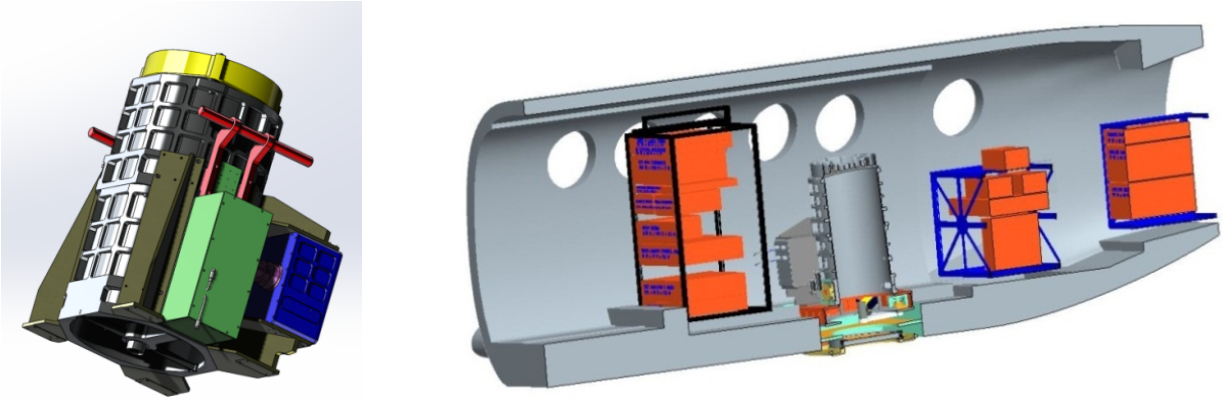

Figure 5-40 Illustration of 2-μm, double-pulsed IPDA lidar for airborne CO_2 measurements. (Left) Integrated, 2-μm, double-pulsed IPDA lidar for airborne CO_2 measurement (Ramanathan et al., 2013). (Right) 2-μm CO_2 double-pulsed IPDA system integration inside an aircraft, such as the NASA B-200 (Ramanathan et al., 2013).

Initially the assembled CO_2 IPDA instrument will be ground tested in a mobile trailer with a calibrated horizontal hard target setup and then will be airborne demonstrated on the NASA Langley UC-12/B-200 aircraft. In ground testing the number density of CO_2 along with pressure, temperature, and relative humidity information obtained from ancillary measurements from in situ sensors are used to retrieve dry CO_2 mixing ratios. The data obtained during instrument testing will be evaluated, including comparisons to the in situ instruments and validation of the data with respect to the weather and geographical environment. IPDA instrument ground testing will include CO_2 retrieval algorithms development and comparison with in-situ sensors. The main validation goal is to evaluate the IPDA performance relative to the scientific objectives.

CO_2 airborne validation will be achieved by comparison with in situ sensors (Picarro, Inc., and Li-Cor, Inc.) that will be included in the aircraft. Once validated, the plan is that this lidar will be useful for providing correlative measurements of column CO_2 to support the passive remote sensing satellites such as OCO-2, and GOSAT.

5.5 Plans for Demonstration of New Capabilities and Measurements

The airborne lidar campaigns provide an important opportunity to demonstrate the performance of candidate lidar techniques for ASCENDS. This is valuable given the wide variety of combinations of atmospheric scattering and extinction and surface backscatter and morphology that CO_2 measurements must be made under. As stated in the introduction, ASCENDS has several

fundamentally unique capabilities. The airborne campaigns enable demonstrations of those capabilities and performance assessments for a variety of environmental conditions. With each successive campaign, the instruments, data analysis approaches and CO_2 retrieval algorithms improve. These demonstrations and measurements result in improved modeling of candidate lidar techniques for the ASCENDS mission. This section highlights the present plans for new demonstrations and measurements during the next few years.

5.5.1 Additional Measurements Over Snow

Due to the optical absorption bands of water ice near 1560 and 2000 nm, snow has a low reflectivity (typically a few percent) at both candidate CO_2 measurement wavelengths. The reflectivity varies with the grain size of the ice crystals, and hence with the age and temperature of the snow. In addition to these effects on the lidar backscatter, the degree to which other materials are deposited on the snow can have a dramatic influence on the strength of the backscatter. Due to the importance of the ASCENDS measurements at high latitudes, particularly in the winter season, it is important to assess how the candidate lidars operate over a variety of snow-covered surfaces and conditions.

As described in Section 5.3, an ASCENDS airborne campaign was conducted during March 2013 primarily to target measurements over different types of snow-covered areas. One flight was made over fresh snow-fields in high altitude mountain basins in the Rocky Mountains in Colorado. A longer flight was also made east over the Rocky Mountains over Missouri, Iowa and Wisconsin. When east of Nebraska, the second flight had extensive snow cover, intermixed with houses and roads. The lidar directional reflectance (backscatter) as measured by the lidars when flying over snow was largely consistent with Aoki et al. (2000) measurements. Flights over snow-covered areas will be included in future flight campaigns, since demonstrating performance over these conditions is directly relevant to the all-latitudes, all-seasons ASCENDS capability. One characteristic of the snow-covered land areas that have been encountered to date is that they are not completely snow-covered, which causes a wide dynamic range of lidar backscatter to occur over relatively small spatial scales. Bare surfaces with much different reflectances include trees, roads, rocks, dirt, and buildings. This raises the backscattered signal level when averaged over a few km along the flight track. To what extent is there a reduction in dynamic range in remote areas that are nearly or completely snow-covered? Currently we do not have an accurate model for aged snow, or “dirty” snow due to deposition processes. Additional flight measurements will address these questions and needs.

5.5.2 Measurements Over Forests

Lidar measurements over areas with tall trees are also of interest. These are more complex due to the rapidly varying amount of time spreading (or time smear) in the reflected laser signals that simultaneously illuminate the tree top, mid canopy, and ground beneath the tree. ASCENDS will have a unique capability to measure the scattering surface elevation (SSE) over these areas and use the SSE data to reduce uncertainties in CO_2 column retrievals. Since some areas of high interest for the ASCENDS mission (such as Amazon region) are forested, understanding measurement characteristics over areas with tall trees is important. Rapid changes in topographic height when measuring over mountains also may cause a similar effect. During the 2013 campaign a flight was conducted over the coastal range of redwood trees from San Francisco CA north to the Oregon border. This permitted a variety of lidar measurements over hills and low mountains covered by redwood trees of various densities. All the primary lidar systems operated

well over this region, and their measurement datasets are being analyzed now. The 2014 ASCENDS airborne campaign also included additional lidar measurements over forested areas, and these data are also being investigated. Future flights are needed to address lidar measurements over the snow-covered forest environment.

5.5.3 Demonstrating CO_2 Flux Measurements with Airborne Lidar

It is important to further demonstrate the capabilities of airborne CO_2 IPDA lidars to provide measurements related to the determination of CO_2 fluxes from both natural and anthropogenic sources. Logical candidates are CO_2 fluxes from large areas of rapidly growing crops (such as corn) in the summertime, and CO_2 emissions from cities. Airborne campaigns that target these types of measurements are important as initial demonstrations of ASCENDS-type measurements to address local and regional scale questions about carbon exchange between the surface and atmosphere.

5.5.4 Comparisons with Satellite Measurements Made with Passive Spectrometers

It will be valuable to compare airborne lidar measurements of CO_2 with those from passive satellite instruments. Some initial attempts at these comparisons have been made with GOSAT. OCO-2 has a denser sampling pattern on the Earth's surface. The planned start of measurements with OCO-2 in August 2014 might allow for the first comparisons with that instrument. Comparing lidar and OCO-2 measurements made nearly simultaneously under a variety of conditions should be quite valuable and informative to the remote sensing community. Underflights would most likely take place within the continental U.S. Lidar cal/val would also include comparisons with on-board in situ CO_2 data made during spirals down to and within the boundary layer. Methods for modeling the CO_2 column above the aircraft (~ 10-12 km) will be a topic of discussion.

5.5.5 Improvements in Numerical Simulations of the ASCENDS Mission

The initial space mission simulations (Kawa et al., 2010) have been quite useful to start the requirements analysis for the mission, to initiate simulations of flux retrievals, and to start to assess the impacts of random and bias errors in the lidar measurements. However the initial representations of the lidar measurements in these simulations were simplified. The existing simulations are not yet adequate to fully exploit key features of the ASCENDS mission, such as day/night measurements or measurements in polar regions during winter and during freeze/thaw periods. It is highly desirable to improve the fidelity of the lidar measurement models in these simulations. It is also desirable to expand the simulations to include range and CO_2 column measurement to the tops of certain types of optically opaque clouds, such as marine stratus and fair weather cumulus. Airborne measurements are beginning to show that such measurements can provide useful additional information.

5.6 Needed Technology Developments for the ASCENDS Space Lidar

Many important capabilities for ASCENDS have been demonstrated by several of the airborne lidar teams. These include CO_2 column absorption and range measurements with high precisions and low biases over a wide variety of surface types, and measurements over a wide range of altitudes. Some measurements have been demonstrated to cloud tops and through thin clouds. Several teams have demonstrated accurate retrievals of CO_2 mixing ratios based on the airborne lidar data in comparison with in situ data. Airborne measurements of O_2 column absorption and

range have also been demonstrated which showed the expected variability with surface pressure. Almost all measurement results have been presented at conferences and most have been published in peer-reviewed journals. This work has greatly improved the ad hoc science definition team's understanding of the capabilities needed from space for ASCENDS and represents significant progress toward meeting the demands of the space mission. However, this work has also identified key challenges that must be addressed to meet the requirements of the ASCENDS mission. Some specific improvements needed in technology are summarized below.

5.6.1 Generic Needs for Up-scaling Existing Airborne Lidar as "Bridge" to Space

For space use, a lidar has additional technical and engineering challenges beyond those for an airborne lidar. These include: (1) a much longer range to the scattering surface (typically 400 km for space vs $\leq$ 12 km for airborne). This significantly increases the loss from photon scattering to the receiver (typically a factor of $\geq$ 1100), which must be overcome by much more laser power and a larger receiver telescope. (2) A much faster along track velocity (7 km/sec vs 0.25 km/sec) which increases the rate of reflectance variability. (3) A larger spot diameter (typically 100 m vs 2 m) on the surface, which can increase range spreading. (4) The need to withstand the launch vibration and the vacuum and radiation environment of space. (5) For space, the lidar design and instrument technology (including components like detectors) also must provide a high confidence for at least 3-5 years of unattended operation.

All the airborne lidar candidates need further investments to attain a high technical readiness for space. The largest common factor is the need for improvement of the product of laser power and telescope area to overcome the signal loss due to increased range from orbit. Direct detection lidar can benefit by using a larger diameter telescope, but the laser power still must be increased significantly, typically by a factor of 10-100, over current airborne instruments. The highest common need is for a laser, that meets all other requirements and that also has the needed power for space. The approach needs to have a viable technical path to achieve these ends in a robust and mechanically rugged design that can be shown to have long unattended lifetime and also can withstand the radiation and vacuum environment of space. The individual teams have addressed the scaling of their approaches to space, and their progress towards this are summarized below.

5.6.1.1 Scaling the CO_2 Sounder to Space

For space the CO_2 Sounder plan is to sample both gas absorption lines with 8 wavelengths, as shown in Figure 5-41 and Figure 5-43. The time resolved laser backscatter is detected and range resolution is used to isolate the return pulses from the surface and measure range.

A block diagram of the space lidar concept is shown in Figure 5-41. The seed lasers are rapidly switched from fixed locked wavelengths points, producing a repeating wavelength-stepped pulse train. The lasers cycle through their wavelength steps every 1 msec. At an 8-KHz pulse rate, the pulses are separated by 125 μsec, which permits them to clear the bottom 19 km of the atmosphere before the next pulse, to minimize crosstalk from cloud scattering. A 5-KHz pulse rate can also be used to allow a 30 km unambiguous range, if needed, to accommodate higher clouds. At the 7-km/sec spacecraft velocity the ~50-m diameter laser spot in the surface moves 0.9 m for each wavelength step. It is easy to show that in 10-second averaging time, this sampling with highly overlapped footprints minimizes any random errors caused by variability in surface reflectivity.

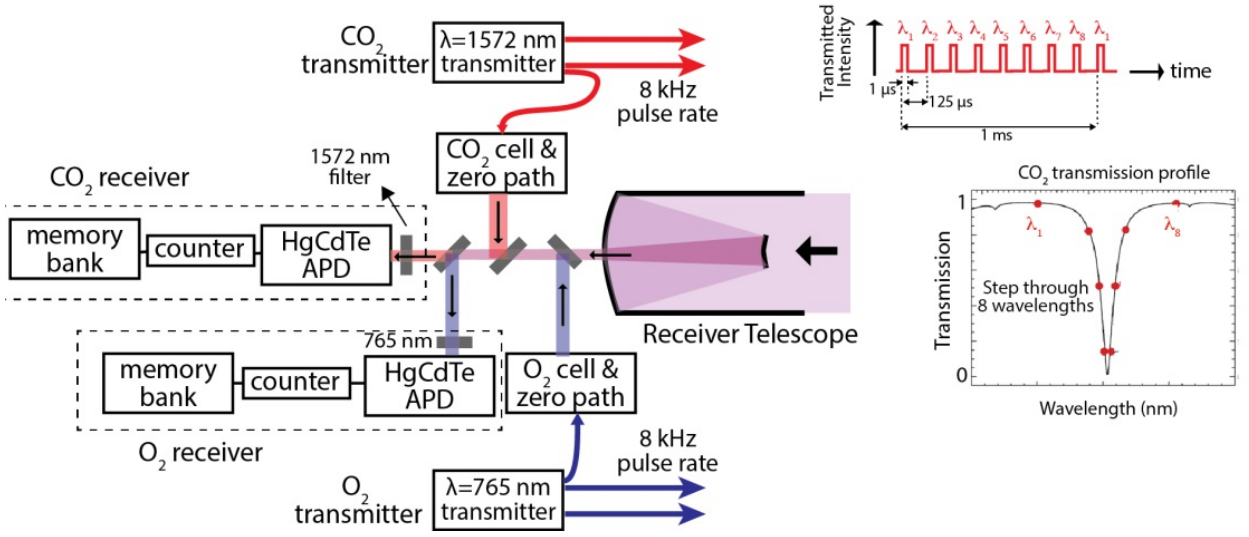

Figure 5-41 Block diagram of the space lidar instrument and wavelength-stepped pulse-train. (Left) Simultaneous measurements are made of CO_2, and O_2, absorption line shapes, time of flight, and backscatter profiles at 1572.33 and 764.7 nm, respectively. The return light is collected by a common 1.2-m telescope and detected. *(Right)* Diagram of the wavelength-stepped laser pulse-train used to measure the CO_2 & O_2 line absorptions.

The CO_2 Sounder team has regularly assessed the measurement performance needed for the space measurement. This work builds on space lidar SNR models, which their team has evolved from work on the CO_2 Sounder airborne instrument and from ICESat/GLAS (Ice, Cloud and land Elevation Satellite/Geoscience Laser Altimeter System) (Abshire et al., 2005). The calculations analyze the signal, noise, and uncertainty in gas concentrations by calculating the average number of signal photons, solar background photons, and detector noise observed over each 1-μsec pulse interval. Preliminary analyses of errors in the airborne lidar are given in (Abshire et al., 2013, 2014). Recent examples and the presently targeted specifications for a space lidar are shown in Figure 5-42.

The calculations for space show that the random errors are limited by the detected signal photons for the measurement wavelengths near the peak of the absorption line. That is the retrievals are limited by the shot noise of the detected signal photons on the absorption line. The analysis of the 2011 airborne measurements is consistent with this model (Abshire et al., 2014), although the space measurements benefit substantially from the higher sensitivity of the HgCdTe APD detector.

At the accuracies required for ASCENDS, there are many potential sources of bias error, both from the environment (the atmosphere and the surface) and from the instrument. Some are atmospheric scatter, varying topographic height, line spectroscopy, pressure shifts of the absorption line, and instrument wavelength or baseline offsets. The CO_2 Sounder approach using pulsed measurements with multiple wavelength samples on both sides of the CO_2 line allows additional parameters to be "solved for" in the retrievals. This makes the measurements quite robust against many potential causes of measurement bias. Analysis of the 2011 airborne measurements shows that presently the bias errors are small (< 1.4 ppm) for aircraft altitudes > 5 km (Abshire et al., 2014). This residual error level will be reduced further as the airborne lidar and the retrievals algorithms are improved.

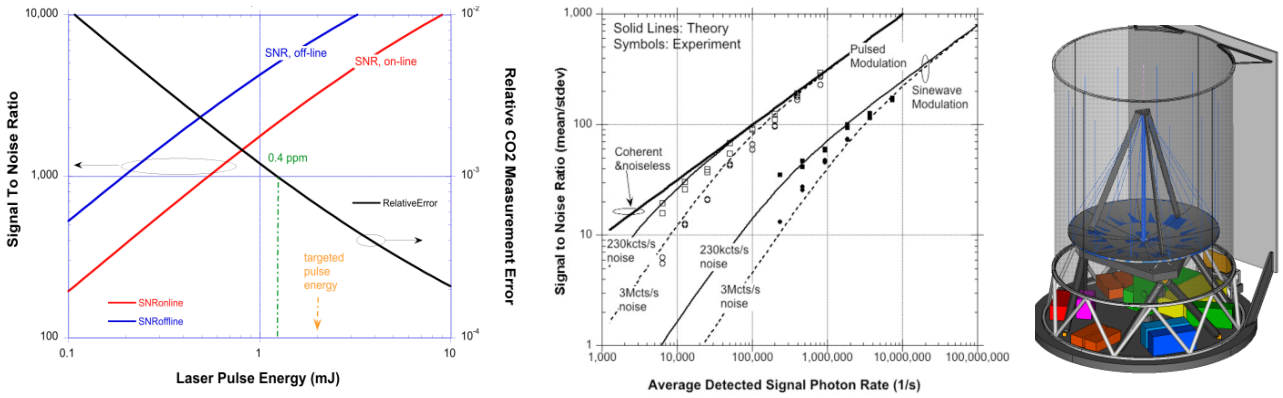

Common Parameters	Value	Specific values for :	CO2
Orbit Altitude	400 km	Online wavelength	1572.33 nm
Equator crossing time	dawn/dusk	Beam divergence	125 urad
Integration Time	10 sec (70 km)	Wavelength sequence rate	1.25 KHz
Telescope diameter	1.5 m	# of wavelengths in scan	8
Time between laser pulses	125 usec	On line (side of line) absorptio	40%
Laser Pulse widths	1 usec	Detector type & QE	HgCdTe APD, 75%

Figure 5-42 Modeled and measured SNR for efficient pulse modulation technique. *(Left top)* Calculations of SNR and relative error in CO_2 column densities for the space lidar vs laser energy. 1.2-mJ laser pulse energies are needed for a 0.4-ppm precise measurement over a 40% diffuse reflectivity surface, similar to RRV Nevada. A conservative goal (with margin) is assuming 2-mJ energy is needed. The calculations above also have 3-dB margin. *(Middle top)* Results of a comparison (Sun and Abshire, 2012) of the receiver SNR vs signal for IPDA lidar using coherent detection with continuous wave (CW) lasers and direct detection with sinewave and pulse modulations. Our pulse modulation technique is much more efficient and requires only ~10% of the laser power to achieve the same SNR as sine wave modulation. *(Right top)* Drawing from a previous space instrument design lab study for the space lidar. (*Bottom*) Parameters for the SNR calculations.

Lidar Requirements Analysis for Space – The CO_2 Sounder team periodically assesses the lidar performance needed for the space CO_2 measurement. This builds on our space lidar SNR models, which we have evolved from ICESat/GLAS (Ice, Cloud and land Elevation Satellite/Geoscience Laser Altimeter System) (Ehret et al., 2008) and applied to the IPDA measurement of CO_2. The calculations analyze the signal, noise, and uncertainty in gas concentrations by calculating the average number of signal photons, solar background photons, and detector noise observed over each 1-μsec interval of the laser pulses. Recent results are shown in Figure 5-42.

The calculations show that the CO_2 transmitter must emit ~1.2 mJ/pulse (12-W average power) to produce a 0.4-ppmv mixing ratio measurements from space to desert surfaces with a 1.5-m diameter telescope. To allow margin, our targeted energy is 2 mJ. The analysis of the CO_2 Sounder team (Sun et al., 2010) shows this is a very power-efficient approach to meet the CO_2 measurement requirements.

5.6.1.1.1 Space Lidar Technology for the CO_2 Sounder

Laser Transmitter – The CO_2 Sounder approach uses a master-oscillator power-amplifier (MOPA) approach for both the lasers. It uses tunable diode seed lasers, fiber laser preamplifiers, and power amplifier stages. This modular approach is flexible, and it leverages the lower power

stages that have already been demonstrated in airborne campaigns. The power increase needed for space is achieved adding power amplifiers to the prior stages, and so that the space laser is an incremental step and is not a new development.

The diode seed lasers for the CO_2 and O_2 wavelengths are highly developed, and have been space qualified. To meet the precision, the online lasers need to be frequency stabilized to ~1 MHz (Numata et al., 2012). The CO_2 Sounder Team has demonstrated locking the master laser diode (DFB-LD) to the CO_2 line center and achieved frequency drifts < 0.3 MHz over 72 hours. They have also demonstrated a new dynamically step-locked single laser diode seed source shown in Figure 5-43. This source accurately and dynamically locks its output to 8 or more wavelengths around the CO_2 absorption line. This allows a significant simplification to the seed laser stage.

Laser amplifiers - The airborne lidar uses a commercial Erbium Doped Fiber Amplifier (EDFA) as a preamplifier, and the total output energy is 25 μJ/pulse with 0.25-W average power. Lucent LGS (Lucent Government Solutions) had previously developed a set of highly reliable EDFA technologies for aircraft and space use. They previously space-qualified a 10-W brassboard EDFA (Wysocki et al., 2006).

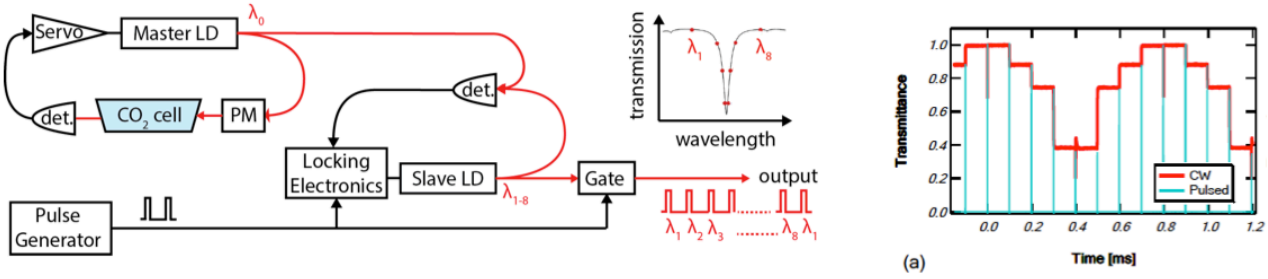

Figure 5-43 Schematic of a stepped wavelength locked source as shown in (Numata et al., 2012). *(Left)* The master wavelength is locked to a CO_2 absorption cell. By offset-locking a slave laser at different frequency offsets to the master, this approach generates a pulse train step-locked 8 discrete points on the 1572.335 nm CO_2 line. (*Right)* Output from the laboratory demonstration when seed laser was wavelength stepping across a CO_2 line, as in the middle sketch.

For space this needs to be increased by ~80 times by a laser power amplifier. The team has investigated two different approaches for the power amplifier stage: using a single channel Planar WaveGuide amplifier (PWG - Raytheon) and using multiple large mode area fiber amplifier channels in parallel (Fibertek). These amplifier approaches can be used both for the CO_2 and O_2 lasers. Both approaches are attractive, although they have different engineering aspects and tradeoffs. A breadboard of the Raytheon planar waveguide power amplifier is under final development now, and a demonstration is planned during fall 2014.

Receiver Telescope – For a space lidar, a large receiver telescope collects more backscatter, and so be used reduce the laser power. The calculation above assumed a 1.5-m diameter receiver telescope, which is available.

Lidar Detectors –Both the CO_2 and O_2 lidar receivers need sensitive detectors. The CO_2 Sounder plan is to utilize the new DRS HgCdTe e-APD (Beck et al., 2013) developed under the IIP-10 shown in Figure 5-44 as the detector for both channels. This detector has gain > 500, Quantum Efficiency (QE) > 70% from 0.5 to 4 μm, photon-noise limited response) and a NEP < 0.4 fW/

$Hz^{1/2}$. Initial radiation tests show the detector is tolerant to the expected space radiation dose. More radiation tests are scheduled.

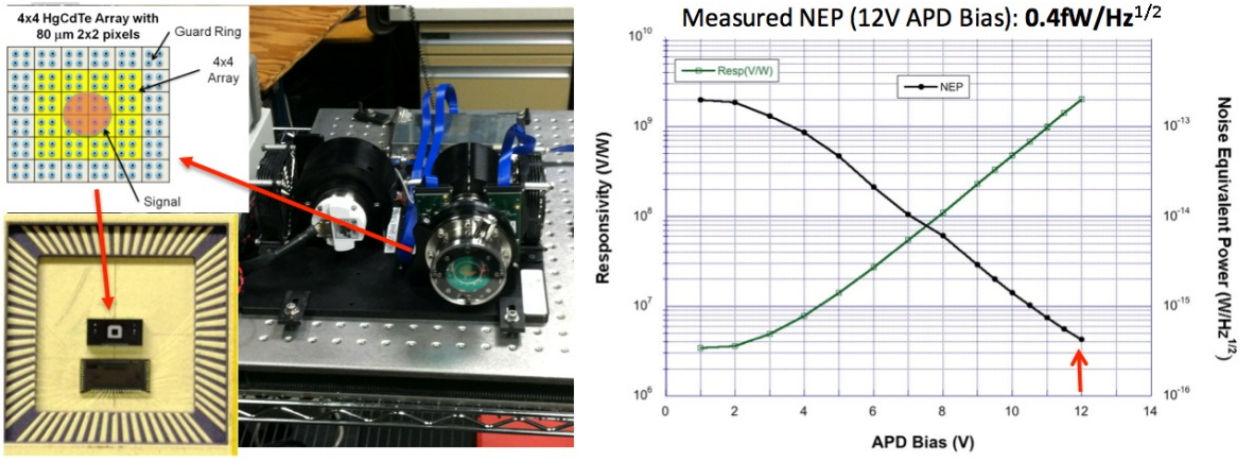

Figure 5-44 The highly sensitive 4x4 element HgCdTe APD array inside a mini-dewar/cryocooler assembly *(Photo)*. This was developed by DRS for the CO_2 Sounder's IIP-10 task and was delivered in April 2013. The pixels are square 80 μm on a side, which was chosen to match the needs for a CO_2 space lidar receiver. *(Plot)* Results from Goddard's evaluation of the detector sensitivity shows at 12-V bias, the pixels have QE = 80% and noise equivalent power of ~0.4 fW/root (HZ). This > 30 times more sensitive than previous solid-state detectors at 1.57 μm.

The DRS detector operates at 80 K, which requires a cryo-cooler. A recent paper (Raab et al., 2010) summarizes space cryocoolers since 1995. One option is a pulse-tube microcooler from Northrup Grumman. This is attractive because it is small and can pump 1.3 W from a source load at 77 K, more than is needed.

5.6.1.2 Advancing Airborne IM-CW instruments to Space

The LaRC ASCENDS team has developed a model for LAS system and CO_2 measurement simulations (Lin et al., 2013). Such models are essential for the improvement of LAS systems and the prediction of the performance of space CO_2 measurements for future space missions. Validation tests show excellent agreements of simulated results with ground-based and airborne LAS measurements (Lin et al., 2013). The simulations show a potential for the ASCENDS mission using technologies that currently exist or are expected to be available within next few years. The studied spaceborne IM-CW LAS instrument will achieve root-mean-square errors of CO_2 column measurements for surfaces similar to the playa of Railroad Valley, NV within 0.1% for 10-s averages (Lin et al., 2013). Figure 5-45 illustrates the basic structure of the space LAS instrument which is expected to have a system architecture similar to that of the airborne LAS instrument.

Compared to the airborne lidar, the main changes for space are using two sideline wavelengths with one at +3 pm (called Side-1) and the other at +10 pm (called Side-2) offset from the CO_2 absorption line center; increasing the transmitted laser output power to 42 W; increasing the telescope diameter to 1.5 m; reducing the receiver optical bandpass filter bandwidth to 0.5 nm FWHM; and reducing the laser half-angle divergence to 50 μrad (Lin et al., 2013). The receiver's FOV will be set to be 33% larger than that of laser divergence, and the optical throughput is expected to be 0.65. The sideline wavelengths are selected to avoid excessive absorption by CO_2 in the upper troposphere and lower stratosphere when tuned to the absorption line center, and to have more sensitivity to CO_2 absorption across the mid to lower troposphere (lower-altitude

weighting function), where most of the CO_2 flux exchanges with ecosystems and transports within the atmosphere take place.

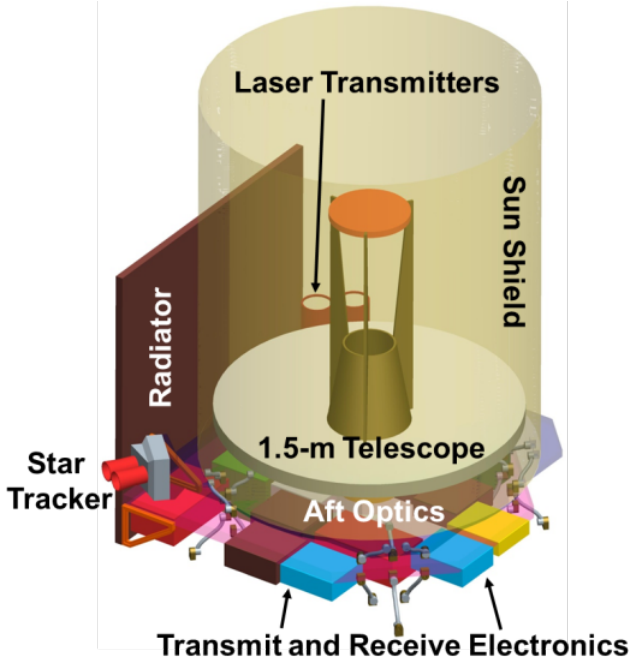

Figure 5-45 Concept for a space-based LAS lidar.

5.6.1.2.1 Model and Simulations for MFLL Space Lidar

The performance of the space lidar for CO_2 measurements was simulated using a model developed by the LaRC Team (Lin et al., 2013). This model for the lidar and its measurement environment are important to guide improvement of LAS systems and allows for predictions of CO_2 measurements for future space missions. The model accounts for fundamental physics and characteristics of the instruments and their related measurement environments. The model results are presented statistically from simulation ensembles that include noise sources and uncertainties related to the LAS instruments and the CO_2 measurement environment. The characteristics of simulated LAS systems are based on existing technologies and their implementation in existing systems.

The modeled lidar is assumed to be IM-CW LAS systems such as the Multifunctional Fiber Laser Lidar (MFLL) operating in the 1.57 μm CO_2 absorption band. Environmental effects due to variations in atmospheric CO_2, solar radiation, turbulence, surface reflectance, and aerosols and thin clouds are also included in the model. The simulated results show excellent agreement with measurements (Lin et al., 2013). Figure 5-46 shows an example of the comparison of model-simulated results with instrument measurements for the Railroad Valley playa flight on 3 August 2011 at 6.1-km altitude. The differences in CO_2 DAOD between model results and observations are very small, clearly demonstrating the capability of the model in modeling the performance of LAS systems and their CO_2 column measurements.

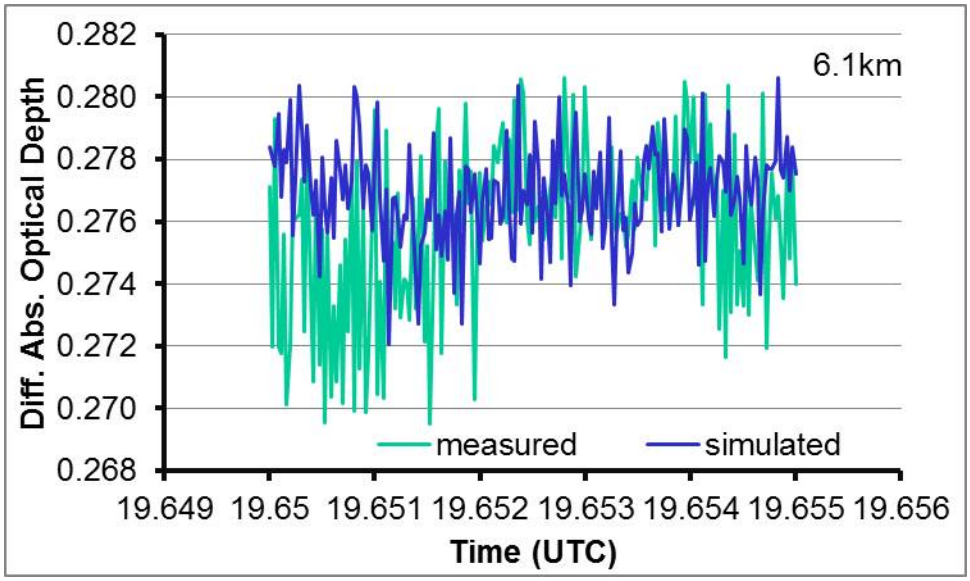

Figure 5-46 Comparison of simulated results of DAODs with observations for RRV. The Railroad Valley playa flight was on 3 August 2011. Data analyzed are for the flights at 6.1-km altitude.

For the ASCENDS space mission, the assumptions are a sun-synchronous, dawn/dusk orbit (Ehret et al., 2008) with an altitude of 390 km. Under clear conditions, simulation shows that the precision of the DAOD measurements for surfaces similar to the playa of Railroad Valley, NV (reflectance 0.176 sr^{-1}) will be better than 0.07% for 10-s averages (Figure 5-47).

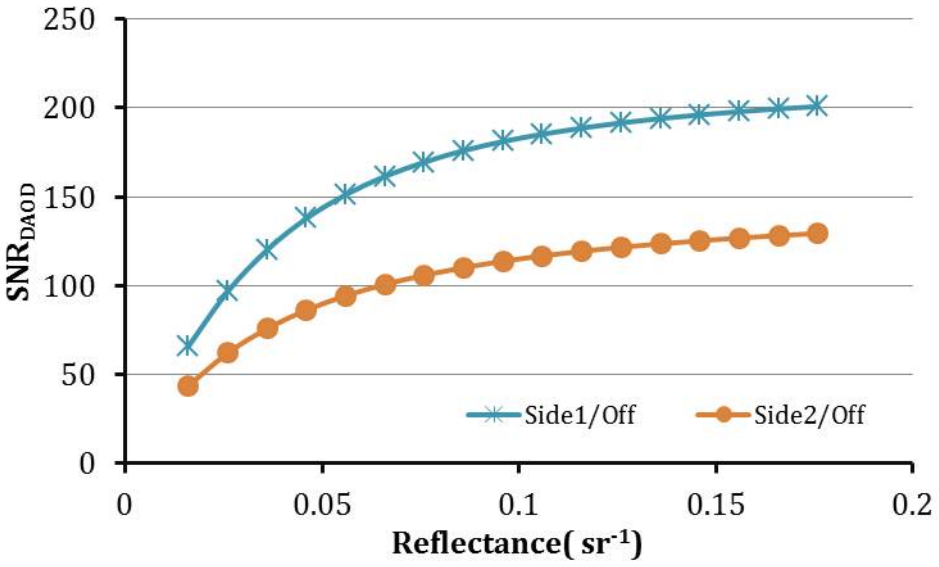

Figure 5-47 Simulated 0.1-s SNR_{DAOD} for the space IM-CW LAS instrument for a range of surface reflectance conditions.

For other types of surfaces such as low-reflectivity snow and ice surfaces, the precision will be within 0.23%. Including measurements through thin clouds with optical depths up to 1, the CO_2 SNR_{DAOD} measurements with 0.1-s integration period for surfaces similar to that of Railroad Valley, NV will be greater than 94 and 65 for Side-1 and Side-2, respectively (Figure 5-48).

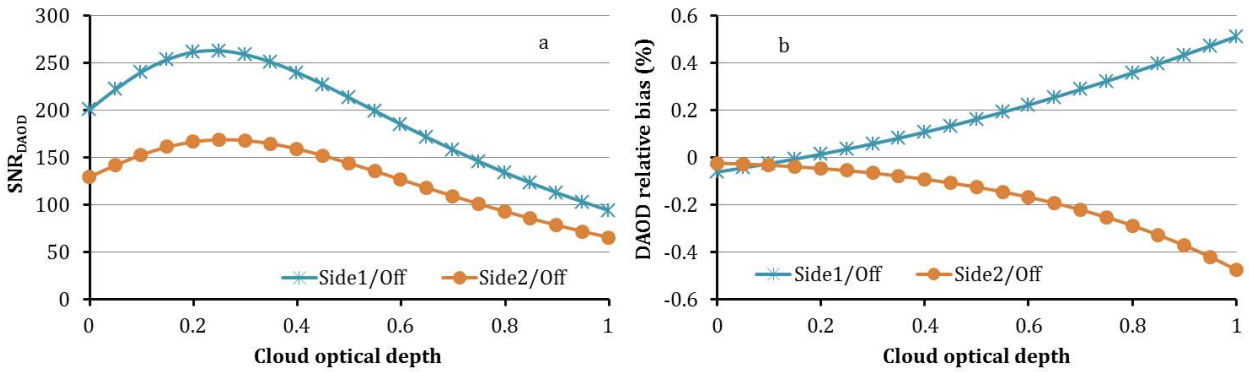

Figure 5-48 Simulated 0.1-s results for a spaceborne lidar under thin cirrus cloud conditions. The CO_2 SNR_{DAOD} (a) and relative bias error (b) values are calculated for the surface assuming the reflectance of Railroad Valley, NV.

The CO_2 column bias errors introduced by the thin clouds are $\leq$ 0.1% for cloud optical depth $\leq$ 0.4, but they could reach ~0.5% for more optically thick clouds with optical depths up to 1 (Figure 5-48 b).

When the cloud and surface ranges and scattering amplitudes are obtained from the analysis of matched filter outputs, the cloud bias errors can be further reduced as seen from the compensating feature of the bias errors between the retrievals of the two sidelines (Figure 5-48 b). Other simulation studies indicate that the present IM-CW LAS concept for space can provide ASCENDS required CO_2 measurements from not only the dawn/dusk orbit but also other Low Earth Orbits (LEOs) such as sun-synchronous, day/night orbits, maximizing the flexibility of the space instrumentation to various CO_2 measurement needs.

5.6.1.3 Scaling the BBL Lidar to Space

It can be shown using simple arguments that to achieve a precision of 1 ppm the lidar receiver must detect on the order of 1-2 million photons per integration time. With a large telescope and sensitive detectors the million photons threshold can be reached with 20-40 Watts of emitted laser power. It is highly desirable that the detector used for ASCENDS have a high Quantum Efficiency (QE) and be able to respond to individual photons. As noted the latest version of the BBL splits the two detector functions—ranging and signal level measurement between two separate detectors. The BBL lidar plan is to use single photon counting modules (SPCM) used on ICESAT are employed to measure the LIDAR range and InGaAs or Mercury Cadmium Telluride (MCT) cameras as employed on SCanning Imaging Absorption Spectrometer for Atmospheric CartograpHY (SCIAMACHY) are used to measure signal level. The BBL calculations show this combination of detectors allows the BBL to achieve ~2 million detected photons with a laser source that emits ~ 40 Watts. The BBL performance simulations show that the Broad Band Lidar meeting the specifications summarized in Table 5-11 can meet the ASCENDS measurement requirements operating in clear air over surfaces including snow and open ocean.

Table 5-11 Space-based Broad Band Lidar Parameters

Space-based Broad Band Lidar Parameters	
Laser Average Output power:	
2.05 μm	30-40 W
0.68 μm	1 W
Laser-Pulse-Rate	8000 Hz
Telescope-Diameter	1 m
Detector type:	
2.05 μm	Rockwell HgCdTe Array
0.68 μm	Perkin-Elmer SPCM

5.6.1.4 Scaling the Pulsed 2-μm CO_2 IPDA Lidar to Space

The 2-μm IPDA lidar approach has also examined its pathway for CO_2 measurements from space. Table 5-12 summarizes technology parameters of the present airborne IPDA lidar, future IPDA system, and recently released pulsed 2-μm IPDA technology development requirements from European Space Agency (ESA) (Ingmann et al., 2008) for their future space borne active sensing mission for measuring the dry-air mixing ratio of carbon dioxide throughout the atmosphere with a accuracy on the ppm level (Ingmann et al., 2008; NASA, 2008; Lawrence, 2011).

The plans for laser development are consistent with the transmitter requirements as summarized in the table. This early development of a space qualifiable laser and airborne operation will reduce the risk towards space operation. Extending the CO_2 IPDA instrument capability to space also requires a detector with better performance than the present InGaAs pin detector. The electron avalanche photodiodes (eAPD) developed by DRS Technologies provide a possible solution (Beck et al., 2011). Table 5-12 lists a comparison between the selected pin detector and the eAPD with space requirements. The detector approach is an important aspect in this comparison.

Table 5--12 Comparison of CO_2 state-of-the-art 2-μm current and proposed technology with space requirement

	Current Technology	Proposed Technology	Projected Space Requirement [2]
	Laser Transmitter		
	Single Laser	**Single Laser**	**Two Lasers**
Technology	Liquid-Cooled, Airborne laser	Conductively-Cooled Space Qualifiable laser	Column CO_2 Space Mission
Technique	Double-Pulse	Triple-Pulse	Single-Pulse
Laser Wavelength (μm)	2.051	2.051	2.051
Pulse Energy (mJ) $1^{st}/2^{nd}/3^{rd}$ Pulse	100/30 Double Pulse	50/15/5 Triple Pulse	40/5 Single Pulse
Pulse Repetition Rate (Hz)	10	50	50
Power (W)	1.3	3.5	2.25
Pulse Width FWHM (ns)	200	30-100	50
Optical to Optical Efficiency (%)	4.0	5.0	5.0
Wall Plug Efficiency (%)	1.44	2.1	>2.0
Delay between pulses (200 μsec)	200	200	250+/-25
Transverse/Longitudinal Modes	TEM_{00}/Single Mode	TEM_{00}/Single Mode	TEM_{00}/Single Mode
Pulse Spectral Width FWHM (MHz)	2.2	4-14	> 60
Beam Quality (M2)	2	2	< 2
Frequency Control Accuracy (MHz)	0.3	0.3	0.2
Seeding Success Rate /Spectral Purity (%)	>99/99.9	>99/99.9	>99/99.9
	Detector		
Material	InGaAs	HgCdTe	N/A
Structure	Pin photodiode	eAPD	APD
Quantum Effficiency (%)	68	80	75
Excess-Noise-Factor	---	1.1	1.5
Noise-Equivalent-Power (fW/Hz1/2)	200	8	100

5.7 Ongoing Technology Development Activities and Planned for Results

So far during the formulation of the ASCENDS mission, NASA has supported several different candidate lidar approaches and teams. This has yielded many benefits, has engaged many lidar researchers, and has helped develop a broader understanding of the mission needs and candidate lidar approaches. This work, including the airborne campaigns, has been very valuable and it

should continue. However as the ASCENDS mission matures, the mission needs will shift more toward lidar technology and engineering.

Several of the airborne instrument teams are addressing different aspects of the space instrument needs. These include studies to determine the required laser power, simulations of space measurements, and preliminary engineering studies of candidate space instruments. Some initial airborne lidar demonstrations of the O_2 column measurements have also been made. Under ESTO IIP support there has been the successful development of candidate detectors for the space mission, and there is ongoing work to demonstrate some approaches toward laser power scaling.

5.7.1 Technology Developments Needed for ASCENDS

There are several types of technology development activities needed to increase the readiness and reduce the risk of the ASCENDS space lidar(s). The lowest risk approach is to incrementally build on capabilities already demonstrated in airborne campaigns. These include work to:

a. Improve the fidelity of the space instrument requirements via more realistic mission simulations and with improved models to infer CO_2 fluxes.

b. Update tradeoff assessments addressing mission benefits vs costs/risks for the O_2 lidar.

c. Improve the airborne O_2 lidar's column measurement capabilities with the goal to reach a similar state of readiness already shown for CO_2. A particular need is for increased O_2 laser power in the airborne lidar.

d. In the context of an overall lidar instrument design, including spacecraft resource requirements (mass, power, envelope, data rate), demonstrate the space-needed power for the CO_2 laser(s), while maintaining the other required laser properties.

e. Depending on the outcome of (b), demonstrate the space-needed output power and efficiency for the O_2 laser, while maintaining the other required laser properties.

f. Demonstrate measurements with the space evolving subsystems, perhaps via an ASCENDS airborne simulator, to verify they achieve the needed performance and science measurements.

g. Conduct preliminary designs for the space lasers that address the required output power; power conversion efficiency; mechanical design; thermal, vacuum and radiation tolerance; and lifetimes.

h. Assess lifetime and radiation tolerance of candidate detectors.

i. Conduct preliminary lidar instrument and mission studies to allow an early view on tradeoffs and an initial assessment of critical areas.

To be cost effective it is recommended that NASA: (1) develop a process for evaluating and selecting the highest priority space lidar approaches to concentrate on for this part of the mission development, and (2) develop acquisition and implementation strategies for the ASCENDS payload.

6. Mission Design

6.1 Introduction

In 2012, NASA's Earth Science Division (ESD) requested the Earth Systematic Mission Program Office (ESMPO) to perform a mission study to determine the feasibility of accommodating a conceptual ASCENDS instrument on commercially available spacecraft buses as well as the feasibility of flying a conceptual observatory on an Evolved Expendable Launch Vehicle (EELV) and in a Dual Spacecraft System (DSS) configuration. The team was made up of representatives from the ESMPO, the Goddard Space Flight Center (GSFC), the Jet Propulsion Laboratory (JPL) and the Langley Research Center (LaRC). The mission study covered eight areas and includes assessments in the areas of mass, power, mechanical/thermal interface, volumetric, attitude determination and control (AD&CS), telecom, mission operations, and de-orbit considerations. Assessments captured design requirements, assumptions, finding and results, design rationale, design risks, and additional comments. The generic instrument parameters used in the study are captured in the Table 6-1 shown below. The final report (Hyon et al., 2012) has documented the results and findings of the assessments, summarized those results and findings, and provided recommendations for future studies.

Throughout the report, Ball's BCP 2000 bus has been used as an example of a bus appropriate for supporting the ASCENDS mission. Buses from other manufacturers, including Boeing, Lockheed Martin, Northrop Grumman, Orbital Dulles and Orbital Gilbert are also quite capable of supporting the ASCENDS mission. The Figure 6-1 depicts one of the spacecraft configurations with hosted payload and the ASCENDS instrument.

Table 6-1 ASCENDS Generic Instrument Parameters

Parameter	Generic Payload 1	Generic Payload 2
Mission Parameters:		
Measurement	CO_2, O_2, and altimetry	CO_2 and altimetry
Launch Requirements:		
Nominal Orbit	Sun-sync, ~noon crossing	Sun-sync, ~noon crossing
Altitude (Km)	~450 km ± TBD km	~450 km ± TBD km
Inclination	Polar	Polar
Design Operational Life	3 yrs with propellant for 6 yrs	3 yrs with propellant for 6 yrs
Current Best Estimate (CBE) Instrument Size (m)	<2.5 tall x 2 x 2	<2.5 tall x 1.5 x 1.5

Parameter	Generic Payload 1	Generic Payload 2
Science and C&D Handling:		
Average Science Data Rate (Mbps)	20	20
Maximum Science Data Rate (Mbps)	-	-
Instrument Housekeeping Telemetry		
Instrument Housekeeping Telemetry Data Rate (Mbps)	0.1	0.1
Onboard Data Storage (Gbits/day)	~1750/day	~1750/day
Instrument Mass:		
Total Instrument Mass Allocation (CBE+Margin, kg)	<470	<400
Instrument Power:		
Total Instrument Power Allocation (CBE+Margin, W)	<1100	<750
Mechanical Interface:		
Mechanical Interface, e.g., kinematic, planar, etc.	Instrument to I/F panel - Kinematic	Instrument to I/F panel - Kinematic
Interface Panel or hard mount to bus	I/F panel	I/F panel
Field of View (FOV)	<1.5° about nadir	<1.5° about nadir
Attitude Control:		
Pointing Knowledge	5 arc sec	5 arc sec
Pointing Control	20 arc sec	20 arc sec
Jitter	0.4 arc sec over 4 ms and 5 arc sec over 20 ms	0.4 arc sec over 4 ms and 5 arc sec over 20 ms
Attitude Control Subsystem (ACS):		

Parameter	Generic Payload 1	Generic Payload 2
Global Positioning System (GPS) Receiver	YES	YES
Post Processing GPS onboard knowledge	-	-
Star Trackers	YES	YES
Major Maneuvers	Yaw flip as required; calibration as required; on orbit stability after maneuvers	Yaw flip as required; calibration as required; on orbit stability after maneuvers
Instrument Thermal Requirement:		
Thermally isolated	YES	YES
Thermal FOV	Based on instrument thermal requirements	Based on instrument thermal requirements
Cryo Cooler	Will be provided as part of the ASCENDS instrument	Will be provided as part of the ASCENDS instrument
Propulsion	Required for orbit maintenance.	Required for orbit maintenance.
Design	Standard biprop or monoprop blowdown	Standard biprop or monoprop blowdown
Observatory Environmental & Facility (driven by Instrument):		
NASA Risk Classification	Sensor: C Platform: B	Sensor: C Platform: B
Electromagnetic Interference / Electromagnetic Compatibility (EMI/EMC)	Per MIL-STD-461C, tailored as required	Per MIL-STD-461C, tailored as required
Vibe	General Environmental Verification Specification (GEVS) for Atlas & F9 LV	GEVS for Atlas & F9 LV
Thermal Vacuum (TVAC)	YES	YES
Radiation	Meet orbit levels	Meet orbit levels
Cleanroom Class	As required	As required

Parameter	Generic Payload 1	Generic Payload 2
Special Facility Needs	Per instrument type	Per instrument type
Mission Operations:		
S/C ballistic coefficient	2.2	2.2
Cross-sectional area	19.1 m^2	19.1 m^2

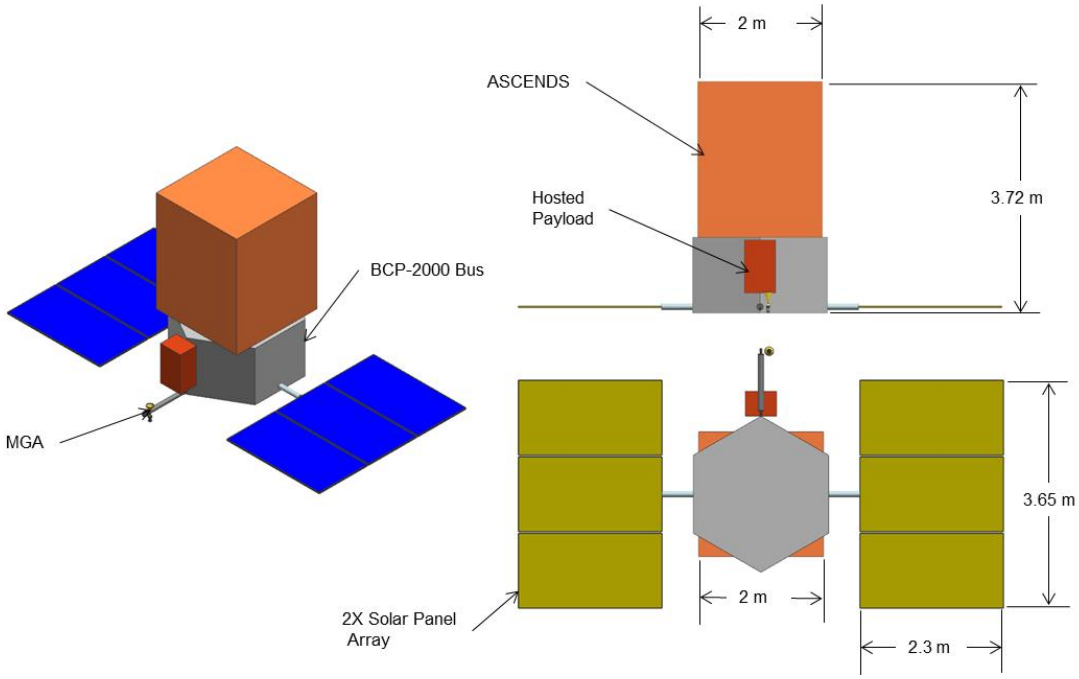

Figure 6-1 Hosted payload mounted to the side of the spacecraft bus.

The team has concluded that there are many commercial buses available with Falcon 9 or Atlas V launch vehicle in order to accommodate existing lidar concepts. With a CO_2 lidar only option, a follow-on study will develop more cost effective spacecraft bus and launch options.

6.2 Summary of Assessment

6.2.1 Summary

A preliminary study of conducting a lidar-based, CO_2 mapping mission of ASCENDS has been published in the report (Hyon et al., 2012). Although a variety of potential spacecraft buses have been included in the sections on volumetric assessment of accommodating the ASCENDS instrument, the Ball BCP2000 bus has been assumed as the baseline for the sections on power, mechanical/thermal, AD&CS, and telecom assessment. The design assessments are developed based on a preliminary design from Ball, as enhanced via a JPL Team X study conducted in June 2012

Therefore, the results of this study are that multiple commercially available spacecraft buses should be able to support accommodating an ASCENDS instrument with the parameters used in this study with minor mission specific modifications. Examples include but are not limited to a larger propulsion system and propellant for orbit maintenance maneuvers as well as a larger power system to accommodate the instrument power requirements. Additionally, the Falcon 9 or Atlas V (EELV) launch vehicle can accommodate an ASCENDS observatory with the parameters used in this study in a single manifest configuration. A dual manifest configuration is also possible if the ASCENDS instrument is limited in volume to approximately 2.5m tall by 1.8m by 1.8m.

6.2.2 Recommendations for Future Studies

Future studies of spacecraft buses capable of supporting the ASCENDS mission and a TBD hosted payload (e.g., EV-I) should consider a more thorough and detail approach to describing the subsystems as documented in the report (Hyon et al., 2012). Of course, the point-of-departure should be the existing buses as documented by Ball, Boeing, Lockheed Martin, Northrop Grumman, and Orbital. Any other approach that assumes the design of a customized bus would result in an ASCENDS mission priced beyond the estimated, future NASA budget for the ASCENDS mission.

In addition to future spacecraft studies mentioned above, the trade studies listed below are planned to be assessed by each center in the near future.

1. Determination of risk classification for the spacecraft bus and instrument
2. Orbital debris assessment to determine if a controlled re-entry will be required
3. Evaluating orbit altitudes from 350 – 450 km and impact on the mission
4. Examination of the trade space for the next generation of laser instruments
5. Investigations to determine if the instrument resolution needs to change to accommodate orbit and/or spacecraft attitude control capability

6.2.3 Recommendation for an Implementation Schedule

As a notional launch date of no earlier than 2021, we recommend a mission implementation duration for 5.5 years between start of Phase A to launch. From the past mission implementations of this class of missions, it is reasonable to have this phase duration with sufficient reserves to control risks. As a result, the project Preliminary Design Review (PDR) can occur as late as 5 years before the launch and Mission Concept Review (MCR) will occur 2 years before PDR.

Table 6-2 provides a notional schedule of mission implementation, where FY N denotes the first year of Phase A. Establishment of a science working group will occur 3 years before Phase A. The level 1 mission requirements will be finalized 1 year before Phase A, and the level 2 mission requirements will be finalize by MCR.

Table 6-2 Notional schedule of mission implementation

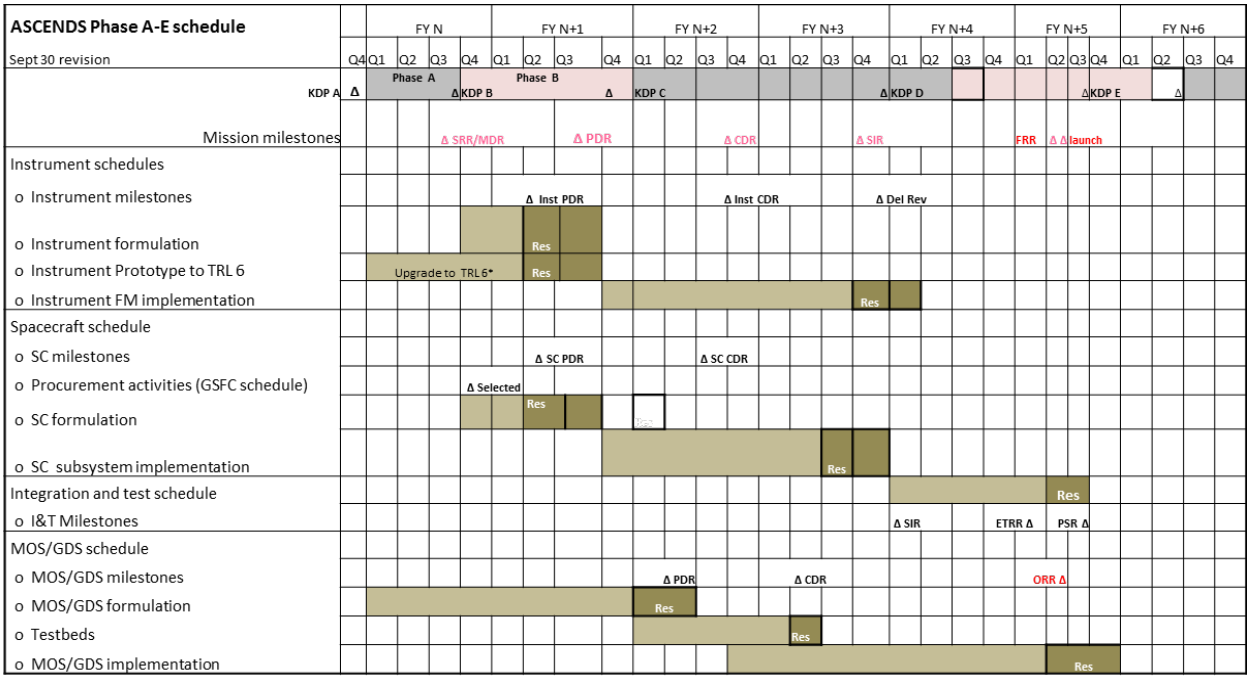

7. Summary

7.1 Summary

Globally-distributed atmospheric CO_2 measurements are essential for understanding the Earth's carbon cycle and its interactions with the climate. A critical remote sensing challenge is to provide atmospheric CO_2 measurements with sufficient coverage, accuracy and sampling frequency to allow the locations and magnitudes of CO_2 sources and sinks to be inferred from the small changes they cause in atmospheric CO_2 concentrations.

Two satellite missions have been developed specifically to measure atmospheric CO_2 using passive spectrometers: the Japanese GOSAT satellite and NASA's OCO-2 mission. The contributions of these passive missions to understanding the global carbon cycle are significant. When conditions are favorable, these approaches allow accurate measurements of atmospheric CO_2 from space.

However, passive approaches also have inherent limitations in coverage, since favorable conditions require sunlit scenes, free of clouds, with low scattering, and with accurate estimates of surface elevation within their footprint. There are many important regions for carbon cycle and climate studies where favorable conditions seldom occur. For passive sensors, atmospheric conditions such as clouds and variations in scattering, coupled with surface elevation errors (which change the length of the measurement path) can cause bias. These biases grow with cloudy scenes and with solar zenith angle and so are particularly troublesome in the tropics and at high latitudes. The sparse coverage at high latitudes is a serious limitation, particularly for the Northern Hemisphere, since this region exhibits substantial emissions even in low-light conditions.

In contrast, the ASCENDS mission carries its own laser source whose characteristics are carefully optimized for these measurements. This approach allows simultaneous measurements of CO_2 column absorption and range to be taken day and night, over ocean and land surfaces, at all latitudes, and at all times of year. The lidar approach also allows altitude-weighted measurements with enhanced sensitivity to CO_2 in the lower troposphere, where the CO_2 concentrations respond more strongly to surface fluxes. Because the lidar has a small FOV and is nadir pointed, it can see through gaps in clouds. The ASCENDS capability will enable more frequent observations of the southern ocean, especially in the wintertime, where the oceans are otherwise inaccessible to passive measurements. Since ASCENDS can make measurements regardless of sun angle and local time, various non-sun synchronous orbits also can be considered to provide additional information about the diurnal cycle of flux.

NASA has organized the ASCENDS Ad Hoc Science Definition Team to lead the mission definition activities. Their work has focused on developing the mission's science and measurement objectives, conducting science mission modeling studies, and carrying out initial engineering studies of spacecraft concepts. A large fraction of the ASCENDS work has involved developing and demonstrating candidate lidar approaches in airborne campaigns. Candidate techniques that have been demonstrated include two direct-detection lidar approaches that measure both range and CO_2 using an absorption line near 1570 nm. Two approaches have demonstrated measurements of CO_2 using a line near 2051 nm: a CW heterodyne approach and a pulsed direct detection approach that measures both range and CO_2 absorption using the same

line. NASA's Earth Science Technology Office has supported the development of the key lidar technologies.

In parallel with the technique development and system-level demonstrations, Observing System Simulation Experiments (OSSEs) are being conducted to assess the characteristics of the CO_2 fluxes that can be inferred from space-based lidar measurements with various candidate levels of measurement precision and accuracy. The mission simulations have used a lidar measurement model with surface reflectivity maps from MODIS and information on cloud and aerosol heights and extinctions from the Calipso Mission. OSSE analysis has identified some mission science tradeoffs and the formulation of an initial set of ASCENDS measurement requirements.

Preliminary instrument and space mission engineering studies also have been conducted on generic lidar candidate instruments that are suitable for the mission. The payload parameters are consistent with a medium-sized spacecraft bus to be flown in a polar ~400 km altitude orbit. No significant engineering issues have been identified at this stage of mission definition.

7.2 Ongoing Work and Plans

A number of activities are either ongoing or planned for the near future. These are summarized below by focus area.

7.2.1. Activities Planned for the Modeling Group Include:

- *Further quantification of bias reduction impacts on CO_2 flux inference. These include assembling and better estimating OCO-2 biases, refining the ASCENDS bias scenarios, and computing updated flux and uncertainty reduction estimates.*
- *Updating random error comparison with actual OCO-2 error magnitudes and distributions.*
- *Testing the impact of surface pressure errors from meteorological analyses on flux errors and comparing those to the expected flux errors from a laser-based O_2 pressure measurement*
- *Testing the possible benefit of ASCENDS diurnal information by examining dawn/dusk and precessing orbits.*
- *Exploring the potential advantages of vertical profile information from ASCENDS measurements above cloud tops*
- *More closely examining the impact of solving for flux processes*
- *Developing recommendations to NRC's Decadal Survey for CO_2 measurement requirements from space in the post-OCO-2 timeframe*

7.2.2 Activities Planned for Atmospheric Analysis Include:

- *Completing the baseline analyses of surface and upper-air model uncertainties, and developing common statistical metrics to provide uniform analysis results, and enable comparisons between metric results*
- *Summarizing the analyses of surface and upper-air model uncertainties results in a peer review publication.*
- *Completing the baseline impact analysis of uncertainty in knowledge of atmospheric state*

on retrieved XCO_2 by expanding study to 2051 nm and 765 nm wavebands, and providing the characterization of expected end-to-end errors on notional retrieval process.

- *Providing a common representative data set of surface/upper-air observed and modeled atmospheric state values for use in assessment of proposed instrument performance.*

7.2.3 Activities Planned and Needed for the Measurment Group Include Further Demonstrating Capabilities and Measurements from Aircraft. Some Ongoing Needs are:

- *Additional measurements over snow - Snow has a low reflectivity at CO_2 measurement wavelengths. The reflectivity varies with the age and temperature of the snow.*
- *Additional measurements over forests - Some areas of high interest for the ASCENDS mission (such as Amazon region) are forested, understanding measurements over areas with tall trees is important.*
- *Demonstrating CO_2 flux retrievals based on airborne lidar data - Logical candidates are CO_2 fluxes from large areas of rapidly growing crops (such as corn) in the summertime, and CO_2 emissions from cities.*
- *Comparing airborne lidar to satellite measurements – Further comparing lidar and OCO-2 measurements made nearly simultaneously, under a variety of conditions, will be quite valuable and informative*
- *Improving the fidelity of numerical simulations of instrument performance for the ASCENDS mission.*
- *Expanding the mission simulations to include measurements to the tops of some clouds, where initial analysis of airborne measurements show they provide valuable information.*

7.2.4 Activities are Needed to Further Develop Lidar Technology.

All the lidar candidate approaches need technology improvements to attain a high technical readiness for space. The lowest risk approach is to incrementally build on capabilities already demonstrated in the airborne campaigns. These include work to:

- *Improve the fidelity of the derived space instrument requirements via more realistic mission simulations and with improved models to infer CO_2 fluxes.*
- *Demonstrate the laser power needed to meet the required performance for the ASCENDS mission, while maintaining the other required laser properties.*
- *Update tradeoff assessments addressing mission benefits vs. costs/risks for the O_2 lidar.*
- *If the O_2 measurement is retained as a mission requirement, then improve the airborne O_2 lidar column measurement capabilities to reach a similar state of readiness as CO_2.*
- *Assess space lifetime of candidate detectors.*
- *Conduct further lidar instrument and mission studies to allow updated views on tradeoffs and assessments of critical areas.*

7.2.5 Activities Needed for the ASCENDS Mission Planning and Development Include:

- *Assessing instrument accommodations for CO2 and range measurement-only options,*
- *Studying launch vehicle accommodations,* and

- *Updating the preliminary study of lidar and mission costs.*

Accurate and globally-distributed atmospheric CO_2 measurements are essential to improve our understanding the Earth's carbon cycle and its interactions with the climate. The ASCENDS approach, using an orbital IPDA lidar, will allow these measurements over a much wider variety of conditions than is possible with passive sensors. These more accurate measurements, with wider spatial coverage, are key to address important questions about the locations, strengths and evolution of the regional CO_2 fluxes needed for climate models.

Appendices

A. References

[ACOS B2.10 REF] ACOS Level 2 Standard Product: Data User's Guide, v3.4. (2013). *CO_2 Virtual Science Data Environment*. Retrieved from: https://co2.jpl.nasa.gov/static/docs/v3.4_DataUsersGuide-RevB_131028.pdf

[Anon, n.d.] Anon. (n.d.). Standard atmospheric lapse rate. *National Oceanic and Atmospheric Administration (NOAA), NASA, United States Air Force.* Retrieved from: http://ntrs.nasa.gov/archive/nasa/casi.ntrs.nasa.gov/19770009539.pdf

[Aben et al., 2007] Aben, I., O. Hasekamp and W. Hartmann. (2007, April 3). Uncertainties in the space-based measurements of CO_2 columns due to scattering in the Earth's atmosphere. *J. Quant. Spectrosc. Radiat. Transfer, Vol. 104* (Issue 3), pp. 450-459

[Abshire et al., 2005] Abshire J. B., X. Sun, H. Riris, J. M. Sirota, J. F. McGarry, S. Palm, D. Yi and P. Liiva. (2005, November). Geoscience Laser Altimeter System (GLAS) on the ICESat Mission: On-orbit measurement performance. *Geophys. Res. Lett., Vol. 32* (Issue 21). L21S02. DOI: 10.1029/2005GL024028

[Abshire et al., 2008] Abshire, J. B., H. Riris, G. Allan, S. Kawa, J. Mao, E. Wilson, M. Stephen, M. Krainak, X. Sun and C. Weaver. (2008). Laser sounder approach for global measurements of tropospheric CO_2 mixing ratio from space. 24th International Laser Radar Conference, Boulder, Colorado.

[Abshire et al., 2010a] Abshire, J. B., H. Riris, G. R. Allan, C. J. Weaver, J. Mao, X. Sun, W. E. Hasselbrack, … and E. V. Browell. (2010, November 2). A lidar approach to measure CO_2 concentrations from space for the ASCENDS Mission. *Proc. SPIE Vol. 7832, Lidar Technologies, Techniques, and Measurements for Atmospheric Remote Sensing VI,* paper 78320D. Retrieved from: http://dx.doi.org/10.1117/12.868567. DOI: 10.1117/12.868567

[Abshire et al., 2010b] Abshire, J. B., H. Riris, G. R. Allan, C. J. Weaver, J. Mao, X. Sun, W. E. Hasselbrack, S. R. Kawa, and S. Biraud. (2010, November). Pulsed airborne lidar measurements of atmospheric CO_2 column absorption. *Tellus B, Vol. 62* (Issue 5), pp. 770-783. DOI: 10.1111/j.1600-0889.2010.00502.x

[Abshire et al., 2011] Abshire, J. B., H. Riris, G. R. Allan, C. J. Weaver, J. Mao, X. Sun, W. E. Hasselbrack, M. Rodriguez, and E. V. Browell. (2011). Pulsed airborne lidar measurements of CO_2 column absorption. 2011 Earth Science Technology Forum (ESTF2011), Pasadena, CA, June 21-23, 2011, NASA ESTO ESTF-2011 Conference. Avail from: http://esto.nasa.gov/conferences/estf2011/papers/Abshire_ESTF2011.pdf

[Abshire et al., 2013] Abshire, J. B., H. Riris, C. J. Weaver, J. Mao, G. R. Allan, W. E. Hasselbrack and E.V. Browell. (2013). Airborne measurements of CO_2 column absorption and range using a pulsed direct-detection integrated path differential absorption lidar. *Appl. Opt., Vol. 52* (Issue 19), pp. 4446-4461

[Abshire et al., 2014] Abshire, J.B., A. Ramanathan, H. Riris, J. Mao, G.R. Allan, W.E. Hasselbrack, C.J. Weaver, and E.V. Browell. (2014). Airborne Measurements of CO_2

Column Concentration and Range Using a Pulsed Direct-Detection IPDA Lidar. *Remote Sensing, Vol. 6* (Issue 1), pp. 443-469. DOI:10.3390/rs6010443

[Allan et al., 2008] Allan, G.R., H. Riris, J.B. Abshire, X. Sun; E. Wilson, J. F. Burris, and M. A. Krainak. (2008, March). Laser Sounder for Active Remote Sensing Measurements of CO_2 Concentrations. *Proceedings of Aerospace Conference, 2008 IEEE*, pp. 1-7. DOI: 10.1109/AERO.2008.4526387

[Amediek et al., 2008] Amediek, A., A. Fix, M. Wirth and G. Ehret. (2008). Development of an OPO system at 1.57 μm for integrated path DIAL measurement of atmospheric carbon dioxide. *Applied Physics B, 92,* pp. 295

[Amediek et al., 2012] Amediek A., X. Sun, J. B. Abshire. (2012, May). Analysis of Range Measurements From a Pulsed Airborne CO_2 Integrated Path Differential Absorption Lidar. *IEEE Transactions on Geoscience and Remote Sensing, Vol. 5*1 (Issue 5), pp. 1-7. DOI: 10.1109/TGRS.2012.2216884

[Amediek et al., 2013] Amediek A., X. Sun, and J. B. Abshire. (2013, May). Analysis of Range Measurements From a Pulsed Airborne CO_2 Integrated Path Differential Absorption Lidar. *IEEE Transactions on Geoscience and Remote Sensing, Vol. 51* (Issue 5), pp. 2498-2504. DOI: 10.1109/TGRS.2012.2216884

[Andres et al., 2011] Andres, R. J., J. S. Gregg, L. Losey, G. Marland, and T. A. Boden. (2011, July). Monthly, global emissions of carbon dioxide from fossil fuel consumption. *Tellus B, Vol. 63* (Issue 3), pp. 309-327.. DOI: 10.1111/j.1600-0889.2011.00530.x

[Andres et al., 2012] Andres, R. J., T. A Boden, F.-M. Bréon, P. Ciais, S. Davis, D. Erickson, J. S. Gregg, … and K. Treanton. (2012). A synthesis of carbon dioxide emissions from fossil-fuel combustion. *Biogeosciences Discuss, Vol. 9,* pp. 1299-1376. DOI: 10.5194/bgd-9-1299-2012

[Aoki et al., 2000] Aoki, T., T. Aoki, M. Fukabori, A. Hachikubo, Y. Tachibana, and F. Nishio. (2000). Effects of snow physical parameters on spectral albedo and bidirectional reflectance of snow surface. *J. Geophys. Res.: Atomospheres, Vol. 105* (Issue D8), pp. 10219-10236. DOI: 10.1029/1999JD901122

[Archer et al., 2009] Archer, D., M. Eby, V. Brovkin, A. Ridgwell, L. Cao, U. Mikolajewicz, K. Caldeira, … and K. Tokos. (2009, May). Atmospheric Lifetime of Fossil Fuel Carbon Dioxide. *Annual Review of Earth and Planetary Sciences, Vol. 37,* pp. 117 -134.

[Badger et al., 2013] Badger, M. P. S., D. N. Schmidt, A. Mackensen, and R. D. Pancost. (2013, October 28). High-resolution alkenone palaeobarometry indicates relatively stable pCO_2 during the Pliocene (3.3–2.8 Ma). *Phil. Trans. R. Soc. A, Vol. 371.*

[Baker et al., 2006] Baker, D. F., S. C. Doney, and D. S. Schimel. (2006, November). Variational data assimilation for atmospheric CO_2. *Tellus Series B Chemical and Physical Meteorology, Vol. 58* (Issue 5), pp. 359-365.

[Baker et al., 2008] Baker, I.T., L. Prihodko, A.S. Denning, M. Goulden, S. Miller, and H.R. da Rocha. (2008, March). Seasonal drought stress in the Amazon: Reconciling models and observations. *Journal of Geophysical Research: Biogeosciences (2005–2012), Vol. 113,* (Issue G1). G00B01, DOI: 10.1029/2007JG000644

[Ballantyne et al., 2012] Ballantyne, A. P., C.B. Alden, J.B. Miller, P.P. Tans, and J.W.C. White. (2012, Augist 2). Increase in observed net carbon dioxide uptake by land and oceans during the past 50 years. *Nature 488,* pp.70-72. DOI: 10.1038/nature11299

[Basu et al., 2013] Basu, S., S. Guerlet, A. Butz, S. Houweling, O. Hasekamp, I. Aben, P. Krummel, … and D. Worthy. (2013). Global CO_2 fluxes estimated from GOSAT retrievals of total column CO_2. *Atmospheric Chemistry and Physics, 13,* pp. 8695–8717. DOI: 10.5194/acp-13-8695-2013

[Beck et al., 2011] Beck, J.D., R. Scritchfield, P. Mitra, W. Sullivan III, A.D. Gleckler, R. Strittmatter and R.J. Martin. (2011, May 12). Linear-mode photon counting with the noiseless gain HgCdTe e-APD. *Proc. SPIE 8033, Advanced Photon Counting Techniques V,* 80330N. DOI: 10.1117/12.886161

[Beck et al., 2013] Beck, J., J. McCurdy, M. Skokan, C. Kamilar, R. Scritchfield, T. Welch, P. Mitra, X. Sun, J. Abshire, and K. Reiff. (2013, May 21). A highly sensitive multi-element HgCdTe e-APD detector for IPDA lidar applications. *Proc. SPIE 8739, Sensors and Systems for Space Applications VI, 87390V*. Retrieved from: http://dx.doi.org/10.1117/12.2018083. DOI: 10.1117/12.2018083

[Belikov et al., 2014] Belikov, D.A., A. Bril, S. Maksyutov, S. Oshchepkov, T. Saeki, H. Takagi, Y. Yoshida, … and T. Yokota. (2014). Column-averaged CO_2 concentrations in the subarctic from GOSAT retrievals and NIES transport model simulations *Polar Science*. Retrieved from: http://dx.doi.org/10.1016/j.polar.2014.02.002

[Boden et al., 2013] Boden, T.A., G. Marland, and R.J. Andres. (2013). Global, Regional, and National Fossil-Fuel CO_2 Emissions. *Carbon Dioxide Information Analysis Center.* Retrieved from http://cdiac.ornl.gov/trends/emis/meth_reg.html DOI: 10.3334/CDIAC/00001_V20

[Bösch et al., 2011] Bösch, H., D. Baker**,** B. Connor, D. Crisp and C. Miller. (2011). Global Characterization of CO_2 Column Retrievals from Shortwave-Infrared Satellite Observations of the Orbiting Carbon Observatory-2 Mission. *Remote Sens., Vol. 3* (Issue 2), pp. 270-304. DOI: 10.3390/rs3020270, 2011

[Bovensmann et al., 2010] Bovensmann, H., M. Buchwitz, J. P. Burrows, M. Reuter, T. Krings, K. Gerilowski, O. Schneising, J. Heymann, A. Tretner, and J. Erzinger. (2010). A remote sensing technique for global monitoring of power plant CO_2 emissions from space and related applications. *Atmos. Meas. Tech., 3,* pp. 781–811. DOI: 10.5194/amt-3-781-2010

[Bréon et al., 2002] Bréon, F.M., F. Maignan, M. Leroy, and I. Grant. (2002). Analysis of hot spot directional signatures measured from space. *J. Geophys. Res., Vol. 107* (Issue 16), pp. 4282-4296.

[Browell et al., 2008] Browell, E. V., M. E. Dobbs, J. Dobler, S. Kooi, Y. Choi, F. W. Harrison, B. Moore III, and T. S. Zaccheo. (2008). Airborne demonstration of 1.57-micron laser absorption spectrometer for atmospheric CO_2 measurements. Proc. of 24th International Laser Radar Conference, S06P-13, Boulder, CO, June 23-27, 2008.

[Browell et al., 2009a] Browell, E. V., M. E. Dobbs, J. Dobler, S. Kooi, Y. Choi, F. W. Harrison, B. Moore III, and T. S. Zaccheo. (2009). First airborne laser remote measurements of atmospheric CO_2 for future active sensing of CO_2 from Space. Presented at the

Proceedings of the 8th International Carbon Dioxide Conference, Jena, Germany, 13–18 September 2009a.

[Browell et al., 2009b] Browell, E. V., M. E. Dobbs, J. Dobler, S. Kooi, Y. Choi, F. W. Harrison, B. Moore III, and T. S. Zaccheo. (2009). First Airborne Laser Remote Measurements Of Atmospheric Carbon Dioxide. Presented at Fourth Symposium on Lidar Atmospheric Applications, Proc. 89th AMS Annual Meeting, Phoenix, Arizona, January 11-15, 2009.

[Browell et al., 2010] Browell, E.V., J. Dobler, S. Kooi, Y. Choi, F.W. Harrison, B. Moore III, and T. Scott Zaccheo. (2010). Airborne Validation of Laser Remote Measurements of Atmospheric Carbon Dioxide. Proc., 25th International Laser Radar Conference 2010, *S6O-03*, St. Petersburg, Russia, July 5-9, 2010 (ILRC 25).

[Browell et al., 2011] Browell, E.V., J.T. Dobler, S.A. Kooi, M.A. Fenn, Y. Choi, S.A. Vay, F.W. Harrison, and B. Moore. (2011). Airborne laser CO_2 column measurements: Evaluation of precision and accuracy under wide range of conditions. Presented at the Fall AGU Meeting, San Francisco, California, 5–9 December 2011.

[Browell et al., 2012] Browell, E.V., J.T. Dobler, S.A. Kooi, M.A. Fenn, Y. Choi, S.A. Vay, F. W. Harrison, and B. Moore III. (2012). Airborne Validation of Laser CO_2 and O_2 Column Measurements. Proc. 92nd AMS Annual Meeting, New Orleans, LA, January 22-26, 2012.

[Bruneau et al., 2006] Bruneau, D., F. Gibert, P.H. Flamant and J. Pelon. (2006). Complementary study of differential absorption lidar optimization in direct and heterodyne detections. *Appl. Opt., Vol. 45* (Issue 20), pp. 4898-4908.

[Camacho-de Coca et al., 2004] Camacho-de Coca, F., F.M. Bréon, M. Leroy, and F.J. Garcia-Haro. (2004). Airborne measurement of hot spot reflectance signatures, *Remote Sens. Environ., Vol. 90* (Issue 1), pp. 63-75.

[Campbell et al., 2014] Campbell, J.F., B. Lin, and A. Nehrir. (2014). Advanced sine wave modulation of continuous wave laser system for atmospheric CO_2 differential absorption measurements. *Applied Optics, Volume 53* (Issue 5), pp. 816-829.
Retrieved from: http://www.opticsinfobase.org/ao/abstract.cfm?URI=ao-53-5-816

[Caron and Durand, 2009] Caron, J., and Y. Durand. (2009). Operating wavelengths optimization for a spaceborne lidar measuring atmospheric CO_2. *Appl. Opt., Vol. 48* (Issue 28), pp. 5413-5422.

[Chen et al., 2006] Chen, Y., S. Sun-Mack, R. F. Arduini, and P. Minnis. (2006). Clear-sky and surface narrowbandalbedo variations derived from VIRS and MODIS data. *Proc. AMS 12th Conf. Atmos. Radiation,* Madison, WI, July 10-14, CD-ROM, 5.6.

[Chevallier et al., 2007] Chevallier, F., F.-M. Bréon, and P. J. Rayner. (2007). Contribution of the Orbiting Carbon Observatory to the estimation of CO_2 sources and sinks: Theoretical study in a variational data assimilation framework. *J. Geophys. Res., 112,* D09307, DOI: 10.1029/2006JD007375

[Chevallier et al., 2009] Chevallier, F., S. Maksyutov, P. Bousquet, F. M. Bréon, R. Saito, Y. Yoshida, and T. Yokota. (2009). On the accuracy of the CO_2 surface fluxes to be estimated from the GOSAT observations. *Geophys. Res. Lett., Vol. 36,* L19807. DOI: 10.1029/2009GL040108

[Chevallier et al., 2014] Chevallier, F., P. I. Palmer, L. Feng, H. Boesch, C. W. O'Dell, and P. Bousquet. (2014). Toward robust and consistent regional CO_2 flux estimates from in situ and spaceborne measurements of atmospheric CO_2. *Geophys. Res. Lett.*, *Vol. 41* (Issue 3), pp. 1065–1070. DOI: 10.1002/2013GL058772

[Choi et al., 2008] Choi, Y., S. A. Vay, K. P. Vadrevu, A. J. Soja, J–H Woo, S. R. Nolf, G. W. Sachse, … and H. E. Fuelberg. (2008). Characteristics of the atmospheric CO_2 signal as observed over the conterminous United States during INTEX NA (Intercontinental Chemical Transport Experiment-North America). *J. Geophys. Res., Vol. 113* (Issue D7). D07301, DOI: 10.1029/2007JD008899

[Ciais et al., 2010] Ciais, P., J. G. Canadell, S. Luyssaert, F. Chevallier, A. Shvidenko, Z. Poussi, M. Jonas, P. Peylin, A. W. King, E.-D. Schulze, S. Piao, C. Rödenbeck, W. Peters, and F.-M. Bréon. (2010, October). Can we reconcile atmospheric estimates of the Northern terrestrial carbon sink with land-based accounting? *Current Opinion in Environmental Sustainability, Vol. 2* (Issue 4)*,* pp. 225-230.

[Clough and Iacono, 1995] Clough, S. A., and M. J. Iacono. (1995). Line-by-line calculation of atmospheric fluxes and cooling rates: 2. Application to carbon dioxide, ozone, methane, nitrous oxide and the halocarbons. *J. of Geophys. Res., Vol. 100* (Issue D8), pp. 16519-16535. DOI: 10.1029/95JD01386

[Clough et al., 2005] Clough, S.A., M. W. Shephard, E.J. Mlawer, J.S. Delamere, M.J. Iacono, K. Cady-Pereira, S. Boukabara, and P.D. Brown. (2005, March). Atmospheric radiative transfer modeling: a summary of the AER codes. Short Communication. *J. Quant. Spectrosc. Radiat. Transfer, Vol. 91* (Issue 2), pp.233-244.

[Conway et al., 1994] Conway, T. J., P. P. Tans, L. S. Waterman, K. W. Thoning, D. R. Kitzis, K. A. Masarie, and N. Zhang. (1994). Evidence for interannual variability of the carbon cycle from the National Oceanic and Atmospheric Administration/Climate Monitoring and Diagnostics Laboratory Global Air Sampling Network. *J. Geophys. Res., Vol. 99,* (Issue D11), pp. 22831–22855. DOI: 10.1029/94JD01951

[Conway et al., 2009] Conway, T.J., P.M. Lang, and K.A. Masarie. (2009, July 15). Atmospheric Carbon Dioxide Dry Air Mole Fractions from the NOAA ESRL Carbon Cycle Cooperative Global Air Sampling Network, 1968-2008., Version: 2009-07-15. Retrieved from: ftp://cdiac.ornl.gov/pub/ndp005/README_flask_co2.html

[Creeden et al., 2008] Creeden D., M. Jiang, P. A. Budni, P. A. Ketteridge, S. D. Setzler, Y. E. Young, J. C. McCarthy, P. G. Schunemann, T. M. Pollak, P. Tayebati, and E. P. Chicklis. (2008, April 14). Thulium fiber laser-pumped mid-IR OPO. *SPIE Proc., Vol. 6952.* DOI: 10.1117/12.775196

[Crisp et al., 2012] Crisp, D., B. M. Fisher, C. O'Dell, C. Frankenberg, R. Basilio, H. Bösch, L. R. Brown, … and Y. L. Yung. (2012). The ACOS CO_2 retrieval algorithm -- Part II: Global X_{CO2} data characterization. (2012). *Atmos. Meas. Tech., Vol. 5,* pp. 687–707. DOI: 10.5194/amt-5-687-2012

[Crowell et al., 2015] Crowell, S., P. Rayner, S. Zaccheo, and B. Moore. (2015). Impacts of

Atmospheric State Uncertainty on O_2 Measurement Requirements for the ASCENDS Mission. *(EGU). Atmos. Meas. Tech. Vol. 8,* pp. 2685-2697. DOI:10.5194/amt-8-2685-2015

[Davis and Grainger, 2003] Davis, and C. A. Grainger. (2003). A near-field tool for simulating the upstream influence of atmospheric observations: The Stochastic Time-Inverted Lagrangian Transport (STILT) model, *Geophys. Res., Vol. 108* (D16), pp. 4493. DOI: 10.1029/2002JD003161

[Dee et al., 2011] Dee, D.P., S. M. Uppala, A. J. Simmons, P. Berrisford, P. Poli, S. Kobayashi, U. Andrae, … and F. Vitart. (2011, April 28). The ERA-Interim reanalysis: configuration and performance of the data assimilation system. *Quarterly Journal of the Royal Meteorological Society, Vol. 137* (Issue 656), pp.553-597. DOI: 10.1002/qj.828. Retrieved from http://onlinelibrary.wiley.com/doi/10.1002/qj.828/abstract

[DeFries et al., 2002] DeFries, R.S., R. A. Houghton, M. C. Hansen, C. B. Field, D. Skole, and J. Townshend. (2002). Carbon emissions from tropical deforestation and regrowth based on satellite observations for the 1980s and 1990s. *Proc. Natl. Acad. Sci., Vol. 99* (No. 22), pp.14256-14261. DOI: 10.1073/pnas.182560099

[Denning et al., 1996] Denning, A.S., G.J. Collatz, C. Zhang, D.A. Randall, J.A. Berry, P.J. Sellers, G.D. Colello, and D.A. Dazlich. (1996, September). Simulations of terrestrial carbon metabolism and atmospheric CO_2 in a general circulation model, Part 1: Surface carbon fluxes. *Tellus B*, *Vol. 48* (Issue 4), pp. 521-542. DOI: 10.1034/j.1600-0889.1996.t01-2-00009.x

[Deng, et al., 2014] Deng, F., D. B. A. Jones, D. K. Henze, N. Bousserez, K. W. Bowman, J. B. Fisher, R. Nassar, … T. Warneke. (2014, April 11). Inferring regional sources and sinks of atmospheric CO2 from GOSAT XCO2 data. *Atmos. Chem. Phys., Vol. 14,* pp. 3703–3727. DOI: 10.5194/acp-14-3703-2014

[Devi et al., 2007a] Malathy Devi, V., D. C. Benner, L. R. Brown, C. E. Miller, and R. A. Toth. (2007). Line mixing and speed dependence in CO_2 at 6348cm^{-1}: Positions, intensities, and air- and self-broadening derived with constrained multispectrum analysis. *Journal of Molecular Spectroscopy*, *Vol. 242* (Issue 2), pp. 90-117. Retrieved from http://adsabs.harvard.edu/abs/2007JMoSp.242.90M

[Devi et al., 2007b] Malathy Devi, V., D. C. Benner, L. R. Brown, C. E. Miller, and R. A. Toth. (2007, September). Line mixing and speed dependence in CO_2 at 6227.9cm^{-1}: Constrained multispectrum analysis of intensities and line shapes in the 30013←00001 band. *Journal of Molecular Spectroscopy, Vol. 245* (Issue 1), pp.52-80. Retrieved from http://www.sciencedirect.com/science/article/pii/S0022285207001300

[Disney et al., 2009] Disney, M. I., P. E. Lewis, M. Bouvet, A Prieto-Blanco, and S. Hancock. (2009). Quantifying surface reflectivity for spaceborne lidar via two independent methods, *IEEE Trans. on Geoscience and Remote Sensing, Vol. 47,* pp. 3262-3271. DOI:10.1109/TGRS.2009.2019268

[Dlugokencky et al., 2013] Dlugokencky, E.J., P.M. Lang, K.A. Masarie, A.M. Crotwell, and M.J. Crotwell. (2013). Atmospheric Carbon Dioxide Dry Air Mole Fractions from the NOAA ESRL Carbon Cycle Cooperative Global Air Sampling Network, 1968-2012,

Version: 2013-08-28. Retrieved from: ftp://aftp.cmdl.noaa.gov/data/trace_gases/co2/flask/surface/

[Dobbs et al., 2007] Dobbs, M., W. Sharp, and J. Jenny. (2007). A Sinusoidal Modulated-CW Integrated Path Differential Absorption LIDAR for Mapping Sources and Sinks of Carbon Dioxide from Space. Proc. 14th Coherent Laser Radar Conference 2007, Snowmass, CO, July 8-13, 2007.

[Dobbs et al., 2008] Dobbs, M., J. Dobler, M. Braun, D. McGregor, J. Overbeck, B. Moore III, E. Browell, and T. S. Zaccheo. (2008). A Modulated CW Fiber Laser-Lidar Suite for the ASCENDS Mission. *Proc. 24th International Laser Radar Conference, S01O-04,* Boulder, CO, June 23-27, 2008.

[Dobler et al., 2011] Dobler, J. T., J. Nagel, V. Temyanko, B. Karpowicz, S. Zaccheo, and M. Braun. (2011). Fiber Raman Amplifier Development for Laser Absorption Spectroscopy Measurements of Atmospheric Oxygen near 1.26 Micron. *The 2011 Earth Science Technology Forum (ESTF2011),* Pasadena, CA, June 21-23, 2011. Retrieved from: http://esto.nasa.gov/conferences/estf2011/papers/Dobler_ESTF2011.pdf

[Dobler et al., 2013] Dobler, J. T., F. W. Harrison, E. V. Browell, B. Lin, D. McGregor, S. Kooi, Y. Choi, and S. Ismail. (2013). Atmospheric CO_2 column measurements with an airborne intensity-modulated continuous-wave 1.57 μm fiber laser lidar. *Applied Optics, Vol. 52* (Issue 12), pp. 2874-2892. Retrieved from: http://dx.doi.org/10.1364/AO.52.002874

[Doney et al., 2006] Doney, S.C., K. Lindsay, I. Fung and J. John. (2006, July). Natural Variability in a Stable, 1000-Yr Global Coupled Climate-Carbon Cycle Simulation. *J. Climate, Vol. 19 (Issue 13)* pp. 3033-3054.

[Doney et al., 2009] Doney, S. C., I. Lima, R. A. Feely, D.M. Glover, K. Lindsay, N.Mahowald, J. K. Moore, and R. Wanninkhof. (2009, April). Mechanisms governing interannual variability in upper-ocean inorganic carbon system and air-sea CO_2 fluxes: Physical climate and atmospheric dust. *Deep Sea Res., Part II,* Vol. 56 (Issues 8–10), pp. 640–655. DOI: 10.1016/j.dsr2.2008.12.006

[DTC, n.d.] Developmental Testbed Center (DTC). (n. d.). *Model evaluation tools* [Data file]. Retrieved from: http://www.dtcenter.org/met/users/downloads/observation_data.php

[Dufour and Bréon, 2003] Dufour, E. and F.-M. Bréon. (2003). Spaceborne Estimate of Atmospheric CO_2 Column by Use of the Differential Absorption Method: Error Analysis. *Applied Optics, Vol. 42* (Issue 18), pp. 3595-3609. Retrieved from: http://dx.doi.org/10.1364/AO.42.003595

[Dumont et al., 2010] Dumont, M., O. Brissaud, G. Picard, B. Schmitt, J.-C. Gallet, and Y. Arnaud. (2010). High-accuracy measurements of snow bidirectional reflectance distribution function at visible and NIR wavelengths -- comparison with modeling results. *Atmos. Chem, Phys., Vol. 10,* pp. 2507-2520. www.atmos-chem-phys.net/10/2507/2010/

[Duren and Miller, 2012] Duren, R. M. and C. E. Miller. (2012, August). Measuring the carbon emissions of megacities. *Nature Climate Change, Vol. 2,* pp. 560–562. DOI: 10.1038/ nclimate1629

[Ehrenreich et al., 2010] Ehrenreich T., R. Leveille, I. Majid, K. Tankala, G. Rines, and P. Moulton. (2010, January 28). 1-kW, All-Glass Tm:fiber Laser. *SPIE Photonics West,*

2010: LASE, Fiber Lasers VII: Technology, Systems, and Applications, Conference 7580, Session 16: Late Breaking News. Retrieved from: http://www.qpeak.com/Meetings/PW%202010%201kW%20Tm_fiber%20laser.pdf

[Ehret et al., 2008] Ehret, G., C. Kiemle, M. Wirth, A. Amediek, A. Fix, and S. Houweling. (2008). Space-borne remote sensing of CO_2, CH_4, and N_2O by integrated path differential absorption lidar: a sensitivity analysis. *Appl. Phys. B 90,* pp. 593–608. DOI: 10.1007/s00340-007-2892-3

[Engelen et al., 2002] Engelen, R. J., A. S. Denning, K. R. Gurney, and TransCom3 modelers. (2002). On error estimation in atmospheric CO_2 inversions. *J. Geophys. Res., Vol. 107* (Issue D22), pp. 4635. DOI: 10.1029/2002JD002195

[Enting, 2002] Enting, I.G. (2002). *Inverse Problems in Atmospheric Constituent Transport*. Cambridge University Press, Cambridge.

[EPA, 2010] Environmental Protection Agency. (2010, April 15). *Inventory of U.S. Greenhouse Gas Emissions and Sinks: 1990 – 2008,* pp. 407. Retrieved from:

http://www.epa.gov/climatechange/Downloads/ghgemissions/508_Complete_GHG_1990_2008.pdf

[ESA, 2008] European Space Agency (ESA). (2008, November). *A-SCOPE (Advanced Space Carbon and Climate Observation of Planet Earth) Mission Assessment report,* Chapter 4. Retrieved from: http://esamultimedia.esa.int/docs/SP1313-1_ASCOPE.pdf

[Etheridge et al., 1998] Etheridge, D. M., L. P. Steele, R. J. Francey, and R. L. Langenfelds. (1998). Atmospheric methane between 1000 AD and present: Evidence of anthropogenic emissions and climatic variability. *Journal of Geophysical Research-Atmospheres*, Vol. *103,* pp. 15979-15993.

[Evensen, 2004] Evensen, G. (2004). Sampling strategies and square root analysis schemes for the EnKF. *Ocean Dynamics,Vol.* 54, pp. 539-560. DOI: 10.1007/s10236-004-0099-2

[Fan et al., 1998] Fan, S., M. Gloor, J. Mahlman, S. Pacala, J. Sarmiento, T. Takahashi, and P. Tans. (1998, October 16). A Large Terrestrial Carbon Sink in North America Implied by Atmospheric and Oceanic Carbon Dioxide Data and Models. *Science, Vol. 282* (No. 5388), pp. 442-446. DOI: 10.1126/science.282.5388.442

[Geibel et al., 2012] Geibel, M. C., J. Messerschmidt, C. Gerbig, T. Blumenstock, H. Chen, F. Hase, O. Kolle, … and D. G. Feist. (2012). Calibration of column-averaged CH_4 over European TCCON FTS sites with airborne in-situ measurements. *Atmos. Chem. Phys., Vol. 12,* pp. 8763–8775. DOI: 10.5194/acp-12-8763-2012

[Georgieva et al., 2006] Georgieva E.M., E. L. Wilson, M. Miodek, and W.S. Heaps. (2006, November). Total column oxygen detection using a Fabry-Perot interferometer. *Optical Engineering, Vol. 45* (Issue 11), pp. 115001. DOI: 10.1117/1.2387878

[Georgieva et al., 2008] Georgieva E.M., W. S. Heaps, and E. L. Wilson. (2008, October), Differential Radiometers Using Fabry-Perot Interferometric Technique for Remote Sensing of Greenhouse Gases. *IEEE Transactions on Geoscience and Remote Sensing (TGARS), Vol. 46* (Issue 10), pp. 3115-3122. DOI: 10.1109/TGRS.2008.921570

[Gibert et al., 2006] Gibert F., P. Flamant, D. Bruneau and C. Loth. (2006). Two-micrometer heterodyne differential absorption lidar measurements of the atmospheric CO_2 mixing ratio in the boundary layer. *Applied Optics, Vol. 45*, pp. 4448.

[Goodno et al., 2009] Goodno G.D., L. D. Book, and J. E. Rothenberg. (2009). Low-phase-noise, single-frequency, single-mode 608 W thulium fiber amplifier. *Opt. Lett. Vol. 34* (Issue 8), pp. 1204-1206.

[Gourdji et al., 2012] Gourdji, S. M., K. L. Mueller, V. Yadav, D. N. Huntzinger, A. E. Andrews, M. Trudeau, G. Petron, … and A. M. Michalak. (2012). North American CO_2 exchange: intercomparison of modeled estimates with results from a fine-scale atmospheric inversion, *Biogeosciences*, *Vol. 9,* pp. 457–475. DOI: 10.5194/bgd-8-6775-2011

[Guan et al., 2012] Guan, D., Z. Liu, Y. Geng, S. Lindner, and K. Hubacek. (2012). The gigatonne gap in China/'s carbon dioxide inventories. *Nature Climate Change, Vol. 2* (Issue 9), *pp.* 672-675. DOI: 10.1038/nclimate1560

[Guerlet et al., 2013] Guerlet, S., S. Basu, A. Butz, M. Krol, P. Hahne, S. Houweling, O. P. Hasekamp, and I. Aben. (2013). Reduced carbon uptake during the 2010 Northern Hemisphere summer from GOSAT. *Geophysical Research Letters, Vol. 40* (Issue 10), pp. 2378–2383. DOI: 10.1002/grl.50402

[Gurney et al., 2002] Gurney, K. G., et al. (2002). Towards robust regional estimates of CO_2 sources and sinks using atmospheric transport models, *Nature*, 415, pp. 626–630. DOI: 10.1038/415626a

[Gurney et al., 2009] Gurney, K. R., D. L. Mendoza, Y. Zhou, M. L. Fischer, C.C. Miller, S. Geethakumar, and S. de la Rue du Can. (2009). High Resolution Fossil Fuel Combustion CO_2 Emission Fluxes for the United States. *Environmental Science & Technology, Vol. 43* (Issue 14), pp. 5535-5541. DOI: 10.1021/es900806c

[Hammerling et al., 2012a] Hammerling, D.M., A.M. Michalak, and S.R. Kawa. (2012). Mapping of CO_2 at high spatiotemporal resolution using satellite observations: Global distributions from OCO-2. *J. Geophys. Res., Vol. 117 (Issue D6).* DOI: 10.1029/2011JD017015

[Hammerling et al., 2012b] Hammerling, D. M., A. M. Michalak, C. O'Dell, and S. R. Kawa (2012). Global CO_2 distributions over land from the Greenhouse Gases Observing Satellite (GOSAT). *Geophys. Res. Lett., Vol. 39* (Issue 8). DOI: 10.1029/2012GL051203

[Hammerling et al., 2015] Hammerling, D. M., S. R. Kawa, K. Schaefer, S. Doney, A. M. Michalak. (2015). Detectability of CO_2 flux signals by a space-based lidar mission, *J. Geophys. Res. Atmos*., *Vol. 120* (Issue 5), pp. 1794–1807. DOI: 10.1002/2014JD022483

[Hapke, 1986] Hapke, B., Bidirectional Reflectance Spectroscopy: 4. The extinction coefficient and opposition effect. *Icarus Vol. 67,* pp. 264-280. DOI:10.1016/0019-1035(86)90108-9

[Hapke et al., 1996] Hapke, B., D. DiMucci, R. Nelson, and W. Smythe. (1996). The cause of the hot spot in vegetation canopies and soils: shadow-hiding versus coherent backscatter. *Remote Sens. Environ., Vol.58*, pp. 63-68.

[Heaps et al., 2008] Heaps, W.S., E.L. Wilson, and E.M. Georgieva. (2008, September). Precision Measurement of Atmospheric Trace Constituents Using a Compact Fabry-Perot

Radiometer. *International Journal of High Speed Electronics and Systems (IJHSES), Vol. 18* (Issue 3), pp. 601. DOI: 10.1142/S0129156408005606

[Hintze, et al., 1998] Hintze, J. L. and R. D. Nelson. (1998). Violin plots: a box plot-density trace synergism. *The American Statistician*, *Vol. 52* (Issue 2), pp. 181-4. Retrieved from: http://www.jstor.org/discover/10.2307/2685478?uid=16777912&uid=3739560&uid=2&uid=3&uid=16752808&uid=67&uid=62&uid=3739256&sid=21106108757843

[Houghton, 1999] Houghton, R. A. (1999, April). The annual net flux of carbon to the atmosphere from changes in land use 1850–1990, *Tellus B, Vol. 51* (Issue 2), pp. 298–313. DOI: 10.1034/j.1600-0889.1999.00013.x

[Houghton, 2003] Houghton, R. A. (2003, April). Revised estimates of the annual net flux of carbon to the atmosphere from changes in land use and land management 1850-2000. *Tellus B, Vol. 55* (Issue 2), pp. 378-390. DOI: 10.1034/j.1600-0889.2003.01450.x

[Houweling et al., 2004] Houweling, S., F. M. Breon, I. Aben, C. Rödenbeck, M. Gloor, M. Heimann and P. Ciais. (2004). Inverse modeling of CO_2 sources and sinks using satellite data: A synthetic inter-comparison of measurement techniques and their performance as a function of space and time. *Atmos. Chem. Phys., Vol. 4,* pp. 523-548.

[Hu et al., 2008] Hu, Y., K. Stamnes, M. Vaughan, J. Pelon, C. Weimer, D. Wu, M.Cisewski, W. Sun, P. Yang, B. Lin, A. Omar, D. Flittner, C. Hostetler, C. Trepte, D. Winker, G. Gibson, and M. Santa-Maria. (2008). Sea surface wind speed estimation from space-based lidar measurements. *Atmos. Chem. Phys., Vol. 8,* pp. 2771-2793 and 3593-3601. DOI: 10.5194/acp-8-3593-2008 and www.atmos-chem-phys-discuss.net/8/2771/2008/.

[Hudson et al., 2006] Hudson, S. R., S. G. Warren, R. E. Brandt, T. C. Grenfell, and D. Six. (2006). Spectral bidirectional reflectance of Antarctic snow: Measurements and parameterization. *J. Geophys. Res., Vol. 111,* D18106, doi:10.1029/2006JD007290

[Hungershoefer et al., 2010] Hungershoefer, K., F.-M. Breon, P. Peylin, F. Chevallier, P. Rayner, A. Klonecki, S. Houweling, and J. Marshall. (2010). Evaluation of various observing systems for the global monitoring of CO_2 surface fluxes. *Atmospheric Chemistry and Physics, Vol. 10* (Issue 21), pp.10503–10520. DOI: 10.5194/acp-10-10503-2010

[Hyon et al., 2012] Hyon, J., K. Anderson, B. Bienstock, G. Andrew, M. DiJoseph, J. Demsey, C. Jones (2012, August). ASCENDS Mission Study Summary. *NASA SER-SE-001, Vol. 1.0.*

[Ingmann et al., 2008] Ingmann P., P. Bensi, Y. Durand, A. Griva, and P. Clissold. (2008, November). A-Scope – advanced space carbon and climate observation of planet earth. *ESA Report for Assessment*. SP-1313/1. ISBN 978-92-9221-406-7, ISSN 0379-6566

[Inoue et al., 2013] Inoue, M., I. Morino, O. Uchino, Y. Miyamoto, Y. Yoshida, T. Yokota, T. Machida, … and P. K. Patra. (2013). Validation of XCO_2 derived from SWIR spectra of GOSAT TANSO-FTS with aircraft measurement data. *Atmos. Chem. Phys., Vol. 13,* pp. 9771-9788. DOI: 10.5194/acp-13-9771-2013

[IPCC, 2007] IPCC. (2007, September 19-21). Towards new scenarios for analysis of emissions, climate change, impacts, and response strategies. Intergovernmental Panel on Climate Change Report, IPPC Expert Meeting Report. Noordwijkerhout, The Netherlands. Retrieved from: http://www.ipcc.ch/pdf/supporting-material/expert-meeting-report-scenarios.pdf

[IPCC, 2007] Core Writing Team, Pachauri, R.K and Reisinger, A. (eds.) (2007). Synthesis report. Contribution of working groups I, II and III to the fourth .assessment report of the intergovernmental panel on climate change. *Climate Change 2007, IPCC*, Geneva, Switzerland, pp. 104.

[IPCC, 2013] Stocker, T.F., D. Qin, G.-K. Plattner, M. Tignor, S.K. Allen, J. Boschung, A. Nauels, Y. Xia, V. Bex and P.M. Midgley (eds.). (2013). The Physical Science Basis. Contribution of Working Group I to the Fifth Assessment Report of the Intergovernmental Panel on Climate Change. *Climate Change 2013,* Cambridge University Press, Cambridge, United Kingdom and New York, NY, USA, 1535 pp. DOI: 10.1017/CBO9781107415324

[Irvine and Pollack, 1968] Irvine, W.M. and J.B. Pollack. (1968). Infrared optical properties of water and ice spheres. *Icarus, Vol. 8,* pp. 324-360.

[Ismail and Browell, 1989] Ismail, S., and E. V. Browell. (1989, September 1). Airborne and spaceborne lidar measurements of water vapor profiles: a sensitivity analysis. *Applied Optics, Vol. 28 (No. 17),* pp. 3603-3615.

[Ishii et al., 2008] Ishii, S., K. Mizutani, H. Fukuoka, T. Ishikawa, H. Iwai, P. Baron, J. Mendrok, … and T. Itabe. (2008). "Development of 2 micron coherent differential absorption lidar," *24th International Laser Radar Conference,* Boulder, Colorado.

[Jackson, 2004] Jackson, S.D. (2004, January 2004). Cross relaxation and energy transfer upconversion processes relevant to the functioning of 2 μm Tm^{3+}-doped silica fibre lasers. *Optics Communications Vol. 230* (Issues 1-3), pp.197-203. DOI: 10.1016/j.optcom.2003.11.045

[Kameyama et al., 2011] Kameyama, S., M. Imaki,1 Y. Hirano, S. Ueno, S.Kawakami, D. Sakaizawa, T. Kimura and M. Nakajima. (2011). Feasibility study on 1:6 μm continuous-wave modulation laser absorption spectrometer system for measurement of global CO_2 concentration from a satellite. *Appl. Opt., Vol. 50* (Issue 14), pp. 2055-2068.

[Kaminski et al., 2001] Kaminski, T., P. J. Rayner, M. Heimann, and I. G. Enting. (2001, March 16). On aggregation errors in atmospheric transport inversions. *Journal of Geophys. Res., Vol. 106* (Issue D5), pp. 4703–4715. DOI: 10.1029/2000JD900581

[Kaasalainen et al., 2006] Kaasalainen, S., M. Kaasalainan, T. Mielonen, J. Suomalainen, J.I. Peltoniemi, and J. Naranen. (2006). Optical properties of snow in backscatter*, J. Glaciology, Vol. 52*, pp. 574-584.

[Kawa et al., 2004] Kawa, S. R., D. J. Erickson III, S. Pawson, and Z. Zhu. (2004). Global CO_2 transport simulations using meteorological data from the NASA data assimilation system. *J. Geophys. Res., Vol.109 (Issue D18).* DOI: 10.1029/2004JD004554

[Kawa et al., 2010] Kawa, S. R., J. Mao, J. B. Abshire, G. J. Collatz, X. Sun and C. J. Weaver. (2010, November). Simulation studies for a space-based CO_2 lidar mission. *Tellus B, Vol. 62* (Issue 5), pp.759-769. DOI: 10.1111/j.1600-0889.2010.00486.x

[Keeling, 1960] Keeling, C. D. (1960). The concentration and isotopic abundances of carbon dioxide in the atmosphere. Tellus, Vol. 12 (Issue 2), pp. 200-203. DOI: 10.1111/j.2153-3490.1960.tb01300.x

[Keppel-Aleks et al., 2012] Keppel-Aleks, G., P. O. Wennberg, R. A. Washenfelder, D. Wunch, T. Schneider, G. C. Toon, R. J. Andres, … and S. C. Wofsy (2012). The imprint of surface fluxes and transport on variations in total column carbon dioxide. *Biogeosciences, Vol. 9*, pp. 875-891. DOI: 10.5194/bg-9-875-2012

[Kiemle et al., 2014] Kiemle, C, S. R. Kawa, M. Quatrevalet, E. V. Browell. (2014). Performance simulations for a spaceborne methane lidar mission. *J Geophys Res Atmos*, *Vol. 119* (Issue 7), pp. 4365–79. Retrieved from: http://dx.doi.org/10.1002/2013JD021253

[Koch et al., 2008] Koch G. J., J. Y. Beyon, F. Gibert, B. W. Barnes, S. Ismail, M. Petros, P. J. Petzar, … and U. N. Singh (2008). Side-line tunable laser transmitter for differential absorption lidar measurements of CO_2: design and application to atmospheric measurements. *Applied Optics, Vol. 47* (Issue 7), pp. 944-956.

[Kulawik et al., 2015] Kulawik, S., D. Wunch, C. O'Dell, C. Frankenberg, A. R. Jacobson, M. Reuter, T. Oda, and C. Miller. (2015). Consistent evaluation of GOSAT, SCIAMACHY, CarbonTracker, and MACC through comparisons to TCCON. *Atmos. Chem. Phys. Disc*.

[Kuze et al., in press] Kuze, A., D. M. O'Brien, T. E. Taylor, J. O. Day, C. W. O'Dell, F. Kataoka, M. Yoshida, … and H. Suto. (2011). Vicarious Calibration of the GOSAT Sensors Using the Railroad Valley Desert Playa. *IEEE Trans. on Geoscience and Remote Sensing*, *Vol. 49,* pp. 1781-1795. DOI: 10.1109/TGRS.2010.2089527

[Lancaster et al., 2005] Lancaster, R. S., J. D. Spinhirne, and S. P. Palm. (2005). *Geophys. Res. Lett.,* Vol. 32, L22S10. DOI: 10.1029/2005GL023732

[Larsson et al., 2006] Larsson, H., O. Steinvall, T. Chevalier, and F. Gustafsson. (2006). Characterizing laser radar snow reflection for the wavelengths 0.9 and 1.5 μm. *Optical Eng., Vol. 45,* pp. 116201-1-11. doi:10.1117/1.2386026

[Lawrence, 2011] Lawrence, James. (2011). Differential absorption lidar for the total column measurement of atmospheric CO_2 from space. *Department of Physics and Astronomy Dissertation*, University of Leicester. Retrieved from: http://hdl.handle.net/2381/10379

[Lemke et al., 2007] Lemke, P., J. Ren, R. B. Alley, I. Allison, J. Carrasco, G. Flato, Y. Fujii, … and T. Zhang. (2007). Observations: changes in snow, ice and frozen ground. *Climate Change 2007: the physical science basis; summary for policymakers, technical summary and frequently asked questions. Part of the Working Group I contribution to the Fourth Assessment Report of the Intergovernmental Panel on Climate Change.* Cambridge Univ. Press, Cambridge, UK. *ISBN: 92-9169-121-6.*

[Le Quéré et al., 2009] Le Quéré, C., M. R. Raupach, J G. Canadell, G. Marland, L. Bopp, P. Ciais, T. J. Conway, … and F. I. Woodward. (2009). Trends in the sources and sinks of carbon dioxide. *Nature Geosci., Vol. 2,* pp. 831-836. DOI: 10.1038/ngeo689

[Le Quéré et al., 2013] Le Quéré, C., G. P. Peters, R. J. Andres, R. M. Andrew, T. Boden, P. Ciais, P. Friedlingstein, … and C. Yue. (2013). Global carbon budget 2013. *Earth System Science Data Discussions*, *Vol. 6,* pp. 689-760. Retrieved from: http://www.earth-syst-sci-data-discuss.net/6/689/2013, DOI: 10.5194/essdd-6-689-2013

[Lin et al., 2003] Lin, J. C., C. Gerbig, S. C. Wofsy, A. E. Andrews, B. C. Daube, K. J. Davis, and C. A. Grainger. (2003, August 19). A near-field tool for simulating the upstream influence

of atmospheric observations: the stochastic time-inverted lagrangian transport (stilt) model. *Journal of Geophysical Research: Atmospheres, Vol. 108 (Issue D16),* pp. 10001-10021. DOI: 10.1029/2002JD003161

[Lin et al., 2013] Lin, B., S. Ismail, F. W. Harrison, E. V. Browell, A. R. Nehrir, J. Dobler, B. Moore, T. Refaat and S. A. Kooi. (2013). Modeling of intensity-modulated continuous-wave laser absorption spectrometer systems for atmospheric CO_2 column measurements. *Applied Optics, Vol. 52 (Issue 29),* pp. 7062-7077.

[Long et al., 2010] Long D. A., D.K. Havey, M. Okumura, C.E. Miller, and J.T. Hodges. (2010). O_2 A-band line parameters to support atmospheric remote sensing. *J. of Quant. Spectr. And Rad. Transfer, Vol.* 111 (Issue 14), pp. 2021-2036.

[Long et al., 2011] Long, D. A., K. Bielska, D. Lisak, D. K. Havey, M. Okumura, C. E. Miller, and J. T. Hodges. (2011). The air-broadened, near-infrared CO_2 line shape in the spectrally isolated regime: Evidence of simultaneous Dicke narrowing and speed dependence, *Journal of Chemical Physics, Vol. 135,* 064308. Retrieved from: http://dx.doi.org/10.1063/1.3624527

[Lüthi et al., 2008] Lüthi, D., M. Le Floch, B. Bereiter, T. Blunier, J.-M. Barnola, U. Siegenthaler, D. Raynaud, … and T. F. Stocker (2008). High-resolution carbon dioxide concentration record 650,000-800,000 years before present. *Nature 453*, pp. 379-382. DOI: 10.1038/nature06949

[Mao and Kawa, 2004] Mao, J. and S. R. Kawa. (2004). Sensitivity studies for space-based measurement of atmospheric total column carbon dioxide by reflected sunlight. *Applied Optics, Vol. 43* (Issue 4), pp. 914-927.

[Mao et al., 2007] Mao, J., S. R. Kawa, J. B. Abshire and H. Riris. (2007). Sensitivity studies for a space-based CO_2 laser sounder. *Eos Trans., Vol 88 (Issue 52), AGU 2007 Fall Meeting,* Suppl. Abstract A13D-1500. 2007AGUFM.A13D1500M

[Mao et al., 2013] Mao, J., A. Ramanathan, M. Rodriguez, G. R. Allan, W. Hasselbrack, J. B. Abshire, H. Riris, … and E. V. Browell. (2013). Retrieval of vertical structure of atmospheric CO_2 concentration from airborne lidar measurements during the 2011 and 2013 ascends science campaigns. 2*013 Fall AGU Meeting,* San Francisco, December 9-13, 2013, Paper A23H-03.

[Marland et al., 2009] Marland, G., K. Hamal and M. Jonas. (2009). How uncertain are estimates of CO_2 emissions? *J. Ind. Ecol., Vol. 13,* pp. 4-7. DOI: 10.1111/j.1530-9290.2009.00108.x

[McGuckin and Menzies, 1992] McGuckin B.T. and R.T. Menzies. (1992). Efficient CW diode-pumped tm,ho:ylf laser with tunability near 2.06 μm. *IEEE J. Quantum Electronics*, *Vol. 28,* pp. 1025-1028.

[Measures, 1992] Measures, R. (1992, January 1). Laser remote sensing: fundamentals and applications, *Krieger Publishing Company,* New York.

[Menzies et al., 1998] Menzies, R.T., D. M. Tratt, and W. H. Hunt. (1998). Lidar in-space technology experiment measurements of sea surface directional reflectance and the link to surface wind speed. *Appl. Opt, Vol. 37* (Issue 24), pp. 5550-5558.

[Menzies and Tratt, 2003] Menzies, R. T., and D. M. Tratt. (2003). Differential laser absorption spectrometry for global profiling of tropospheric carbon dioxide: selection of optimum

sounding frequencies for high-precision measurements. *Appl. Opt., Vol. 42 (Issue 33),* pp. 6569-6577. Retrieved from: http://dx.doi.org/10.1364/AO.42.006569

[Menzies and Spiers, 2008] R. Menzies and G. Spiers. (2008). Airborne laser absorption spectrometer for IPDA measurement of atmospheric effects on attainable precision and a technique for cloud and aerosol filtering. 24th International Laser Radar Conference, Boulder, Colorado.

[Menzies et al., 2014] Menzies, R.T., G.D. Spiers, and J. Jacob. (2014, February). Airborne laser absorption spectrometer measurements of atmospheric CO_2 column mole fractions: source and sink detection and environmental impacts on retrievals. *J. Atmos. And Oceanic Technology*, *Vol. 31,* pp. 404–421. DOI: http://dx.doi.org/10.1175/JTECH-D-13-00128.1

[Meredith et al., 2012] Meredith, M. P., A. C. N. Garabato, A. M. Hogg, and R. Farneti. (2012, January). Sensitivity of the overturning circulation in the southern ocean to decadal changes in wind forcing. *J.Climate, Vol. 25* (Issue 1), pp. 99-110.

[MERRA, 1979-Present] MERRA. (1979-Present). *Modern Era-Retrospective Analysis for Research and Applications* [Data file]. Retrieved from: http://gmao.gsfc.nasa.gov/research/merra/intro.php and http://disc.sci.gsfc.nasa.gov/daac-bin/FTPSubset.pl

[Messerschmidt et al., 2013] Messerschmidt, J., N. Parazoo, D. Wunch, N.M. Deutscher, C. Roehl, T. Warneke, and P. O. Wennberg. (2013). Evaluation of seasonal atmosphere–biosphere exchange estimations with TCCON measurements. *Atmos. Chem. Phys., Vol. 13,* pp. 5103-5115. DOI: 10.5194/acp-13-5103-2013

[Michalak et al., 2004] Michalak, A.M., L. Bruhwiler, and P.P. Tans. (2004, July 27). A geostatistical approach to surface flux estimation of atmospheric trace gases. *Journal of Geophysical Research, Vol. 109 (Issue D14), D14109.* DOI: 10.1029/2003JD004422

[Miles et al., 2012] Miles, N.L., S.J. Richardson, K.J. Davis, T. Lauvaux, A.E. Andrews, T.O. West, V. Bandaru, and E.R. Crosson. (2012). Large amplitude spatial and temporal gradients in atmospheric boundary layer CO_2 mole fractions detected with a tower-based network in the U.S. upper Midwest. *J. Geoophys. Res., Vol. 117,* G01019. DOI: 10.1029/2011JG001781

[Miller et al., 2007] Miller, C.E., D. Crisp, P. L. DeCola, S. C. Olsen, J. T. Randerson, A. M. Michalak, A. Alkhaled, … and R. M. Law. (2007, May 27). Precision requirements for space-based XCO_2 data. *J. Geophys. Res.-Atmos., Vol. 112 (Issue D10)*, D10314. DOI: 10.1029/2006JD007659

[Najjar et al., 2007] Najjar, R.G., X. Jin, F. Louanchi, O. Aumont, K. Caldeira, S. C. Doney, J.-C. Dutay, … and A. Yool. (2007, September). Impact of circulation on export production, dissolved organic matter, and dissolved oxygen in the ocean: Results from phase ii of the ocean carbon-cycle model intercomparison project (OCMIP-2). *Global Biogeochem. Cy., Vol. 21* (Issue 3), GB3007. DOI: 10.1029/2006GB002857

[NAC, 2007] The 2007 NRC Decadal Survey for Earth Science. (2007). *National Academies Press.* Retrieved from: http://www.nap.edu/catalog/11820/earth-science-and-applications-from-space-national-imperatives-for-the

[NASA, n.d.] The NASA ASCENDS Mission. Retrieved from:

http://decadal.gsfc.nasa.gov/ascends.html

[NASA, n.d.] NASA Goddard Space Flight Center. CO_2 sounder. *Papers, Posters, and Related Studies*. Retrieved from: http://ssed.gsfc.nasa.gov/co2sounder/

[NASA, 2008] NASA. (2008). Active sensing of CO_2 emission over nights, days, and seasons (ASCENDS) mission. *NASA Science Definition and Planning Workshop Report,* University of Michigan in Ann Arbor, Michigan, July 23-25, 2008. Retrieved from: http://cce.nasa.gov/ascends/12-30-08%20ASCENDS_Workshop_Report%20clean.pdf

[NASA, 2008] NASA Science Definition and Planning Workshop Report for ASCENDS Mission. (2008). University of Michigan in Ann Arbor, Michigan. Retrieved from: http://decadal.gsfc.nasa.gov/documents/12-30-08-ASCENDS_Workshop.pdf

[NCDC, n.d.] NCDC. (n.d.). *NCDC's* Integrated *Surface Database (ISD)* [Data file]. Retrieved from: http://www.ncdc.noaa.gov/oa/climate/isd/index.php

[NCDC, n.d. b] NCDC. (n.d.). *NCDC's NOMADS* [Data file]. Retrieved from: ftp://nomads.ncdc.noaa.gov

[NCEP, n.d. c] *NCEP. (n.d.). PREPBUFR Usage* [Data file]. Retrieved from: http://www.emc.ncep.noaa.gov/mmb/data_processing/prepbufr.doc

[Nehrkorn et al., 2010] Nehrkorn, T., J. Eluszkiewicz, S. C. Wofsy, J. C. Lin, C. Gerbig, M. Longo, and S. Freitas. (2010). Coupled weather research and forecasting -- stochastic time-inverted Lagrangian transport (WRF-STILT) model. *Meteor. Atmos. Phys., Vol. 107* (Issues 1-2), pp. 51–64.

[Nicodemus et al., 1977] Nicodemus, F.E., J.C. Richmond, J.J. Hsia, I.W. Ginsburg, and T. Limperis. (1977). Geometrical Considerations and Nomenclature for Reflectance. *National Bureau of Standards. U.S. Monograph 160*.

[NOAA, 2003] NOAA, Washington, D.C. (2003, November). The GFS Atmospheric Model, *NCEP Office Note 422*, Environmental Modeling Center. Retrieved from: http://search.usa.gov/search?affiliate=nws.noaa.gov&v%3Aproject=firstgov&query=The+GFS+Atmospheric+Model%2C+NCEP+Office+Note+422

[NOAA, n.d.] NOAA. (n.d.). *NOAA's ESRL's archive*. [Data file]. Retrieved from: http://www.esrl.noaa.gov/raobs/intl/ and http://www.esrl.noaa.gov/raobs/ or http://www.esrl.noaa.gov/raobs/General_Information.html

[NRC, 2007] NRC. (2007). Earth science and applications from space: national imperatives for the next decade and beyond. *The National Academies Press,* Washington, DC. Retrieved from: http://www.nap.edu/

[NRC, 2013] NRC. (2013). Abrupt Impacts of Climate Change: Anticipating Surprises. Committee on Understanding and Monitoring Abrupt Climate Change and its Impacts. *US National Research Council, National Academies Press,* Washington, DC.

[Numata et al., 2012] Numata, K., J. R. Chen and S. T. Wu. (2012). Precision and fast wavelength tuning of a dynamically phase-locked widely-tunable laser. *Optics Express, Vol. 20 (Issue 13)*, pp. 14234-14243. http://dx.doi.org/10.1364/OE.20.014234

[Obland et al., 2012] Obland, M. D., N. S. Prasad, F. W. Harrison, E. V. Browell, S. Ismail, J. T. Dobler, B. Moore, … and W. Welch. (2012). ACES: the ASCENDS carbonhawk experiment simulator. *2012 American Geophysical Union Fall Meeting*, San Francisco, CA, December 3-7, 2012. Paper A53H-0230.

[Obland et al., 2013] Obland, M. D., C. Antill, E. V. Browell, J. F. Campbell, S. Chen, C. Cleckner, M. S. Dijoseph, … and W. Welch. (2013). Technology advancement for the ASCENDS mission using the ASCENDS carbonhawk experiment simulator (ACES), *2013 American Geophysical Union Fall Meeting,* San Francisco, CA, December 9-13, 2013, Paper A13C-0212.

[O'Brien and Rayner, 2002] O'Brien, D. M. and Rayner, P. J. (2002). Global observations of the carbon budget 2. CO_2 column from differential absorption of reflected sunlight in the 1.61 μm band of CO_2. *J. Geophys. Res., Vol. 107*, ACH6-1. DOI: 10.1029/2001JD000617

[Oda and Maksyutov, 2011] Oda, T., and S. Maksyutov. (2011). A very high-resolution (1 km×1 km) global fossil fuel CO_2 emission inventory derived using a point source database and satellite observations of nighttime lights. *Atmos. Chem. Phys.* Vol. 11, pp. 543-556.

[O'Dell et al., 2012] O'Dell, C. W., B. Connor, H. Bösch, D. O'Brien, C. Frankenberg, R. Castano, M. Christi, D., … and D. Wunch. (2012). The ACOS CO_2 retrieval algorithm – Part 1: Description and validation against synthetic observations. *Atmos. Meas. Tech., Vol. 5,* pp. 99–121. DOI: 10.5194/amt-5-99-2012

[Olivier et al., 2012] Olivier, J. G., J. A. Peters and G. Janssens-Maenhout. (2012). Trends in global CO_2 emissions 2012 report. *PBL Netherlands Environmental Assessment Agency; Ispra: Joint Research Centre,* The Hague, The Netherlands.

[Oren et al., 2001] Oren, R., D.S. Ellsworth, K. H. Johnsen, N. Phillips, B. E. Ewers, C. Maler, K.V. R. Schafer, … and G. G. Katul. (2001), Soil fertility limits carbon seqestration by forest ecosystems in a CO_2-enriched atmosphere. *Nature* Vol. 411, pp. 469-472. DOI: 10.1038/35078064

[Pan et al., 2011] Pan Y., Birdsey R.A., Fang J., et al. (2011). A large and persistent carbon sink in the world's forests. *Science, Vol. 333 (No. 6045)*. pp. 988-993. DOI: 10.1126/science.1201609

[Peters et al., 2010] Peters, W., M. C. Krol, G. R. Van Der Werf, S. Houweling, C. D. Jones, J. Hughes, K. Schaefer, … and P. P. Tans. (2010). Seven years of recent European net terrestrial carbon dioxide exchange constrained by atmospheric observations. *Global Change Biology, Vol. 16* (Issue 4), pp. 1317-1337. DOI: 10.1111/j.1365-2486.2009.02078.x

[Peters et al., 2011] Peters, G. P., G. Marland, C. L. Quéré, T. Boden, J. G. Canadell, and M. R. Raupach. (2011). Rapid growth in CO_2 emissions after the 2008-2009 global financial crisis. *Nature Climate Change, Vol. 2*, pp. 2-4. DOI: 10.1038/nclimate1332

[Peters et al., 2012] Peters, G. P., G. Marland, C. Le Quere, T. Boden, J. G. Canadell, and M. R. Raupach. (2012). Rapid growth in C02 emissions after the 2008-2009 global financial crisis. *Nature Climate Change, Vol.* 2 (Issue 1), pp. 2-4. DOI: 10.1038/nclimate1332

[Picarro, Inc.] Picarro, Inc., 480 Oakmead Parkway, Sunnyvale, CA 94085, USA.

[Pillai et al., 2010] Pillai, D., C. Gerbig, J. Marshall, R. Ahmadov, R. Kretschmer, T. Koch, and U. Karstens. (2010). High resolution modeling of CO_2 over Europe: implications for representation errors of satellite retrievals. *Atmos. Chem. Phys., Vol. 10,* pp. 83–94. DOI: 10.5194/acp-10-83-2010

[Raab and Tward, 2010] Raab, J., and E. Tward. (2010, September). Northrop Grumman Aerospace Systems cryocooler overview. *Cryogenics, Volume 50* (Issue 9), pp. 572-581. ISSN 0011-2275. DOI: 10.1016/j.cryogenics.2010.02.009

[Ramanathan et al., 2013] Ramanathan, A., J. Mao, G. R. Allan, H. Riris, C. J. Weaver, W. E. Hasselbrack, E. V. Browell, and J. B. Abshire. (2013). Spectroscopic measurements of a CO_2 absorption line in an open vertical path using an airborne lidar. *Applied Physics Letters, Vol. 103* (Issue 21), 214102. DOI: http://dx.doi.org/10.1063/1.4832616

[Ramanathan et al., 2015] Ramanathan, A. K., J. Mao, J. B. Abshire, and G. R. Allan. (2015). Remote sensing measurements of the CO_2 mixing ratio in the planetary boundary layer using cloud slicing with airborne lidar. *Geophys. Res. Lett., Vol. 42.* DOI: 10.1002/2014GL062749

[Randerson et al., 1997] Randerson, J.T., M.V. Thompson, T. J. Conway, I. Y. Fung and C. B. Field. (1997, December). The contribution of terrestrial sources and sinks to trends in the seasonal cycle of atmospheric carbon dioxide. *Global Biogeochem. Cy., Vol. 11* (Issue 4), pp. 535-560. DOI: 10.1029/97GB02268

[Rayner and O'Brien, 2001] Rayner, P. J., and D. M. O'Brien. (2001). The utility of remotely sensed $C0_2$ concentration data in surface source inversions. *Geophysical Research Letters, Vol. 28* (Issue 1), pp. 175-178. DOI: 10.1029/2000GLO 11912

[Rayner et al., 2002] Rayner, P. J., R. M. Law, D. M. O'Brien, T. M. Butler, and A. C. Dilley. (2002). Global observations of the carbon budget - 3. Initial assessment of the impact of satellite orbit, scan geometry, and cloud on measuring $C0_2$ from space. *Journal of Geophysical Research-Atmospheres, Vol. 107* (Issue D21). DOI: l0.1029/2001JD000618

[Rayner et al., 2010] Rayner, P. J., M. R. Raupach, M. Paget, P. Peylin, and E. Koffi. (2010). A new global gridded data set of CO_2 emissions from fossil fuel combustion: Methodology and evaluation. *J. Geophys. Res., Vol. 115,* D19306, DOI: 10.1029/2009JD013439

[Refaat et al., 2010] Refaat, T. F., S. Ismail, G. J. Koch, L. Diaz, K. Davis, and M. Rubio. (2010). Field Testing of a Two-Micron DIAL System for Profiling Atmospheric Carbon Dioxide. *25th International Laser Radar Conference,* 5-9 Jul. 2010, St. Petersburg, Russia.

[Refaat et al., 2011] Refaat, T. F., S. Ismail, G. J. Koch, M. Rubio, T. L. Mack, A. Notari, J. E. Collins, … and U. N. Singh. (2011, January). Backscatter 2-μm Lidar Validation for Atmospheric CO_2 Differential Absorption Lidar Applications. *IEEE Transaction on Geoscience and Remote Sensing, Vol. 49 (Issue 1)* pp. 572-580. DOI: 10.1109/TGRS.2010.2055874

[Remsberg and Gordley, 1978] Remsberg, E. E., and L. L. Gordley. (1978). Analysis of differential absorption lidar from the space shuttle. *Appl. Opt. Vol. 17 (Issue 4)*, pp. 624-630. Retrieved from: http://dx.doi.org/10.1364/AO.17.000624

[Rienecker et al., 2011] Rienecker, M. M., M. J. Suarez, R. Gelaro. R. Todling, J. Bacmeister, E. Liu, M. G. Bosilovich, … and J. Woollen. (2011, July). MERRA: NASA's Modern-Era Retrospective Analysis for Research and Applications. *Journal of Climate, Vol. 24 (Issue 14),* pp.3624-3648. Retrieved from: http://journals.ametsoc.org/doi/abs/10.1175/jcli-d-11-00015.1

[Riris et al., 2011] Riris, H., M. D. Rodriguez, G. R. Allan, W. E. Hasselbrack, M. A. Stephen, and J. B. Abshire. (2011, September 13). Airborne lidar measurements of atmospheric pressure made using the oxygen A-band. *Proc. SPIE 8159, Lidar Remote Sensing for Environmental Monitoring XII, 815909.* DOI: 10.1117/12.892021

[Riris et al., 2007] Riris, H., J. Abshire, G. Allan, J. Burris, J. Chen, S. Kawa, J.-P. Mao, … and E. Wilson. (2007, October 3). A laser sounder for measuring atmospheric trace gases from space. *Proc. of SPIE Vol. 6750, Lidar Technologies, Techniques, and Measurements for Atmospheric Remote Sensing III,* 67500U. DOI: 10.1117/12.737607

[RMT, Inc., 2011] RMT, Inc. (2011). *Four Corners Generating Station Project.* Retrieved from: http://www.cpuc.ca.gov/environment/info/mha/fourcorners/images/FourCorners_Sept2011web.pdf

[Rothman et al., 2009] Rothman, L. S., I. E. Gordon, A. Barbe, D. C. Benner, P.F. Bernath, M. Birk, V. Boudon, … and J. Vander Auwera. (2009). The HITRAN 2008 molecular spectroscopic database. *Journal of Quantitative Spectroscopy and Radiative Transfer, Vol. 110* (Issues 9-10), pp.533-72. Retrieved from: http://adsabs.harvard.edu/abs/2009JQSRT.110.533R. DOI: 10.1016/j.jqsrt.2009.02.013

[Saha et al., 2010] Saha, S., S. Moorthi, H.-L. Pan, X. Wu, J. Wang , S. Nadiga, P. Tripp, R. … and M. Goldberg. (2010). The NCEP Climate Forecast System Reanalysis. *Bulletin of the American Meteorological Society*, *Volume 91* (Issue 8), pp.1015-57. Retrieved from: http://www.sciencedirect.com /science/article/pii/S0022407309000727

[Sakaizawa et al., 2008] D. Sakaizawa, C. Nagasawa, M. Abo, Y. Shibata, and T. Nagai. (2008). Development of a 1.6 μm CO_2 DIAL transmitter using OPM-OPO. *24th International Laser Radar Conference*.

[Salstein et al., 2008] Salstein, D.A., R.M. Ponte, and K. Cady-Pereira. (2008). Uncertainties in atmospheric surface pressure fields from global analyses. *Journal of Geophysical Research: Atmospheres, Vol. 113* (Issue D14), Retrieved from: http://onlinelibrary.wiley.com/doi/10.1029/2007JD009531/abstract. DOI: 10.1029/2007JD009531

[Sarmiento et al., 2002] Sarmiento, J. L. and N. Gruber. (2002). Sinks for Anthropogenic Carbon. *Physics Today*, Vol. 55 (Issue 8), pp.30-36.

[Schaefer et al., 2011] Schaefer, K., T. Zhang, L. Bruhwiler, and A. P. Barrett. (2011). Amount and timing of permafrost carbon release in response to climate warming. *Tellus B, Vol. 63 (Issue 2),* pp. 165-180. DOI: 10.1111/j.1600-0889.2011.00527.x

[Shiga et al, 2014] Shiga, Y. P., A. M. Michalak, S. M. Gourdji, K. L. Mueller, and V. Yadav. (2014). Detecting fossil fuel emissions patterns from sub-continental regions using North American in-situ CO_2 measurements. *Geophys. Res. Lett.*, 2014GL059684. DOI: 10.1002/2014GL059684

[Simard, et al., 2011] Simard, M., N. Pinto, J. B. Fisher, and A. Baccini. (2011). Mapping forest canopy height globally with spaceborne lidar. *J. Geophys. Res., Vol. 116,* G04021. DOI: 10.1029/2011JG001708

[Singh et al., 2013] Singh, U. N., J. Yu, M. Petros, T. Refaat, and K. Reithmaier. (2013, September 17). Development of a pulsed 2-micron integrated path differential absorption lidar for CO_2 measurement. *Proceeding of SPIE. Vol. 8872, Lidar Remote Sensing for Environmental Monitoring XIV, 887209.* San Diego, CA, DOI: 10.1117/12.2028245

[Sitch et al., 2003] Sitch, S., B. Smith, I.C. Prentice, A. Arneth, A. Bondeau, W. Cramer, J.O. Kaplan, … and S. Venevsky. (2003). Evaluation of ecosystem dynamics, plant geography and terrestrial carbon cycling in the LPJ dynamic global vegetation model. *Global Change Biology, Vol 9* (Issue 2), pp. 161-185.

[Skamarock et al., 2008] Skamarock, W. C. and J. B. Klemp. (2008, March). A time-split nonhydrostatic atmospheric model for weather research and forecasting applications. *J. Comput. Phys., Vol. 227* (Issue 7), pp. 3465–3485.

[SOCCR, 2008] SOCCR. (2008). The First State of the Carbon Cycle Report (SOCCR): The North American Carbon Budget and Implications for the Global Carbon Cycle. A Report by the U.S. Climate Change Science Program and the Subcommittee on Global Change Research. Ashville, TN: National Oceanic and Atmospheric Administration, National Climatic Data Center. Retrieved from: http://www.carboncyclescience.gov/sites/default/files/documents/2013/sap2-2-final-all.pdf

[Solomon et al., 2007] Solomon, S., Qin, D., Manning, M., Chen, Z., Marquis, M., Averyt, K., M.Tignor and Miller, H., ed. (2007). IPCC, 2007: Climate Change 2007: The Physical Science Basis. *Contribution of Working Group I to the Fourth Assessment Report of the Intergovernmental Panel on Climate Change.* Cambridge, United Kingdom and New York, NY, USA.

[Spiers et al., 2002] Spiers, G.D., R.T. Menzies, D.M. Tratt, and M. Phillips. (2002). The Laser Absorption Spectrometer for Carbon Dioxide Sink and Source Detection. Proceedings of the Second Annual Earth Science Technology Conference, Greenbelt, MD.

[Spiers et al., 2011a] Spiers, G.D., R.T. Menzies, J. Jacob, L.E. Christensen, M.W. Phillips, Y. Choi, and E.V. Browell. (2011a). Atmospheric CO_2 measurements with a 2 μm airborne laser absorption spectrometer employing coherent detection. *Appl. Opt. Vol. 50* (Issue 14), pp. 2098-2111.

[Spiers et al., 2011b] Spiers, G.D., R.T. Menzies, and J.C. Jacob. (2011b). CO_2 Mixing Ratio Retrievals from JPL Airborne Laser Absorption Spectrometer Flight Campaigns in 2010-11. 2011 AGU Fall Meeting, Paper A21D-0105.

[Spiers et al., 2012] Spiers, G.D., R.T. Menzies, J.C. Jacob, and S. Geier. (2012). The Remote Measurement of Carbon Dioxide by the CO_2LAS Instrument during the 2011 ASCENDS Field Campaign. 2012 AGU Fall Meeting, Paper, A51H-04.

[Spiers et al., 2013] Spiers, G. D., R.T. Menzies, J. Jacob, J.B. Abshire, H. Riris, M.M. Yang, Y. Choi, and B.L. Meadows. (2013). Recent measurement results from the Carbon Dioxide Laser Absorption Spectrometer for the ASCENDS Mission. 2013 AGU Fall Meeting, Paper A23H-02.

[Stephen et al., 2007] Stephen, M., M. Krainak, H. Riris and G. R. Allan. (2007, August). Narrowband, tunable, frequency-doubled, erbium-doped fiber-amplified transmitter. *Optics Letters, Vol. 32* (No. 15), pp. 2073-2075.

[Stohl, 1998] Stohl, A. (1998). Computation, accuracy and applications of trajectories – A review and bibliography. *Atmos. Environ., Vol. 32* (Issue 6), pp. 947–966.

[Sun et al., 2010] Sun, B., A. Reale, D. J. Seidel, and D. C. Hunt. (2010). Comparing radiosonde and COSMIC atmospheric profile data to quantify differences among radiosonde types and the effects of imperfect collocation on comparison statistics. *J. Geophys. Res.: Atmospheres, Vol. 115* (Issue D23), D23104. DOI: 10.1029/2010JD014457

[Sun and Abshire, 2012] X. Sun and J. B. Abshire. (2012). Comparison of IPDA lidar receiver sensitivity for coherent detection and for direct detection using sine-wave and pulsed modulation. *Opt. Express, Vol. 20* (Issue 19), pp. 21291-21304. Retrieved from: http://dx.doi.org/10.1364/OE.20.021291

[Sun et al., 2013] Sun, X., J.B. Abshire, J.F. McGarry, G.A. Neumann, J.C. Smith, J.F. Cavanaugh, D. J. Harding, … and M.T. Zuber. (2013, June). Space lidar developed at the nasa goddard space flight center - the first 20 years. *IEEE Journal of Selected Topics in Applied Earth Observations and Remote Sensing, Vol.6* (No. 3), pp. 1660-1675. DOI: 10.1109/JSTARS.2013.2259578

[Takahashi et al., 1999] Takahashi, T., R. H. Wanninkhof, R A. Feely, R. F. Weiss, D. W. Chipman, N. Bates, J. Olafsson, C. Sabine, and S.C. Sutherland. (1999). Net sea-air CO_2 flux over the global oceans: an improved estimate based on the sea-air pCO_2 difference. Proceedings of the 2nd International Symposium: CO_2 in the Oceans, the 12th Global Environmental Tsukuba, 18-22 January 1999, Tsukuba Center of Institutes.

[Takahashi et al., 2002] Takahashi, T., S. C. Sutherland, C. Sweeney, A. Poisson, N. Metzl, B. Tilbrook, N. Bates, … and Y. Nojiri. (2002). Global sea-air CO_2 flux based on climatological surface ocean pCO_2, and seasonal biological and temperature effects. *Deep-Sea Res.Part II: Topical Studies in Oceanography, Vol.49* (Issues 9-10), pp.1601-1622.

[Takahashi et al., 2009] Takahashi, T., S. C. Sutherland, R. Wanninkhof, C. Sweeney, R. A. Feely, D. W. Chipman, B. Hales, … and N. R. Bates. (2009). Climatological mean and decadal changes in surface ocean pCO_2, and net sea-air CO_2 flux over the global oceans, *Deep Sea Res., Part II, Vol. 56,* pp. 554–577. Retrieved from: http://cdiac.ornl.gov/oceans/LDEO_Underway_Database/air_sea_flux_2010.html. DOI: 10.1016/j.dsr2.2008.12.009

[Tans and Keeling, n.d.] Tans, P., and R. Keeling. (n. d.). Trends in Atmospheric Carbon Dioxide. *National Oceanic & Atmosphere Administration, Earth System Research Laboratory (NOAA/ESRL)*. Retrieved from: http://www.esrl.noaa.gov/gmd/ccgg/trends/

[Tans et al., 1990] Tans, P. P., I. Y. Fung, and T. Takahashi. (1990), Observational Constraints on the Global Atmospheric CO_2 Budget. *Science, Vol. 247,* pp.1431-1438.

[Tarnocai et al., 2009] Tarnocai, C., J.G. Canadell, E.A.G. Schuur, P. Kuhry, G. Mazhitova and S. Zimov. (2009). Soil organic carbon pools in the northern circumpolar permafrost

region. *Global Biogeochemical Cycles, Vol 23* (Issue 2), GB2023. DOI: 10.1029/ 2008GB003327

[Tippett et al., 2003] Tippett, M. K., J. L. Anderson, C. H. Bishop, T. M. Hamill, T. M. and J. S. Whitaker. (2003, July). Ensemble Square Root Filters*. *Monthly Weather Review, Vol. 131 (Issue 7),* pp.1485-1490.

[Tran et al., 2006] Tran, H., C. Boulet, and J.-M. Hartmann. (2006, August). Line mixing and collision-induced absorption by oxygen in the A band: Laboratory measurements, model, and tools for atmospheric spectra computations. *J. of Geophysical Res., Vol. 111 (Issue D15),* pp. 16. D15210, 2006. DOI: 10.1029/2005JD006869

[Uliasz, 1994] Uliasz, M. (1994), Lagrangian particle dispersion modeling in mesoscale applications. *Environmental Modeling, Vol. II,* pp. 71-102.

[UN, 2013] UN. (2013). United Nations Statistics Division. Retrieved from: http://unstats.un.org/unsd/default.htm

[U.S. DOC/NOAA, 2005] U.S. DOC/NOAA OFCM, Washington, D.C. (2005, September). *Federal Meteorological Handbook No. 1 - Surface Weather Observations and Reports.* Retrieved from: http://www.ofcm.gov/fmh-1/fmh1.htm

[Vay et al., 2003] Vay, S. A., J. H. Woo, B. E. Anderson, K. L. Thornhill, D. R. Blake, D. J. Westberg, C. M. Kiley, … and S. R. Nolf. (2003, October). Influence of regional-scale anthropogenic emissions on CO_2 distributions over the western North Pacific. *J. Geophys. Res. Atmospheres, Vol. 108 (Issue D20),* pp. 8801. DOI: 10.1029/2002JD003094

[Wang et al., 2014] Wang, J. S., S. R. Kawa, J. Eluszkiewicz, D. F. Baker, M. Mountain, J. Henderson, T. Nehrkorn, and T. S. Zaccheo. (2014). A Regional CO_2 Observing System Simulation Experiment for the ASCENDS Satellite Mission.

[Wennberg et al., 2012] Wennberg, P. O., W. Mui, D. Wunch, E. A. Kort, D. R. Blake, E. L. Atlas, G. W. Santoni, … and M. L. Fischer. (2012). On the Sources of Methane to the Los Angeles Atmosphere. *Environmental Science & Technology, Vol. 46* (Issue 17), pp. 9282-9289. DOI: 10.1021/es301138y

[Werle et al., 1993] Werle, P., R. Mucke, and F. Slemr. (1993). The limits of signal averaging in atmospheric trace-gas monitoring by tunable diode-laser absorption spectroscopy (TDLAS). *Applied Physics B Photophysics and Laser Chemistry, Volume 57* (Issue 2), pp. 131-139. DOI: 10.1007/BF00425997

[Werle et al., 2004] Werle P. W., P. Mazzinghi, F. D'Amato, M. De Rosa, K. Maurer, F. Slemr. (2004). Signal processing and calibration procedures for in situ diode-laser absorption spectroscopy. *Spectrochimica Acta Part A: Molecular and Biomolecular Spectroscopy, Volume 60* (Issue 8), pp. 1685-1705. DOI: 10.1016/j.saa.2003.10.013

[Wilson et al., 2007] Wilson E.L., E. M. Georgieva, and W. S. Heaps. (2007). Development of a Fabry-Perot interferometer for ultra-precise measurements of column CO_2. *Meas. Sci. Technology, Vol. 18* (Issue 5), pp. 1495-1502, 2007

[Winker et al. 2013] Winker, D. M., J. L. Tackett, B. J. Getzewich, Z. Liu, M. A. Vaughan, and R. R. Rogers. (2013). The global 3-D distribution of tropospheric aerosols as characterized

by CALIOP, *Atmos. Chem. Phys., Vol. 13,* pp. 3345-3361. Retrieved from: www.atmos-chem-phys.net/13/3345/2013/ DOI:10.5194/acp-13-3345-2013

[Wunch et al., 2011] Wunch, D., P. O. Wennberg, G. C. Toon, B. J. Connor, B. Fisher, G. B. Osterman, C. Frankenberg, … and S. C. Wofsy. (2011). A method for evaluating bias in global measurements of CO_2 total columns from space. *Atmospheric Chemistry and Physics, Vol. 11* (Issue 23), pp.12317-12337. DOI: 10.5194/acp-11-12317-2011

[Wunch et al., 2013] Wunch, D., P. O. Wennberg, J. Messerschmidt, N. C. Parazoo, G. C. Toon, N. M. Deutscher, G. Keppel-Aleks, … and J. Notholt. (2013). The covariation of Northern Hemisphere summertime CO_2 with surface temperature in boreal regions. *Atmospheric Chemistry and Physics, Vol. 13*, pp. 9447–9459. DOI: 10.5194/acp-13-9447-2013

[Wysocki et al., 2006] Wysocki, P., T. Wood, A. Grant, D. Holcomb, K. Chang, M. Santo, L. Braun, and G. Johnson. (2006, March 5). High Reliability 49 dB Gain, 13 W PM Fiber Amplifier at 1550 nm with 30 dB PER and Record Efficiency. Optical Society of America / Optical Fiber Communication Conference, Anaheim. ISBN: 1-55752-802-0

[Yang et al., 2006] Yang, F. et al. (2006). Evaluation of the NCEP Global Forecast System at the ARM SGP Site. *Monthly Weather Review, Vol. 134* (Issue 12), pp.3668-90. Retrieved from: http://journals.ametsoc.org/doi/abs/10.1175/MWR3264.1

[Yoshida et al., 2012] Yoshida, Y., N. Kikuchi, I. Morino, O. Uchino, S. Oshchepkov, A. Bril, T. Saeki, … and T. Yokota. (2013). Improvement of the retrieval algorithm for GOSAT SWIR XC02 and XCH4 and their validation using TCCON data. *Atmospheric Measurement Techniques, Vol.* 6 (Issue 6), pp. 1533-1547. DOI: l0.5194/amt-6-1533-2013

[Yu et al., 2003] Yu J., A. Braud, and M. Petros. (2003). 600-mJ, double-pulse 2-μm laser. *Optics Letters, Vol. 28 (Issue 7)*, pp. 540-542. http://dx.doi.org/10.1364/OL.28.000540

[Yu et al., 2012] Yu J., M. Petros, K. Reithmaier, Y. Bai, B. C. Trieu, T. F. Refaat, M. J. Kavaya, and U. N. Singh. (2012). A 2-micron pulsed integrated path differential absorption lidar development for atmospheric CO_2 concentration measurements. 26th International Laser Radar Conference, June 25-29, 2012, Porto Heli, Greece.

[Zaccheo et al., 2014] Zaccheo, T. Scott, Timothy Pernini, Hilary E. Snell, and Edward V. Browell. Impact of atmospheric state uncertainties on retrieved XCO2 columns from laser differential absorption spectroscopy measurements. *Journal of Applied Remote Sensing (SPIE) Vol. 8,* No. 1.

[Zhang et al., 1999] Zhang, T., R. G. Barry, K. Knowles, J. A. Heginbottom, and J. Brown. (1999). Statistics and characteristics of permafrost and ground-ice distribution in the Northern Hemisphere. *Polar Geography Vol. 23* (Issue 2), pp. 147–169.

[Zhao and Tans, 2006] Zhao, C. L. and P.P. Tans. (2006). Estimating uncertainty of the WMO mole fraction scale for carbon dioxide in air. *J. Geophys. Res. Vol. 111* (Issue D8), D08S09. DOI: 10.1029/2005JD006003

[Zimov et al., 1999] Zimov, S. A., S. P. Davidov, G. M. Zimova, A. I. Davidova, F. S Chapin III, M. C. Chapin & J. F. Reynolds. (1999). Contribution of Disturbance to Increasing Seasonal Amplitude of Atmospheric CO_2, *Science, Vol. 284,* pp. 1973-1976.

B. Acronyms

4DVAR	4-Dimensional Variational
ABL	Atmospheric Boundary Layer
ACOS	Atmospheric CO_2 Observations from Space
ACES	ASCENDS CarbonHawk Experiment Simulator
ACS	Attitude Control Subsystem
AD&CS	Attitude Determination and Control System
AER	Atmospheric and Environmental Research
AGCM	Atmospheric General Circulation Model
AIRS	Atmospheric Infrared Sounder
AOM	Acousto-Optic Modulator
APD	Avalanche Photodiode Detector
ASCENDS	Active Sensing of CO_2 Emissions over Nights, Days, and Seasons
A-SCOPE	Advanced Space Carbon and Climate Observation of Planet Earth
AVOCET	Atmospheric Vertical Observations of Carbon Dioxide in the Earth's Troposphere
BBL	Broad Band Lidar
CA	California
CALIPSO	Cloud-Aerosol Lidar and Infrared Pathfinder Satellite Observations
Caltech	California Institute of Technology
CASA	Carnegie-Ames-Stanford-Approach
CBE	Current Best Estimate
CCGG	Carbon Cycle Greenhouse Gas
CCSM	Community Climate System Model
CDF	Cumulative Distribution Function
CDIAC	Carbon Dioxide Information Analysis Center
CFSR	Climate Forecast System Reanalysis
CH_4	Methane, Natural Gas
CIRA	Cooperative Institute for Research in the Atmosphere
CNES	Centre National d'Etudes Spatiales (French Space Agency)
CO_2	Carbon Dioxide
CONUS	Contiguous United States, Continental United States
CSU	Colorado State University

CW	Continuous Wave
DAOD	Differential Absorption Optical Depth
DEM	Digital Elevation Model
DFB	Distributed Feedback
DFB-LD	Distributed Feedback Laser Diode
DIAL	Differential Absorption Lidar
DOD	Differential Optical Depth
DOI	Digital Object Identifier
DRS	DRS Technologies Sensors and Targeting Systems, Inc., in Dallas, TX.
DSS	Dual Spacecraft System
eAPD	electron initiated Avalanche Photodiode Detector
ECMWF	European Centre for Medium-Range Weather Forecasts
EDFA	Erbium Doped Fiber Amplifier
EE8	Earth Explorer 8
EELV	Evolved Expendable Launch Vehicle
EMC	Electromagnetic Compatibility
EMI	Electromagnetic Interference
EnKF	Ensemble Kalman Filter
ENSO	El Niño Southern Oscillation
EnviSAT	Environmental SATellite
EPA	Environmental Protection Agency
ESA	European Space Agency
ESD	Earth Science Division
ESMPO	Earth Systematic Mission Program Office
ESRL	Earth System Research Laboratory
ESRL GMD	Earth System Research Laboratory Global Monitoring Division
ESTO	Earth Science Technology Office
EU	European Union
FF	Fossil Fuel
$FFCO_2$	Fossil Fuel CO_2
FFT	Fast Fourier Transform
FM/CW	Frequency-Modulated/Continuous Wave
FOV	Field of View

FP	Fabry-Perot
FTS	Fourier Transform Spectrometer
FWHM	Full Width at Half Maximum
GAW	Global Atmospheric Watch
GCM	General Circulation Model
GEVS	General Environmental Verification Specification
GFED	Global Fire Emissions Database
GFS	Global Forecast System
GIM	Geostatistical Inverse Modeling
GHG	Green House Gas
GLAS	Geoscience Laser Altimeter System
GMAO	Global Modeling and Assimilation Office, Goddard Modeling and Assimilation Office
GOSAT	Greenhouse gases Observing SATellite
GPP	Gross Primary Production, Gross Primary Productivity
GPS	Global Positioning System
GSFC	Goddard Space Flight Center
Gt	Gigatons
GTOPO30	30-arc second resolution Digital Elevation Model developed by USGS
HgCdTe	Mercury Cadmium Telluride
HITRAN	High Resolution Transmission
Hz	Hertz
IASI	Infrared Atmospheric Sounding Interferometer
IAV	InterAnnual Variability
ICE/Sat	Ice, Cloud and land Elevation Satellite
ICESAT	Ice, Cloud and land Elevation Satellite
IF	Intermediate Frequency
IIP	Instrument Incubator Program
IM-CW	Intensity-Modulated Continuous-Wave
INTEX	Intercontinental Chemical Transport Experiment
INTEX-NA	Intercontinental Chemical Transport Experiment-North America
IPCC	Intergovernmental Panel on Climate Change
IPDA	Integrated Path Differential Absorption

IR	Infrared
ISD	Integrated Surface Database
Exelis	ITT Exelis, Inc.
JPL	Jet Propulsion Laboratory
kHz	Kilohertz (1thousand Hertz)
KTP	Potassium Titanyl Phosphate
LAI	Leaf Area Index
LaRC	Langley Research Center
LAS	Laser Absorption Spectrometer
LBLRTM	Line-By-Line Radiative Transfer Model
LEO	Low Earth Orbit
LGS	Lucent Government Solutions
LIDAR	Light Detection and Ranging
LO	Local Oscillator
LPJ	Lund–Potsdam–Jena Dynamic Global Vegetation Model
LPDM	Lagrangian Particle Dispersion Model
MCR	Mission Confirmation Review
MCT	Mercury Cadmium Telluride
MERRA	Modern Era Retrospective-analysis for Research and Applications
MFLL	Multifunctional Fiber Laser Lidar
MHz	Megahertz (1 million Hertz)
MOPA	Master Oscillator Power Amplifier
NA	North America
NAM	North American Mesoscale Model
NASA	National Aeronautics and Space Administration
NCAR	National Center for Atmospheric Research
NCDC	National Climatic Data Center
NDP	Numeric Data Package
NEE	Net Ecosystem Carbon Exchange
NEP	Noise-Equivalent Power
NGA	Northrop Grumman Aerospace
NOAA	National Oceanic and Atmospheric Administration
NM	New Mexico

NRC	National Research Council
NWP	Numerical Weather Prediction
O_2	Oxygen
OCO	Orbiting Carbon Observatory
OCO-2	Orbiting Carbon Observatory-2
OCO-3	Orbiting Carbon Observatory-3
OD	Optical Depth
ODIAC	Open-source Data Inventory of Anthropogenic CO_2 emission
OFCM	Office of the Federal Coordinator for Meteorology
OPA	Optical Parametric Amplifier
ORNL	Oak Ridge National Laboratory
OSSE	Observing Systems Simulation Experiment
P	Pressure
PCTM	Parameterized Chemistry and Transport Model
PDR	Preliminary Design Review
PIN	PIN diode (PIN corresponds to the diode construction)
PN	Pseudorandom Noise
ppm	Parts Per Million
ppmv	Parts Per Million by Volume
PWG	planar waveguide amplifier
QE	Quantum Efficiency
RAOB	RAdiosonde OBservation
RMS	Root Mean Square
RMSE	Root Mean Square Error
RRV	Railroad Valley, Nevada
SCIAMACHY	SCanning Imaging Absorption Spectrometer for Atmospheric CartograpHY
SH	Southern Hemisphere
SiB3	Simple Biosphere model, version 3
SiB-CASA	Simple Biosphere/Carnegie-Ames-Stanford Approach
SLED	SuperLuminExcent Diode
SNR	Signal to Noise Ratio
SOCCR	State of the Carbon Cycle Report
SPCM	Single Photon Counting Module

SRTM	Shuttle Radar Topography Mission
SSE	Scattering Surface Elevations
STILT	Stochastic Time-Inverted Lagrangian Transport
SZA	Solar Zenith Angle
T	Temperature
TANSO	Thermal And Near infrared Sensor for carbon Observation
TBD	To Be Determined
TBR	To Be Reviewed?
TCCON	Total Carbon Column Observing Network
TVAC	Thermal Vacuum
US	United States
USGS	United States Geological Survey
UTC	Universal Time Coordinated
WBI	West Branch Iowa
WDCGG	World Data Centre for Greenhouse Gases
WMO	World Meteorological Organization
WRF	Weather Research and Forecasting
WV	Water Vapor

C. Detailed Comparison of Modeling Approaches

Table C-1 Detailed Comparison of Modeling Approaches

Modeling Approaches					
	4DVAR-TM5	**4DVAR-PCTM**	**EnKF-GEOS-Chem**	**Bayesian**	**GIM**
Team	OU/Melbourne	CSU-CIRA	CSU-CIRA	GSFC/AER	Stanford-Carnegie
Inversion Method	Four-dimensional variational data assimilation	Four-dimensional variational data assimilation	Ensemble Kalman filter	Batch Bayesian synthesis inversion	Batch geostatistical synthesis inversion
Transport Model	TM5 (Global Eulerian, 6°x4°, winds regridded from 1°x1.25° ECWMF)	PCTM (Global Eulerian, 6°x4.5°, winds regridded from 1°x1.25° MERRA)	GEOS-Chem (Global Eulerian, 2°x2.5°, winds regridded from 1°x1.25° MERRA)	WRF-STILT (Regional Lagrangian particle dispersion model, 40 km WRF meteorology)	WRF-STILT (Regional Lagrangian particle dispersion model, 40 km WRF meteorology)
Domain and Flux Spatial Resolution	Global 6°x4°, with North America nest at 1°x1°	Global 6°x4.5°	Global 2°x2.5° regularization via spatial covariance smoothing	North America 1°x1° (with spatial correlation)	North America 1°x1° (with spatial correlation and constrained by geostatistical model)
Flux Temporal Resolution	Monthly	Weekly	Two weeks	Weekly (with temporal correlation)	3-hourly (with temporal correlation)
Truth Emissions:					
Ocean	Takahashi et al. (2009)	NCAR Ocean Model (Doney et al., 2006; Najjar et al., 2007)	Prior + decreased seasonal cycle	--	--
Anthropogenic	CDIAC/Oak Ridge National Laboratory(ORNL) Numeric Data Package (NDP) 058 v2011	None	Same as Prior	--	VULCAN/ODIAC
Biosphere	CASA-GFED2	LPJ (Sitch et al., 2003)	Prior + enhanced sinks (Amazon, Europe, east Asia)	--	CASA-GFED2
Prior Emissions:					
Ocean	Perturbed Truth	Takahashi, et al. (1999)	Woods Hole Institute (Doney)	--	--
Anthropogenic	Perturbed Truth	None	ODIAC (Oda et al., 2009)	--	--

Modeling Approaches					
	4DVAR-TM5	**4DVAR-PCTM**	**EnKF-GEOS-Chem**	**Bayesian**	**GIM**
Biosphere	Perturbed Truth	CASA land model (Randerson et al, 1997)	SiB3 (Baker et al., 2008)	--	--
Prior Uncertainties:					
Variances	Prior - Truth	Prior - Truth	Estimated by EnKF	Variability of CASA-GFED v3 NEE, scaled up to CSU/NOAA overall magnitudes	Monthly varying (See Shiga et al., 2014.)
Spatial Correlation	0km	0km	800km (land), 1600km (ocean)	Monthly varying (300-650km, Gourdji et al. (2012))	Monthly varying (See Shiga et al., 2014.)
Temporal Correlation	none	None	none	Monthly varying (2-17 days, Gourdji et al. (2012))	Monthly varying (See Shiga et al., 2014.)

EnKF Inversion Detail

NEE is optimized by estimating scaling factors to a priori GPP and respiration. As opposed to 4DVAR techniques that provide a simultaneous flux estimate across time, the EnKF proceeds sequentially, thus the prior flux (first guess) evolves through time. The initial guess for mean flux is the unperturbed flux case (annual net zero NEE SiB3 fluxes described above) while the 'truth' consists of the initial guess plus the tested perturbations. The initial uncertainty consists of an independent 15% standard deviation on both GPP and total respiration, Gaussian distributed. Due to the independent errors, this allows for the uncertainty on the difference (NEE) to be even larger than 15%. The correlation structure *within* GPP (and respiration) is then formed from an isotropic exponential covariance model which effectively constrains the solution to be smooth in geographic space (Table C-1 in Appendix C). This "initial guess" then evolves through time by weighting incremental adjustments to the state estimate over time with the original prior flux guess at time zero, as well as a small multiplicative inflation factor (5%). With this setup, there is an implicit assumption made regarding where we think flux corrections should occur, i.e. in locations of strong a priori flux but otherwise there are no a priori assumptions made on where the correction will be made. The strength of the EnKF is providing explicit uncertainty estimates, as shown in **Error! Reference source not found.**, however we note that these are heavily dependent upon the nature of the propagation of the covariance between assimilation cycles, which often requires extensive testing and tuning.

Box C-1 Calculation of Model-Data Mismatch Errors

The Bayesian and GIM OSSEs carried out by teams at GSFC and Carnegie-Stanford use only observation locations that fall within the domain used in the WRF meteorological runs (excluding those within 400 km of the boundaries to provide adequate WRF coverage to simulate back trajectory calculations inside the domain). Soundings with total column cloud-plus-aerosol OD > 0.7 are rejected. The errors for each 5 km (0.74 s) individual CALIPSO observation point are aggregated over 10-s intervals to increase signal-to-noise for the pseudo-data, using the formula

$$\sigma(10\text{s}) = \sqrt{\frac{\sum_{i=1}^{N} \sigma(5\text{km})_i^{\,2}}{N^2}} \qquad \text{(C-1)}$$

where N is the number of valid 5 km observations across the 10-s span. The uncertainties in the series of 10-s pseudo-data are assumed to be uncorrelated.

The 4D-VAR-TM5 and EnKF OSSEs led by the teams at OU and CSU first identify 'n' continuous (along track) soundings that fall within a single grid cell of their model. Soundings with total column OD > 0.3 are rejected. Equation 3-1 is used to calculate the monthly scale factors for each observation. Finally, a variance weighted mean across all the observations in the grid cell is calculated.

In the 4D-VAR-PCTM OSSEs a single measurement is applied per orbit for each model grid box that the satellite views. This measurement characterizes the information content of all the individual measurements taken along-track inside the box. Furthermore, the same measurement uncertainty value is assumed for all satellite crossings in a single month per grid box, whatever the optical depth conditions happen to be during each overpass: the applied uncertainty in increased statistically to account for climatological optical depth conditions at that grid box during that month. If a grid box has an optical depth of zero half the time and infinity the other half, the uncertainty applied will be √2 times the clear-sky value. Using the monthly scale factors from Equation 3-1, the measurement uncertainties applied for any grid box crossing in the assimilation are given by

$$\sigma = f\sigma_{RRV}\sqrt{P_o / P} \qquad \text{(C-2)}$$

where P is the time that the satellite FOV falls within the grid box in [sec], and P_o = 10 sec is the base time that the uncertainties are referenced to.

D. ASCENDS Surface Reflectance Considerations

This section documents the rationale and numerical values for spectral lidar backscatter that were used in the random error calculations for the ASCENDS OSSE modeling through 2014. For further discussion and updated reflectance results from experimental measurements see Sections 5.3.3, 5.3.4, and 5.5.1.

1. Land Surfaces

The IPDA approach depends on the bidirectional reflectance from land or ocean surface to provide the backscatter signals that are used to measure the differential absorption due to the atmospheric absorber (e.g., CO2). In the reflectance nomenclature, the lidar data are a measure of the surface bidirectional reflectance factor with the view angle direction being the same as the incident angle (Nicodemus, et al., 1977), i.e., backscatter. If the surface material can be considered Lambertian, then bidirectional reflectance distribution function (BRDF) is constant for all reflected angles. Most of the Earth's land surfaces, however, have BRDF properties that deviate from Lambertian; consequently consideration of the hot spot, or opposition effect, is important. Even if a surface is Lambertian to a good approximation, the backscatter enhancement due to the hot spot effect can be significant (Hapke, 1986; Hapke et al., 1996; Breon et al., 2002). Amediek et al. (2009) observed that incorporation of a hotspot enhancement was necessary to make their 1.57-μm airborne lidar reflectance measurements consistent with predictions based on MODIS measurements.

Hot spot enhancements from various land surface types have been observed and reported using airborne spectrometers (Camacho-de Coca et al., 2004) and Earth orbiting Polarization and Directionality of Earth Reflectances (POLDER) instrument data (Breon et al., 2002). In addition measurements by Kaasalainen et al. (2006) in the visible and GLAS observations at 1064 nm show strong evidence of an opposition peak in snow reflectance data. The same physical mechanisms for an opposition enhancement should be present at 1.57 and 2.05 μm (Nayar and Oren, 1995.) Disney et al. (2009) have attempted to quantify the lidar reflectivity enhancement due to the hot spot effect, using vegetation structural models and Monte Carlo ray tracing as well as MODIS and POLDER datasets. One consistent inference from these investigations is that the magnitude of the enhancement varies over a wide range even within a particular land cover type.

The ASCENDS XCO_2 measurement precision is related to the strength of the surface backscattering when illuminated by a nadir-pointed lidar system. The surface backscatter (β) is larger than would be calculated from a diffuse reflectivity/albedo (α) in the zenith direction (α/π for a Lambertian surface), and this enhancement factor (EF) is applied to the diffuse reflectivity to represent the lidar surface backscatter factor, $\beta = EF\ \alpha/\pi$. The publication by Disney et al. (2009) attempts to quantify the value of EF for a solar zenith angle near zero for a number of land cover types. In their paper EF was found to range from 1.10 to 1.33 with an average of 1.23 for six land types (not including snow/ice).

Based on this work, the ASCENDS OSSE's use the MODIS 1.62-μm and 2.13-μm diffuse reflectances/albedos (α) with an average EF value of 1.23 for non-snow surfaces as determined from NASA Goddard's Global Modeling and Assimilation Office (GMAO) weather analysis. For the case of missing MODIS 1.62-μm reflectance data over land, we use a surface albedo of 0.2 with EF = 1.23 to fill in the data gaps.

2. Snow/Ice Surfaces

Here we have used EF = 1 for snow/ice surfaces in the current ASCENDS backscatter calculations. Continued lidar measurements of snow/ice backscatter at 1.57 and 2.06 μm are needed to improve snow/ice surface reflectance characterization and further improve modeling of ASCENDS measurements over these surfaces.

The Dumont et al., 2010, paper shows that the MODIS 1.62-μm reflectances (α) at large solar zenith angles (SZA) are significantly larger than the reflectances at low SZA's (e.g., at SZA = 60^o, $\alpha = 0.1$, while at SZA = 0^o, $\alpha = 0.05$). Based on this dataset we use a constant snow/ice albedo of 0.05 at 1.62 μm. In addition, as shown by Hudson et al. (2006), Dumont et al. (2010), and many other authors, the snow/ice albedo at 1.57 μm is about 70% of the albedo at 1.62 μm. Therefore, in lieu of using the MODIS reflectances for snow and ice, which are generally at high SZA's, we use a constant albedo for snow and ice of 0.035 at 1.57 μm.

For ice and land surfaces with a snow cover fraction >0.95, as defined by the GMAO weather analysis, the albedo is set to 0.035. Over land, where MODIS reflectances are unrealistic (that is α <0.035 or α >1.0), or where MODIS reflectance data are missing, backscatter data is filled with α from 0.2 to 0.035 and EF from 1.23 to 1.0 with both parameters scaled based on the snow cover fraction from 0 to 0.95. The same procedure is applied for backscatter at 2.06 μm using fill values of $\alpha = 0.1$ for land and 0.01 for snow/ice.

The numbers in the tables below were used for all calculations in the ASCENDS white paper initial release. Subsequent measurements of lidar backscatter from aircraft over snow at 1.57 and 2.06 μm (Menzies et al., 2014) as well as review of data from Aoki et al., (2000), however, indicate that our default estimates for these values (0.0111 and 0.0032 sr^{-1}, respectively) are too low. Backscatter values of 0.016 sr^{-1} for 1.57 μm wavelength and 0.0064 sr^{-1} for 2.06 μm are more representative of snow in general, and these numbers are recommended for subsequent estimation of ASCENDS random errors (see Section 5.3.3, 5.3.4, and 5.5.1).

3. Water Surfaces

The strength of laser backscatter from a water surface from a nadir-directed laser beam depends on wind speed. Hu et al. (2008) derived the following functional relationship between the CALIPSO lidar backscatter (β) measurements at 1.064 μm and AMSR-E surface wind speed (V) measurements:

$\beta = 0.0193/4\pi/mss$

where mss = 0.0146*sqrt(V) for wind speeds below 7 m/s or

mss = 0.003 + 0.00512*V for wind speeds of 7 to 13.5 m/s.

For wind speeds above ~13.5 m/s, there can be a mixture of white caps and foam on the sea surface, and at these wind speeds we recommend using a constant surface backscatter equal to the backscatter at 13.5 m/s. This approach is consistent with the results in the Lancaster et al. [2005] paper which only had one data point at ~16 m/s, and its value was nearly the same as that at 13.5 m/s.

In addition, it is believed that these equations can be used down to very low wind speeds due to the relatively large size of the laser footprint (of order 100 m) and the ubiquitous nature of low frequency gravity waves on most large water surfaces (e.g., oceans, Great Lakes). For these conditions, it is estimated by Hu (private communication) that the backscatter would peak at a wind speed value of about 1 m/s.

For estimating the ocean backscatter, the OSSE's use the global GMAO 10-m wind speed analysis with the above relationships given by Hu.

4. Reference Surface and Atmosphere for Scaling of ASCENDS Measurements

For the scaling of the ASCENDS XCO_2 measurement precision, we have chosen to normalize the global land and water backscatter reflectances to the Railroad Valley (RRV), NV, backscatter reflectance and the global aerosol/cloud transmissions to an assumed aerosol/cloud-free condition over RRV.

The average value of the diffuse reflectance for RRV was found to be 0.45 at 1.57 μm and 0.41 at 2.05 μm (Kuze et al., 2011). Following the above treatment for land surface reflectances, the reference backscatter values for RRV are $\beta = 1.23*0.45/\pi = 0.176$ sr^{-1} and $\beta = 1.23*0.41/\pi = 0.160$ sr^{-1}, respectively.

Please see Box 3.1 for discussion of scaling the random errors in the ASCENDS XCO_2 measurement simulations. A series of OSSE's were run with different generic ASCENDS XCO_2 measurement precisions, which are presumed to be valid over RRV under clear (no aerosol/cloud) conditions. These generic XCO_2 measurement precisions are modified based on how the surface backscatter and aerosol/cloud transmissions deviate from the reference conditions over RRV.

The following table summarizes the relationships discussed above that are used to define the surface backscatter used in the ASCENDS OSSE's.

Summaries of Surface Backscatter Relationships

Table D-1 For 1.57-μm CO_2 Column Measurements

Surface Type	MODIS 1.62-μm Reflect. (α)	GMAO Snow/Ice Fract. (F)	GMAO Wind Spd (V, m/s)	Surface Backscatter (β, sr^{-1})
Land	$0.035 \le \alpha \le 1.0$	$0 \le F \le 0.95$	N/A	$\beta=(1.23-0.23*F)(\alpha/\pi)$
	$\alpha<0.035$, $\alpha>1.0$, or α missing	$0 \le F \le 0.95$	N/A	$\beta=(1.23-0.23*F)(0.2-0.165*F)/\pi$
	All cases	$F>0.95$	N/A	$\beta=0.035/\pi=0.0111$
Water	N/A	no ice	$V \le 1$	Set V=1, $\beta=0.105$
	N/A	no ice	$1<V<7$	$\beta=0.00154/(0.0146*\sqrt{V})$
	N/A	no ice	$7 \le V \le 13.5$	$\beta=0.00154/(0.003+0.00512*V)$

	N/A	no ice	V>13.5	Set V=13.5, β=0.0213
	N/A	ice	N/A	β=0.035/π=0.0111
Reference: Railroad Valley	N/A	N/A	N/A	β=1.23*0.45/π=0.176 at 1.57 μm

Table D-2 For 2.06-μm CO_2 Column Measurements

Surface Type	**MODIS 2.1-μm Reflect. (α)**	**GMAO Snow/Ice Fract. (F)**	**GMAO Wind Spd (V, m/s)**	**Surface Backscatter (β, sr^{-1})**
Land	0.01≤α≤1.0	0≤F≤0.95	N/A	β=(1.23-0.23*F)(α/π)
	α<0.01, α>1.0, or α missing	0≤F≤0.95	N/A	β=(1.23-0.23*F)(0.1-0.09*F)/π
	all cases	F>0.95	N/A	β=0.01/π=0.00318
Water	N/A	no ice	N/A	Same as for 1.57 μm
	N/A	ice	N/A	β=0.01/π=0.00318
Reference: Railroad Valley	N/A	N/A	N/A	β=1.23*0.41/π=0.161 at 2.0 μm

Table D-3 For 1.26-μm O_2 Column Measurements

Surface Type	**MODIS 1.24-μm Reflect. (α)**	**GMAO Snow/Ice Fract. (F)**	**GMAO Wind Spd (V, m/s)**	**Surface Backscatter (β, sr^{-1})**
Land	0.035≤α≤1.0	0≤F≤0.95	N/A	β=(1.23-0.23*F)(α/π)
	α<0.035, α>1.0, or α missing	0≤F≤0.95	N/A	β=(1.23-0.23*F)(0.31)/π
	0.035≤α≤1.0	F>0.95	N/A	β=0.31/π=0.0987

Water	N/A	no ice	N/A	Same as for 1.57 μm
	N/A	ice	N/A	β=0.36/π=0.115
Reference: Railroad Valley	N/A	N/A	N/A	β=1.23*0.43/π=0.168 at 1.26 μm

Table D-4 For 0.765-μm O_2 Column Measurements

Surface Type	**MODIS 0.86-μm Reflect. (α)**	**GMAO Snow/Ice Fract. (F)**	**GMAO Wind Spd (V, m/s)**	**Surface Backscatter (β, sr^{-1})**
Land	0.035≤α≤1.0	0≤F≤0.95	N/A	β=(1.23-0.23*F)(0.95+0.13*F)(α/π)
	α<0.035, α>1.0, or α missing	0≤F≤0.95	N/A	β=(1.23-0.23*F)(0.33)/π
	0.035≤α≤1.0	F>0.95	N/A	β=(1.23-0.23*F)(1.08)/(α/π)
Water	N/A	no ice	N/A	Same as for 1.57 μm
	0.035≤α≤1.0	ice	N/A	β=1.08(α/π)
	missing	ice	N/A	β=0.85/π=0.271
Reference: Railroad Valley	N/A	N/A	N/A	β=1.23*0.43/π=0.168 at 0.76 μm